Investigating the Potential of Therapeutic Candidates and Their Mechanism of Action Against Lung and Breast cancer

A Thesis Submitted
In Partial Fulfillment of the Requirements
For the Degree of

DOCTOR OF PHILOSPHY

by

Kumari Bhavya

(2019BMZ0002)

DEPARTMENT OF BIOMEDICAL ENGINEERING

INDIAN INSTITUTE OF TECHNOLOGY ROPAR

December, 2024

Dedicated to
my beloved mother
&
family

Declaration of Originality

I hereby declare that the work which is being presented in the thesis entitled **Investigating the Potential of Therapeutic Candidates and Their Mechanism of Action Against Lung and Breast Cancer** has been solely authored by me. It presents the result of my own independent investigation/research conducted during the time period from **July, 2019** to **July 2024** under the supervision of **Dr. Durba Pal**, Assistant Professor, **Indian Institute of Technology Ropar**. To the best of my knowledge, it is an original work, both in terms of research content and narrative, and has not been submitted or accepted elsewhere, in part or in full, for the award of any degree, diploma, fellowship, associateship, or similar title of any university or institution. Further, due credit has been attributed to the relevant state-of-the-art and collaborations (if any) with appropriate citations and acknowledgments, in line with established ethical norms and practices. I also declare that any idea/data/fact/source stated in my thesis has not been fabricated/ falsified/ misrepresented. All the principles of academic honesty and integrity have been followed. I fully understand that if the thesis is found to be unoriginal, fabricated, or plagiarized, the Institute reserves the right to withdraw the thesis from its archive and revoke the associated Degree conferred. Additionally, the Institute also reserves the right to appraise all concerned sections of society of the matter for their information and necessary action. If accepted, I hereby consent for my thesis to be available online in the Institute's Open Access repository, inter-library loan, and the title & abstract to be made available to outside organizations.

Signature

Name: Kumari Bhavya
Entry number: 2019bmz0002
Program: Ph.D.
Department: Biomedical Engineering
Indian Institute of Technology, Ropar
Rupnagar, Punjab (140001)
Date: December 19, 2024

Acknowledgements

"***Where there is a will, there is a way***." This journey, filled with constant determination and hard work, has led me to the completion of my PhD. I would first like to express my deepest gratitude to the Almighty **Lord Krishna** and my mom (**Dr. Manorma Jhaa**), whose unwavering support and blessings have been my guiding light.

I extend my deepest and heartfelt gratitude to my advisor, **Dr. Durba Pal**, for her unwavering guidance, encouragement, and support throughout my PhD journey at IIT Ropar. Despite facing her own critical challenges, she stood by me, especially in shaping my future. Her mentorship has been key to shaping my research and academic journey, and I am deeply grateful for her support in making this possible.

I also extend my gratitude to the **Ministry of Education** (MoE) for providing the fellowship that supported my research. I am grateful to IIT Ropar's Biomedical Engineering (BME) infrastructure and the Central Research Facilities for their excellent lab facilities. My thanks also go to **Dr. Rajesh**, the Head of the Department of BME, technical and non-technical staffs for providing the essential departmental resources.

I am deeply grateful to my collaborators: **Dr. Rambabu Gundla**, for providing the IMPA derivatives compound; **Dr. Nilkanth Nirmalkar**, for supplying L-ONB; **Dr. Jaspreet Randhawa**, for providing liposome nanoparticles; and a special thanks to **Dr. Anita Kamra Verma** for offering laboratory facilities for animal work. I also want to acknowledge **Dr. Suman Das Gupta** from Tezpur University for his support and scientific discussions.

I sincerely thank my chairperson **Dr. Srivastava Naidu** doctoral committee members **Dr. Yashveer Singh**, **Dr. Tarak Mondal**, and **Dr. Anupam Bandyopadhyay**, for their guidance and constructive feedback throughout my research.

I would like to express my gratitude to **DST SERB**, **Government of India**, and the Ministry of Education for awarding me the international travel grant to attend the ESMO Congress 2023 in Madrid. Their support enabled me to present my work at the conference.

I would like to extend my deepest gratitude to my friend **Dr. Deepa Negi** for her unwavering support throughout this journey. She provided invaluable assistance not only in the laboratory but also offered immense emotional and mental encouragement, both during the challenges of my experiments and beyond, also I would like to thanks to **Bijit Basumatary**, **Rahul Shukla**, **Adarsha Narayan Mallick**, and **Varun Rathi** for their continuous support through the ups and downs of my PhD journey. I would also like to thank my labmates **Soumyajit**, **Moyna**, **Ankit**, **Ram Prasad**, **Akanksha**, **Afrin**, **Dr. Debarun** and **Dr. Leena** for creating a supportive and positive environment during this time. I would like to thanks to **Karishma** and **Priyanka** for her incredible support in animal work, as well as I extend my heartfelt gratitude to **Yashika** for always being available whenever I needed. I am also deeply thankful to **Arpita** and **Deepika** for their help with western blot imaging using the Chemidoc facility,

and to **Vatan**, **Prithavi**, **Dr. Momita** and **Dr. Nahida** for their support and encouragement throughout my journey.

I am deeply grateful to my friends, **Dr. Saket Patel**, **Chitra** and **Vimal Keerthi**, for their constant support and encouragement, despite the distance. Their belief in me has been truly inspiring. I would like to extended thanks to **Meghna** and **Rajil** for continuous support throughout this journey.

Finally, I owe my deepest thanks to my father (**Dr. Satendra Prasad Thakur**), my entire family, especially my **Didi** (**Bhawna Mishra**) **Jiju** (**Murari Mishra**), my nephew **Pulkit**, who has been continuously available for me no matter what, and **Peehu** and **Prem**. Also I deeply thank to **Dr. Krishna Kant Sharma**, **Aparajita Sharma** and his family, whose love and encouragement have been a constant source of strength, without my families support and love it was impossible to reach here.

I sincerely thank our funding agencies - **DST SERB India**, **DBT Wellcome**, and **DBT Fund -** for their generous support and funding, which made this research work possible. Finally, I would like to extend my heartfelt thanks to everyone who has directly or indirectly supported me throughout this journey. I sincerely apologize if I have inadvertently missed acknowledging anyone. Your contributions, no matter how small, have been invaluable.

Certificate

This is to certify that the thesis entitled "**Investigating the Potential of Therapeutic Candidates and Their Mechanism of Action Against Lung and Breast Cancer"**, submitted by **Kumari Bhavya** (2019BMZ0002) for the award of the degree of **Doctor of Philosophy** of Indian Institute of Technology Ropar, is a record of bonafide research work carried out under my (our) guidance and supervision. To the best of my knowledge and belief, the work presented in this thesis is original and has not been submitted, either in part or full, for the award of any other degree, diploma, fellowship, associateship or similar title of any university or institution.

In my opinion, the thesis has reached the standard fulfilling the requirements of the regulations relating to the Degree.

Signature of the Supervisor

Name: Dr. Durba Pal
Associate Professor
Department of Biomedical Engineering,
Indian Institute of Technology Ropar,
Rupnagar, Punjab 140001
Date: December 19, 2024

Lay Summary

Cancer is a global health challenge; among them, lung and breast cancer are top-ranked and one of the leading causes of death throughout the world. The challenges include dealing with solid tumors/cancer that doesn't respond to drugs, or therapies due to low oxygen levels (hypoxia) within the microenvironment. In this thesis, we have explored three different therapeutic approaches and their efficacy against non-small cell lung cancer and triple negative breast cancer. We have synthesized and tested fifteen new compounds called imidazo[1,2-a] pyridine (IMPA) derivatives by combining them with another chemical, 2-amino-4H-pyran, to improve their effectiveness against non-small cell lung cancer (NSCLC). These derivatives showed potent anti-cancer effects by increasing oxidative stress, and activating programmed cell deaths. Moreover, delivering oxygen directly to the tumor with tiny oxygen-carrying bubbles (L-ONBs), diminished the aggressiveness of lung and breast tumors by destabilizing HIF-1α. Additionally, we found hypoxia induced Zeb1 promotes endothelial cells formation in 3D tumor spheroids, thus we used a gene therapy approach with siRNA therapeutics targeting Zeb1 to prevent new blood vessel formation within tumor.

In a nutshell, we explored the mechanistic action of three different therapeutic approaches: IMPA derivatives as synthetic drug, L-ONBs as advanced oxygen-based therapy, and LNPZeb1siRNA as targeted gene therapy to combat against lung and breast tumors, aiming to overcome drug resistance, halt tumor aggression, and prevent new blood vessel formation in low-oxygen conditions.

Abstract

Solid tumors are a major global public health challenge, characterized by limited treatment options, poor prognosis, and high mortality rates. According to WHO GLOBOCAN 2022 data, lung cancer has an incidence of 12.4% and a mortality rate of 18.7%, while breast cancer ranks second with an incidence of 11.6% and a mortality rate of 6.9%. Current treatments for lung and breast cancers include surgery, radiation, and chemotherapy. Despite chemotherapy being a key treatment, it is associated with drug resistance and non-specific toxicity. Due to a lack of targeted therapies, patients continue to receive drugs like docetaxel, doxorubicin, and cisplatin, which have severe side effects, highlighting the urgent need for advanced therapeutic strategies. Tumor hypoxia drives progression, metastasis, and drug resistance by stabilizing HIF-1α, which activates pathways involved in angiogenesis, apoptosis, and epithelial-to-mesenchymal transition (EMT). Zeb1, a hypoxia-induced transcription factor, promotes angiogenesis and metastasis by upregulating VEGF. Targeting Zeb1 may disrupt pro-angiogenic and immunosuppressive roles of macrophages within the tumor microenvironment (TME), offering a promising approach for cancer therapy.

In this study, *firstly,* we synthesized fifteen novel imidazo[1,2-a] pyridine (IMPA) derivatives by hybridizing imidazo[1,2-a] pyridine with 2-amino-4H-pyran, aiming to develop potent anti-cancer agents. Among them five derivatives (IMPA-2, -5, -6, -8, and -12) showed significant cytotoxicity against lung cancer cells, promoting apoptosis and cell cycle arrest by upregulating p53-mediated genes and enhancing NOX activity. *Secondly,* rapid proliferation of cancer cells in solid tumors creates a hypoxic microenvironment, promoting aggressiveness and resistance to conventional chemotherapies. To mitigate this, oxygen delivery at the tumor site is done by developing of highly efficient lipid-shelled ONBs (L-ONBs) that significantly reduced lung and breast cancer aggressiveness by destabilizing hypoxia-inducible factor 1α (HIF-1α), thereby inhibiting cancer cell invasion and migration. *Lastly,* we developed highly efficient, less toxic cationic lipid-based nanoparticles (LNPs) using DOTAP and DC-Chol for delivering Zeb1siRNA to target tumor angiogenesis and also revealing Zeb1's role in converting tumor macrophage into endothelial like cell phenotypes the observed plasticity of TAMs suggests that targeting Zeb1 may also disrupt the pro-angiogenic and immunosuppressive roles of macrophages within the TME, offering a multifaceted approach to cancer therapy. Overall, our findings suggest that novel IMPA derivatives, L-ONBs, and LNP conjugated Zeb1siRNA hold promise as innovative therapeutic candidates/strategies for treating NSCLC, TNBC, and other solid tumors, by addressing key challenges such as chemoresistance and hypoxia.

Keywords: Solid tumor; Hypoxia; Angiogenesis; Metastasis; Therapeutic intervention; Zeb1; Gene therapy; IMPA; L-ONB; Zeb1SiRNA

List of Publications from Thesis

Research articles

1. **Bhavya, K.,** Mantipally, M., Roy, S., Arora, L., Badavath, V. N., Gangireddy, M., ... & Pal, D. (2022). Novel imidazo [1, 2-a] pyridine derivatives induce apoptosis and cell cycle arrest in non-small cell lung cancer by activating NADPH oxidase mediated oxidative stress. *Life Sciences*, *294*, 120334.
2. **Bhavya, K**.; Agarwal, K.; Negi, D.; Niveria, K.; Singh, Y.; Kamra, A.; Dasgupta, S.; Nirmalkar, N.; Pal, D. (2024). Oxygen Nanobubbles Halt Tumor Aggression and Metastasis by Inhibiting Hypoxia-Induced Epithelial-to-Mesenchymal Transition in Lung and Mammary Adenocarcinoma. *ACS Applied Nano Materials,* 25198-25211.

Review articles

1. Kalia, M., **Bhavya, K**., & Pal, D. (2024). Tumor Microenvironment Regulates Immune Checkpoints: Emerging Need of Combinatorial Therapies. *Current Tissue Microenvironment Reports*, *5*(1), 1-11.

Conference Proceeding

1. **Bhavya, K**., Agrawal, K., Negi, D., Niveria, K., Verma, A. K., Singh, Y., ... & Pal, D. (2023). 2310P Oxygen nano-bubbles attenuate hypoxia-induced tumour malignancy in tumour xenograft models. *Annals of Oncology*, *34*, S1180.

Book chapter

1. Patra, D., **Bhavya, K**., Ramprasad, P., Kalia, M., & Pal, D. (2023). Anti-cancer drug molecules targeting cancer cell cycle and proliferation. Advances in Protein Chemistry and Structural Biology, 135, 343-395.

2. Arora L.; Kalia M.; **Bhavya K**, Pal D. (2023). Oxidative stress: A source of cellular plasticity and tumor heterogeneity**.** Nova Science Publishers DOI: https://doi.org/10.52305/TRSI2511.

Manuscript to be submitted

1. **Bhavya, K**.;Randhawa, J.; Kamra A.; Pal, D.; Understanding the role of Zeb1 in tumor microenvironment and Targeting Tumor Angiogenesis by using Novel Lipid Nanoparticles Encapsulating Zeb1 siRNA (Manuscript under preparation).
2. Vora, Y., **Bhavya, K.,** Pal, D., Kuperkar, K. Solubility of anticancer drug (Quercetin) in Deep Eutectic Solvent (DES): Experimental and Molecular Dynamics Study (Manuscript under preparation).

Patent

1. Mantipally Manohar, Gundla Rambabu, Pal Durba, **Kumari Bhavya** Badavath Vishnu Nayak. 2-Amino-4H-Pyran coupled imidazo[1,2-a] pyridine Compounds, compositions and method of synthesis thereof. Patent no. 202111040855 dated 09.09.2021.

List of Publications from Collaborations

Research articles

1. Singh, G., Mittal, M., Singh, J., Gill, A. S., Pal, D., & **Bhavya, K**. (2024). Enhancing the performance of reinforced hydroxyapatite coatings through post coating treatment. *Results in Surfaces and Interfaces*, *14*, 100207.
2. Negi, D., **Bhavya, K**., Pal, D., & Singh, Y. (2024). Acemannan coated, cobalt-doped biphasic calcium phosphate nanoparticles for immunomodulation regulated bone regeneration. *Biomaterials Science*.
3. Mukherjee., S.; **Bhavya., K**.; Dan., S.; Pal., D.; Sah., M.K.; Exploring the role of keratin nanoparticles loaded vitamins for repurposing in cancer therapy via inhibiting MCM7 oncoprotein. Journal of material chemistry B *(under press).*
4. Vora, Y**., Bhavya, K**., Pal, D., Kuperkar, K. Solubility of anticancer drug (Quercetin) in Deep Eutectic Solvent (DES): Experimental and Molecular Dynamics Study.

List of conferences attended

1. Participated in 9th Annual Cell and Gene Therapy Symposium; Aug 1st to 3rd 2024 organized by centre for stem cell research CMC Vellore, India (**Poster**).
2. Participated in National Science Day at IIT Ropar, Punjab, delivering an oral presentation on Feb 28, 2024 (**Oral Presentation**).
3. Attended 5 days International Conference ESMO Congress 2023 (European Society for Medical Oncology); Oct 20 to 24th 2023 IFEMA Convention center, Madrid, Spain (**Poster**).
4. Attended 4 days International Conference BIO-Remedi 2022 (International Conference on Biomaterials, Regenerative Medicine and Devices); Dec 14th to 18th 2022 IIT Guwahati, Assam, India (**Poster**).
5. Participated in an Invited talk at 3rd International Conference on Cell and experimental Biology (CEB-2022); April 18-20,2022/Hybrid/Boston, MA USA (**Oral Presentation**).
6. Attended Two – Day International conference Via virtual Platform on "Nanomedicine: Biomolecules For human Health- (NBHH 2021); Sep 27-28, 2021 at Kirori Mal College University of Delhi, India (**Oral Presentation**).
7. Attended 2-Days International conference on "International Symposium on Emerging Trends & Challenges in Cancer Chemoprevention Diagnosis & Therapeutics; Feb 17-18, 2020 at Department of Molecular Biology & Biotechnology, Tezpur University, Guwahati, India (**Poster**).

Awards and Honors

1. Received a **SERB International Travel Grant** by Govt. of India, for financial assistance for participating in "ESMO Congress 2023, Spain 20th -24th oct 2023.
2. **Best oral presentation award** for presentation of research work at NBHH-2021 conference (27th-28th Sep 2021) Delhi University, India.
3. **Secured top 30 Rank All India level** Fight Corona Ideathon March 27th- 29th AICTE, MHRD innovation cell, and FORGE.
4. **Best Poster presentation award**, for presentation of research work at Tezpur University in an International conference (17th -18th Feb 2020).

Table of Contents

List of Figures

List of Tables

Abbreviations

ABC	ATP binding cassette
AKT	AK strain transforming/Protein kinase B
ALK	Anaplastic lymphoma kinase
AP-1	Activator protein-1
AR	Androgen receptor
ARNT	Aryl hydrocarbon receptor nuclear translocator
ASR	Age standardized incidence rates
BALB/c	Bagg albino mice/colour
BAK-1	BCL-2 antagonist/killer -1
BAX	BCL-2 associated X-protein
BCA	Bicinchoninic acid
BCL-2	B-cell lymphoma 2
BRAF	v-raf murine sarcoma viral oncogene homolog B1
BRCA1/2	Breast cancer gene 1/2
BSA	Bovine serum albumin
4EBP1	Eukaryotic translation initiation factor 4E binding protein
CBP	cAMP-response element binding protein
C57BL/6	C57 black 6
CD11b	Cluster of differentiation molecules 11b
CD31	Cluster of differentiation 31
CK5/6	Cytokeratin 5/6
CAF	Cancer associated fibroblast
CXCR-4	C-X-C chemokine receptor type 4
CREB	Cyclic AMP-responsive element binding protein
DC-Chol	3β- [N- (N', N-dimethylaminoethane) carbamoyl]-cholesterol
DCIS	Ductal carcinoma in situ
DCFDA	2',7' – dichlorofluorescein diacetate
DOTAP	1,2-dioleoyl-3-trimethylammonium propane
DOX	Doxorubicin
DNA	Deoxyribonucleic acid

DPPC	Dipalmitoyl phosphatidylcholine
ECs	Endothelial cells
EGFR	Epidermal growth factor receptor
EMT	Epithelial to mesenchymal transition
EPR	Enhanced permeability and retention effect
ER	Estrogen receptor
ERK	Extracellular signal regulated kinase
FACS	Fluorescence activated cell sorting
FESEM	Filed emission scanning electron microscope
FGFR1	Fibroblast growth factor receptor-1
FITC	Fluorescein isothiocyanate
FOXO3	Forkhead Box O3
GEPIA	Gene expression profiling interactive analysis
GLUT-1	Glucose transporter type-1
GSK	Glycogen synthase kinase -1
HER2/neu	Human epidermal growth factor receptor 2/neu protooncogene
HIF-1α	Hypoxia inducible factor-1 alpha
HRE	Hypoxia response element
IARC	International agency for research on cancer
IDC	Invasive ductal carcinoma
IHC	Immunohistochemistry
ILC	Invasive lobular carcinoma
IMPAs	Imidazo [1,2-a] pyridine derivatives
iPSC	Induced pluripotent stem cell
JAK	Janus kinase
JNK	c-Jun N-terminal kinase
KRAS	Kirsten rat sarcoma viral oncogene homolog
LAR	Luminal androgen receptor
LCIS	Lobular carcinoma in situ
LNP	Liposome nano particle
L-ONB	Liposomal oxygen nanobubble

LUAD	Lung adenocarcinoma
MAC	Mammary adenocarcinoma
MACS	Magnetic activated cell sorting
MAPK	Mitogen activated protein kinase
MDM2	Murine double minute 2
MDR1	Multidrug resistance protein-1
MET	Mesenchymal epithelial transition
MNB	Micro/nanobubbles
MMPs	Matrix metalloproteinase
mTOR	Mammalian target of rapamycin
miRNAs	MicroRNAs
NAC	N-acetyl cysteine
NBs	Nanobubbles
NADPH	Nicotinamide adenine dinucleotide phosphate
NCI	National cancer institute
ncRNA	Non-coding RNA
NFκB	Nuclear factor kappa B
NOTCH	Neurogenic locus notch homolog protein
NOX	NADPH oxidase
NSCLC	Non-small cell lung cancer
OCT-4	Octamer-binding transcription factor 4
PARP	Poly (ADP-ribose) polymerase
PDT	Photodynamic therapy
PEG	Polyethylene glycol
PI	Propidium iodide
P^{38}MAPK	P38 mitogen-activated protein kinase B
PD-L1	Programmed cell death ligand-1
PIK3CA	Phophatidylinositol-4,5-bisphospho 3-kinase catalytic subunit alpha
PI3K	Phosphoinositide-3-kinase
piRNAs	Piwi interacting RNAs
PR	Progesterone receptor

PHD	Prolyl hydroxylase domain
pSmad2/3	Phosphorylated small mothers against decapentaplegic homolog 3
PTEN	Phosphatase and tensin homolog
RAF	Rapidly accelerated fibrosarcoma
RAS	Rat sarcoma
RFA	Radio frequency ablation
ROS	Reactive oxygen species
RISC	RNA inducing silencing complex
SBRT	Stereotactic body radiation therapy
SEM	Scanning electron microscopy
SIP1	Smad-interacting protein-1
siRNA	Small interfering ribonucleic acid
SIL	Symmetric branched ionizable lipid
SNAIL	Snail family transcriptional repressor 1
SOX-2	Sex determining region y-box 2
SRC	Src proto-oncogene
STAT	Signal transducer and activator of transcription
TAM	Tumor associated macrophage
TEM	Transmission electron microscopy
TME	Tumor microenvironment
TNBC	Triple negative breast cancer
TP53	Tumor protein 53
TTR	Transthyretin
TWIST	Twist-related protein 1
TGF-β	Transforming growth factor-β1
US	Ultrasound
VEGF	Vascular endothelial growth factor
VE-cad	Vascular endothelial cadherin
vWF	Von Willebrand factor
Wnt	Wingless-related integration site
ZEB1	Zinc finger E-box binding homebox 1

Chapter 1

Introduction

" A solid tumor, as defined by the National Cancer Institute (NCI), as an abnormal mass of tissue that typically lacks cysts or liquid regions. These tumor can be benign (not cancerous) or malignant (cancerous), and they are named based on the type of cell from which they originate."

Solid tumor include sarcomas, carcinomas, and lymphomas. Carcinomas are the most common type of solid tumors and originate in the epithelial cells, which cover the inside and outside surfaces of internal organs, such as breast carcinoma, lung carcinoma, colorectal carcinoma, prostate carcinoma, and liver carcinoma etc [1,2]. Tumor progression is driven by the acquisition of key biological characteristics, known as the hallmarks of cancer. These include sustaining proliferative signaling, evading growth suppressors, resisting cell death, enabling replicative immortality, inducing angiogenesis, activating invasion and metastasis, deregulating cellular energetics, and avoiding immune destruction [3,4]. The hallmarks of cancer empower malignant cells to survive, proliferate, and invade new tissues. Crucial mechanisms, such as genomic instability and modulation of the immune system, drive the acquisition and maintenance of these hallmark traits, enabling cancer progression and metastasis [5].

According to WHO (World health organization) GLOBCON 2022 data, lung cancer is one of the top-ranked cancers worldwide with a 12.4% incidence rate and an 18.7% mortality rate, in which Lung adenocarcinoma is the most common type of non-small cell lung cancer (NSCLC), accounting for about 85% of all lung cancer cases based on cellular origin [6-8]. The global cancer burden is projected to exceed 35 million new cases by 2050 [2]. Breast cancer is the most common cancer in women worldwide, with triple-negative breast cancer (TNBC) being particularly lethal, accounting for 15% to 20% of all breast cancer cases and characterized by the absence of estrogen, progesterone, and human epidermal growth factor 2 receptors [8-10]. Breast cancer accounted for 23.8% of all new cancer diagnoses and was the leading cause of cancer-related mortality among women, responsible for 15.4% of cancer deaths, in the year 2022 [1]. According to IARC (International Agency for Research on Cancer) 2022 data, India reported approximately 72,510 new lung cancer cases with 66,279 annual deaths, and 178,361 new breast cancer cases with 90,408 deaths, highlighting a critical need for early detection and advanced treatments (gco.iarc) (gco.iarc.who). The age-standardized incidence rates (ASR) were 9.6 per 100,000 for males and 2.5 for females in lung cancer, and 29.8 per 100,000 for females in breast cancer (gco.iarc.who). These high prevalence rates pressing an urgent need for early detection, advanced treatments, and new therapeutic modalities to improve cancer outcomes and reduce mortality worldwide [1,2].

1.1 Background : Tumor hypoxia and their impact on therapeutic modalities for NSCLC and TNBC

The physiological oxygen level in healthy tissues is known as physoxia (also known as Tissue normoxia), which varies widely between the organs with an median range from 9.5% to 4.5% O_2. While tumor hypoxia is a condition of low oxygen levels within the tumor, which is a common feature of solid malignant tumor, develops due to uncontrollable cell proliferation, altered metabolism, and abnormal tumor blood vessels resulting in reduced oxygen tension which promote tumor growth, metastasis, and contributes to therapy resistance by inducing cell quiescence [11-13]. NSCLC and TNBC breast cancer exhibit severe hypoxia of 2.2% O_2 and 1.5% O_2 respectively [11,14]. Hypoxia induces a number of intracellular signalling molecules majorly hypoxia-inducible factor (HIF consisting of an oxygen-sensitive alpha subunit and a constitutive beta subunit). Under physoxia, HIF-1α undergoes oxygen-dependent hydroxylation **(Fig. 1.1)**, leading to its degradation. However, under hypoxic conditions, HIF-1α stabilizes and stimulates PI3K/AKT/mTOR, MAPK, and NFκB signaling pathways which are involved in cell proliferation, survival, apoptosis, metabolism, migration, inflammation, angiogenesis, EMT (epithelial to mesenchymal transition) and metastasis **(Fig. 1.1)** [13-15]. Additionally, tumor hypoxia also triggers the generation of reactive oxygen species (ROS) - chemically reactive molecules that include singlet oxygen, superoxide anion, and hydroxyl radical, produced through intracellular metabolism [16-18]. These ROS play a pivotal role in stabilizing hypoxia-inducible factor 1-alpha (HIF-1α) by inhibiting its repressor, Prolyl Hydroxylase Domain (PHD) [19-23]. Once stabilized, HIF-1α translocate to the nucleus, where it binds to hypoxia-responsive elements (HREs) in the promoters of target genes, thereby activating their transcription, including that of Zeb1 [24]. HIF-1α enhances Zeb1 expression, a transcription factor that promotes epithelial-mesenchymal transition (EMT), a key process in tumor progression and metastasis. Zeb1 downregulates E-cadherin and upregulates mesenchymal markers, facilitating cancer cell invasion and metastasis [25]. Recent studies indicate that tumors with high Zeb1 upregulates VEGF expression in tumor endothelium and stimulates angiogenesis which increases the prevalence of metastasis. Targeting Zeb1 not only impedes tumor progression and angiogenesis but also sensitizes tumor to conventional drug therapies [26,27].

On the other side, siRNA-based therapies for cancer treatment face challenges such as poor cellular uptake, low biological stability due to rapid degradation by nucleases, and unfavourable pharmacokinetics [28,29]. Thus, there is a need for advanced approaches to mitigate the detrimental effects of tumor hypoxia as well as efficient silencing of molecular target which is responsible for tumor proliferation and metastasis.

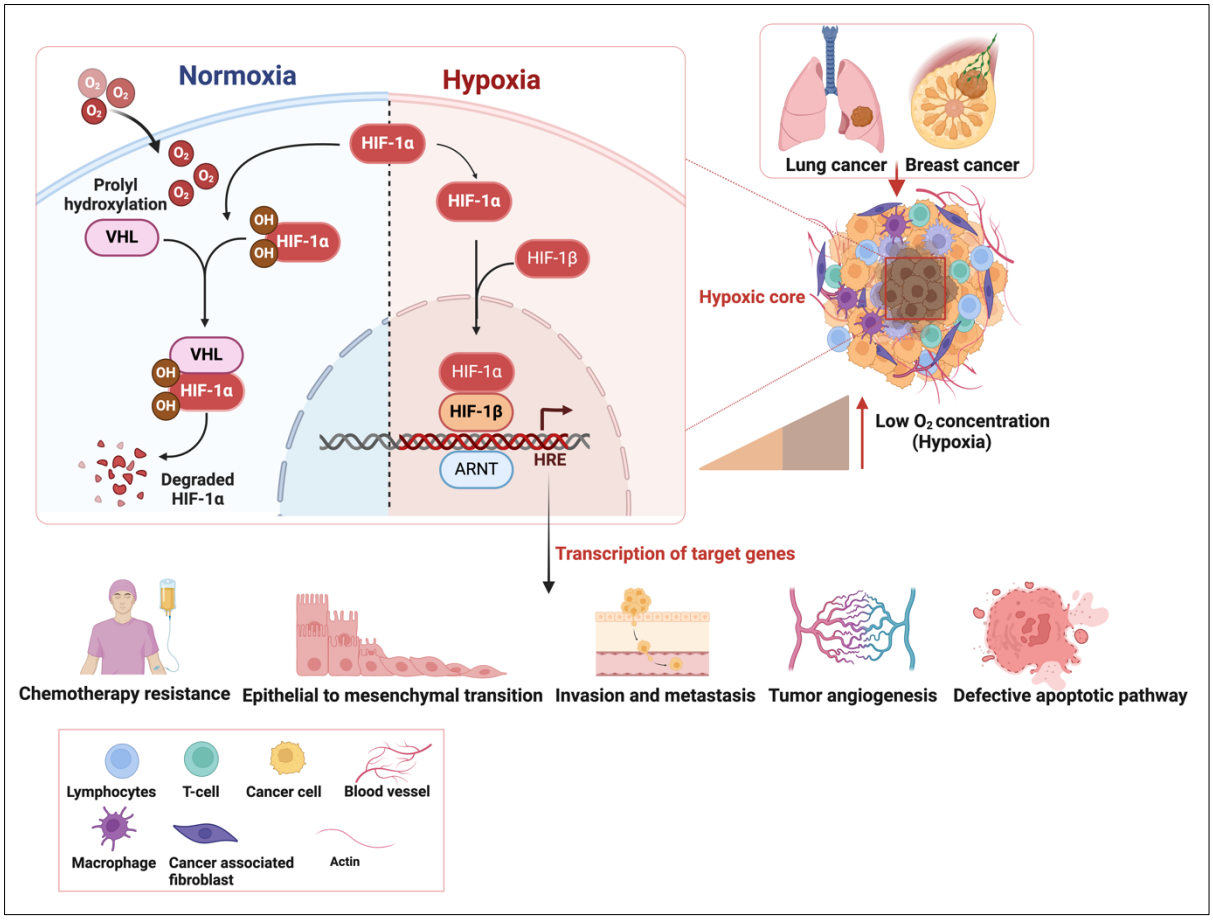

Figure 1.1: Overview of the HIF1a signaling in normoxia and hypoxia and their role in tumor progression; *under normoxic conditions degradation of HIF-1α via proteasomal pathway, while in hypoxic conditions HIF-1α gets stabilized activate the transcription of hundreds of target genes involves in chemoresistance, epithelial to mesenchymal transition, invasion and metastasis, tumor angiogenesis, and defective apoptotic pathway.*

1.2 Context

Chemotherapy remains a cornerstone of cancer treatment despite its limitations, primarily due to the scarcity of selective alternatives. Consequently, the development of novel anti-cancer molecules is of critical importance [30]. Currently, patients are treated with conventional chemotherapeutic agents such as docetaxel, doxorubicin, and cisplatin, which, despite their efficacy, are associated with significant side effects. Among the family of anti-tumor compounds, heterocyclic organic compounds have been extensively studied by many researchers in order to treat neoplastic disease. Pyrrole, pyrimidine, indole, quinoline, and purine are few classes of heterocycles that showed interesting cytotoxicity profiles [11,12,31]. Heterocycles are key structural components of many of the marketed anti-cancer drugs [32] due to being extremely common in nature, its unique physicochemical properties and versatility for regulating many cellular signaling and metabolism and thus poised them as true cornerstones of medicinal chemistry. Among the various heterocycles, the imidazo [1,2-a]pyridine moiety is the most important in the area of natural products and pharmaceuticals [17] showing a wide range of biological

activities including anti-tumor effects [19,20]. Several drugs that contain the imidazo[1,2-a]pyridine moiety such as zolpidem used in the treatment of insomnia, alpidem used as an anxiolytic agent, olprinone used for the treatment of acute heart failure, zolimidine used for the treatment of peptic ulcer, necopidem and saripidem both works as an anxiolytic agent [20-23]. Conversely, pyran family associated with excellent pharmacological efficacy [22]. Therefore, it is imperative to design and synthesize new hybridized molecule for cancer therapy. In this study, we hypothesized these novel derivatives can be utilized in the treatment of non-small cell lung cancer (NSCLC).

Our next question on another hallmark - epithelial to mesenchymal transition (EMT), which comprises dynamic changes in cellular organization from epithelial to mesenchymal phenotypes, leads to functional changes in cell migration and invasion, by upregulating HIF1a induced many signalling pathways [32-34]. Therefore, our overall aim is to diminish hypoxia-related effects, by supplying oxygen molecules within the tumor through any stable and efficient approach [35].

Besides, tumor hypoxia serves as a primary signal to proximal and distal endothelial cells (ECs) to activate angiogenesis, which in turn enhances tumor invasiveness and the risk of metastasis by modulating various transcription factors, most notably by Zeb1 [36]. Although Zeb1 has been well studied, and reported that tumor with high Zeb1 expression, upregulates the VEGF (Vascular Endothelial Growth Factor) stimulating angiogenesis and tumor plasticity [24,33]. Therefore, we hypothesize targeting Zeb1 could serve as a targeted therapy against tumor angiogenesis.

1.3 Research questions

To explore the efficacy of various therapeutic modalities against non-small cell lung cancer (NSCLC) and triple-negative breast cancer (TNBC), we investigated several key research questions:

1. How do novel IMPA-pyran derivatives, created by coupling imidazo[1,2-a]pyridine with 2-amino-4H-pyran, function as an efficient anti-tumor agent NSCLC?
2. How does liposomal oxygen nanobubble (L-ONB) attenuate hypoxia-induced epithelial-mesenchymal transition (EMT), known for contributing to chemoresistance, thus improving therapy outcomes for NSCLC and TNBC?
3. How can lipid nanoparticle-loaded Zeb1siRNA target angiogenesis pathways to inhibit tumor progression and metastasis in NSCLC and TNBC?

This thesis explores the efficacy and mechanistic actions of IMPA derivatives, L-ONB therapy, and LNP-Zeb1siRNA gene therapy against lung or/and breast tumors.

1.4 Relevance

The thesis aims to understand the molecular mechanistic pathways of various therapeutic candidates used against non-small cell lung cancer (NSCLC) and/or triple-negative breast cancer (TNBC) to

overcome chemoresistance, tumor aggression, and tumor angiogenesis pathways. A novel IMPA derivative compounds (IMPA-2, -5, -6, -8, and -12) is employed as potential anti-cancer drug molecule to treat NSCLC in both *in vitro* and 3D multicellular spheroid models. We also elucidate the mechanistic action of IMPA derivative compounds in p53-dependent cell cycle arrest and the activation of intrinsic apoptotic pathways.

Secondly, liposomal oxygen nanobubbles (L-ONB), is used as an adjuvant therapy against hypoxia-mediated EMT in cancer treatments. Studies are designed on *in vitro* lung adenocarcinoma (A549) and triple-negative breast cancer (MDA-MB-231) cell lines, as well as *in vivo* tumor models, such as the adult LUAD xenograft model in zebrafish and the 4T1 BALB/C mouse model for physiological relevance.

Lastly, we aim to develop targeted therapies utilizing RNA interference techniques against Zeb1 gene to suppress migratory, invasive, and angiogenic properties. To achieve this, a liposome nanoparticle formulation is utilized to deliver Zeb1siRNA into human umbilical vein endothelial cells (HUVEC), and the *in vivo* C57BL/6 mouse xenograft model to assess their role as anti-angiogenic. Interestingly, we explored the role of Zeb1 in tumor endothelial cell formation. Altogether, these findings suggest new therapeutic avenues for researchers and clinicians to conduct further preclinical studies for the development of therapies against non-small cell lung cancer and triple-negative breast cancer.

1.5 Specific aims

Specific aims of the study include:

Aim 1: Investigating the novel role of Imidazo[1,2-a] pyridine (IMPA) derivatives against non-small cell lung cancer

Aim 2: Elucidating the role of liposomal oxygen nanobubble for the treatment of lung and breast cancer

Aim 3: Delineating the role of LNP-conjugated Zeb1 siRNA as a targeted therapy against tumor angiogenesis

1.6 Thesis outlines

This thesis is organized into **six chapters** starting with **chapter 1** - the introduction and **chapter 2** is the review of literature. The detailed research conducted to explore the potential of therapeutic candidates and their mechanistic action against non-small cell lung cancer and triple negative breast cancer are described in **chapters 3-5**. **Chapter 6** is the concluding chapter. Briefly, **chapter 3** highlights the designed and synthesized a series of fifteen novel imidazo[1,2-a]pyridine (IMPA) derivatives by hybridizing imidazo[1,2-a]pyridine with 2-amino-4H-pyran, aiming to enhance biological efficacy against NSCLC. Five IMPAs particularly, IMPA-2, -5, -6, -8, and -12 showed significant cytotoxicity against human adenocarcinoma cell line A549, by increasing NOX activity. These IMPAs promote oxidative stress induced apoptosis by targeting mitochondrial intrinsic apoptosis pathway and initiate cell cycle arrest through the upregulation of p53 mediated p16, p21,

and p27 expressions in human A549 lung cancer cells. The anti-proliferative effect of these IMPAs on the 3D multicellular lung tumor spheroid further confirms that IMPA derivatives could be promising anti-cancer therapeutics against human lung adenocarcinoma [37].

In the **chapter 4**, the rapid proliferation of cancer cells in solid tumors creates a hypoxic microenvironment, promoting aggressiveness and resistance to conventional chemotherapies. To mitigate this, oxygen delivery at the tumor site is done by the development of highly efficient and stable lipid-shelled ONBs (L-ONBs) that significantly reduced lung and breast tumor aggressiveness by destabilizing hypoxia-inducible factor 1α (HIF-1α), thereby inhibiting cancer cell migration. L-ONB facilitated the prolyl hydroxylation of HIF-1α, leading to its subsequent proteasomal degradation resulting in significant downregulation of transforming growth factor-β (TGF-β), vascular endothelial growth factor-A (VEGF-A), and phosphorylated Smad 2/3 (pSmad 2/3), thereby impeding the epithelial-to-mesenchymal transition. This suggests that oxygen nanobubbles delivery could be a better therapeutic choice for managing hypoxia- mediated EMT associated cancers and other clinical ailments [38].

In the **chapter 5**, we elucidate the role of tumor hypoxia in stimulating angiogenesis through Zeb1-induced tumor plasticity, transforming tumor-associated macrophages into endothelial cells. To address these challenges, we employed siRNA-based gene therapy, delivered via cationic liposome nanoparticles (LNPs). Despite challenges such as poor cellular uptake, low biological stability, and unfavourable pharmacokinetics, targeting Zeb1 can inhibit angiogenesis and metastasis. Our study is the first to investigate Zeb1's role in macrophage-to-tumor endothelial cell transformation using a 3D spheroid tumor model. We fabricated LNPs using DOTAP and DC-Chol for delivering Zeb1 siRNA into 2D cell cultures such as lung adenocarcinoma (A549) cells, macrophages (differentiated THP-1 cells), and human umbilical vein endothelial cells (HUVECs), achieving high transfection efficiency with no cellular toxicity. This approach effectively reduces endothelial characteristics and inhibits tumor angiogenesis, thereby preventing metastasis in lung adenocarcinoma cells, 3D lung tumor spheroids, and xenograft 4T1 C57BL/6 mouse tumor models. Consequently, silencing of Zeb1 through the LNP-Zeb1siRNA delivery represents a promising strategy to impede angiogenesis and metastasis in lung adenocarcinoma (LUAD) by disrupting the formation of new endothelial cells. Thus, this study unveiling a novel trans differentiation and the anti-angiogenic effect of Zeb1 siRNA and presenting a novel therapeutic approach for managing solid tumor angiogenesis.

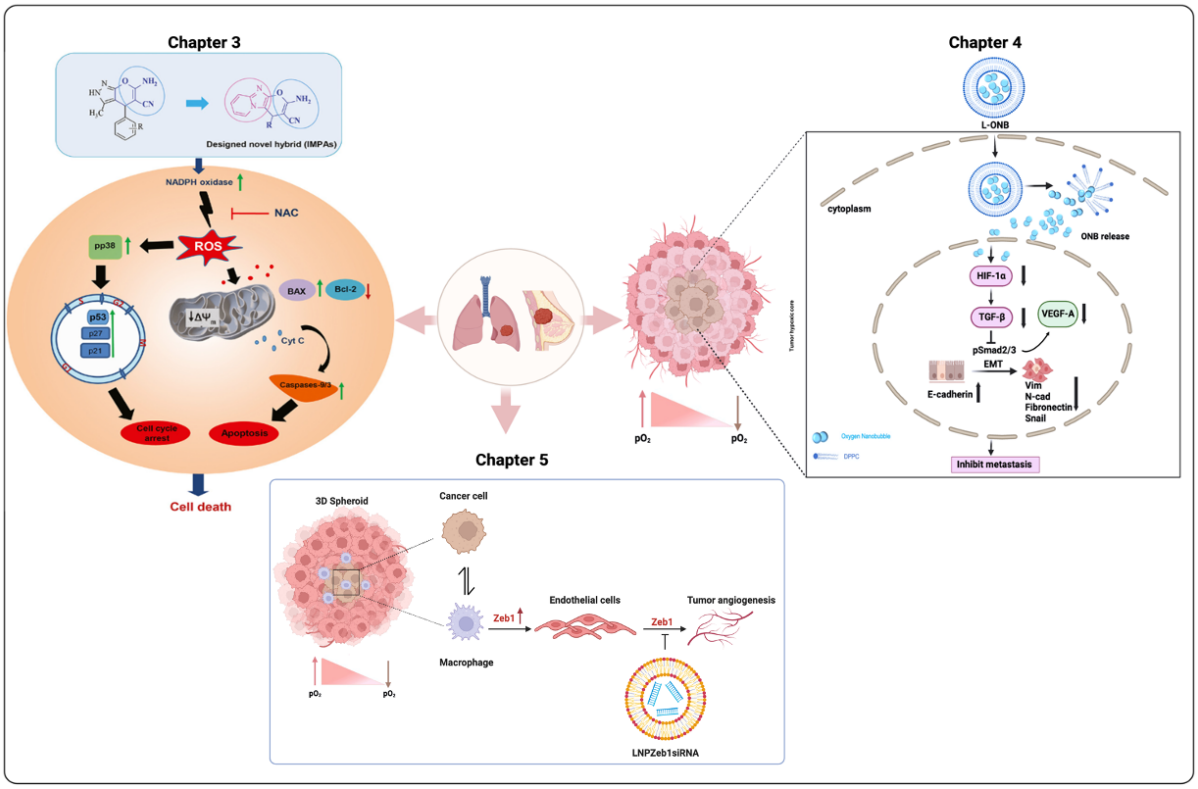

Figure 1.2: Schematic overview of the thesis outline.

The research work done in the thesis is divided into three main chapters: 3-5. ***Chapter 3*** *explains the anti-cancer activities of novel five IMPAs 2,-5,-6,-8 and -12 against non-small cell lung cancer.* ***Chapter 4*** *explains the mechanistic intervention of L-ONB within a non-small cell lung cancer and triple negative breast cancer, targeting Hypoxia-Inducible Factor 1α (HIF-1α) induced EMT and effectively suppresses metastatic progression.* ***Chapter 5*** *explains the potential role of Zeb1 macrophage differentiation to tumor endothelial like cell, promoting tumor angiogenesis. We also delineating the role of LNP conjugated Zeb1siRNA as an anti-angiogenic therapy against solid tumors.*

References

1. Bray, F., Laversanne, M., Sung, H., Ferlay, J., Siegel, R. L., Soerjomataram, I., & Jemal, A. (2024). Global cancer statistics 2022: GLOBOCAN estimates of incidence and mortality worldwide for 36 cancers in 185 countries. *CA: a cancer journal for clinicians*, *74*(3), 229-263.
2. Sedeta, E., Sung, H., Laversanne, M., Bray, F., & Jemal, A. (2023). Recent mortality patterns and time trends for the major cancers in 47 countries worldwide. *Cancer Epidemiology, Biomarkers & Prevention*, *32*(7), 894-905.
3. Hanahan, D., & Weinberg, R. A. (2017). Biological hallmarks of cancer. *Holland-Frei Cancer Medicine*, *1*, 1-10.
4. Hanahan, D., & Weinberg, R. A. (2011). Hallmarks of cancer: the next generation. *cell*, *144*(5), 646-674.
5. Hanahan, D. (2022). Hallmarks of cancer: new dimensions. *Cancer discovery*, *12*(1), 31-46.
6. Gray, L. H., Conger, A., Ebert, M., Hornsey, S., & Scott, O. C. A. (1953). The concentration of oxygen dissolved in tissues at the time of irradiation as a factor in radiotherapy. *The British journal of radiology*, *26*(312), 638-648.
7. Gridelli, C., Rossi, A., Carbone, D. P., Guarize, J., Karachaliou, N., Mok, T., ... & Rosell, R. (2015). Non-small-cell lung cancer. *Nature reviews Disease primers*, *1*(1), 1-16.
8. Ettinger, D. S., Akerley, W., Bepler, G., Blum, M. G., Chang, A., Cheney, R. T., ... & Yang, S. C. (2010). Non–small cell lung cancer. *Journal of the national comprehensive cancer network*, *8*(7), 740-801.
9. Goldstraw, P., Ball, D., Jett, J. R., Le Chevalier, T., Lim, E., Nicholson, A. G., & Shepherd, F. A. (2011). Non-small-cell lung cancer. *The Lancet*, *378*(9804), 1727-1740.
10. Weigelt, B., Geyer, F. C., & Reis-Filho, J. S. (2010). Histological types of breast cancer: how special are they?. *Molecular oncology*, *4*(3), 192-208.
11. Tang, Y., Wang, Y., Kiani, M. F., & Wang, B. (2016). Classification, treatment strategy, and associated drug resistance in breast cancer. *Clinical breast cancer*, *16*(5), 335-343.
12. Chen, Z., Fillmore, C. M., Hammerman, P. S., Kim, C. F., & Wong, K. K. (2014). Non-small-cell lung cancers: a heterogeneous set of diseases. *Nature Reviews Cancer*, *14*(8), 535-546.
13. Muz, B., De La Puente, P., Azab, F., & Kareem Azab, A. (2015). The role of hypoxia in cancer progression, angiogenesis, metastasis, and resistance to therapy. *Hypoxia*, 83-92.
14. Li, Y., Zhao, L., & Li, X. F. (2021). Hypoxia and the tumor microenvironment. *Technology in cancer research & treatment*, *20*, 15330338211036304.
15. Petrova, V., Annicchiarico-Petruzzelli, M., Melino, G., & Amelio, I. (2018). The hypoxic tumour microenvironment. *Oncogenesis*, *7*(1), 10.
16. Hapke, R. Y., & Haake, S. M. (2020). Hypoxia-induced epithelial to mesenchymal transition in cancer. *Cancer letters*, *487*, 10-20.

17. Hockel, M., & Vaupel, P. (2001). Tumor hypoxia: definitions and current clinical, biologic, and molecular aspects. *Journal of the National Cancer Institute*, *93*(4), 266-276.
18. Ray, P. D., Huang, B. W., & Tsuji, Y. (2012). Reactive oxygen species (ROS) homeostasis and redox regulation in cellular signaling. *Cellular signalling*, *24*(5), 981-990.
19. Huang, R., Chen, H., Liang, J., Li, Y., Yang, J., Luo, C., ... & Xie, X. (2021). Dual role of reactive oxygen species and their application in cancer therapy. *Journal of Cancer*, *12*(18), 5543.
20. Ray, P. D., Huang, B. W., & Tsuji, Y. (2012). Reactive oxygen species (ROS) homeostasis and redox regulation in cellular signaling. *Cellular signalling*, *24*(5), 981-990.
21. Zhang, Y., Choksi, S., Chen, K., Pobezinskaya, Y., Linnoila, I., & Liu, Z. G. (2013). ROS play a critical role in the differentiation of alternatively activated macrophages and the occurrence of tumor-associated macrophages. *Cell research*, *23*(7), 898-914.
22. Bae, T., Hallis, S. P., & Kwak, M. K. (2024). Hypoxia, oxidative stress, and the interplay of HIFs and NRF2 signaling in cancer. *Experimental & Molecular Medicine*, *56*(3), 501-514.
23. Liu, Q., Guan, C., Liu, C., Li, H., Wu, J., & Sun, C. (2022). Targeting hypoxia-inducible factor-1alpha: A new strategy for triple-negative breast cancer therapy. *Biomedicine & Pharmacotherapy*, *156*, 113861.
24. Zhang, P., Sun, Y., & Ma, L. (2015). ZEB1: at the crossroads of epithelial-mesenchymal transition, metastasis and therapy resistance. *Cell cycle*, *14*(4), 481-487.
25. Jiang, J., Wang, K., Chen, Y., Chen, H., Nice, E. C., & Huang, C. (2017). Redox regulation in tumor cell epithelial–mesenchymal transition: Molecular basis and therapeutic strategy. *Signal Transduction and Targeted Therapy*, *2*(1), 1-12.
26. Sánchez-Tilló, E., Siles, L., De Barrios, O., Cuatrecasas, M., Vaquero, E. C., Castells, A., & Postigo, A. (2011). Expanding roles of ZEB factors in tumorigenesis and tumor progression. *American journal of cancer research*, *1*(7), 897.
27. Liu, L., Tong, Q., Liu, S., Cui, J., Zhang, Q., Sun, W., & Yang, S. (2016). ZEB1 upregulates VEGF expression and stimulates angiogenesis in breast cancer. *PLoS One*, *11*(2), e0148774.
28. Babu, A., Muralidharan, R., Amreddy, N., Mehta, M., Munshi, A., & Ramesh, R. (2016). Nanoparticles for siRNA-based gene silencing in tumor therapy. *IEEE transactions on nanobioscience*, *15*(8), 849-863.
29. Hu, B., Zhong, L., Weng, Y., Peng, L., Huang, Y., Zhao, Y., & Liang, X. J. (2020). Therapeutic siRNA: state of the art. *Signal transduction and targeted therapy*, *5*(1), 101.
30. Martins, P., Jesus, J., Santos, S., Raposo, L. R., Roma-Rodrigues, C., Baptista, P. V., & Fernandes, A. R. (2015). Heterocyclic anticancer compounds: recent advances and the paradigm shift towards the use of nanomedicine's tool box. *Molecules*, *20*(9), 16852-16891.
31. Dasari, S., & Tchounwou, P. B. (2014). Cisplatin in cancer therapy: molecular mechanisms of action. *European journal of pharmacology*, *740*, 364-378.

32. Skok, Z., Zidar, N., Kikelj, D., & Ilaš, J. (2019). Dual inhibitors of human DNA topoisomerase II and other cancer-related targets. *Journal of medicinal chemistry*, *63*(3), 884-904.
33. Son, H., & Moon, A. (2010). Epithelial-mesenchymal transition and cell invasion. *Toxicological research*, *26*, 245-252.
34. Ribatti, D., Tamma, R., & Annese, T. (2020). Epithelial-mesenchymal transition in cancer: a historical overview. *Translational oncology*, *13*(6), 100773.
35. Joshi, H. P. (2011). *Non-canonical pathways of HIF1-alpha regulation in ovarian cancer: Implications for tumor angiogenesis and metastasis*. University of Minnesota.
36. Fu, R., Li, Y., Jiang, N., Ren, B. X., Zang, C. Z., Liu, L. J., ... & Wu, Z. Q. (2020). Inactivation of endothelial ZEB1 impedes tumor progression and sensitizes tumors to conventional therapies. *The Journal of Clinical Investigation*, *130*(3), 1252-1270.
37. Bhavya, K., Mantipally, M., Roy, S., Arora, L., Badavath, V. N., Gangireddy, M., ... & Pal, D. (2022). Novel imidazo [1, 2-a] pyridine derivatives induce apoptosis and cell cycle arrest in non-small cell lung cancer by activating NADPH oxidase mediated oxidative stress. *Life Sciences*, *294*, 120334.
38. Bhavya, K., Agrawal, K., Negi, D., Niveria, K., Verma, A. K., Singh, Y., ... & Pal, D. (2023). 2310P Oxygen nano-bubbles attenuate hypoxia-induced tumour malignancy in tumour xenograft models. *Annals of Oncology*, *34*, S1180.

Chapter 2

Literature Review

Solid tumor is not just an abnormal genetically mutated mass of tissues but so far it is more complex and heterogenous entity comprising both host-resident cells and infiltrating cells that harbour the neoplasm [1,2]. Lung and breast cancers are both examples of solid tumors [1]. Lung cancer, a leading cause of cancer-related mortality worldwide, is marked by uncontrolled cell proliferation in lung tissues [3]. It primarily consists of two types: non-small cell lung cancer (NSCLC) and small cell lung cancer (SCLC), with NSCLC being more prevalent and generally having a better prognosis.

Breast cancer, the most common cancer among women globally, develops in breast tissue, typically in the ducts or lobules [4]. It is classified into subtypes such as hormone receptor-positive, HER2-positive, and triple-negative, each exhibiting unique biological characteristics and treatment responses [5]. Early detection and targeted therapies have improved outcomes, but challenges remain in treating aggressive forms like triple-negative breast cancer.

The physiology of solid tumor diverges significantly from that of normal tissues, primarily because of vascular differences. Tumor blood vessels are typically abnormal, featuring enlarged, leaky capillaries with sluggish blood flow, leading to hypoxia and resistance to radiotherapy and certain anticancer drugs. This irregular vascular environment also causes an uneven distribution of therapeutic agents, resulting in some areas receiving high doses while others get very little, complicating effective treatment [2,6]. Moreover, the disordered nature of tumor vasculature can make regions both hypoxic and acidic due to the accumulation of metabolic waste, creating a hostile environment for immune cells. This acidity can reduce the effectiveness of chemotherapy, immunotherapy by impairing T-cell function and survival within the tumor microenvironment [1]. Additionally, these conditions promote genetic instability in cancer cells, possibly leading to rapid mutation rates that allow them to evade both drug therapies and immune detection [7].

2.1 Overview of the non-small cell lung cancer and triple negative breast cancer

Non-small cell lung cancer is the most common type of lung cancer, the most common subtypes are adenocarcinoma (originating in the cells that line the alveoli and make mucus). It often occurs in the outer regions of the lungs and most common type of lung cancer in non-smokers; squamous cell carcinoma (originates in the squamous cells that line the inside of the airways in the lungs), and large cell carcinoma (can appear in any part of lungs), a less common subtype and the detailed histological classification has given in **Fig. 2.1** [8,9].

Lung adenocarcinoma is highly prevalent among non-small cell lung cancers (NSCLC) because it originates in the peripheral regions of the lungs, making it more likely to be influenced by environmental factors like smoking and air pollution [6].

Breast cancer is known for its high degree of heterogeneity [10]. A generalized therapeutic approach is not practical in clinical settings because each subgroup has distinct morphology, molecular characteristics, and clinical outcomes. Extensive research has been conducted to categorize patients based on histological and molecular features, aiming to customize treatments for specific subgroups. In histopathology, cytoarchitectural features help determine whether tumors originate from ductal or lobular tissue according to WHO classification standards (**Fig. 2.2**) [10-12]. Another method of classification relies on the molecular characteristics of cells. Pathologists use immunohistochemistry (IHC) to detect markers such as estrogen receptor (ER), progesterone receptor (PR), human epidermal growth factor receptor 2 (HER2), and Ki67. These markers form the basis of clinical subtyping and are crucial for treatment decision-making, serving as the only accepted method of stratification in clinical practice. IHC markers classify tumors into the following subtypes: luminal A (ER+ PR+ HER2- Ki67-), luminal B (ER+ PR-/+ HER2+ Ki67+), HER2 overexpression (ER- PR- HER2+ Ki67+), and basal (ER- PR- HER2- KI67+). Each subtype has its unique morphology, distinct molecular characteristics, and specific clinical outcomes [13]. Luminal A and Luminal B breast cancers make up 65% of all breast cancer cases and generally have a good prognosis (**Table 2.1**). Triple negative breast cancer is a subtype of invasive ductal carcinoma (IDC), is the most common type of breast cancer, originating in the milk ducts and then invading the surrounding breast tissue. TNBC is characterized by the absence of three receptors commonly found in other breast cancers: estrogen receptors (ER), progesterone receptors (PR), and human epidermal growth factor receptor 2 (HER2) [14-16]. TNBC does not respond to hormonal therapy or therapies that target HER2 receptors, making it more challenging to treat compared to other types of breast cancer [17]. TNBC tends to be more aggressive and has a higher likelihood of recurrence.

The primary non-molecular risk factors for non-small cell lung cancer (NSCLC) include cigarette smoking, air pollution, radon exposure (a radioactive gas), and occupational hazards such as exposure to asbestos, arsenic, and other carcinogens [18]. Molecular risk factors include mutations in the EGFR gene, which are common in adenocarcinomas and lead to abnormal cell signaling and proliferation [19]. KRAS mutations, often found in smokers, contribute to uncontrolled cell growth. ALK rearrangements produce abnormal ALK fusion proteins that drive cancer growth, and TP53 mutations result in the loss of tumor suppressor function, promoting cancer development [20].

TNBC is caused by BRCA1 and BRCA2 gene mutations, which significantly increase the risk of TNBC; reproductive history, such as early menarche, late menopause, and not having children; obesity, which is also a risk factor due to hormonal changes; and ethnicity, as evidenced by the high prevalence rate seen in African American women compared to other ethnic groups [21,22]. Looking at the genetic risk factors, BRCA1/BRCA2 mutations cause poor DNA repair pathways, raising cancer risk. P53

mutations are widespread in TNBC, resulting in tumour suppressor function loss, while PI3K/AKT pathway changes, which contribute to cell growth and survival, are frequently observed in TNBC [21-23].

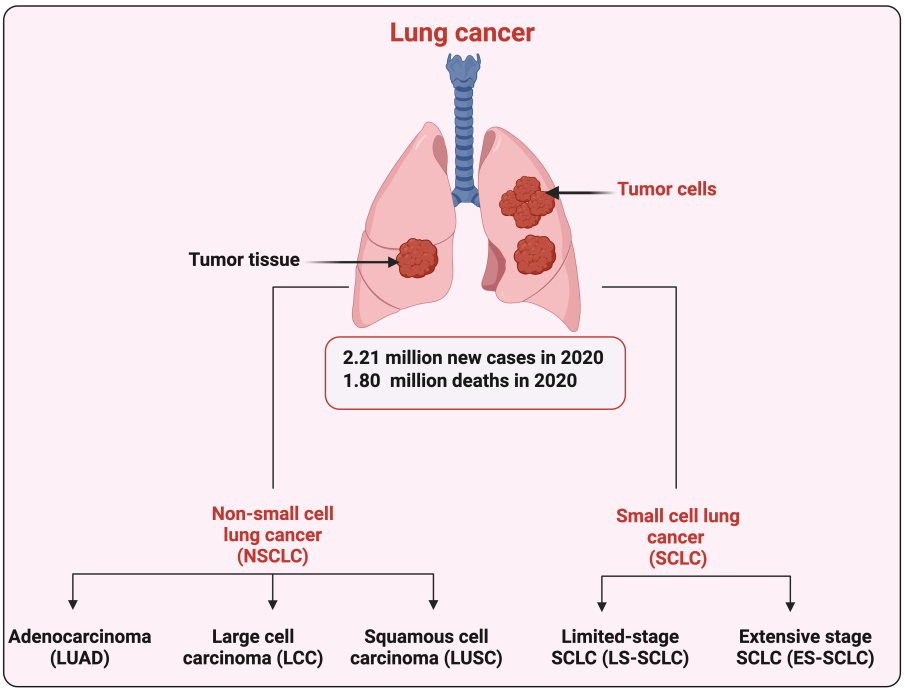

Figure 2.1: *The histological classification of lung cancer [9]*

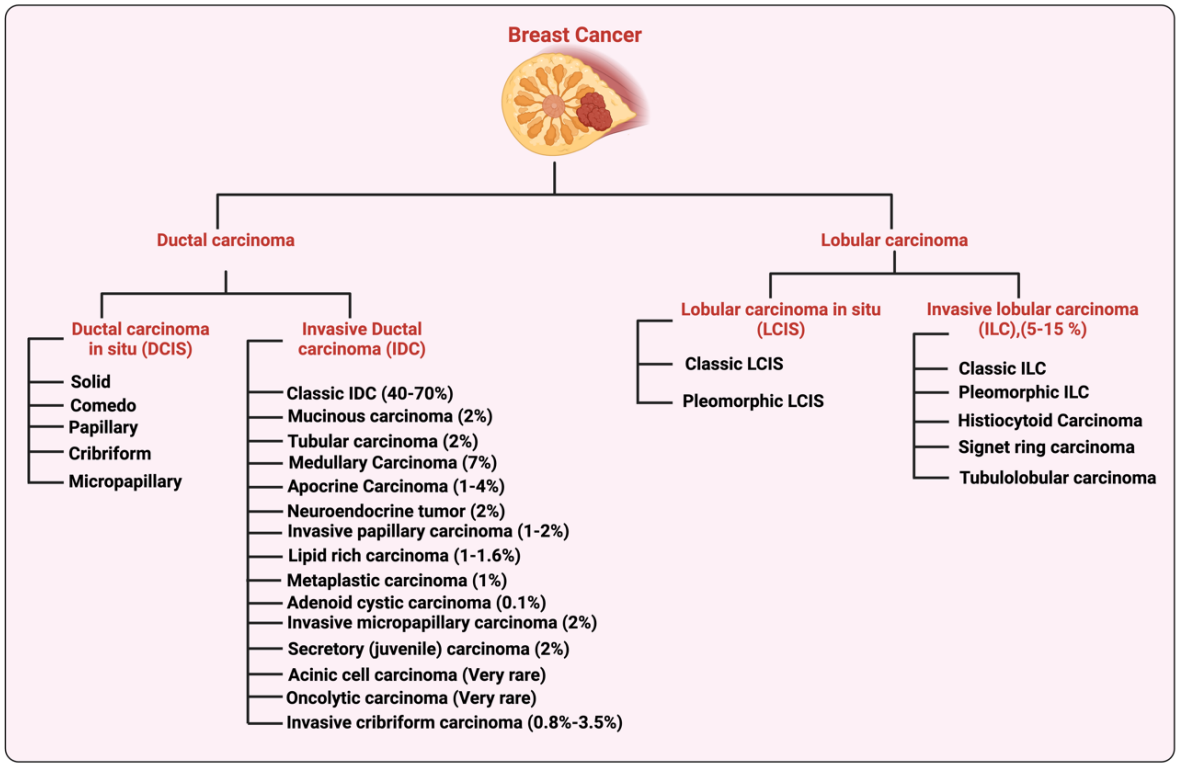

Figure 2.2: *Classification of breast cancer based on cytoarchitectural features as per WHO [modified from,10]*

Table 2.1 Four main intrinsic or molecular subtypes of breast cancer [12,15,17]

	Luminal A	Luminal B	HER2 +ve	TNBC
Frequency (%)	50 (Most prevalent subtype)	15	20	15 (Most aggressive subtype, occurs more often in younger women)
ER	+	+	-	-
PR	+	-/+	-	-
HER2	-	+/-	+	-
Proliferative index	Low Ki67	Low-Med Ki67	High Ki67	High ki67
Mutation	No	BRCA2	p53	P53 and BRCA1
Prognosis	Good	Good	Poor	Poor
Therapy	Hormonal therapies Targeted therapy (Tamoxifen)	Hormonal therapies HER2 targeted therapies	HER2 targeted therapies	Novel targeted therapies
	Chemotherapy			

+ positive, - negative, +/- mostly positive, -/+ mostly negative, ER, estrogen receptor; HER, human epidermal receptor; HER2, human epidermal growth factor receptor 2; PR, progesterone receptor; TNBC, triple-negative breast cancer.

2.1.1 Molecular characteristic features of NSCLC and TNBC

Non-small cell lung cancer (NSCLC) is a complex and diverse disease, composed of several subtypes, each with its unique molecular characteristics [3, 4]. Among these subtypes, adenocarcinoma, squamous cell carcinoma, and large cell carcinoma stand out due to their distinct genetic and molecular profiles. Adenocarcinoma is often driven by specific genetic mutations [24]. Key players include mutations in the EGFR (epidermal growth factor receptor), rearrangements in the ALK (anaplastic lymphoma kinase) gene, and mutations in the KRAS gene [20,21]. These mutations are not just random changes; they lead to continuous cell growth and division by activating critical signalling pathways such as the

PI3K/AKT and MAPK pathways [25]. These pathways, when dysregulated, can drive the uncontrolled proliferation of cancer cells, making adenocarcinoma a formidable foe.

In contrast, squamous cell carcinoma frequently involves alterations in the TP53 gene, which is known as the "guardian of the genome" due to its role in preventing genetic mutations [25, 26]. Additionally, amplifications in the FGFR1 gene and mutations in the PIK3CA gene are common [26]. These genetic changes disrupt normal cell cycle control, promoting relentless cell proliferation and survival. The loss of TP53 function, in particular, removes a crucial barrier to cancer development, allowing squamous cell carcinoma cells to thrive and spread [27]. Large cell carcinoma is a bit more enigmatic, as it can harbour a range of genetic changes, including mutations in TP53 and KRAS [29]. However, it lacks the specific mutations commonly seen in adenocarcinoma and squamous cell carcinoma. Despite this variability, large cell carcinoma often involves disruptions in pathways that control cell growth and apoptosis, much like its NSCLC counterparts [4,26]. These disruptions enable the cancer cells to evade normal growth controls and resist cell death, contributing to their aggressive behaviour. Across all NSCLC subtypes, certain molecular markers are shared, providing valuable targets for treatment. One such marker is PD-L1, a protein expressed on the surface of cancer cells. PD-L1 expression is a significant indicator used to predict response to immunotherapy, a treatment that harnesses the body's immune system to fight cancer [30]. Additionally, MET amplifications and exon 14 skipping mutations are alterations that can drive tumor growth and are targetable with specific inhibitors [31]. Finally, BRAF mutations, though less common, are present in a subset of NSCLC and can be targeted with therapies specifically designed to inhibit BRAF signaling. Understanding these molecular characteristics is crucial for developing personalized treatment approaches [32]. By targeting the specific genetic and molecular abnormalities present in each subtype of NSCLC, it is possible to improve patient outcomes and combat this challenging disease more effectively.

The key molecular characteristics of TNBC. Many TNBC cases are associated with mutations in the BRCA1 and BRCA2 genes [33,34]. These mutations impair DNA repair mechanisms, leading to genomic instability and a higher risk of developing cancer. Additionally, TNBC frequently harbours mutations in the TP53 gene, which encodes the tumor suppressor protein p53 [35]. When p53 function is lost, it results in uncontrolled cell growth and survival, further contributing to the cancer's aggressiveness [35]. Several molecular pathways are significantly altered in TNBC, driving its progression. The PI3K/AKT pathway, for instance, often shows alterations that promote cell proliferation and survival. Another common feature is the overexpression of the epidermal growth factor receptor (EGFR), which drives tumor growth and progression [36]. The JAK/STAT signalling pathway is also frequently activated in TNBC, contributing to tumor growth and helping the cancer evade the immune system [35-37]. TNBC can be divided into different molecular subtypes, each with unique characteristics. The majority of TNBC cases fall into the basal-like category, characterized by the expression of basal cytokeratin such as CK5/6, CK14, and CK17 [38]. This subtype shares similarities with basal cells of the breast and is known for its aggressive clinical course. Another

subtype, the mesenchymal subtype, exhibits features of epithelial-mesenchymal transition (EMT), which increases the cancer's invasiveness and metastatic potential. Some TNBC tumor belong to the immunomodulatory subtype, which is notable for high levels of immune cell infiltration and the expression of immune checkpoint molecules [38]. These tumor are potential candidates for immunotherapy, offering a ray of hope for targeted treatment. Lastly, the luminal androgen receptor (LAR) subtype expresses the androgen receptor (AR) and displays luminal gene expression patterns, despite the absence of ER, PR, and HER2 [39, 40] . Together, these genetic mutations, altered molecular pathways, and diverse subtypes illustrate the complexity of TNBC and emphasize the need for tailored therapeutic approaches to combat this challenging form of cancer.

2.2 Impact of hypoxia in solid tumor

Oxygen is vital for the biological process of all aerobic organisms. In healthy tissues, oxygen levels (pO2) typically range from 10 to 80 mmHg. In contrast, tumors often have areas with very low oxygen concentrations, experiencing severe hypoxia (<0.5 mmHg) and intermediate hypoxia (0.5–20 mmHg) [41]. Solid tumor, which account for 90% of all cancers, frequently exhibit hypoxia, resulting in decreased therapeutic response and increased malignant progression. Hypoxia-inducible factors (HIFs) are key transcriptional regulators that respond to low oxygen conditions, playing a critical role in tumor adaptation to hypoxic environments [42,43]. They comprise an oxygen-sensitive HIF-α subunit (either HIF-1α or HIF-2α), which forms a dimer with HIF-1β under hypoxic conditions. HIF-1 specifically binds to hypoxic response element (HRE)-driven promoters on various genes, including vascular endothelial growth factor (VEGF), heme oxygenase, glucose transporter-1, and erythropoietin. HIF-1 is a heterodimeric complex composed of HIF-1α and HIF-1β subunits. HIF-1β is present in all cells, whereas HIF-1α is the oxygen-regulated subunit. Hypoxia-inducible factor 1 (HIF-1) has been identified as a pivotal regulator of these adaptive processes, promoting tumor cell survival, proliferation, invasion, and metastasis [44,45]. The hypoxic environment promotes genomic instability, leading to mutations and more aggressive tumor traits. Factors such as VEGF drive angiogenesis, enabling tumor cells to escape hypoxic conditions [44]. Consequently, hypoxia contributes to tumor aggressiveness and resistance to treatment.

In the context of lung cancer and breast cancer, hypoxia plays a critical role (**Fig. 2.3**). Both types of cancer, being solid tumors, often experience hypoxic conditions that contribute to their aggressive behaviour and resistance to therapy [46]. In lung cancer, especially non-small cell lung cancer (NSCLC), hypoxia can lead to enhanced tumor growth and metastasis through HIF-1 mediated pathways [47]. Similarly, in breast cancer, particularly in aggressive subtypes like triple-negative breast cancer (TNBC), hypoxia-driven changes promote tumor invasiveness and metastatic potential, complicating treatment efforts and impacting patient outcomes [48,49]. Understanding the role of hypoxia in these cancers is crucial for developing effective therapeutic strategies.

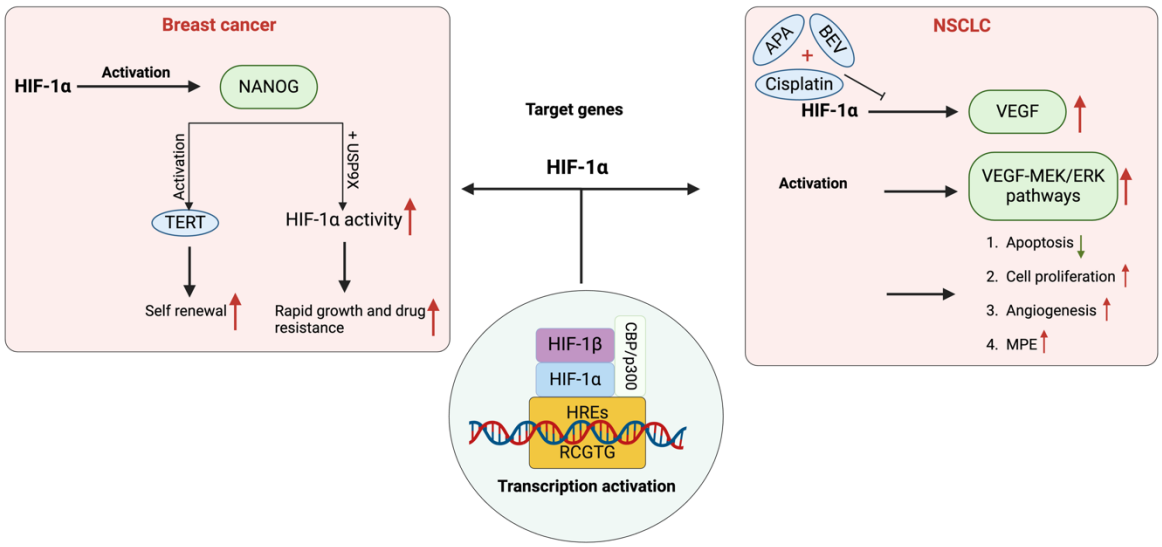

Figure 2.3: Schematic overview of the HIF-1α in solid tumor

The role of HIF-1α in solid tumor. Breast cancer, and NSCLC, non-small-cell lung cancer; EMT, epithelial to mesenchymal transition; APA, apatinib; BEV, bevacizumab; VEGF, vascular endothelial growth factor [50,51,52].

2.2.1 Impact on Epithelial-Mesenchymal transition

At first, EMT and hypoxia are thought to be distinct processes which led to invasion and spread of different kinds of cancer. Because of the relationships between the signalling pathways, the term hypoxia-induced EMT has recently been proposed. Under hypoxic conditions, Hypoxia-Inducible Factor 1-alpha (HIF-1α) promotes the transcription of various genes that facilitate adaptation to low oxygen levels, including those involved in the Epithelial-Mesenchymal Transition (EMT). EMT is a process where epithelial cells lose their characteristics and gain mesenchymal properties, which is critical for cancer metastasis [53, 54]. Key Mechanisms of HIF-1α Mediated EMT Pathways are following;

A. **Transforming Growth Factor β (TGF-β) Pathway**:

   HIF-1α is linked with TGF-β activation, which plays a significant role in inducing EMT. TGF-β can increase HIF-1α stability by suppressing PHD2, a prolyl hydroxylase that promotes HIF-1α degradation under normoxic conditions. TGF-β signaling includes SMAD-dependent and non-SMAD pathways. HIF-1α interacts with these pathways to enhance the transcription of EMT-related genes [54 - 57].

B. **Wnt/β-Catenin Pathway**:

   HIF-1α can potentiate the Wnt/β-catenin pathway, enhancing EMT in certain cancers like hepatocellular carcinoma [58].

C. **Hedgehog Signaling**:

HIF-1α mediates hedgehog signaling, which is involved in EMT and invasion in pancreatic cancer cells [59,60].

As a result, HIF-1a and other EMT signalling pathways were clearly interacting; however, the specifics of these interactions may differ based on the kind of tumour [61]. Apart from research on the interactions between HIF-1a and other EMT pathways, several studies have examined the effects of HIF-1a on different EMT transcription factors, such as TWIST, Snail, Slug, SIP1, and ZEB1 (**Table 2.2**). In hypopharyngeal and breast cancer cell lines, HIF-1a may directly bind to TWIST through HRE in the TWIST proximal promoter. In addition, it encouraged metastasis and, in contrast to other EMT inducers like Snail, TWIST overexpression was non-redundant and necessary for HIF-1a-mediated EMT [62]. The worst prognosis was associated with co-expression of HIF-1a, TWIST, and Snail in primary tumours of individuals with head and neck cancer [62,63].

These pathways illustrate the crosstalk between HIF-1α and other major signaling mechanisms that collectively drive EMT. The interplay is complex and often context-dependent, varying across different cancer types.

Hypoxia-Induced Non-HIF EMT Pathways

In addition to HIF-mediated pathways, hypoxia can induce EMT through several other signaling pathways, each with unique roles and implications in cancer progression.

A. **AMPK (AMP-Activated Protein Kinase)**:

   Hypoxia can upregulate AMPK, a key regulator of cellular energy homeostasis. While traditionally seen as a metabolic tumor suppressor, AMPK has controversial roles in EMT. Some studies suggest AMPK activation promotes EMT via TWIST1, while others indicate it suppresses EMT by modulating the Akt-MDM2-Foxo3 signaling axis [64-67].

B. **PI3K-Akt-mTOR Pathway**:

   This pathway is crucial for cell proliferation and survival and is frequently activated in cancer cells. Under hypoxic conditions, it contributes to EMT by promoting anabolic reactions and autophagy, processes critical for maintaining cancer cell viability and metastasis [68-70].

C. **MAPK Pathways (ERK, JNK, p38 MAPK)**:

   MAPKs are essential for various cellular processes, including proliferation and differentiation. Under hypoxia, MAPK signaling can induce EMT by stabilizing and activating EMT transcription factors like TWIST1, Snail, and Slug. For instance, ERK-mediated EMT is observed in lung cancer cell lines, while JNK and p38 MAPK are involved in TGF-β-induced EMT in various cancers [71,72].

   Hypoxia-induced EMT involves a network of signaling pathways where HIF-1α plays a central role, but other pathways like AMPK, PI3K-Akt-mTOR, and MAPKs also significantly contribute. Understanding these pathways can provide insights into therapeutic targets for inhibiting cancer metastasis by disrupting EMT.

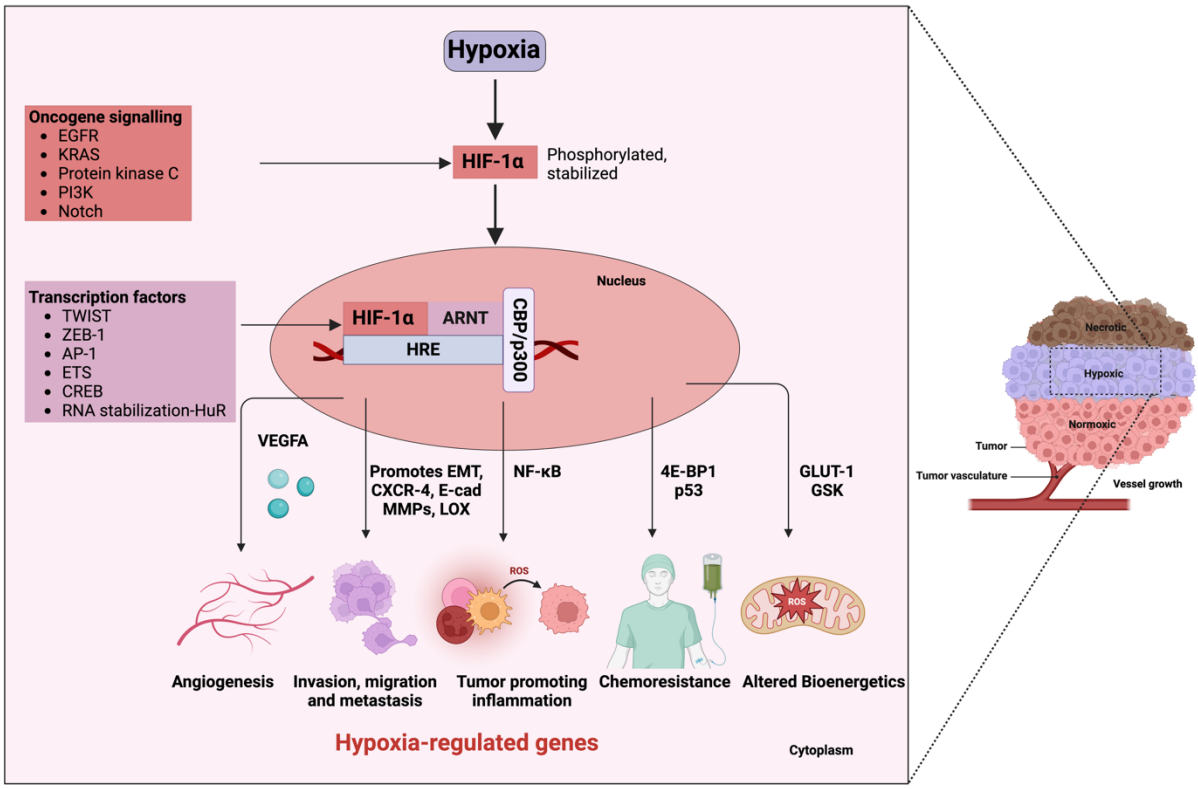

Figure 2.4: Summary of signalling pathways in tumor hypoxia and cancer progression.

The activation of HIF-1α under hypoxic condition Stable HIF-1a forms a heterodimer with the HIF-1b (ARNT) subunit after translocation to the nucleus, which in turn binds to CBP/p300 and binds to hypoxia-responsive elements (HREs) on the promoter of HIF-1 target genes to constitute a transcription initiation complex, which eventually activates downstream of target genes; including angiogenesis, invasion migration and metastasis, tumor promoting inflammation, chemoresistance, and altered bioenergetics [modified form; 42,44].

Table 2.2 : HIF-1α-EMT transcription factors association studies in different cancer types

S.No.	EMT transcription factors	Cancer type (Cell line, samples studied)	References
1.	TWIST	Hypopharyngeal cancer (FaDu) Breast Cancer (MCF-7) Ovarian epithelial cancer (Clinical samples)	[62] [73]
2.	Snail	Hepatocellular carcinoma (HepG2 and SMMC-7721) Lung adenocarcinoma (A549) Renal clear-cell carcinoma (786-O)	[74] [63] [75]

3.	Slug	Head and neck squamous cell carcinoma (UM-SCC1, UM-SCC23, clinical samples Lung adenocarcinoma (A549) Prostate cancer (LNCaP) Pancreatic ductal adenocarcinoma (AsPC-1, BxPc-3, Capan-1, Capan-2 and MIA-PacCa2)	[76] [63] [77] [78]
4.	SIP1	Renal clear cell carcinoma (786-O)	[75]
5.	Zeb1	Pancreatic ductal adenocarcinoma (AsPC-1,BxPC-3, Capan-1, Capan-2 and MIA-PaCa2) Colorectal cancer (HT-29 and HCT-116) Bladder cancer (T24-P, T24-L, clinical samples) Glioblastoma (SNB78 and U87) Pancreatic cancer (PANC-1 and SW-1990)	[78] [79] [80] [81] [82]

2.2.2 Hypoxia induced tumor angiogenesis

Tumour angiogenesis gained popularity in the early 1970s when Folkman et al. demonstrated that developing tumour cells need to replace their own blood supply in order to stay oxygenated and fed [83].Experimental evidence has consistently reported that hypoxia stimulates endothelial cell (EC) proliferation and migration and drives tumor angiogenesis. In cancer cells, the loss of p53 increases HIF-1α levels, boosting the transcriptional activation of HIF-1-dependent genes such as VEGF and erythropoietin (EPO) in response to hypoxia. This promotes EC proliferation, migration, and angiogenesis. Furthermore, hypoxia-induced E74-like ETS transcription factor 3 (ELF3) enhances the secretion of insulin-like growth factor (IGF1) and VEGF, which also drive EC proliferation, migration, and angiogenesis [84-89]. Hypoxia-induced E74-like ETS transcription factor 3 (ELF3) facilitates the increased secretion of insulin-like growth factor 1 (IGF1) and vascular endothelial growth factor (VEGF), which, in turn, promote endothelial cell (EC) proliferation, migration, and angiogenesis [90]. Additionally, HIF-1α mediates β-adrenergic receptor-driven pro-angiogenic effects. In hypoxia, HIF-1α escapes degradation, dimerizes with HIF-1β, and activates target genes by binding to hypoxic response elements (HREs). This activation leads to the expression of vascular endothelial growth factor (VEGF) and other pro-angiogenic factors, promoting endothelial cell proliferation and migration. [91-94]. Hypoxia also stimulates the production of hyaluronic acid, a key component of the vascular basement membrane, and increases hyaluronidase activity. This may further enhance angiogenesis as a

compensatory response to hypoxic conditions, thereby supporting the formation of new blood vessels to improve oxygen supply [95]. Further hypoxia can increase Zeb1 (transcription factor) expression, which in turn can influence VEGFA production [96]. Liu et al. (2016) investigated the role of Zeb 1 in breast cancer and found that ectopic expression of Zeb1 significantly increases VEGFA synthesis in MDA-MB-231 breast cancer cells, thereby promoting tumor angiogenesis both in vitro and in vivo. Additionally, their study revealed that elevated levels of Zeb1 correlate with increased blood vessel density in breast cancer specimens [97]. Zeb1 may activate these pathways, leading to VEGFA production. In lung adenocarcinoma, Zeb1 activates PI3K by repressing miR-200 targets. In breast cancer, it may inhibit PP2A, promoting p38 phosphorylation. Zeb 1 might interact with HIF-1 in a feedback loop.

2.2.3 Hypoxia-mediated drug resistance

In the recent years hypoxia has been widely recognized as a significant factor in tumor therapy resistance across various cancer cells. Roland Wenger and colleagues found that inactivating HIF-1 enhances the effectiveness of carboplatin and etoposide in inhibiting mouse embryonic fibroblast proliferation [99,100]. HIF-1α protein is overexpressed in numerous solid malignant tumors, including breast, colon, gastric, lung, skin, ovarian, pancreatic, prostate, and renal cancers, compared to normal tissues [101,102].

It is known that hypoxia-mediated overexpression of drug efflux proteins is a key factor in chemoresistance. Hypoxia in the tumor microenvironment (TME) leads to decreased pH, which contributes to multidrug resistance (MDR) through mechanisms such as ion trapping, reduced apoptosis, genetic alterations like p53 mutations, and increased activity of the drug transporter P-glycoprotein (P-gp) [103,104]. Ion trapping occurs when uncharged molecules diffuse through cell membranes more easily than charged ones, causing chemotherapeutic drugs to be less effective in acidic environments. This pH dependency of drugs reduces their accumulation in tumor cells, leading to drug resistance [105].

Additionally, HIF-1 activates the multidrug resistance 1 (MDR1) gene under hypoxic conditions, leading to a sevenfold increase in MDR in epithelial cells. MDR1 encodes P- glycoprotein (P-gp), an ATP-binding cassette (ABC) transporter that acts as a drug efflux pump, reducing intracellular concentrations of chemotherapeutic drugs [106]. The ABC transporter family includes at least 48 members, with 12 recognized as drug transporters, such as P-gp (ABCB1), MRP1 (ABCC1), and ABCG2 (breast cancer resistance protein). Chemotherapeutic drugs like benzoate mustard have shown higher efficacy than doxorubicin, but this efficacy decreases with alkalinization [107,108] . Melphalan, effective in slightly acidic environments, also demonstrates this phenomenon. P-gp activity, encoded by the MDR1 gene, increases in low-oxygen conditions, pumping out drugs like doxorubicin and paclitaxel, although its mRNA levels remain unchanged in acidic environments. Moreover studies have

shown that HIF-1α inhibition can reverse MDR in colon cancer cells by downregulating MDR1/P-gp. Additionally, ABC2 overexpression contributes to resistance in an estramustine-resistant ovarian carcinoma cell line, while antisense-mediated downregulation of ABC2 sensitizes these cells to the drug [107]. A study investigating the impact of hypoxia on P-gp and MDR protein expression in the A549 human lung adenocarcinoma cell line found that hypoxia led to elevated levels of HIF-1α, P-gp, and MDR protein, resulting in increased resistance of A549 cells to adriamycin [109]. The loss of apoptotic potential and genomic instability, often due to p53 mutations, further contributes to drug resistance. Hypoxia induces a cascade of reactions, enhancing gene expression and promoting malignancy in the hypoxic core of tumors. Cell-based targeted nanoparticles have been proposed as a strategy to combat drug resistance and improve chemotherapy efficacy [110]. Overall, hypoxia is a significant factor in tumor progression and therapeutic resistance, with HIF-1 playing a crucial role. HIF-1 is overexpressed in many tumors, including breast, prostate, lung, pancreatic, and head and neck cancers, affecting various cellular pathways and mechanisms [111].

2.3 Paradoxical role of ROS in solid tumor

Reactive oxygen species (ROS) have evolved to control important signalling pathways because they are produced by aerobic metabolism in eukaryotic cells. These extremely reactive oxygen-containing molecules are now known to be more important for biological processes than being merely byproducts of cellular respiration [112].

Reactive oxygen species (ROS) are highly reactive molecules containing reactive oxygen such as superoxide ($O_2^{\bullet-}$), hydrogen peroxide (H_2O_2), hydroxyl radical (•OH), singlet oxygen ($^1O_2$), and ozone (O_3) [113]. These species are natural by-products of metabolism and participate in various cellular signalling pathways such as cell proliferation, necrosis, apoptosis, and protease activities, serving a dual function within the human body [113]. The two primary sources of ROS generation in normally functioning cells are mitochondria and NADPH oxidase (NOX) [114,115]. The tumorigenesis-promoting activity of ROS was first investigated in the mid-90s [116,117]. Cancer cells exhibit higher oxidative stress compared to normal cells due to excessive ROS production and impaired antioxidant mechanisms. This imbalance aids in tumor cell survival, progression, and proliferation. In cancer cells, several key signalling pathways regulate reactive oxygen species (ROS) production. Important pathways involved in ROS production in cancer cells are the PI3K/Akt Pathway, RAS/RAF/MEK/ERK Pathway, Hypoxia-Inducible Factor (HIF) Pathway, NF-κB Pathway, p53 Pathway, and NADPH Oxidase (NOX) Pathway. PI3K/Akt Pathway which increases mitochondrial respiration and metabolic activity, is stimulated by growth factors and oncogenic signals, which in turn increase the production of ROS. ROS levels are raised further by PI3K/Akt hyperactivation brought on by inactivating the tumor suppressor PTEN [118-120]. The MEK/ERK/RAS/RAF pathway often activated by mutations in RAS or upstream growth factor receptors frequently trigger this pathway, which promotes cell survival and proliferation and raises ROS generation and mitochondrial activity.

Additionally, oxidative stress inhibits MAPK phosphatase, leading to ERK activation [118,121]. Hypoxia-Inducible Factor (HIF) pathway activated under low oxygen condition, stabilized HIF-1α increase the production of enzymes that produce reactive oxygen species (ROS), such as NOX and mitochondrial respiratory chain enzymes [122,123]. Further, the ROS production can be increased by activating ROS-generating genes and encouraging mitochondrial dysfunction through the NF-κB pathway, which is triggered by inflammatory cytokines, growth factors, and stress signals [124,125]. Antioxidant reactions are often induced by the p53 pathway, which is activated in response to stress and damage to DNA. Yet, because of altered metabolism and malfunctioning mitochondria, p53 mutations or failure frequently result in elevated generation of reactive oxygen species [126,127]. NADPH oxidase (NOX) pathway is activated by various signals, including growth factors and cytokines, NOX enzymes produce ROS by transferring electrons from NADPH to oxygen [128-129]. NOX upregulation in cancer cells significantly contributes to ROS generation. These pathways further elevate ROS levels and decrease the antioxidant expression, maintaining oxidative stress and driving cancer cell proliferation and tumorigenesis [130].

2.4 Conventional therapeutic modalities for the treatment of NSCLC and TNBC

The treatment landscape for lung cancer has evolved significantly, moving from the empirical use of cytotoxic therapies based on physician preference to a more personalized approach. Non-small cell lung cancer (NSCLC) and Triple negative breast cancer (TNBC) are among the most aggressive types of solid tumors [131]. NSCLC is marked by the incorporation of malignant carcinoma into the respiratory system. TNBC is defined by the lack of progesterone receptor, HER2/neu, and estrogen receptor genetic components in breast cancer [132]. Both cancers are linked to low median and overall survival rates, poor progression-free survival, and high relapse rates. These cancers exhibit tumor heterogeneity, genetic mutations, the generation of cancer stem cells, immune resistance, and chemoresistance. Therapeutic regimens for solid tumor, depending on the stage and degree of metastasis, can be divided into localized treatments (such as surgery and radiation) and systemic treatments (including chemotherapy, immunotherapy, gene therapy, and targeted therapy) [132,133]. **Table 2.3** outlines the various treatment approaches for localized therapy in triple negative breast cancer (TNBC) and non-small cell lung cancer (NSCLC). For localized treatment, surgery and/or radiation therapy are commonly used. Research has shown that mastectomy for TNBC and pneumonectomy for NSCLC are less invasive and help preserve the aesthetics of the organs [134-137]. External beam radiation therapy (EBRT) and radiofrequency ablation (RFA) are also utilized in radiotherapy for these cancers. Systemic treatments for both cancers include conventional chemotherapy, immunotherapy, and targeted therapy (**Fig. 2.5**) specific to biomarkers and oncogenes. Metastatic tumors often show poor response rates, with chemoresistance contributing to reduced treatment efficacy [138]. Neoadjuvant chemotherapy is frequently recommended for TNBC, with the anthracycline–cyclophosphamide (AC) regimen proving

highly effective. In cases with BRCA mutations, AC therapy has been associated with improved pathological complete response rates (pCR) and reduced relapse rates. Additionally, the use of platinum-based therapies in neoadjuvant settings has further improved prognosis, showing higher pCR rates compared to AC therapy [139-142]. Still 50% of patients diagnosed with early-stage triple-negative breast cancer (stages I to III) experience disease recurrence, and 37% die in the first 5 years after surgery [143] . In fact, 30% to 55% of patients with NSCLC develop recurrence and die of their disease despite curative resection [145].

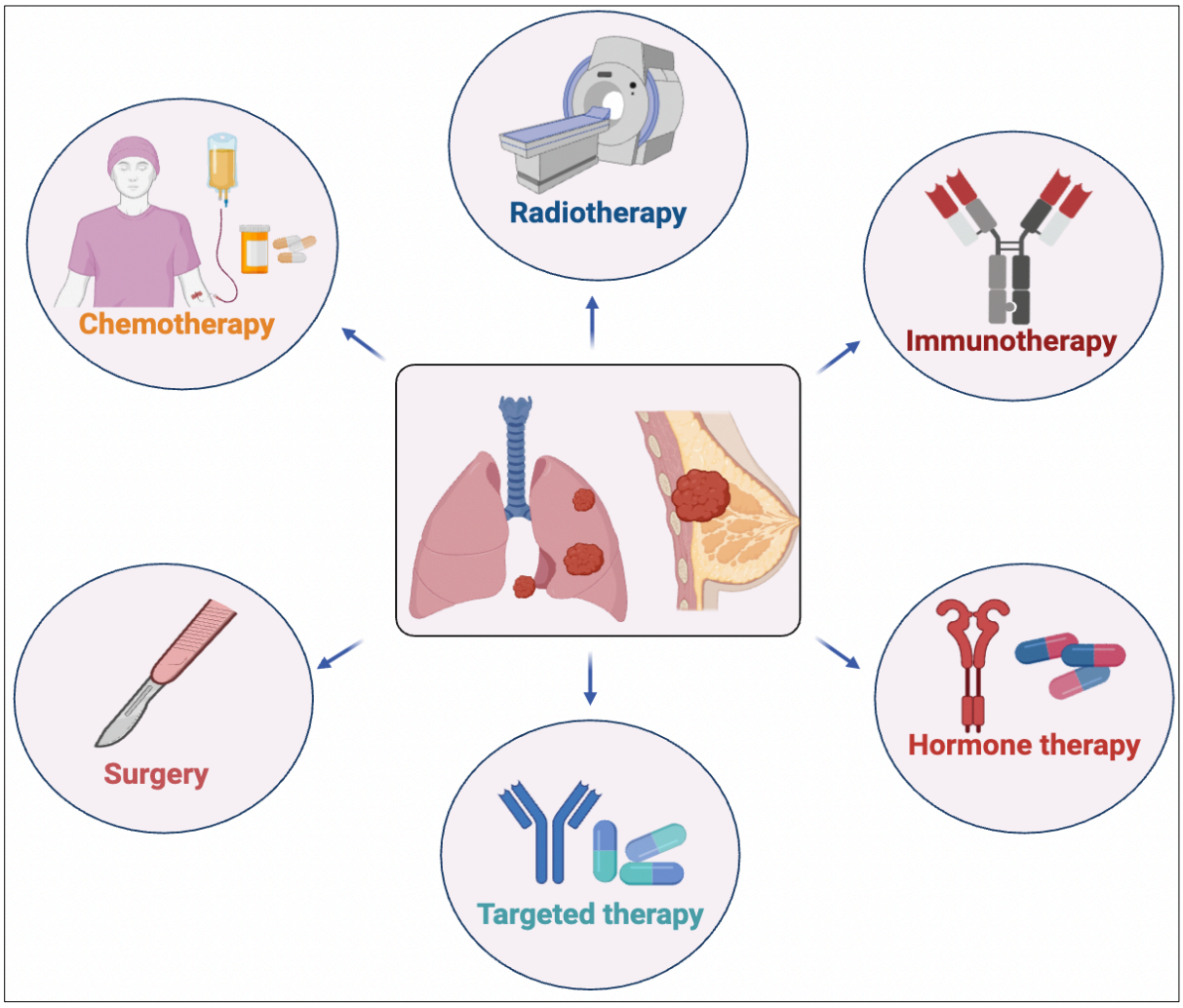

Figure 2.5: An overview of existing therapeutic strategies for treating NSCLC and TNBC. *Chemotherapy, radiotherapy, immunotherapy, hormone therapy, targeted therapy, and surgery [modified form; 133].*

Table 2.3: Conventional and current treatment strategies for NSCLC and TNBC

Non-Small Cell Lung Cancer (NSCLC)			
	Radiation therapy	1. Radio Frequency Ablation (RFA) 2. External beam radiation therapy (A) Stereotactic body radiation therapy (SBRT)/ Stereotactic ablative	[140]

Local treatment	Surgery (Early stage of Cancer)	1. Pneumonectomy 2. Lobectomy 3. Segmentectomy or Wedge resection 4. Sleeve resection	
Systematic treatments	Chemotherapy	1. Neoadjuvant and Adjuvant therapy 2. For locally advanced NSCLC 3. For metastatic (stage IV) NSCLC 4. Chemotherapy Regimens used with Radiation Therapy (RT)	
	Targeted therapy	1. Angiogenesis inhibitors: Bevacizumab Ramucirumab 2. Epidermal growth factor receptor (EGFR) inhibitors: Erlotinib, Afatinib,	
	Immunotherapy	Immune checkpoint inhibitors: 1. PD-1/PD-L1inhibitors: Nivolumab and pembrolizumab. 2. Atezolizumab 3. Durvalumab	
	Palliative procedures	Treating fluid build-up in the area around the lung (Pleural effusion): 1. Thoracentesis 2.Pleurodesis: Chemical a. pleurodesis b. Surgical pleurodesis 3.Catheter placement	
Triple Negative breast cancer (TNBC)			
Local treatment	Radiation therapy	External beam radiation therapy (EBRT) 1. Whole breast radiation 2. Hypofractionated radiation therapy 3. Accelerated partial breast irradiation (APBI) 4. Intraoperative radiation therapy (IORT) 5. 3D-conformal radiotherapy (3D-CRT) 6. Intensity-modulated radiotherapy (IMRT) 7. Brachytherapy (internal radiation) Intracavitary brachytherapy Interstitial brachytherapy	[141, 142]
	Surgery (Early stage of Cancer)	1. Breast-conserving surgery lumpectomy, quadrantectomy, partial mastectomy, or segmental mastectomy) or Mastectomy 2. Sentinel lymph node biopsy (SLNB) or axillary lymph node dissection (ALND) 3. Breast reconstruction	

		4. To relieve symptoms of advanced cancer	
Systematic treatments	Chemotherapy	1. After surgery (adjuvant chemotherapy) 2. Before surgery (neoadjuvant chemotherapy) A. PARP inhibitors Carboplatin, Cisplatin Other chemotherapeutics mTOR inhibitors B. Growth-factor inhibitors C. PD1/PD-L1 inhibitors Other immune checkpoint inhibitors D. mTOR inhibitors EMT- targeted therapy CSC- targeted therapy AXL inhibitor. E. PI3K inhibitors, Antiangiogenic therapy, Src antagonist F. Antiandrogen blockade, CDK4/6 inhibitors, Immune checkpoint inhibitors Examples: Anthracyclines, such as doxorubicin (Adriamycin) and epirubicin (Ellence), Taxanes, such as paclitaxel (Taxol) and docetaxel (Taxotere), 5-fluorouracil (5-FU) or capecitabine, Cyclophosphamide, Carboplatin 4. For advanced breast cancer: Taxanes, such as paclitaxel, docetaxel, and albumin-bound paclitaxel, Anthracyclines (Doxorubicin, pegylated liposomal doxorubicin, and Epirubicin), Platinum agents (cisplatin, carboplatin), Vinorelbine, Capecitabine, Gemcitabine, Ixabepilone, Eribulin 5. Dose-dense chemotherapy: Doxorubicin (Adriamycin) and cyclophosphamide, followed by weekly paclitaxel. 6. Nanocarriers: Liposomal doxorubicin (Doxil™), albumin-bound paclitaxel or Nab-Paclitaxel (Abraxane™).	
	Immunotherapy/ Targeted therapy	Advanced therapeutic strategies Passive, Active and Immunotherapy Poly ADP-ribose polymerase (PARP) enzyme inhibitors Avastin, Ibrance, Kisqali, Lynparza, Piqray, Trodelvy, Talzenna, Verzenio Eg.: Anitbody-drug conjugate: Sacituzumab govitecan	
	Gene Therapy	Metastasis suppressor genes (MSGs) and Metastasis promoter genes (MPGs). A. Epidermal growth factor receptor and their inhibitors B. Inhibitors of multiple receptors of EGFR	

		C. HER2 inhibitors: D. Dual inhibitors of EGFR and HER2 E. Inhibition of the urokinase-type plasminogen activator system (uPA) F. Matrix metalloproteinases inhibitors G. Histone acetyl transferases (HATs) and histone deacetylases (HDACs) insulin-like growth factor and insulin-like growth factor inhibitors (IGF-IR) H. Vascular endothelial growth factor(VEGF) and five glycoproteins VEGFA, VEGFB, VEGFD, and placental growth factor.	

In this thesis, we explore three innovative therapeutic strategies, emphasizing their mechanisms of action against solid tumors, specifically targeting non-small cell lung cancer (NSCLC) and triple-negative breast cancer (TNBC). These approaches aim to tackle the aggressive nature and treatment resistance of these cancers, offering potential advancements in patient outcomes and novel avenues for cancer therapy. The strategies include:

1. Investigating the novel role of Imidazo[1,2-a] pyridine (IMPA) derivatives in combating NSCLC.
2. Elucidating the therapeutic potential of liposomal oxygen nanobubbles in the treatment of both lung and breast cancers.
3. Delineating the effectiveness of LNP-conjugated Zeb1 siRNA as a targeted therapy to inhibit tumor angiogenesis.

This chapter will provide a comprehensive literature review on the anticancer activity of imidazopyridine-based derivatives, the role of oxygen nanobubbles, and the potential of LNP-loaded Zeb1 siRNA in targeting tumor angiogenesis.

2.4.1 Imidazo [1,2-a] pyridine promising therapeutic candidates for anti-tumor activity

Chemotherapy, surgery, and radiotherapy have traditionally been the pillars of cancer treatment, with chemotherapy being the most commonly utilized method, as previously discussed. A wide range of chemotherapeutic agents have been discovered and developed to target different types of cancers through various mechanisms. However, the side effects, toxicity, and the issue of drug resistance associated with these treatments have driven researchers to find out compounds with fewer adverse effects [145].

Among the various classes of anti-tumor compounds, heterocyclic organic molecules have garnered significant attention from researchers for their potential in treating neoplastic diseases. Compounds

such as pyrrole, pyrimidine, indole, quinoline, and purine are examples of heterocycles that have demonstrated noteworthy cytotoxic profiles [146]. Heterocycles are fundamental structural elements in many approved anti-cancer drugs. In fact, nearly two-thirds of FDA-approved anti-cancer agents contain heterocyclic rings within their molecular frameworks (**Figure 2.6**) [147]. Their widespread use in anti-cancer drug design is attributed to their natural abundance, unique physicochemical properties, and their ability to modulate a wide range of cellular signaling pathways and metabolic processes, making them indispensable in medicinal chemistry [148]. When the imidazole ring is fused with a pyridine ring, it forms the bicyclic 5–6 heterocyclic structure known as imidazo[1,2-a]pyridine [149]. This moiety is well recognized for its therapeutic potential due to its biologically active nitrogen-containing heterocycle. Among the derivatives of imidazopyridine, the imidazo[1,2-a]pyridine scaffold is particularly significant in the field of natural products and pharmaceuticals, exhibiting a wide range of biological activities, including notable anti-tumor effects. Several drugs containing the imidazo[1,2-a]pyridine structure, such as zolpidem (used to treat insomnia), alpidem (an anxiolytic), olprinone (for acute heart failure), and zolimidine (for peptic ulcer treatment), highlight its therapeutic versatility [150-155]. Other compounds like necopidem and saripidem also function as anxiolytic agents. The broad pharmacological activity and diverse biological applications of imidazo[1,2-a]pyridine derivatives underscore their importance as potential anti-proliferative agents. These compounds are actively being explored for their efficacy against various cancers. In parallel, oxygen-containing heterocycles, particularly those in the pyran family, have shown excellent pharmacological efficacy [152]. Additionally, Imidazopyridines, in particular, have gained attention as potential anticancer agents due to their strong inhibitory effects on the proliferation of various cancer cells. Studies have shown that different substituted imidazopyridines exhibit considerable anticancer activity through multiple mechanisms [153].

Many pyran derivatives are accessible and can be fused with both carbocyclic and heterocyclic frameworks [156]. Among these, 2-amino-4H-pyrans have emerged as particularly attractive candidates in medicinal chemistry due to their selective cytotoxic and antimicrobial properties [157]. However, despite their promising activity, the precise mechanisms of action of amino pyran heterocycles remain largely unclear. Significantly, imidazo[1,2-a]pyridine compounds stand out not only for their therapeutic applications but also for their role in the ongoing search for more effective anti-cancer agents [158,160]. Their structural versatility and ability to interact with key biological targets make them prime candidates for further research and development in the quest to overcome cancer's resistance to conventional therapies.

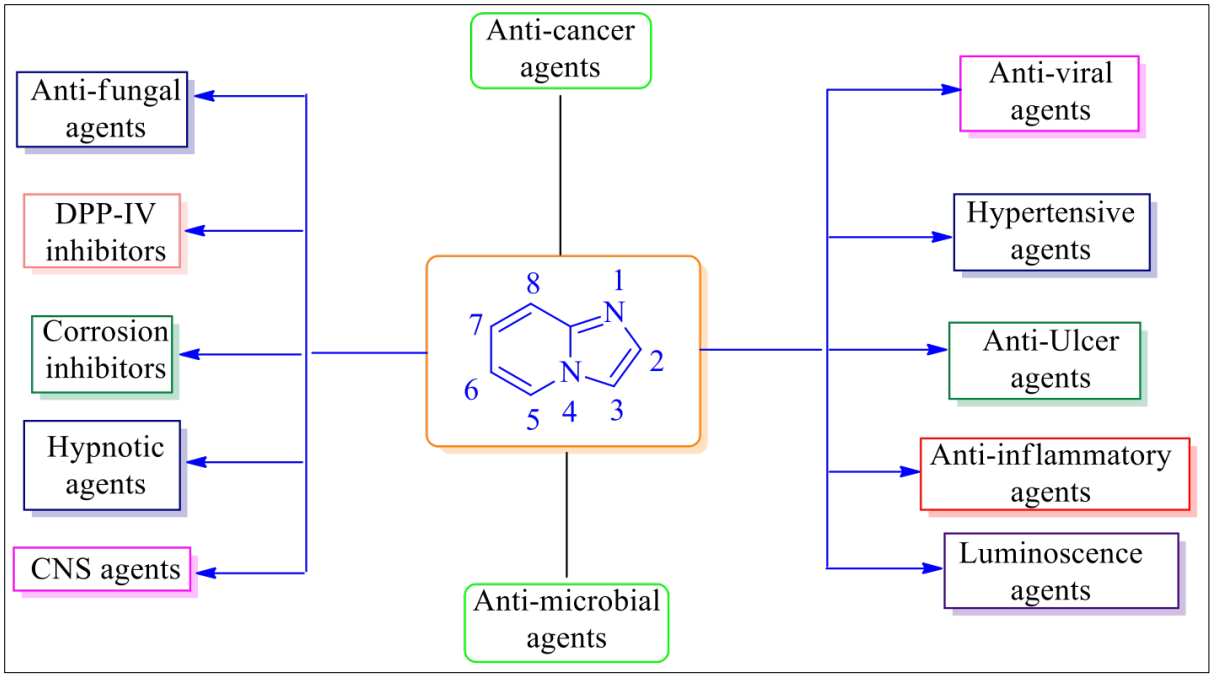

Figure 2.6: Diverse pharmacological activity of Imidazo [1,2-a] pyridine derivatives compound; *anti-cancer, anti-fungal, DPP-IV inhibitors, corrosion inhibiotrs, hypnotic agents, CNS agents, anti-viral agent, hypertensive agents, anti-ulcer agents, anti-inflammatory agent, and luminescence agents[modified from 152,155].*

Several small molecule inhibitors, including buparlisib, everolimus, vandetanib, apatinib, olaparib, and salidroside, have been identified as potential therapeutics for treating triple-negative breast cancer (TNBC). These inhibitors target various signaling pathways such as VEGF, PARP, STAT3, MAPK, EGFR, P13K, and SRC (**Table 2.4**). Despite these advancements, drug development for TNBC remains challenging due to the absence of specific biomarkers, making chemotherapy the primary treatment. However, chemotherapy is often associated with chemoresistance and high toxicity to healthy cells. Consequently, there is a continuous need for small molecule inhibitors that specifically target the abnormally expressed signaling pathways in TNBC.

Table 2.4 Examples of small molecule inhibitors, used for NSCLC and TNBC [modified from 160]

S.N.	Small Molecule	Clinical stage	Mechanism of Action	Class of Drug	Reference
1.	Buparlisib (BKM120, Norvatis)	NCT015766666 (Phase 1)	An orally bioavailable Class I PI3K inhibitor	PI3K/AKT/mTOR/ small molecule inhibitors	[161]
2.	Ipatasertib	Phase 1	Potent small-molecule kinase inhibitor that shows selectivity for AKT. It competes for ATP		[162]

			and is sensitive to high levels of phosphorylated AKT and mutations in PIK3CA and PTEN		
3.	Capivasertib (AZD5363)	PAKT trial	Novel pyrrolopyrimidine-derived small molecule inhibitor that inhibits all forms of AKT		[163]
4.	Everolimus (RAD001)	NCT01931163 (phase 2), NCT02616848 (phase 1), NCT02456857 (phase 2), NCT02120469 (phase 1), NCT02890069 (phase 1)	A small-molecule derivative of sirolimus (rapamycin), inhibits mTOR, thereby preventing cell cycle growth, progression, and proliferation		[164]
5.	Olaparib	PhaseI,II	First PARP inhibitor approved in 2018 by the FDA for the treatment of cancer in patients with metastatic breast cancer and a germline BRCA mutation	PARP inhibitors	[164]
6.	Velaparib	Phase II	Potent, orally bioavailable selective inhibitor of PARP protein onto the DNA site		[164]
7.	Talazoparib	EMBRACA Phase III	PARPi (poly(ADP-ribose) polymerase inhibitor) that exhibits its anti-tumor activity by firmly trapping PARP onto damaged DNA, thereby causing cell death in BRCA-mutated BC		[166]
8.	Ruxolitinib	NCT01562873 (phase 1)	an orally bioavailable inhibitor of JAK1 and JAK2,	JAK/STAT3 inhibitors.	[164]
9.	LLL12B		An orally Bioavailable carbamate prodrug of LLL12		[167]
10.	Flubendazole		Inhibition of tubulin polymerization, and		[164]

			dysfunction in the activation of STAT3		
11.	Salinomycin		Act through the reduction of CD44+/Cd24-		[164]
12.	E6201	None	An ATP-competitive dual kinase inhibitor of MEK1	MAPK inhibitors.	[168]
13.	Cobimetinib		MEK inhibitor that has been reported in a three-cohort phase II COLET (NCT02322814) to ascertain its anti-tumor efficacy in combination with chemotherapy with or without atezolizumab in advanced or metastatic TNBC patients		[169]
14.	Nifetepimine		Endoplasmic stress induced apoptosis in TNBC		[170]
15.	BL-E1001		A small molecule inhibitor, has been reported to induce mitochondrial apoptosis, independent of the Ras/Raf/MEK pathway		[171]
16.	Cannabidiol	NCT02338245 (phase 2)	CBD induces programmed cell death, decreases ID1 (metastatic) factors, increases ID2 (pro-differentiation) factors, and acts as an inverse agonist for CB2, as well as an antagonist for CB1 and GPR55 receptors, all being G-protein coupled receptors	EGFR pathway inhibitors	[172]
17.	Varlitinib		Potent reversible HER inhibitor of the receptor tyrosine		[173]
18.	Salidroside		Regulate the STAT3 and JAK2 and EGFR pathways through MMPs		[174]
19.	Vandetanib		Inhibition of EGFR phosphorylation		[175]

20.	Dasatinib	NCT02720185 (phase 2)	A small molecule inhibitor of Src and abl proteins.	SRC inhibitors.	[176]
21.	Bj-2302				[177]
22.	1j				[178]

2.4.2 Oxygen nanobubble (ONB) for oxygenation as anti-cancer therapy

An oxygen nanobubble is a tiny, gas-filled pocket containing oxygen, typically in the form of a spherical cap. These nanobubbles have a height ranging from more than 10 nanometres (nm) to less than 100 nm. The radius at the contact line, which is the three-phase boundary where the gas, liquid, and solid meet, generally falls between 50 nm and 500 nm [179].

Looking at the history, in the early 1950s, Donald A. Glaser discovered that as charged particles moved through a superheated liquid within a glass chamber, the liquid would vaporize along the particle's path, forming a trail of microscopic bubbles that could be observed [180]. The concept of bulk NBs originated from early speculations that submicron gas units, stabilized by organic films, could serve as nuclei for microbubble growth during cavitation [181-184]. The first experimental evidence of interfacial NBs came from Parker et al., who measured attractive forces between hydrophobic surfaces in water [185]. Since then, extensive research has been conducted on generating and characterizing NBs, revealing their surprising stability in pure water or surfactant solutions shown in **Fig. 2.7** [186].

To analyze the morphological appearance of nanobubbles (NBs), atomic force microscopy was first used in 2000, providing direct observation of these structures. By 2004, NBs were investigated as ultrasound (US) contrast agents [186]. Their unique ability to remain suspended in liquid, attributed to their negative surface potential, prevents them from coalescing or disappearing. This stability allows for continuous gas transfer throughout the liquid volume until the NBs eventually collapse. In 2013, the International Standards Organization (ISO) formed a technical committee (ISO TC/281) to develop standards and regulatory procedures for fine bubble technology. In 2017, they officially defined nanobubbles as ultrafine bubbles with a diameter of less than 1 micrometer (<1 μm) [188].

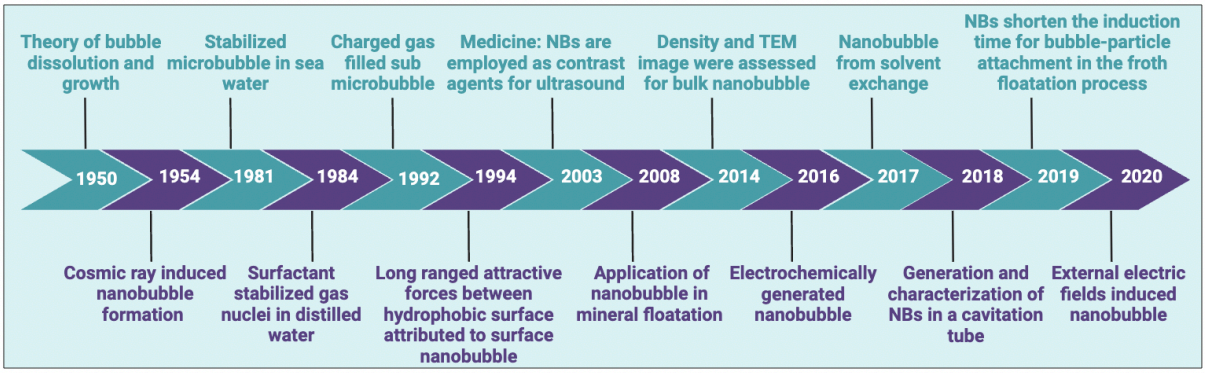

Figure 2.7: *Highlighting the key milestones in the research and development of nanobubble generation, properties, and applications [modified from 179,180,181].*

Characterization and compositions of micro/nanobubbles (MNBs)

Micro/nanobubbles (MNBs) exhibit enhanced echogenicity due to the encapsulated gas, which significantly improves ultrasound backscatter [189]. The core of MNBs typically contains a medical gas, while the shell is composed of biomolecules such as lipids, proteins, polymers, or surfactants [190]. These components ensure efficient gas solubility inside the shell. Under the influence of acoustic waves, MNBs oscillate, which can either enhance stable gas diffusion through stable cavitation or lead to violent collapse during inertial cavitation. MNBs generally range from 0.1 to 20 micrometers in size. Their stability is governed by Laplace pressure, and surfactants are used to stabilize the bubbles by reducing interfacial tension [190-192].

Research indicates that unstabilized gas bubbles dissolve rapidly. The stability and biocompatibility of micro/nanobubbles (MNBs), as well as the release rate of the core gas, are influenced by both the type of shell and the core gas used [193]. The shell creates a protective barrier around the gas, enhancing stability and shielding the bubbles from endogenous scavengers. It also slows the diffusion of the core gas into the surrounding environment. The properties of the shell, including its stiffness, elasticity, gas exchange capability, half-life, resistance to ultrasonic pressure, and ease of excretion from the body, are crucial in determining the overall performance of MNBs [194]. Below is a summary of the key properties associated with different types of shells.

A. Lipid Shells: These are biocompatible and flexible, can be functionalized, and are often stabilized with polyethylene glycol (PEG) [194-196].
B. Protein Shells: Known for their rigidity and biocompatibility, protein shells are used in commercial products such as Albunex [197].
C. Polymer Shells**:** These shells are thicker, provide a higher drug-loading capacity, and offer enhanced stability [197].
D. Core Gas: The core of bubble can contain various medical gases, such as oxygen. The use of mixed gases can improve the stability and longevity of the bubbles [198,199].

Further synthesized, MNBs/NBs characterized by employing a different techniques, including optical microscopy, dynamic light scattering (DLS), scanning electron microscopy (SEM), transmission electron microscopy (TEM), electrochemical sensing, fiber-optic based sensing, and fluorescence quenching. MNBs possess unique properties, such as high echogenicity, efficient gas solubility, and stability due to negative surface potential [197-199]. These features make them promising for diverse medical applications, including drug delivery, oxygen delivery, and ultrasound imaging. The flexibility offered by different shell compositions allows for tailored stability, biocompatibility, and functionalization. Challenges remain in maintaining the stability and uniformity of micro bubble or nanobubble [200,201]. Careful control of MNBs/NBs size is crucial to prevent blockages in capillaries. Additionally, long-term in vivo stability and biocompatibility require further research to avoid immune responses and ensure safe excretion. Several research findings highlight the significant potential of oxygen nanobubbles (ONBs) and their applications in cancer therapy:

A. **Lipid-polymer bilaminar oxygen nanobubbles for photodynamic therapy (PDT):** Using an emulsion evaporation and phase separation method, researchers developed lipid-polymer bilaminar oxygen nanobubbles conjugated with Ce6 for PDT. These nanobubbles can be stored as freeze-dried powders and demonstrate excellent biocompatibility, stability, and higher cellular uptake and tumor targeting efficiency compared to free Ce6. In vitro and in vivo experiments showed significant therapeutic efficacy and improved survival rates in C6 glioma tumors, indicating a potent photodynamic anticancer strategy for hypoxic tumors [202].
B. **Combining nanobubbles (NBs) with ultrasound (US):** The combination of NBs with US presents a promising approach for targeted anticancer therapy. This method enhances drug efficacy and minimizes off-target effects. US, an established non-invasive imaging technique, when paired with NBs, improves the delivery and distribution of therapeutic agents in specific tissues. This approach is highly promising for cancer treatment and is expected to see broader applications with ongoing research [203].
C. **Oxygen nanobubbles (ONBs) and epigenetic regulation:** P. Bhandari et al. (2017) demonstrated that ONBs could reverse global DNA hypomethylation in hypoxic tumors, stabilizing the epigenome and reactivating tumor suppressor genes to inhibit cell proliferation. Synthesized using FDA-approved sodium carboxymethyl cellulose, ONBs are non-cytotoxic, localize easily in tumor regions, and deliver supplemental oxygen directly to tumor cells, arresting tumor progression. Additionally, ONBs enable real-time diagnosis and monitoring, targeted delivery to hypoxic tumor areas, and enhanced effectiveness of epigenetic therapy [204].

Together, these findings emphasize the potential of ONBs in improving cancer outcomes through targeted delivery, enhanced therapeutic efficacy, and innovative treatment strategies for hypoxic tumors.

2.4.3 RNAi based therapeutic approaches

RNA interference (RNAi) is an innovative method that involves introducing noncoding double-stranded RNA (dsRNA) into cancer cells to induce the homology-dependent degradation of target messenger RNA (mRNA), resulting in specific gene silencing. This mechanism was first described by Fire and colleagues in (1998) [205]. Unlike traditional drugs that target proteins directly, RNAi-based therapeutics primarily target mRNA. These drugs utilize non-coding RNA (ncRNA) to cleave and downregulate the targeted mRNA, reducing protein production. Epigenetically-related ncRNAs include small interfering RNAs (siRNAs), microRNAs (miRNAs), piwi-interacting RNAs (piRNAs), and long intervening noncoding RNAs (lincRNAs). SiRNAs, consisting of 21–23 nucleotides, are a notable group of short ncRNAs. Synthetic siRNAs leverage the natural RNAi mechanism in a predictable and consistent manner, making them attractive as therapeutic agents [206]. Introducing siRNAs leads to the degradation of mRNA sequences that match those in the siRNAs, making RNAi a valuable method for cancer therapy through gene silencing.

RNA interference (RNAi) is an effective mechanism for post-transcriptional gene silencing. The RNAi process occurs in the cytoplasm of cells [207]. It begins with the enzyme Dicer, a dsRNA-specific endonuclease, which cleaves long double-stranded RNAs into shorter duplexes consisting of 19 base pairs with two-nucleotide overhangs at the 3' ends. These short dsRNAs are known as siRNAs [208]. The siRNA duplex then associates with a multiprotein complex called RISC. RISC unwinds the siRNA duplex, separating the strands. The sense strand is degraded by cellular nucleases due to RISC's RNA helicase activity, while the antisense strand remains bound to RISC. This antisense strand guides the RISC complex to the complementary mRNA sequence through Watson-Crick base pairing. Once bound, the RISC complex cleaves the target mRNA through its endonucleolytic activity, preventing its translation into protein [209,210]. The degraded mRNA fragments are further broken down by cellular nucleases, and the RISC complex can then target additional mRNA molecules, continuing the gene silencing process [211,212].

Lipid nanoparticles (LNPs) have emerged as effective delivery systems for siRNAs, which are potent therapeutic agents against cancer due to their ability to silence genes involved in tumorigenesis and metastasis [213]. LNPs protect siRNAs from degradation, enhance their bioavailability, and enable selective delivery to target cells, thereby reducing off-target effects [214,215]. Numerous studies have focused on LNP-based siRNA delivery systems for therapeutic applications. In 2018, a clinical trial demonstrated breakthrough results with the siRNA drug "**Patisiran**," used to treat hereditary transthyretin (TTR) amyloidosis [216]. Patisiran, delivered via LNPs, effectively induced the degradation of TTR mRNA in the liver, leading to its FDA approval as the first siRNA drug [216,217].

Recent advancements include the development of siP2X7-LNPs, a lipid nanocarrier system for delivering siRNA targeting the P2X7 receptor in mouse mammary carcinoma cells. This system,

which incorporates a novel symmetric branched ionizable lipid (SIL), has successfully transfected siP2X7 and induced apoptosis, demonstrating therapeutic efficacy in a triple-negative breast cancer cell line [218]. To further enhance therapeutic outcomes, co-delivery of chemotherapeutic drugs and siRNA within LNPs has been explored. However, this approach presents challenges, such as disrupting the LNP structure and reducing encapsulation efficiency.

To address these issues, a study in 2023 introduced surface-modified siRNA-loaded LNPs for co-delivery. By using a sulfur-containing phospholipid to conjugate a DOX derivative onto the LNPs, researchers achieved effective Bcl-2 knockdown and successful delivery of DOX-EMCH to the cell nucleus, leading to significant tumor growth inhibition *in vivo* in a mouse model [219]. Despite these advancements, challenges like hypoxic drug resistance remain prevalent in the tumor microenvironment.

In this thesis, we explore three innovative therapeutic strategies, emphasizing their mechanisms of action against solid tumors, specifically targeting non-small cell lung cancer (NSCLC) and triple-negative breast cancer (TNBC). These approaches aim to tackle the aggressive nature and treatment resistance of these cancers, offering potential advancements in patient outcomes and novel avenues for cancer therapy. The strategies include:

1. Investigating the novel role of Imidazo[1,2-a] pyridine (IMPA) derivatives in combating NSCLC.
2. Elucidating the therapeutic potential of liposomal oxygen nanobubbles in the treatment of both lung and breast cancers.
3. Delineating the effectiveness of LNP-conjugated Zeb1 siRNA as a targeted therapy to inhibit tumor angiogenesis.

This thesis presents a comprehensive literature review on the anticancer properties of imidazopyridine-based derivatives, the therapeutic potential of oxygen nanobubbles (ONBs), and the innovative use of lipid nanoparticle (LNP)-loaded Zeb1 siRNA in inhibiting tumor angiogenesis. The review explores the molecular mechanisms and therapeutic efficacy of imidazopyridine derivatives in cancer treatment, highlighting their ability to interfere with various signaling pathways involved in tumor progression. Additionally, it delves into the role of oxygen nanobubbles as a novel approach to enhance oxygen delivery to hypoxic tumor microenvironments, thereby improving the efficacy of conventional therapies and inducing epigenetic changes that suppress tumor growth. The chapter also examines recent advancements in LNP technology for siRNA delivery, focusing on Zeb1 siRNA's ability to target and disrupt angiogenesis in tumors. By integrating these diverse therapeutic strategies, the review underscores the potential for developing multifaceted approaches to cancer treatment, aiming to improve therapeutic outcomes and reduce adverse effects.

References

1. Brown, J. M., & Giaccia, A. J. (1998). The unique physiology of solid tumors: opportunities (and problems) for cancer therapy. *Cancer research*, *58*(7), 1408-1416.
2. Najafi, M., Majidpoor, J., Toolee, H., & Mortezaee, K. (2021). The current knowledge concerning solid cancer and therapy. *Journal of biochemical and molecular toxicology*, *35*(11), e22900.
3. Gridelli, C., Rossi, A., Carbone, D. P., Guarize, J., Karachaliou, N., Mok, T., ... & Rosell, R. (2015). Non-small-cell lung cancer. *Nature reviews Disease primers*, *1*(1), 1-16.
4. Ettinger, D. S., Akerley, W., Bepler, G., Blum, M. G., Chang, A., Cheney, R. T., ... & Yang, S. C. (2010). Non–small cell lung cancer. *Journal of the national comprehensive cancer network*, *8*(7), 740-801.
5. Lakhani, S. R., Ellis, I. O., Schnitt, S., Tan, P. H., & van de Vijver, M. J. (2019). World Health Organization classification of tumours, volume 2: breast tumours.
6. Gray, L. H., Conger, A., Ebert, M., Hornsey, S., & Scott, O. C. A. (1953). The concentration of oxygen dissolved in tissues at the time of irradiation as a factor in radiotherapy. *The British journal of radiology*, *26*(312), 638-648.
7. Sedeta, E., Sung, H., Laversanne, M., Bray, F., & Jemal, A. (2023). Recent mortality patterns and time trends for the major cancers in 47 countries worldwide. *Cancer Epidemiology, Biomarkers & Prevention*, *32*(7), 894-905.
8. Sadeghi, M. S., Lotfi, M., Soltani, N., Farmani, E., Fernandez, J. H. O., Akhlaghitehrani, S., ... & Gholizadeh, O. (2023). Recent advances on high-efficiency of microRNAs in different types of lung cancer: a comprehensive review. *Cancer Cell International*, *23*(1), 284.
9. Goldstraw, P., Ball, D., Jett, J. R., Le Chevalier, T., Lim, E., Nicholson, A. G., & Shepherd, F. A. (2011). Non-small-cell lung cancer. *The Lancet*, *378*(9804), 1727-1740.
10. Tan PH, Ellis I, Allison K, Brogi E, Fox SB, Lakhani S, et al. WHO classification of tumours editorial board. The 2019 world health organization classification of tumours of the breast. Histopathology. 2020;77(2):181–5.
11. Weigelt, B., Geyer, F. C., & Reis-Filho, J. S. (2010). Histological types of breast cancer: how special are they?. *Molecular oncology*, *4*(3), 192-208.
12. Tang, Y., Wang, Y., Kiani, M. F., & Wang, B. (2016). Classification, treatment strategy, and associated drug resistance in breast cancer. *Clinical breast cancer*, *16*(5), 335-343.
13. Singh, D. D., & Yadav, D. K. (2021). TNBC: potential targeting of multiple receptors for a therapeutic breakthrough, nanomedicine, and immunotherapy. *Biomedicines*, *9*(8), 876.
14. Makki, J. (2015). Diversity of breast carcinoma: histological subtypes and clinical relevance. *Clinical medicine insights: Pathology*, *8*, CPath-S31563.

15. Onitilo, A. A., Engel, J. M., Greenlee, R. T., & Mukesh, B. N. (2009). Breast cancer subtypes based on ER/PR and Her2 expression: comparison of clinicopathologic features and survival. *Clinical medicine & research*, *7*(1-2), 4-13.
16. Goldhirsch, A., Winer, E. P., Coates, A. S., Gelber, R. D., Piccart-Gebhart, M., Thürlimann, B., ... & Wood, W. C. (2013). Personalizing the treatment of women with early breast cancer: highlights of the St Gallen International Expert Consensus on the Primary Therapy of Early Breast Cancer 2013. *Annals of oncology*, *24*(9), 2206-2223.
17. Vuong, D., Simpson, P. T., Green, B., Cummings, M. C., & Lakhani, S. R. (2014). Molecular classification of breast cancer. *Virchows Archiv*, *465*, 1-14.
18. Chen, Z., Fillmore, C. M., Hammerman, P. S., Kim, C. F., & Wong, K. K. (2014). Non-small-cell lung cancers: a heterogeneous set of diseases. *Nature Reviews Cancer*, *14*(8), 535-546.
19. Bethune, G., Bethune, D., Ridgway, N., & Xu, Z. (2010). Epidermal growth factor receptor (EGFR) in lung cancer: an overview and update. *Journal of thoracic disease*, *2*(1), 48.
20. Huang, L., Guo, Z., Wang, F., & Fu, L. (2021). KRAS mutation: from undruggable to druggable in cancer. *Signal transduction and targeted therapy*, *6*(1), 386.
21. Feng, Y., Spezia, M., Huang, S., Yuan, C., Zeng, Z., Zhang, L., ... & Ren, G. (2018). Breast cancer development and progression: Risk factors, cancer stem cells, signaling pathways, genomics, and molecular pathogenesis. *Genes & diseases*, *5*(2), 77-106.
22. Ma, H., Ursin, G., Xu, X., Lee, E., Togawa, K., Duan, L., ... & Bernstein, L. (2017). Reproductive factors and the risk of triple-negative breast cancer in white women and African-American women: a pooled analysis. *Breast Cancer Research*, *19*, 1-14.
23. Gorodetska, I., Kozeretska, I., & Dubrovska, A. (2019). BRCA genes: the role in genome stability, cancer stemness and therapy resistance. *Journal of Cancer*, *10*(9), 2109.
24. Cruz, C. S. D., Tanoue, L. T., & Matthay, R. A. (2011). Lung cancer: epidemiology, etiology, and prevention. *Clinics in chest medicine*, *32*(4), 605-644.
25. Harada, G., Yang, S. R., Cocco, E., & Drilon, A. (2023). Rare molecular subtypes of lung cancer. *Nature Reviews Clinical Oncology*, *20*(4), 229-249.
26. Cai, X., Sheng, J., Tang, C., Nandakumar, V., Ye, H., Ji, H., ... & Lin, H. (2014). Frequent mutations in EGFR, KRAS and TP53 genes in human lung cancer tumors detected by ion torrent DNA sequencing. *PloS one*, *9*(4), e95228.
27. Miller, C. W., Simon, K., Aslo, A., Kok, K., Yokota, J., Buys, C. H., ... & Koeffler, H. P. (1992). p53 mutations in human lung tumors. *Cancer research*, *52*(7), 1695-1698.
28. Greulich, H. (2010). The genomics of lung adenocarcinoma: opportunities for targeted therapies. *Genes & cancer*, *1*(12), 1200-1210.
29. Halvorsen, A. R., Silwal-Pandit, L., Meza-Zepeda, L. A., Vodak, D., Vu, P., Sagerup, C., ... & Helland, Å. (2016). TP53 mutation spectrum in smokers and never smoking lung cancer patients. *Frontiers in genetics*, *7*, 85.

30. Pawelczyk, K., Piotrowska, A., Ciesielska, U., Jablonska, K., Glatzel-Plucinska, N., Grzegrzolka, J., ... & Nowinska, K. (2019). Role of PD-L1 expression in non-small cell lung cancer and their prognostic significance according to clinicopathological factors and diagnostic markers. *International journal of molecular sciences*, *20*(4), 824.
31. Yu, H., Boyle, T. A., Zhou, C., Rimm, D. L., & Hirsch, F. R. (2016). PD-L1 expression in lung cancer. *Journal of Thoracic Oncology*, *11*(7), 964-975.
32. Yan, N., Guo, S., Zhang, H., Zhang, Z., Shen, S., & Li, X. (2022). BRAF-mutated non-small cell lung cancer: current treatment status and future perspective. *Frontiers in oncology*, *12*, 863043.
33. Derakhshan, F., & Reis-Filho, J. S. (2022). Pathogenesis of triple-negative breast cancer. *Annual Review of Pathology: Mechanisms of Disease*, *17*(1), 181-204.
34. Sadeghi, Fatemeh, et al. "Molecular contribution of BRCA1 and BRCA2 to genome instability in breast cancer patients: Review of radiosensitivity assays." *Biological procedures online* 22 (2020): 1-28.
35. Rivlin, N., Brosh, R., Oren, M., & Rotter, V. (2011). Mutations in the p53 tumor suppressor gene: important milestones at the various steps of tumorigenesis. *Genes & cancer*, *2*(4), 466-474.
36. He, Y., Sun, M. M., Zhang, G. G., Yang, J., Chen, K. S., Xu, W. W., & Li, B. (2021). Targeting PI3K/Akt signal transduction for cancer therapy. *Signal transduction and targeted therapy*, *6*(1), 425.
37. Long, L., Fei, X., Chen, L., Yao, L., & Lei, X. (2024). Potential therapeutic targets of the JAK2/STAT3 signaling pathway in triple-negative breast cancer. *Frontiers in Oncology*, *14*, 1381251.
38. Hubalek, M., Czech, T., & Müller, H. (2017). Biological subtypes of triple-negative breast cancer. *Breast care*, *12*(1), 8-14.
39. Thompson, K. J., Leon-Ferre, R. A., Sinnwell, J. P., Zahrieh, D. M., Suman, V. J., Metzger, F. O., ... & Kalari, K. R. (2022). Luminal androgen receptor breast cancer subtype and investigation of the microenvironment and neoadjuvant chemotherapy response. *NAR cancer*, *4*(2), zcac018.
40. Vidula, N., Yau, C., Wolf, D., & Rugo, H. S. (2019). Androgen receptor gene expression in primary breast cancer. *NPJ breast cancer*, *5*(1), 47.
41. Hockel, M., & Vaupel, P. (2001). Tumor hypoxia: definitions and current clinical, biologic, and molecular aspects. *Journal of the National Cancer Institute*, *93*(4), 266-276.
42. Harris, A. L. (2002). Hypoxia—a key regulatory factor in tumour growth. *Nature reviews cancer*, *2*(1), 38-47.
43. Tam, S. Y., Wu, V. W., & Law, H. K. (2020). Hypoxia-induced epithelial-mesenchymal transition in cancers: HIF-1α and beyond. *Frontiers in oncology*, *10*, 486.

44. Muz, B., De La Puente, P., Azab, F., & Kareem Azab, A. (2015). The role of hypoxia in cancer progression, angiogenesis, metastasis, and resistance to therapy. *Hypoxia*, 83-92.
45. Lee, J. W., Bae, S. H., Jeong, J. W., Kim, S. H., & Kim, K. W. (2004). Hypoxia-inducible factor (HIF-1) α: its protein stability and biological functions. *Experimental & molecular medicine*, *36*(1), 1-12.
46. Ancel, J., Perotin, J. M., Dewolf, M., Launois, C., Mulette, P., Nawrocki-Raby, B., ... & Dormoy, V. (2021). Hypoxia in lung cancer management: a translational approach. *Cancers*, *13*(14), 3421.
47. Shi, Y., Lin, X., Wang, J., Zhou, Z., Chen, S., & Chen, G. (2024). Advances of HIF-1α/glycolysis axis in non-small cell lung cancer. *Oncology Reports*, *51*(4), 1-11.
48. Srivastava, N., Usmani, S. S., Subbarayan, R., Saini, R., & Pandey, P. K. (2023). Hypoxia: syndicating triple negative breast cancer against various therapeutic regimens. *Frontiers in Oncology*, *13*, 1199105.
49. Bernardi R, Gianni L. Hallmarks of triple negative breast cancer emerging at last? Cell Res. 2014 Aug;24(8):904-5. doi: 10.1038/cr.2014.61. Epub 2014 May 9. PMID: 24810303; PMCID: PMC4123289.
50. Lu, H., Lyu, Y., Tran, L., Lan, J., Xie, Y., Yang, Y., ... & Semenza, G. L. (2021). HIF-1 recruits NANOG as a coactivator for TERT gene transcription in hypoxic breast cancer stem cells. *Cell Reports*, *36*(13).
51. Bernardi, R., & Gianni, L. (2014). Hallmarks of triple negative breast cancer emerging at last?. *Cell research*, *24*(8), 904-905.
52. Zhao, Y., Xing, C., Deng, Y., Ye, C., & Peng, H. (2024). HIF-1α signaling: Essential roles in tumorigenesis and implications in targeted therapies. *Genes & Diseases*, *11*(1), 234-251.
53. Copple, B. L. (2010). Hypoxia stimulates hepatocyte epithelial to mesenchymal transition by hypoxia-inducible factor and transforming growth factor-β-dependent mechanisms. *Liver International*, *30*(5), 669-682.
54. Zhang, H., Akman, H. O., Smith, E. L., Zhao, J., Murphy-Ullrich, J. E., & Batuman, O. A. (2003). Cellular response to hypoxia involves signaling via Smad proteins. *Blood, The Journal of the American Society of Hematology*, *101*(6), 2253-2260.
55. McMahon, S., Charbonneau, M., Grandmont, S., Richard, D. E., & Dubois, C. M. (2006). Transforming growth factor β1 induces hypoxia-inducible factor-1 stabilization through selective inhibition of PHD2 expression. *Journal of Biological Chemistry*, *281*(34), 24171-24181.
56. Zhang, Y. E. (2009). Non-Smad pathways in TGF-β signaling. *Cell research*, *19*(1), 128-139.
57. Peng, J., Wang, X., Ran, L., Song, J., Luo, R., & Wang, Y. (2018). Hypoxia-inducible factor 1α regulates the transforming growth factor β1/SMAD family member 3 pathway to promote breast cancer progression. *Journal of breast cancer*, *21*(3), 259-266.

58. Zhang, Q., Bai, X., Chen, W., Ma, T., Hu, Q., Liang, C., ... & Liang, T. (2013). Wnt/β-catenin signaling enhances hypoxia-induced epithelial–mesenchymal transition in hepatocellular carcinoma via crosstalk with hif-1α signaling. *Carcinogenesis*, *34*(5), 962-973.
59. Li, Y., Patel, S. P., Roszik, J., & Qin, Y. (2018). Hypoxia-driven immunosuppressive metabolites in the tumor microenvironment: new approaches for combinational immunotherapy. *Frontiers in immunology*, *9*, 1591.
60. Terry, S., Savagner, P., Ortiz-Cuaran, S., Mahjoubi, L., Saintigny, P., Thiery, J. P., & Chouaib, S. (2017). New insights into the role of EMT in tumor immune escape. *Molecular oncology*, *11*(7), 824-846.
61. Ricciardi, M., Zanotto, M., Malpeli, G., Bassi, G., Perbellini, O., Chilosi, M., ... & Krampera, M. (2015). Epithelial-to-mesenchymal transition (EMT) induced by inflammatory priming elicits mesenchymal stromal cell-like immune-modulatory properties in cancer cells. *British journal of cancer*, *112*(6), 1067-1075.
62. Yang, M. H., Wu, M. Z., Chiou, S. H., Chen, P. M., Chang, S. Y., Liu, C. J., ... & Wu, K. J. (2008). Direct regulation of TWIST by HIF-1α promotes metastasis. *Nature cell biology*, *10*(3), 295-305.
63. Liu, K. H., Tsai, Y. T., Chin, S. Y., Lee, W. R., Chen, Y. C., & Shen, S. C. (2018). Hypoxia stimulates the epithelial–to–mesenchymal transition in lung cancer cells through accumulation of nuclear β-catenin. *Anticancer Research*, *38*(11), 6299-6308.
64. Kim, I., & He, Y. Y. (2013). Targeting the AMP-activated protein kinase for cancer prevention and therapy. *Frontiers in oncology*, *3*, 175.
65. Luo, Z., Zang, M., & Guo, W. (2010). AMPK as a metabolic tumor suppressor: control of metabolism and cell growth. *Future oncology*, *6*(3), 457-470.
66. Saxena, M., Balaji, S. A., Deshpande, N., Ranganathan, S., Pillai, D. M., Hindupur, S. K., & Rangarajan, A. (2018). AMP-activated protein kinase promotes epithelial-mesenchymal transition in cancer cells through Twist1 upregulation. *Journal of cell science*, *131*(14), jcs208314.
67. Chou, C. C., Lee, K. H., Lai, I. L., Wang, D., Mo, X., Kulp, S. K., ... & Chen, C. S. (2014). AMPK reverses the mesenchymal phenotype of cancer cells by targeting the Akt–MDM2–Foxo3a signaling axis. *Cancer research*, *74*(17), 4783-4795.
68. Yu, J. S., & Cui, W. (2016). Proliferation, survival and metabolism: the role of PI3K/AKT/mTOR signalling in pluripotency and cell fate determination. *Development*, *143*(17), 3050-3060.
69. Tam, S. Y., Wu, V. W. C., & Law, H. K. W. (2017). Influence of autophagy on the efficacy of radiotherapy. *Radiation Oncology*, *12*, 1-10.
70. Zhang, J., Guo, H., Zhu, J. S., Yang, Y. C., Chen, W. X., & Chen, N. W. (2014). Inhibition of phosphoinositide 3-kinase/Akt pathway decreases hypoxia inducible factor-1α expression and

increases therapeutic efficacy of paclitaxel in human hypoxic gastric cancer cells. *Oncology Letters*, *7*(5), 1401-1408.

71. Xie, L., Law, B. K., Chytil, A. M., Brown, K. A., Aakre, M. E., & Moses, H. L. (2004). Activation of the Erk pathway is required for TGF-β1-induced EMT in vitro. *Neoplasia*, *6*(5), 603-6
72. Shin, S., Buel, G. R., Nagiec, M. J., Han, M. J., Roux, P. P., Blenis, J., & Yoon, S. O. (2019). ERK2 regulates epithelial-to-mesenchymal plasticity through DOCK10-dependent Rac1/FoxO1 activation. *Proceedings of the National Academy of Sciences*, *116*(8), 2967-2976.
73. Kim, K., Park, E. Y., Yoon, M. S., Suh, D. S., Kim, K. H., Lee, J. H., ... & Choi, K. U. (2014). The role of TWIST in ovarian epithelial cancers. *Korean Journal of Pathology*, *48*(4), 283.
74. Zhang, L., Huang, G., Li, X., Zhang, Y., Jiang, Y., Shen, J., ... & Qian, C. (2013). Hypoxia induces epithelial-mesenchymal transition via activation of SNAI1 by hypoxia-inducible factor-1α in hepatocellular carcinoma. *BMC cancer*, *13*, 1-9.
75. Evans, A. J., Russell, R. C., Roche, O., Burry, T. N., Fish, J. E., Chow, V. W., ... & Ohh, M. (2007). VHL promotes E2 box-dependent E-cadherin transcription by HIF-mediated regulation of SIP1 and snail. *Molecular and cellular biology*, *27*(1), 157-169.
76. Zhang, J., Cheng, Q., Zhou, Y., Wang, Y., & Chen, X. (2013). Slug is a key mediator of hypoxia induced cadherin switch in HNSCC: correlations with poor prognosis. *Oral oncology*, *49*(11), 1043-1050.
77. Iwasaki, K., Ninomiya, R., Shin, T., Nomura, T., Kajiwara, T., Hijiya, N., ... & Hamada, F. (2018). Chronic hypoxia-induced slug promotes invasive behavior of prostate cancer cells by activating expression of ephrin-B1. *Cancer Science*, *109*(10), 3159-3170.
78. Salnikov, A. V., Liu, L., Platen, M., Gladkich, J., Salnikova, O., Ryschich, E., ... & Herr, I. (2012). Hypoxia induces EMT in low and highly aggressive pancreatic tumor cells but only cells with cancer stem cell characteristics acquire pronounced migratory potential.
79. Zhang, W., Shi, X., Peng, Y., Wu, M., Zhang, P., Xie, R., ... & Wang, J. (2015). HIF-1α promotes epithelial-mesenchymal transition and metastasis through direct regulation of ZEB1 in colorectal cancer. *PloS one*, *10*(6), e0129603.
80. Zhu, J., Huang, Z., Zhang, M., Wang, W., Liang, H., Zeng, J., ... & Fan, J. (2018). HIF-1α promotes ZEB1 expression and EMT in a human bladder cancer lung metastasis animal model. *Oncology letters*, *15*(3), 3482-3489.
81. Joseph, J. V., Conroy, S., Pavlov, K., Sontakke, P., Tomar, T., Eggens-Meijer, E., ... & Kruyt, F. A. (2015). Hypoxia enhances migration and invasion in glioblastoma by promoting a mesenchymal shift mediated by the HIF1α–ZEB1 axis. *Cancer letters*, *359*(1), 107-116.
82. Deng, S. J., Chen, H. Y., Ye, Z., Deng, S. C., Zhu, S., Zeng, Z., ... & Zhao, G. (2018). Hypoxia-induced LncRNA-BX111 promotes metastasis and progression of pancreatic cancer through regulating ZEB1 transcription. *Oncogene*, *37*(44), 5811-5828.

83. Folkman, J. (1971). Tumor angiogenesis: therapeutic implications. *N Engl j Med*, *285*(21), 1182-1186.
84. Zhong, H., Chiles, K., Feldser, D., Laughner, E., Hanrahan, C., Georgescu, M. M., ... & Semenza, G. L. (2000). Modulation of hypoxia-inducible factor 1α expression by the epidermal growth factor/phosphatidylinositol 3-kinase/PTEN/AKT/FRAP pathway in human prostate cancer cells: implications for tumor angiogenesis and therapeutics. *Cancer research*, *60*(6), 1541-1545.
85. Ravi, R., Mookerjee, B., Bhujwalla, Z. M., Sutter, C. H., Artemov, D., Zeng, Q., ... & Bedi, A. (2000). Regulation of tumor angiogenesis by p53-induced degradation of hypoxia-inducible factor 1α. *Genes & development*, *14*(1), 34-44.
86. Richard, D. E., Berra, E., & Pouysségur, J. (2000). Nonhypoxic pathway mediates the induction of hypoxia-inducible factor 1α in vascular smooth muscle cells. *Journal of Biological Chemistry*, *275*(35), 26765-26771.
87. Xu, T., Hu, X., Yang, G., Liu, Y., Zhang, Q., Yu, S., ... & Zhao, B. (2022). HIF-1alpha/VEGF pathway mediates 1, 3, 6, 8-tetrabromo-9 H-carbazole-induced angiogenesis: a potential vascular toxicity of an emerging contaminant. *Journal of Hazardous Materials*, *432*, 128718.
88. Wu, C., Long, L., Zhang, Y., Xu, Y., Lu, Y., Yang, Z., ... & Wang, Y. (2022). Injectable conductive and angiogenic hydrogels for chronic diabetic wound treatment. *Journal of Controlled Release*, *344*, 249-260.
89. Hlatky, L., Tsionou, C., Hahnfeldt, P., & Coleman, C. N. (1994). Mammary fibroblasts may influence breast tumor angiogenesis via hypoxia-induced vascular endothelial growth factor up-regulation and protein expression. *Cancer research*, *54*(23), 6083-6086.
90. Seo, S. H., Hwang, S. Y., Hwang, S., Han, S., Park, H., Lee, Y. S., ... & Kwon, Y. (2022). Hypoxia-induced ELF3 promotes tumor angiogenesis through IGF1/IGF1R. *EMBO reports*, *23*(8), e52977.
91. Vaupel, P., Kallinowski, F., & Okunieff, P. (1989). Blood flow, oxygen and nutrient supply, and metabolic microenvironment of human tumors: a review. *Cancer research*, *49*(23), 6449-6465.
92. Amato, R., Pisani, F., Laudadio, E., Cammalleri, M., Lucchesi, M., Marracci, S., ... & Bagnoli, P. (2022). HIF-1-dependent induction of β3 adrenoceptor: evidence from the mouse retina. *Cells*, *11*(8), 1271.
93. Krzywinska, E., Kantari-Mimoun, C., Kerdiles, Y., Sobecki, M., Isagawa, T., Gotthardt, D., ... & Stockmann, C. (2017). Loss of HIF-1α in natural killer cells inhibits tumour growth by stimulating non-productive angiogenesis. *Nature communications*, *8*(1), 1597.
94. Carmeliet, P., & Jain, R. K. (2011). Principles and mechanisms of vessel normalization for cancer and other angiogenic diseases. *Nature reviews Drug discovery*, *10*(6), 417-427.

95. Gao, F., Okunieff, P., Han, Z., Ding, I., Wang, L., Liu, W., ... & Zhang, L. (2005). Hypoxia-induced alterations in hyaluronan and hyaluronidase. In *Oxygen Transport to Tissue XXVI* (pp. 249-256). Boston, MA: Springer US.
96. Liao, D., & Johnson, R. S. (2007). Hypoxia: a key regulator of angiogenesis in cancer. *Cancer and Metastasis Reviews*, *26*, 281-290.
97. Liu, L., Tong, Q., Liu, S., Cui, J., Zhang, Q., Sun, W., & Yang, S. (2016). ZEB1 upregulates VEGF expression and stimulates angiogenesis in breast cancer. *PLoS One*, *11*(2), e0148774.
98. Perillo, B., Di Donato, M., Pezone, A., Di Zazzo, E., Giovannelli, P., Galasso, G., ... & Migliaccio, A. (2020). ROS in cancer therapy: the bright side of the moon. *Experimental & molecular medicine*, *52*(2), 192-203.
99. Ueda, S., Saeki, T., Osaki, A., Yamane, T., & Kuji, I. (2017). Bevacizumab induces acute hypoxia and cancer progression in patients with refractory breast cancer: multimodal functional imaging and multiplex cytokine analysis. *Clinical Cancer Research*, *23*(19), 5769-5778.
100. Unruh, A., Ressel, A., Mohamed, H. G., Johnson, R. S., Nadrowitz, R., Richter, E., ... & Wenger, R. H. (2003). The hypoxia-inducible factor-1α is a negative factor for tumor therapy. *Oncogene*, *22*(21), 3213-3220.
101. Mayer, A., Höckel, M., Wree, A., Leo, C., Horn, L. C., & Vaupel, P. (2008). Lack of hypoxic response in uterine leiomyomas despite severe tissue hypoxia. *Cancer research*, *68*(12), 4719-4726.
102. Sun, H. C., Qiu, Z. J., Liu, J., Sun, J., Jiang, T., Huang, K. J., ... & Huang, C. (2007). Expression of hypoxia-inducible factor-1 alpha and associated proteins in pancreatic ductal adenocarcinoma and their impact on prognosis. *International journal of oncology*, *30*(6), 1359-1367.
103. Dean, M., & Annilo, T. (2005). Evolution of the ATP-binding cassette (ABC) transporter superfamily in vertebrates. *Annu. Rev. Genomics Hum. Genet.*, *6*(1), 123-142.
104. Chen, J., Ding, Z., Peng, Y., Pan, F., Li, J., Zou, L., ... & Liang, H. (2014). HIF-1α inhibition reverses multidrug resistance in colon cancer cells via downregulation of MDR1/P-glycoprotein. *PloS one*, *9*(6), e98882.
105. Zub, K. A., Sousa, M. M. L. D., Sarno, A., Sharma, A., Demirovic, A., Rao, S., ... & Slupphaug, G. (2015). Modulation of cell metabolic pathways and oxidative stress signaling contribute to acquired melphalan resistance in multiple myeloma cells. *PloS one*, *10*(3), e0119857.
106. Triner, D., & Shah, Y. M. (2016). Hypoxia-inducible factors: a central link between inflammation and cancer. *The Journal of clinical investigation*, *126*(10), 3689-3698.
107. Shu, X., Shiying, Y., & Xianglin, Y. (2005). Effects of hypoxia on expression of P-gp and mutltidrug resistance protein in human lung adenocarcinoma A549 cell line. *Journal of Huazhong University of Science and Technology [Medical Sciences]*, *25*, 279-281.

108. He, J., Pei, L., Jiang, H., Yang, W., Chen, J., & Liang, H. (2017). Chemoresistance of colorectal cancer to 5-fluorouracil is associated with silencing of the BNIP3 gene through aberrant methylation. *Journal of Cancer*, *8*(7), 1187.

109. Zunino, F., Perego, P., Pilotti, S., Pratesi, G., Supino, R., & Arcamone, F. (1997). Role of apoptotic response in cellular resistance to cytotoxic agents. *Pharmacology & therapeutics*, *76*(1-3), 177-185.

110. Silva, V. L. (2017). Exploiting the cancer niche: tumor-associated macrophages and hypoxia as promising synergistic targets for nano-based therapy. *Journal of Controlled Release*, *253*, 82-96.

111. Gillet, J. P., Efferth, T., & Remacle, J. (2007). Chemotherapy-induced resistance by ATP-binding cassette transporter genes. *Biochimica et Biophysica Acta (BBA)-Reviews on Cancer*, *1775*(2), 237-262.

112. Halliwell, B. (1996). Antioxidants in human health and disease. *Annual review of nutrition*, *16*(1), 33-50.

113. Sagi, M., & Fluhr, R. (2006). Production of reactive oxygen species by plant NADPH oxidases. *Plant physiology*, *141*(2), 336-340.

114. Madamanchi, N. R., & Runge, M. S. (2007). Mitochondrial dysfunction in atherosclerosis. *Circulation research*, *100*(4), 460-473.

115. St. Clair, D. K., Steven Wan, X., Oberley, T. D., Muse, K. E., & St. Clair, W. H. (1992). Suppression of radiation-induced neoplastic transformation by overexpression of mitochondrial superoxide dismutase. *Molecular carcinogenesis*, *6*(4), 238-242.

116. Safford, S. E., Oberley, T. D., Urano, M., & Clair, D. S. (1994). Suppression of fibrosarcoma metastasis by elevated expression of manganese superoxide dismutase. *Cancer research*, *54*(16), 4261-4265.

117. Latimer, H. R., & Veal, E. A. (2016). Peroxiredoxins in regulation of MAPK signalling pathways; sensors and barriers to signal transduction. *Molecules and cells*, *39*(1), 40-45.

118. Han, X., Sun, S., Zhao, M., Cheng, X., Chen, G., Lin, S., ... & Yu, X. (2014). Celastrol stimulates hypoxia-inducible factor-1 activity in tumor cells by initiating the ROS/Akt/p70S6K signaling pathway and enhancing hypoxia-inducible factor-1α protein synthesis. *PloS one*, *9*(11), e112470.

119. Kwon, J., Lee, S. R., Yang, K. S., Ahn, Y., Kim, Y. J., Stadtman, E. R., & Rhee, S. G. (2004). Reversible oxidation and inactivation of the tumor suppressor PTEN in cells stimulated with peptide growth factors. *Proceedings of the National Academy of Sciences*, *101*(47), 16419-16424.

120. Gopalakrishna, R., & Jaken, S. (2000). Protein kinase C signaling and oxidative stress. *Free Radical Biology and Medicine*, *28*(9), 1349-1361.

121. Infantino, V., Santarsiero, A., Convertini, P., Todisco, S., & Iacobazzi, V. (2021). Cancer cell metabolism in hypoxia: role of HIF-1 as key regulator and therapeutic target. *International journal of molecular sciences*, *22*(11), 5703.

122. Manuelli, V., Pecorari, C., Filomeni, G., & Zito, E. (2022). Regulation of redox signaling in HIF-1-dependent tumor angiogenesis. *The FEBS journal*, *289*(18), 5413-5425.

123. Morgan, M. J., & Liu, Z. G. (2011). Crosstalk of reactive oxygen species and NF-κB signaling. *Cell research*, *21*(1), 103-115.

124. Lingappan, K. (2018). NF-κB in oxidative stress. *Current opinion in toxicology*, *7*, 81-86.

125. Liu, B., Chen, Y., & Clair, D. K. S. (2008). ROS and p53: a versatile partnership. *Free Radical Biology and Medicine*, *44*(8), 1529-1535.

126. Cordani, M., Butera, G., Pacchiana, R., Masetto, F., Mullappilly, N., Riganti, C., & Donadelli, M. (2020). Mutant p53-associated molecular mechanisms of ROS regulation in cancer cells. *Biomolecules*, *10*(3), 361.

127. Ju, H. Q., Lin, J. F., Tian, T., Xie, D., & Xu, R. H. (2020). NADPH homeostasis in cancer: functions, mechanisms and therapeutic implications. *Signal transduction and targeted therapy*, *5*(1), 231.

128. Harris, I. S., & DeNicola, G. M. (2020). The complex interplay between antioxidants and ROS in cancer. *Trends in cell biology*, *30*(6), 440-451.

129. Wang, Y., Qi, H., Liu, Y., Duan, C., Liu, X., Xia, T., ... & Liu, H. X. (2021). The double-edged roles of ROS in cancer prevention and therapy. *Theranostics*, *11*(10), 4839.

130. Aggarwal, V., Tuli, H. S., Varol, A., Thakral, F., Yerer, M. B., Sak, K., ... & Sethi, G. (2019). Role of reactive oxygen species in cancer progression: molecular mechanisms and recent advancements. *Biomolecules*, *9*(11), 735.

131. Ghosh, S., Javia, A., Shetty, S., Bardoliwala, D., Maiti, K., Banerjee, S., ... & Bhowmick, S. (2021). Triple negative breast cancer and non-small cell lung cancer: Clinical challenges and nano-formulation approaches. *Journal of Controlled Release*, *337*, 27-58.

132. Pestana, R. C., & Ibrahim, N. K. (2021). Cancer treatment modalities systemic and locoregional approaches: Challenges and opportunities of multidisciplinary approaches. *Locoregional Radionuclide Cancer Therapy: Clinical and Scientific Aspects*, 17-37.

133. Pan, X. B., Qu, S., Jiang, Y. M., & Zhu, X. D. (2015). Triple negative breast cancer versus non-triple negative breast cancer treated with breast conservation surgery followed by radiotherapy: a systematic review and meta-analysis. *Breast Care*, *10*(6), 413-416.

134. Panoff, J. E., Hurley, J., Takita, C., Reis, I. M., Zhao, W., Sujoy, V., ... & Wright, J. L. (2011). Risk of locoregional recurrence by receptor status in breast cancer patients receiving

modern systemic therapy and post-mastectomy radiation. *Breast cancer research and treatment*, *128*, 899-906.

135. Wong, S. T., & Goodin, S. (2009). Overcoming drug resistance in patients with metastatic breast cancer. *Pharmacotherapy: The Journal of Human Pharmacology and Drug Therapy*, *29*(8), 954-965.

136. Rouzier, R., Perou, C. M., Symmans, W. F., Ibrahim, N., Cristofanilli, M., Anderson, K., ... & Pusztai, L. (2005). Breast cancer molecular subtypes respond differently to preoperative chemotherapy. *Clinical cancer research*, *11*(16), 567.

137. Ntellas, P., Spathas, N., Agelaki, S., Zintzaras, E., & Saloustros, E. (2019). Taxane & cyclophosphamide vs anthracycline & taxane-based chemotherapy as adjuvant treatment for breast cancer: a pooled analysis of randomized controlled trials by the Hellenic Academy of Oncology. *Oncotarget*, *10*(11), 1209.

138. Vetter, M., Fokas, S., Biskup, E., Schmid, T., Schwab, F., Schoetzau, A., ... & Zanetti-Dällenbach, R. (2017). Efficacy of adjuvant chemotherapy with carboplatin for early triple negative breast cancer: a single center experience. *Oncotarget*, *8*(43), 75617.

139. Lee, J. S., Yost, S. E., & Yuan, Y. (2020). Neoadjuvant treatment for triple negative breast cancer: recent progresses and challenges. *Cancers*, *12*(6), 1404.

140. García-Fernández, C., Fornaguera, C., & Borrós, S. (2020). Nanomedicine in non-small cell lung cancer: from conventional treatments to immunotherapy. *Cancers*, *12*(6), 1609.

141. Corraliza-Gorjón, I., Somovilla-Crespo, B., Santamaria, S., Garcia-Sanz, J. A., & Kremer, L. (2017). New strategies using antibody combinations to increase cancer treatment effectiveness. *Frontiers in immunology*, *8*, 1804.

142. Medina, M. A., Oza, G., Sharma, A., Arriaga, L. G., Hernandez Hernandez, J. M., Rotello, V. M., & Ramirez, J. T. (2020). Triple-negative breast cancer: a review of conventional and advanced therapeutic strategies. *International journal of environmental research and public health*, *17*(6), 2078.

143. Costa, R. L., & Gradishar, W. J. (2017). Triple-negative breast cancer: current practice and future directions. *Journal of oncology practice*, *13*(5), 301-303.

144. Hu, J., Miao, H., Li, R., & Wen, Z. (2020). Surgery and subsequent risk of non-small cell lung cancer recurrence: a meta-analysis of observational studies. *Translational Cancer Research*, *9*(3), 1960.

145. Ding, H., Yu, X., Hang, C., Gao, K., Lao, X., Jia, Y., & Yan, Z. (2020). Ailanthone: A novel potential drug for treating human cancer. *Oncology Letters*, *20*(2), 1489-1503.

146. Ali, I., Lone, M. N., & Aboul-Enein, H. Y. (2017). Imidazoles as potential anticancer agents. *MedChemComm*, *8*(9), 1742-1773.

147. Baraldi, P. G., Bovero, A., Fruttarolo, F., Preti, D., Tabrizi, M. A., Pavani, M. G., & Romagnoli, R. (2004). DNA minor groove binders as potential antitumor and antimicrobial agents. *Medicinal research reviews*, *24*(4), 475-528.

148. Lang, D. K., Kaur, R., Arora, R., Saini, B., & Arora, S. (2020). Nitrogen-containing heterocycles as anticancer agents: An overview. *Anti-Cancer Agents in Medicinal Chemistry (Formerly Current Medicinal Chemistry-Anti-Cancer Agents)*, *20*(18), 2150-2168.

149. Vitaku, E., Smith, D. T., & Njardarson, J. T. (2014). Analysis of the structural diversity, substitution patterns, and frequency of nitrogen heterocycles among US FDA approved pharmaceuticals: miniperspective. *Journal of medicinal chemistry*, *57*(24), 10257-10274.

150. Bagdi, A. K., Santra, S., Monir, K., & Hajra, A. (2015). Synthesis of imidazo [1, 2-a] pyridines: a decade update. *Chemical Communications*, *51*(9), 1555-1575.

151. Al-Tel, T. H., & Al-Qawasmeh, R. A. (2010). Post Groebke–Blackburn multicomponent protocol: synthesis of new polyfunctional imidazo [1, 2-a] pyridine and imidazo [1, 2-a] pyrimidine derivatives as potential antimicrobial agents. *European journal of medicinal chemistry*, *45*(12), 5848-5855.

152. Reddy Gangireddy, M., Mantipally, M., Gundla, R., Nayak Badavath, V., Paidikondala, K., & Yamala, A. (2019). Design and synthesis of piperazine-linked imidazo [1, 2-a] pyridine derivatives as potent anticancer agents. *ChemistrySelect*, *4*(46), 13622-13629.

153. Peytam, F., Emamgholipour, Z., Mousavi, A., Moradi, M., Foroumadi, R., Firoozpour, L., ... & Foroumadi, A. (2023). Imidazopyridine-based kinase inhibitors as potential anticancer agents: A review. *Bioorganic Chemistry*, 106831.

154. Enguehard-Gueiffier, C., & Gueiffier, A. (2007). Recent Progress in the Pharmacology of Imidazo [1, 2-a] pyridines. *Mini Reviews in Medicinal Chemistry*, *7*(9), 888-899.

155. Deep, A., Kaur Bhatia, R., Kaur, R., Kumar, S., Kumar Jain, U., Singh, H., ... & Kishore Deb, P. (2017). Imidazo [1, 2-a] pyridine scaffold as prospective therapeutic agents. *Current topics in medicinal chemistry*, *17*(2), 238-250.

156. Mohana Roopan, S., Patil, S. M., & Palaniraja, J. (2016). Recent synthetic scenario on imidazo [1, 2-a] pyridines chemical intermediate. *Research on Chemical Intermediates*, *42*, 2749-2790.

157. Karrouchi, K., Radi, S., Ramli, Y., Taoufik, J., Mabkhot, Y. N., Al-Aizari, F. A., & Ansar, M. H. (2018). Synthesis and pharmacological activities of pyrazole derivatives: A review. *Molecules*, *23*(1), 134.

158. Peng, X. M., LV Damu, G., & Zhou, H. (2013). Current developments of coumarin compounds in medicinal chemistry. *Current pharmaceutical design*, *19*(21), 3884-3930.

159. Fesatidou, M., Petrou, A., & Athina, G. (2020). Heterocycle compounds with antimicrobial activity. *Current pharmaceutical design*, *26*(8), 867-904.

160. James, N., Owusu, E., Rivera, G., & Bandyopadhyay, D. (2024). Small Molecule Therapeutics in the Pipeline Targeting for Triple-Negative Breast Cancer: Origin, Challenges, Opportunities, and Mechanisms of Action. *International Journal of Molecular Sciences*, *25*(11), 6285.

161. Liu, H., Murphy, C. J., Karreth, F. A., Emdal, K. B., White, F. M., Elemento, O., ... & Cantley, L. C. (2018). Identifying and targeting sporadic oncogenic genetic aberrations in mouse models of triple-negative breast cancer. *Cancer discovery*, *8*(3), 354-369.

162. Yuan, Y., Yost, S. E., Cui, Y., Ruel, C., Murga, M., Tang, A., ... & Frankel, P. H. (2023). Phase I trial of ipatasertib plus carboplatin, carboplatin/paclitaxel, or capecitabine and atezolizumab in metastatic triple-negative breast cancer. *The Oncologist*, *28*(7), e498-e507.

163. Schmid, P., Abraham, J., Chan, S., Wheatley, D., Brunt, A. M., Nemsadze, G., ... & Turner, N. C. (2020). Capivasertib plus paclitaxel versus placebo plus paclitaxel as first-line therapy for metastatic triple-negative breast cancer: the PAKT trial. *Journal of Clinical Oncology*, *38*(5), 423-433.

164. Liao, M., Zhang, J., Wang, G., Wang, L., Liu, J., Ouyang, L., & Liu, B. (2021). Small-molecule drug discovery in triple negative breast cancer: current situation and future directions. *Journal of medicinal chemistry*, *64*(5), 2382-2418.

165. Somlo, G., Frankel, P. H., Arun, B. K., Ma, C. X., Garcia, A. A., Cigler, T., ... & Weitzel, J. N. (2017). Efficacy of the PARP inhibitor veliparib with carboplatin or as a single agent in patients with germline BRCA1-or BRCA2-associated metastatic breast cancer: California Cancer Consortium Trial NCT01149083. *Clinical Cancer Research*, *23*(15), 4066-4076.

166. Litton, J., Rugo, H. S., Ettl, J., Hurvitz, S., Gonçalves, A., Lee, K. H., ... & Blum, J. L. (2018). Abstract GS6-07: EMBRACA: A phase 3 trial comparing talazoparib, an oral PARP inhibitor, to physician's choice of therapy in patients with advanced breast cancer and a germline BRCA mutation. *Cancer research*, *78*(4_Supplement), GS6-07.

167. Pan, L., Chen, X., Rassool, F. V., Li, C., & Lin, J. (2022). LLL12B, a novel small-molecule STAT3 inhibitor, induces apoptosis and suppresses cell migration and tumor growth in triple-negative breast cancer cells. *Biomedicines*, *10*(8), 2003.

168. Lee, J., Lim, B., Pearson, T., Choi, K., Fuson, J. A., Bartholomeusz, C., ... & Ueno, N. T. (2019). Anti-tumor and anti-metastasis efficacy of E6201, a MEK1 inhibitor, in preclinical models of triple-negative breast cancer. *Breast cancer research and treatment*, *175*, 339-351.

169. Miles, D., Kim, S. B., McNally, V. A., Simmons, B. P., Wongchenko, M., Hsu, J. J., & Brufsky, A. M. (2016). COLET (NCT02322814): A multistage, phase 2 study evaluating the safety and efficacy of cobimetinib (C) in combination with paclitaxel (P) as first-line treatment for patients (pts) with metastatic triple-negative breast cancer (TNBC).

170. An, H., Kim, J. Y., Oh, E., Lee, N., Cho, Y., & Seo, J. H. (2015). Salinomycin promotes anoikis and decreases the CD44+/CD24-stem-like population via inhibition of STAT3 activation in MDA-MB-231 cells. *PloS one*, *10*(11), e0141919.

171. Liu, B., Fu, L., Zhang, C., Zhang, L., Zhang, Y., Ouyang, L., ... & Huang, J. (2015). Computational design, chemical synthesis, and biological evaluation of a novel ERK inhibitor (BL-EI001) with apoptosis-inducing mechanisms in breast cancer. *Oncotarget*, *6*(9), 6762.

172. Elbaz, M., Nasser, M. W., Ravi, J., Wani, N. A., Ahirwar, D. K., Zhao, H., ... & Ganju, R. K. (2015). Modulation of the tumor microenvironment and inhibition of EGF/EGFR pathway: Novel anti-tumor mechanisms of Cannabidiol in breast cancer. *Molecular oncology*, *9*(4), 906-919.

173. Liu, C. Y., Chu, P. Y., Huang, C. T., Chen, J. L., Yang, H. P., Wang, W. L., ... & Tseng, L. M. (2019). Varlitinib downregulates HER/ERK signaling and induces apoptosis in triple negative breast cancer cells. *Cancers*, *11*(1), 105.

174. Zhao, G., Shi, A., Fan, Z., & Du, Y. (2015). Salidroside inhibits the growth of human breast cancer in vitro and in vivo. *Oncology Reports*, *33*(5), 2553-2560.

175. Sun, A. Q., & Ju, X. L. (2020). Inhibitory effects of salidroside on MCF-7 breast cancer cells in vivo. *Journal of International Medical Research*, *48*(11), 0300060520968353.

176. Qian, X. L., Zhang, J., Li, P. Z., Lang, R. G., Li, W. D., Sun, H., ... & Fu, L. (2017). Dasatinib inhibits c-src phosphorylation and prevents the proliferation of Triple-Negative Breast Cancer (TNBC) cells which overexpress Syndecan-Binding Protein (SDCBP). *PLoS One*, *12*(1), e0171169.

177. Gasch, C., Ffrench, B., O'Leary, J. J., & Gallagher, M. F. (2017). Catching moving targets: cancer stem cell hierarchies, therapy-resistance & considerations for clinical intervention. *Molecular cancer*, *16*, 1-15.

178. Turke, A. B., Zejnullahu, K., Wu, Y. L., Song, Y., Dias-Santagata, D., Lifshits, E., ... & Jänne, P. A. (2010). Preexistence and clonal selection of MET amplification in EGFR mutant NSCLC. *Cancer cell*, *17*(1), 77-88.

179. Alheshibri, M., Qian, J., Jehannin, M., & Craig, V. S. (2016). A history of nanobubbles. *Langmuir*, *32*(43), 11086-11100. [160-168]

180. Azevedo, A., Oliveira, H., & Rubio, J. (2019). Bulk nanobubbles in the mineral and environmental areas: Updating research and applications. *Advances in Colloid and Interface Science*, *271*, 101992.

181. Zhou, L., Wang, S., Zhang, L., & Hu, J. (2021). Generation and stability of bulk nanobubbles: A review and perspective. *Current Opinion in Colloid & Interface Science*, *53*, 101439.

182. Glaser, D. A. (1952). Some effects of ionizing radiation on the formation of bubbles in liquids. *Physical Review*, *87*(4), 665.

183. Fox, F. E., & Herzfeld, K. F. (1954). Gas bubbles with organic skin as cavitation nuclei. *The Journal of the Acoustical Society of America*, *26*(6), 984-989.

184. Yount, D. E., Gillary, E. W., & Hoffman, D. C. (1984). A microscopic investigation of bubble formation nuclei. *The Journal of the Acoustical Society of America*, *76*(5), 1511-1521.

185. Parker, J. L., Claesson, P. M., & Attard, P. (1994). Bubbles, cavities, and the long-ranged attraction between hydrophobic surfaces. *The Journal of Physical Chemistry*, *98*(34), 8468-8480.

186. Sun, Y., Xie, G., Peng, Y., Xia, W., & Sha, J. (2016). Stability theories of nanobubbles at solid–liquid interface: A review. *Colloids and Surfaces A: Physicochemical and Engineering Aspects*, *495*, 176-186.

187. Afshari, R., Akhavan, O., Hamblin, M. R., & Varma, R. S. (2021). Review of oxygenation with nanobubbles: possible treatment for hypoxic COVID-19 patients. *ACS Applied Nano Materials*, *4*(11), 11386-11412.

188. International Organization for Standardization (ISO). (2017). Fine bubble technology—General principles for usage and measurement of fine bubbles—Part 1: Terminology.

189. Cavalli, R., Bisazza, A., & Lembo, D. (2013). Micro-and nanobubbles: a versatile non-viral platform for gene delivery. *International journal of pharmaceutics*, *456*(2), 437-445.

190. Hernot, S., & Klibanov, A. L. (2008). Microbubbles in ultrasound-triggered drug and gene delivery. *Advanced drug delivery reviews*, *60*(10), 1153-1166.

191. Kheir, J. N., Polizzotti, B. D., Thomson, L. M., O'Connell, D. W., Black, K. J., Lee, R. W., ... & McGowan, F. X. (2013). Bulk manufacture of concentrated oxygen gas-filled microparticles for intravenous oxygen delivery. *Advanced Healthcare Materials*, *2*(8), 1131-1141.

192. Lee, Mina, Eun Yeol Lee, Daeyeon Lee, and Bum Jun Park. "Stabilization and fabrication of microbubbles: applications for medical purposes and functional materials." *Soft matter* 11, no. 11 (2015): 2067-2079.

193. Unger, E. C., Porter, T., Culp, W., Labell, R., Matsunaga, T., & Zutshi, R. (2004). Therapeutic applications of lipid-coated microbubbles. *Advanced drug delivery reviews*, *56*(9), 1291-1314.

194. Li, F., Mei, H., Gao, Y., Xie, X., Nie, H., Li, T., ... & Jia, L. (2017). Co-delivery of oxygen and erlotinib by aptamer-modified liposomal complexes to reverse hypoxia-induced drug resistance in lung cancer. *Biomaterials*, *145*, 56-71.

195. Swanson, E. J., Mohan, V., Kheir, J., & Borden, M. A. (2010). Phospholipid-stabilized microbubble foam for injectable oxygen delivery. *Langmuir*, *26*(20), 15726-15729.

196. Unger, E. C., Matsunaga, T. O., McCreery, T., Schumann, P., Sweitzer, R., & Quigley, R. (2002). Therapeutic applications of microbubbles. *European journal of Radiology*, *42*(2), 160-168.

197. Sirsi, S. R., & Borden, M. A. (2009). Microbubble compositions, properties and biomedical applications. *Bubble Science, Engineering & Technology*, *1*(1-2), 3-17.

198. Mayer, C. R., Geis, N. A., Katus, H. A., & Bekeredjian, R. (2008). Ultrasound targeted microbubble destruction for drug and gene delivery. *Expert opinion on drug delivery*, *5*(10), 1121-1138.

199. Cavalli, R., Bisazza, A., Giustetto, P., Civra, A., Lembo, D., Trotta, G., ... & Trotta, M. (2009). Preparation and characterization of dextran nanobubbles for oxygen delivery. *International Journal of Pharmaceutics*, *381*(2), 160-165.

200. Riess, J. G. (2005). Understanding the fundamentals of perfluorocarbons and perfluorocarbon emulsions relevant to in vivo oxygen delivery. *Artificial cells, blood substitutes, and biotechnology*, *33*(1), 47-63.

201. Khan, M. S., Hwang, J., Lee, K., Choi, Y., Kim, K., Koo, H. J., ... & Choi, J. (2018). Oxygen-carrying micro/nanobubbles: Composition, synthesis techniques and potential prospects in photo-triggered theranostics. *Molecules*, *23*(9), 2210.

202. Song, R., Hu, D., Chung, H. Y., Sheng, Z., & Yao, S. (2018). Lipid-polymer bilaminar oxygen nanobubbles for enhanced photodynamic therapy of cancer. *ACS applied materials & interfaces*, *10*(43), 36805-36813.

203. Su, C., Ren, X., Nie, F., Li, T., Lv, W., Li, H., & Zhang, Y. (2021). Current advances in ultrasound-combined nanobubbles for cancer-targeted therapy: a review of the current status and future perspectives. *RSC advances*, *11*(21), 12915-12928.

204. Bhandari, P. N., Cui, Y., Elzey, B. D., Goergen, C. J., Long, C. M., & Irudayaraj, J. (2017). Oxygen nanobubbles revert hypoxia by methylation programming. *Scientific reports*, *7*(1), 9268.

205. Fire, A., Xu, S., Montgomery, M. K., Kostas, S. A., Driver, S. E., & Mello, C. C. (1998). Potent and specific genetic interference by double-stranded RNA in Caenorhabditis elegans. *nature*, *391*(6669), 806-811.

206. Wang, Z., Rao, D. D., Senzer, N., & Nemunaitis, J. (2011). RNA interference and cancer therapy. *Pharmaceutical research*, *28*, 2983-2995.

207. Zhang, Y. A., Nemunaitis, J., Samuel, S. K., Chen, P., Shen, Y., & Tong, A. W. (2006). Antitumor activity of an oncolytic adenovirus-delivered oncogene small interfering RNA. *Cancer Research*, *66*(19), 9736-9743.

208. Meister, G., & Tuschl, T. (2004). Mechanisms of gene silencing by double-stranded RNA. *Nature*, *431*(7006), 343-349.

209. Hammond, S. M., Bernstein, E., Beach, D., & Hannon, G. J. (2000). An RNA-directed nuclease mediates post-transcriptional gene silencing in Drosophila cells. *Nature*, *404*(6775), 293-296.

210. Martinez, J., & Tuschl, T. (2004). RISC is a 5′ phosphomonoester-producing RNA endonuclease. *Genes & development*, *18*(9), 975-980.

211. Nykänen, A., Haley, B., & Zamore, P. D. (2001). ATP requirements and small interfering RNA structure in the RNA interference pathway. *Cell*, *107*(3), 309-321.

212. Jain, D., Prajapati, S. K., Jain, A., & Singhal, R. (2023). Nano-formulated siRNA-based therapeutic approaches for cancer therapy. *Nano Trends*, *1*, 100006.

213. Tarab-Ravski, D., Hazan-Halevy, I., Goldsmith, M., Stotsky-Oterin, L., Breier, D., Naidu, G. S., ... & Peer, D. (2023). Delivery of therapeutic RNA to the bone marrow in multiple myeloma using CD38-targeted lipid nanoparticles. *Advanced Science*, *10*(21), 2301377.

214. El Moukhtari, S. H., Garbayo, E., Amundarain, A., Pascual-Gil, S., Carrasco-León, A., Prosper, F., ... & Blanco-Prieto, M. J. (2023). Lipid nanoparticles for siRNA delivery in cancer treatment. *Journal of Controlled Release*, *361*, 130-146.

215. Kang, S. W., Kang, O. J., Lee, J. Y., Kim, H., Jung, H., Kim, H., ... & Choi, E. K. (2024). Evaluation of the anti-cancer efficacy of lipid nanoparticles containing siRNA against HPV16 E6/E7 combined with cisplatin in a xenograft model of cervical cancer. *Plos one*, *19*(2), e0298815.

216. Kristen, A. V., Ajroud-Driss, S., Conceição, I., Gorevic, P., Kyriakides, T., & Obici, L. (2019). Patisiran, an RNAi therapeutic for the treatment of hereditary transthyretin-mediated amyloidosis. *Neurodegenerative disease management*, *9*(1), 5-23.

217. Spänkuch-Schmitt, B., Bereiter-Hahn, J., Kaufmann, M., & Strebhardt, K. (2002). Effect of RNA silencing of polo-like kinase-1 (PLK1) on apoptosis and spindle formation in human cancer cells. *Journal of the National Cancer Institute*, *94*(24), 1863-1877.

218. Butowska, K., Han, X., Gong, N., El-Mayta, R., Haley, R. M., Xue, L., ... & Mitchell, M. J. (2023). Doxorubicin-conjugated siRNA lipid nanoparticles for combination cancer therapy. *Acta Pharmaceutica Sinica B*, *13*(4), 1429-1437.

219. Mirzaei, S., Paskeh, M. D. A., Entezari, M., Bidooki, S. H., Ghaleh, V. J., Rezaei, S., ... & Samarghandian, S. (2023). siRNA and targeted delivery systems in breast cancer therapy. *Clinical and Translational Oncology*, *25*(5), 1167-1188

Chapter 3

Investigating the therapeutic efficacy of Imidazo[1,2-a] pyridine (IMPA) derivatives against non-small cell lung cancer

3.1 Background and Challenges

Non-small cell lung cancer (NSCLC) is the most frequently observed cancer irrespective of men and women [1]. Among all lung cancer types, NSCLC accounts for approximately 85% of all cases of lung cancer [2,3]. NSCLC is any type of epithelial lung cancer other than small cell lung cancer (SCLC). The main subtypes of NSCLC are adenocarcinoma, squamous cell carcinoma, and large cell carcinoma. Lung adenocarcinoma is the most common type. The treatment options for lung cancer patients typically consist of surgery, radiation, and chemotherapy [4]. Due to the poor prognostic nature, chemotherapy remains at the cornerstone of NSCLC treatment [5,6]. Although chemotherapy has many drawbacks especially for drug resistance and non-specific cell toxicity, however, in absence of selective drug candidates, patients still treated with known anti-cancer drugs like Fluorouracil, Doxorubicin and Cisplatin, though that showed severe side effects [3,4]. Therefore, development of new therapeutic drug candidates with higher efficacy to treat NSCLC are critically needed. Among the family of antitumor compounds, heterocyclic organic compounds have been extensively used by many researchers in order to treat neoplastic disease. Pyrrole, pyrimidine, indole, quinoline and purine are few classes of heterocycles which showed interesting cytotoxicity profiles. Heterocycles are key structural components of many of the marketed anti-cancer drugs. Indeed, of the novel molecular anti-cancer agents approved by the FDA between 2010 and 2015, almost two-thirds of them having heterocyclic rings within their structures [5]. Their prevalence in anti-cancer drug design can be partly attributed to their being extremely common in nature, with a vast number of cellular processes and mechanisms having evolved the ability to interact with them. The variety of and distinct physicochemical features have established them as fundamental foundations of pharmaceutical chemistry [6,7]. Structurally, when the imidazole moiety fused with the pyridine ring, it formed imidazopyridine, which is the fused bicyclic 5–6 heterocycles [5-7]. It is well known for its medicinal application due to carrying biologically active nitrogen containing heterocycle. Among the various imidazopyridine derivatives, the imidazo[1,2-a]pyridine moiety is the most important in the area of natural products and pharmaceuticals [8]. These derivatives show a wide range of biological activities such as anti-fungal, anti-inflammatory, anti-tumor, anti-viral, anti-bacterial, anti-protozoal, anti-pyretic, analgesic, anti-apoptotic, hypnoselective, and anxioselective activities. Several drugs such as zolpidem used in the

treatment of insomnia, alpidem used as an anxiolytic agent, olprinone used for the treatment of acute heart failure, zolimidine used for the treatment of peptic ulcer, necopidem and saripidem both work as an anxiolytic agent [9-15]. They all contain the imidazo[1,2-a]pyridine moiety. Due to massive pharmacology activities and biological application of imidazo[1,2-*a*]pyridine and its substituent's are paying attention for anti-proliferative agent [9-11]. On the other direction, oxygen accommodated branch of heterocycles involves magnificent utility in pharmacology, selectively in a pyran family [12]. Most of the pyran motifs are accessible solely and fused to several carbocyclic and heterocycles. Amongst these classes of molecules 2-amino-4*H*-pyrans hold an attractive highlighted in the field of medicinal chemistry from the decades. In between the early 1960s and late 1950s pyranopyranone and pyranopyrazole with spiro conjugates being discovered as foremost molecules. Amino pyran heterocycles possess as anticancer, antimicrobial, antifungal, anti-inflammatory also engaged both biodegradable agrichemicals and pigments [13-16] either way for the treatment of myoclonus and schizophrenia, also for curing of Alzheimer's related harms They are an arrow towards the target of mitigating the diseases selectively in the field of cancer therapy. However, conjugation of imidazo[1,2-*a*]pyridine with pyran, carrying properties of both, had not explored yet to treat any cancer type.

In this study, we synthesized a series of new Imidazo[1,2-*a*]pyridine derivatives by the hybridization of imidazo[1,2-*a*]pyridine with 2-amino-4*H*-pyran to get a highly active small drug candidates. So far we have designed and developed fifteen newly Imidazo [1,2-a] pyridine (IMPA) derivative and we found improved biological efficacy against against NSCLC by targeting apoptosis pathway and arrest the cell-cycle.

3.2 Results

3.2.1 Design, and synthesis of novel imidazo [1,2-a] pyridine- 2-amino-4H-pyran derivatives

We are the first who have designed and synthesized novel derivatives of imidazo[1,2-*a*]pyridine by coupling with 2-amino-4*H*-pyrane through molecular hybridization. The synthesis involves two steps, the commercially available 2-aminopyridine (**compound 1)** reacts with ethyl 2-bromoacetate resulted **compound 2**, which further cyclization to obtain key intermediate of imidazo[1,2-a]pyridin-2-ol (**compound 3**). The final compounds were synthesized involving the multi-component one-pot reaction of intermediate (**compound 3)** with Malononitrile (**compound 4**) and corresponding aromatic aldehydes as an initial step used benzaldehyde (**compound 5**) in a green protocol [17] to obtain 2-amino-4-phenyl-4H-pyrano[2',3':4,5]imidazo[1,2-*a*]pyridine-3-carbonitrile derivatives (IMPA-1 to IMPA-15) in good yield (**Fig. 3.1A-C**). The detailed spectral characterization of IMPA 1-15 is presented in the **Appendix (A-1)**. Furthermore, NMR (^{1}H and ^{13}C), Mass spectroscopy (MS), IR (Infra-red) spectroscopy, and HPLC (High Performance Liquid Chromatography) spectra for IMPA-2, -5, -6, -8, and -12 are also thoroughly discussed in the **Appendix** (**A -2**). Based on the inhibitory concentration

value (IC50) obtained from cell cytotoxicity assay results, six IMPA compounds were further selected from the initial fifteen for their anti-cancer activity against non-small cell lung cancer.

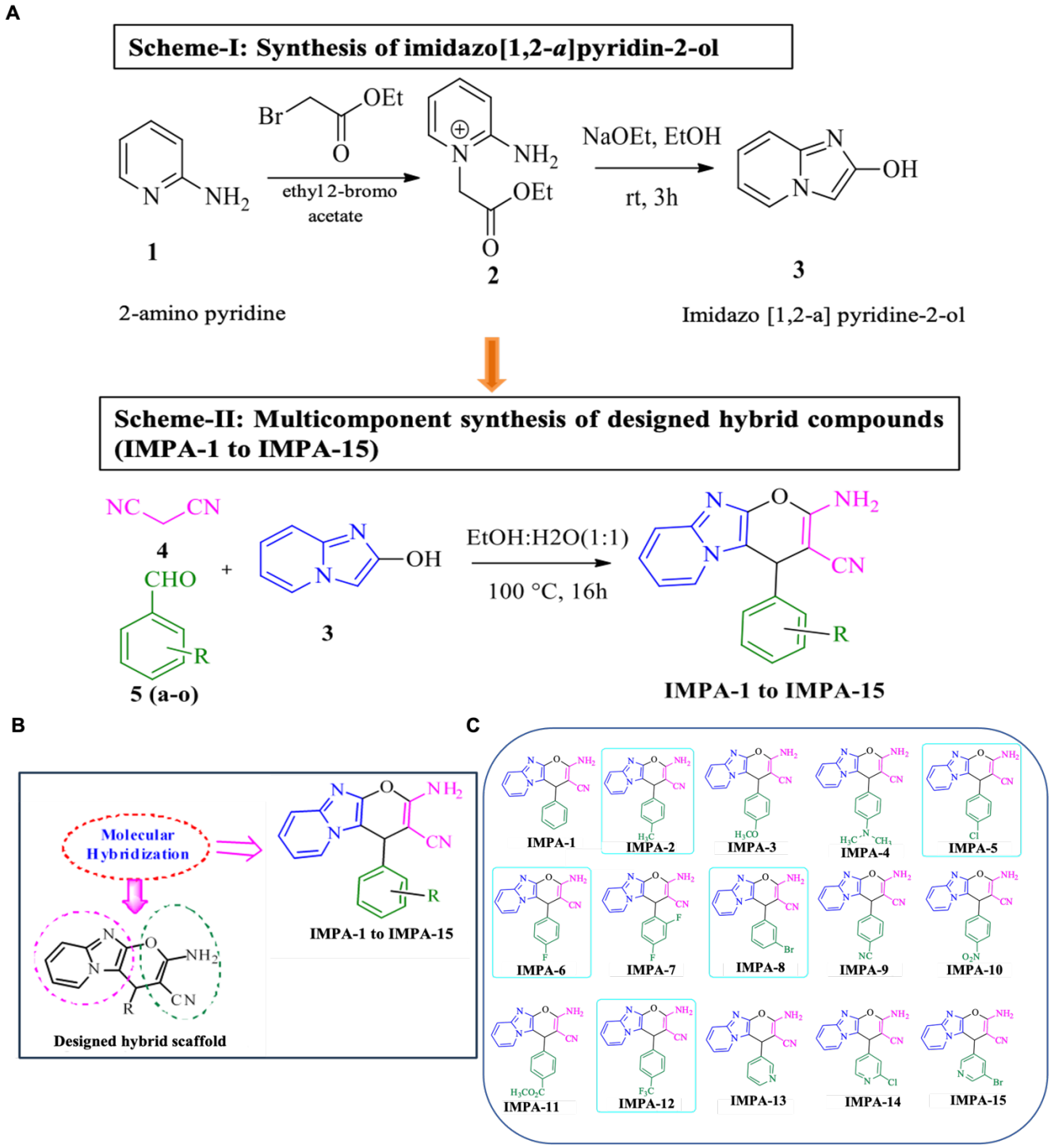

Figure 3.1: Design and synthesis of IMPA derivatives (1-15)*; (A) The IMPA synthesis involves two steps i.e scheme I and II (B) Designed protocol of imidazo[1,2-a]pyridine by coupling with 2-amino-4H-pyrane through molecular hybridization. (C) Chemical structure of IMPA derivatives 1 to 15. Out of 15, IMPA-2,-5,-6,-8, and -12 are highlighted in blue color boxes.*

3.2.2 Anti-cancer activity of novel imidazo [1,2-a] pyridine- 2-amino-4H-pyran derivatives

To evaluate the cytotoxic effect of IMPA derivatives on human lung adenocarcinoma cells, we treated A549 lung adenocarcinoma cells with these newly 15 different IMPAs at varying concentrations for 24h and the cell viability was analyzed by MTT assay. Treatment of A549 cells with these IMPAs significantly decreased cell viability in a dose-dependent manner; however, the cytotoxic effect of five IMPAs (IMPA-2,-5,-6,-8, and -12) was more profound compared to other IMPA derivatives as indicated by the IC_{50} values (**Fig. 3.2 A**). The IC_{50} of IMPA-2,-5,-6,-8, and -12 were 2.1 $\pm$ 0.7 µM, 3.1 $\pm$ 0.07 µM, 3.2$\pm$ 0.08µM, 3.4$\pm$ 0.14µM, and 3$\pm$ 0.7 µM, respectively (**Fig. 3.2 B**). We subsequently examined the impact of these five IMPAs on the viability of normal human lung epithelial BEAS-2B cells and mouse fibroblast L929 cells. No significant mortality was observed at the IC50 concentrations of these IMPAs **(Fig. 3.2 C-D)**. Based on these findings, we selected the following IMPAs for further studies: IMPA-2, -5, -6, -8, and -12. Cellular morphological changes are frequently regarded as indicators of cell pathology. Therefore, we investigated the morphological variations in A549 cancer cells in response to these IMPA derivatives. The Scanning Electron Microscopy (SEM) assay is significant in cancer studies as it provides high-resolution images that reveal detailed cellular structures and surface morphology changes, which are crucial for understanding the effects of therapeutic compounds [18]. The scanning electron microscopy (SEM) images indicated markedly altered epithelial morphology with appearance of membrane blebbing and formation of apoptotic bodies in IMPA-2,-5,-6,-8, and -12 treated A549 cells (**Fig. 3.2 E**). To confirm further the anti-cancer effect of these five IMPAs on A549 lung cancer cells, we performed clonogenic, wound scratch, trans-well migration and invasion assay. IMPA-2,-5,-6,-8, and -12 treatments significantly suppressed cancer cell growth, migration, and invasion as indicated by decreased colony numbers (**Fig. 3.2 F,G**), inhibits wound healing rate (**Fig. 3.2 H,I**) and cellular migration (**Fig. 3.2 J,K**) and invasion (**Fig. 3.2 L,M**) as compared to control untreated cells. All these results suggested that IMPA derivatives IMPA-2,-5,-6,-8, and -12 had promising antitumor activity against human lung adenocarcinoma.

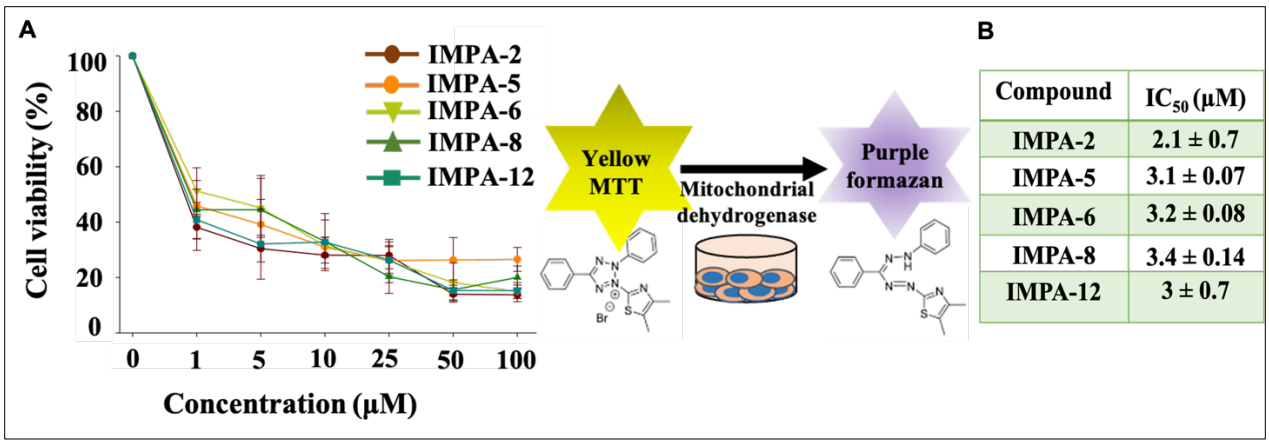

Compound	IC_{50} (µM)
IMPA-2	2.1 ± 0.7
IMPA-5	3.1 ± 0.07
IMPA-6	3.2 ± 0.08
IMPA-8	3.4 ± 0.14
IMPA-12	3 ± 0.7

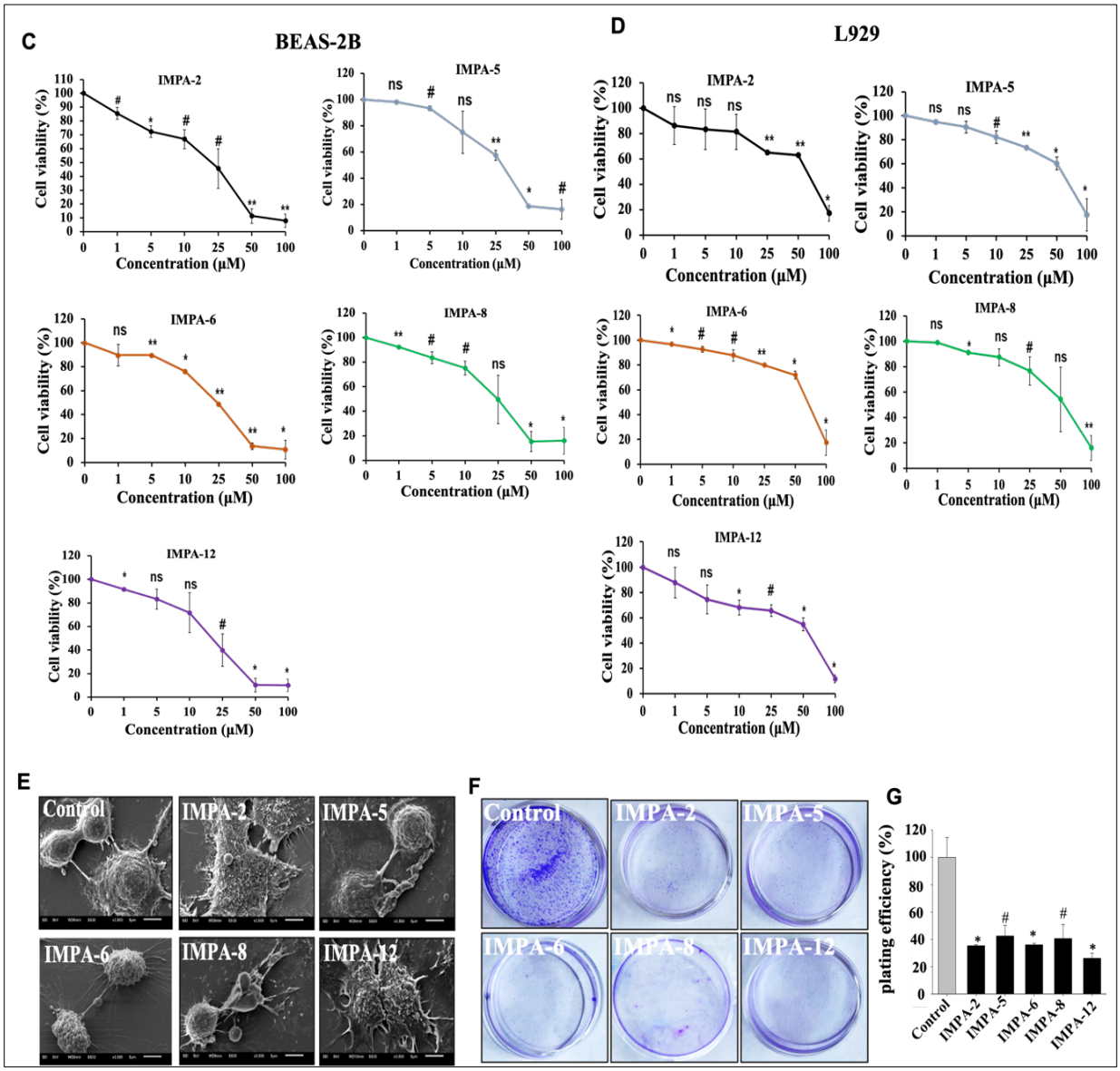

Figure 3.2: Imidazo[1,2-a]pyridine-2-amino-4H-pyrane (IMPA) derivatives induces cytotoxicity, restricts invasion in A549 lung adenocarcinoma. *(**A, B**) Analysis of A549 cell viability after treatment with different concentrations of IMPA derivatives such as IMPA -2,-5,-6,-8, and-12 for 24 h and their (B) minimal inhibitory concentrations (IC_{50}) of IMPA-2, -5, -6, -8, and -12 on A549 cell viability. **(C, D)** Cell cytotoxicity assay of BEAS2B and L929 cells viability at concentrations of IC_{50} values of IMPA-2, -5, -6, -8, and -12. **(E)** Representative scanning electron microscopic images showing morphological characteristics of A549 cells treated with these IMPA derivatives for 24h. **(F, G)** Clonogenic assay images (F) and its quantification(G) showing A549 cells colony development in response to IMPA-2, -5, -6, -8, and-12 incubations for 24h.*

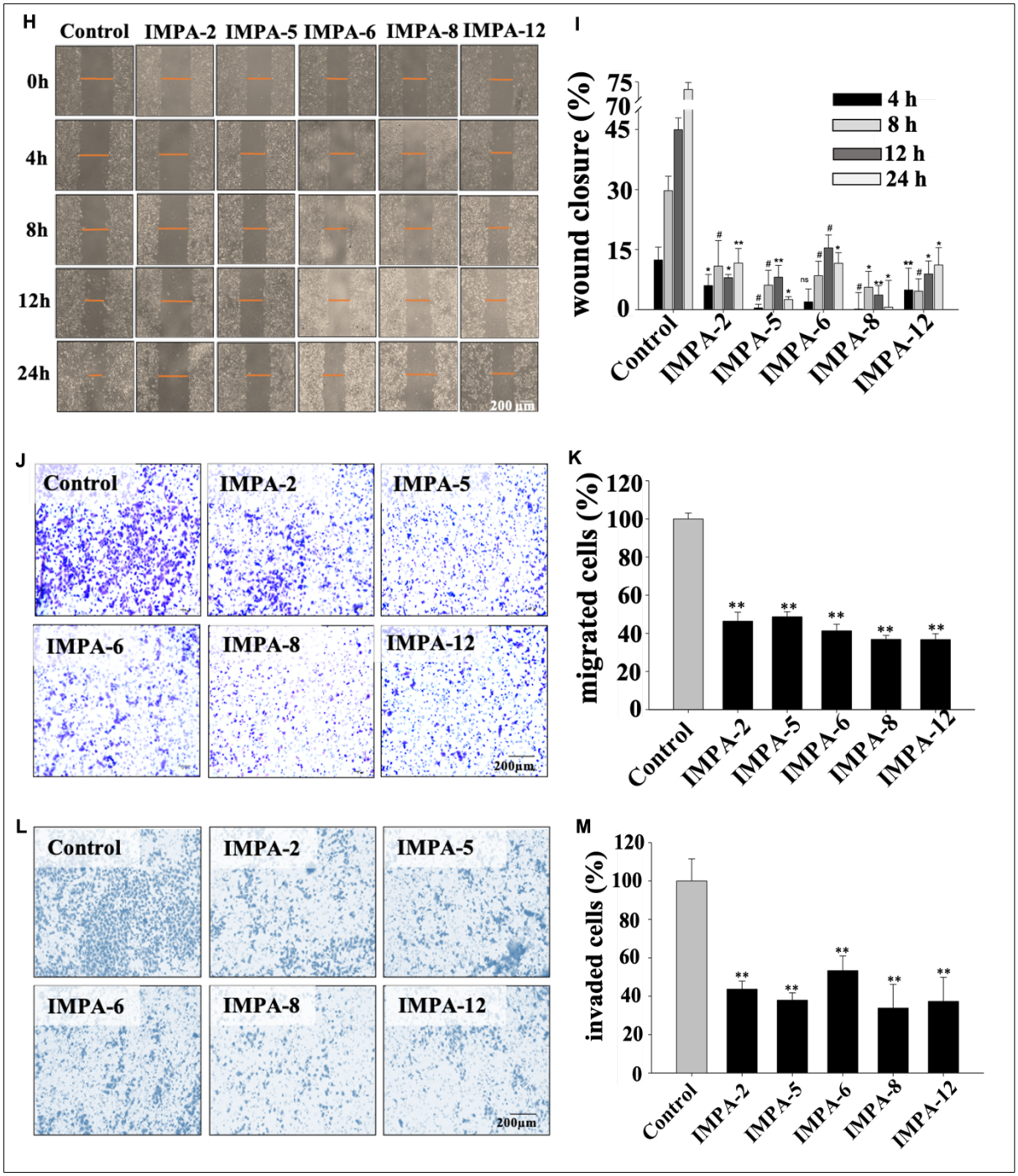

Inhibition of A549 cell migration and invasion in response to IMPAs incubation. ***(H,I)*** *Representative microscopic images (H) and their quantifications (I) of wound healing scratch assays of control and treated A549 cells treated without or with IMPA-2, -5, -6, -8,and -12 for different time periods (0h, 4h, 8h, 12h and 24h).* ***(J,K)*** *Representative images (J) and their quantifications (K) of trans-well migration of A549 cells treated without or with IMPA-2,-5,-6,-8, and -12 for 24 h.* ***(L,M)*** *Representative images (L) and their quantifications (M) of A549 cells invasiveness in control and IMPA-2,-5,-6,-8, and -12 treated A549 cells.*

*Data are expressed as mean ± SD from three independent experiments, *p<0.05, **p<0.01, and ***p<0.001.*

3.2.3 Elevated NOX activity in response to IMPA treatment leads to ROS-mediated disruption of mitochondrial membrane potential in A549 cells

To explore the mechanism of cell death induced by IMPA derivatives, we assessed mitochondrial transmembrane potential (Δψm), a critical and early indicator of the intrinsic pathway of cellular apoptosis. JC-1 staining was utilized to evaluate the loss of Δψm through fluorescence microscopy in A549 cells treated with IMPAs. JC-1 accumulates in the mitochondrial matrix and emits red fluorescence when the membrane potential is high, whereas mitochondria with lower membrane potential emit green fluorescence. Treatment with IMPA-2, -5, -6, -8, and -12 markedly increased green fluorescence and reduced red fluorescence in A549 cells compared to untreated control cells **(Fig. 3.3 A,B,C)**, indicating a compromised mitochondrial membrane potential in the treated cells. Increased production of reactive oxygen species (ROS) has been shown to lead to mitochondrial membrane depolarization and damage, which significantly contribute to apoptotic cell death when exceeding the cellular antioxidant defense mechanisms. Consequently, we measured intracellular ROS levels by evaluating the fluorescence intensity generated from DCFDA through cellular redox reactions. Treatment of A549 cells with IMPA-2, -5, -6, -8, and -12 significantly elevated fluorescence intensity, suggesting a substantial increase in intracellular ROS production by these IMPAs compared to control cells **(Fig. 3.3 D,E)**.

To investigate the potential reasons behind the ROS-mediated loss of Δψm, we analyzed the gene expression profiles of pro-apoptotic markers Bax and Bak and the anti-apoptotic marker Bcl2 in A549 cells treated with IMPA-2, -5, -6, -8, and -12, which are involved in regulating mitochondrial membrane permeability. The results showed that these IMPAs significantly increased the expression of Bax and Bak1 genes **(Fig. 3.3 F)** while decreasing the expression of the Bcl2 gene **(Fig. 3.3 G)**, thereby increasing the pro-apoptotic/anti-apoptotic ratio. Treatment with the ROS inhibitor N-acetyl-L-cysteine (NAC) notably prevented the upregulation of Bax and Bak1 gene expression induced by IMPAs **(Fig 3.3 H)**, indicating the involvement of ROS in the impairment of mitochondrial membrane potential. We also assessed the activity of NADPH oxidase (NOX), key membrane enzymes responsible for ROS generation. We found that IMPA-treated cancer cells exhibited higher NOX activity compared to controls **(Fig. 3.3 I)**, while co-treatment with NAC significantly reduced IMPA-induced NOX activity **(Fig. 3.3 I)**. These findings suggest that IMPAs, by targeting NOX activation, cause ROS-mediated impairment of mitochondrial membrane potential.

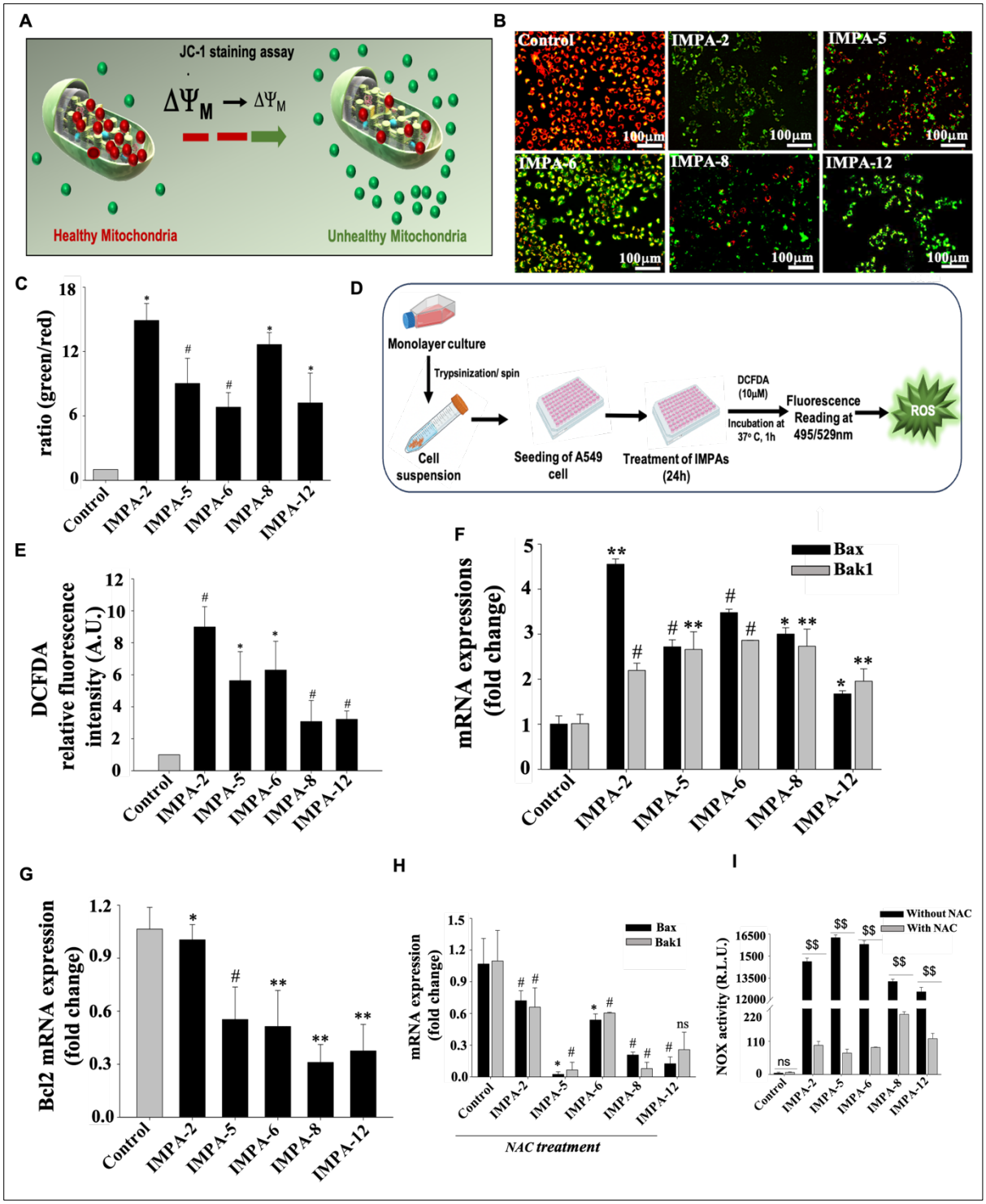

Figure 3.3: IMPA derivatives promote ROS-dependent impairment of mitochondrial membrane potential through NOX activation. ***(A, B, C)*** *Schematic graphical representation of mitochondrial membrane potential JC-1 assay* ***(A)*** *Fluorescence microscopy images* ***(B)*** *and their quantifications* ***(C)*** *representing JC-1 staining of A549 cells exhibiting mitochondrial membrane potential in response to IMPA -2, -5, -6, -8, and -12 treatments* ***(D, E)*** *schematic representation of DCFDA ROS assay* ***(D)*** *Measurement of ROS generation*

*(E) in A549 cells treated without or with these IMPAs using DCFDA reagent. (F, G) RT-qPCR analysis of pro-apoptotic Bax, and Bak1 gene expression (F) and anti-apoptotic Bcl2 gene expression (G) in control untreated and IMPA-2, -5, -6, -8 and -12 treated A549 cells at 24 h. 18s RNA served as an internal control for normalization. (H) RT-qPCR analysis of pro-apoptotic Bax, and Bak1 gene expression in presence of NAC (5mM) for 24h. (I) Relative NOX activity was measured in A549 cells incubated without or with IMPA-2, -5, -6, -8 and -12 in absence or presence of NAC (5mM) for 24h. Data are expressed as mean ± SD from three independent experiments, *p<0.05, **p<0.01, ***p<0.001 vs Con; #p<0.05, ##p<0.01 vs IMPAs.*

3.2.4 IMPAs activate the intrinsic apoptotic pathway in lung adenocarcinoma

To determine whether the inhibition of A549 cell proliferation by IMPA derivatives is due to the induction of apoptosis, we investigated apoptotic markers using flow cytometry. Flow cytometric analysis of FITC-Annexin V/Propidium Iodide (PI) revealed that treating A549 cells with IMPA-2, -5, -6, -8, and -12 for 24 hours significantly decreased the percentage of live cells and induced both early and late apoptosis compared to control cells **(Fig. 3.4 A, B)**. Caspases, central mediators of apoptotic cell death, act as initiators (caspase-8 and -9) in response to apoptotic signals or as effectors (caspase-3, -6, and -7), orchestrating the cleavage of various proteins and DNA leading to programmed cell death. Therefore, we examined caspase activation and its downstream targets in IMPA-treated A549 cells. Treatments with IMPA-2, -5, -6, -8, and -12 notably increased the levels of cleaved caspase-9 and cleaved caspase-3 in A549 cells **(Fig. 3.4 C)**, while cotreatment with NAC significantly prevented the effects of IMPAs **(Fig. 3.4 D)**, suggesting that IMPA treatment induces ROS-mediated intrinsic mitochondrial apoptotic pathways in cancer cells. Additionally, we found a significant downregulation of Poly [ADP-ribose] Polymerase-1 (PARP-1), a DNA damage repair enzyme and a substrate of activated caspase-3, in IMPA-2, -5, -6, -8, and -12 treated A549 cells **(Fig. 3.4 E)**. These results suggest that IMPA treatment stimulates the mitochondrial intrinsic apoptotic pathway of caspase activation, which subsequently degrades its cellular targets, promoting cancer cell apoptosis.

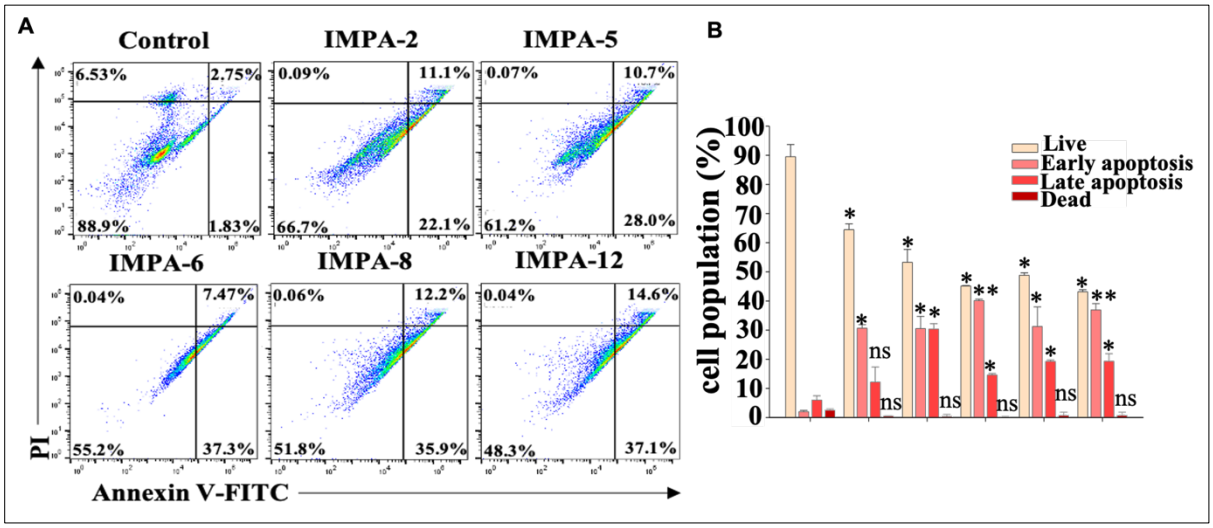

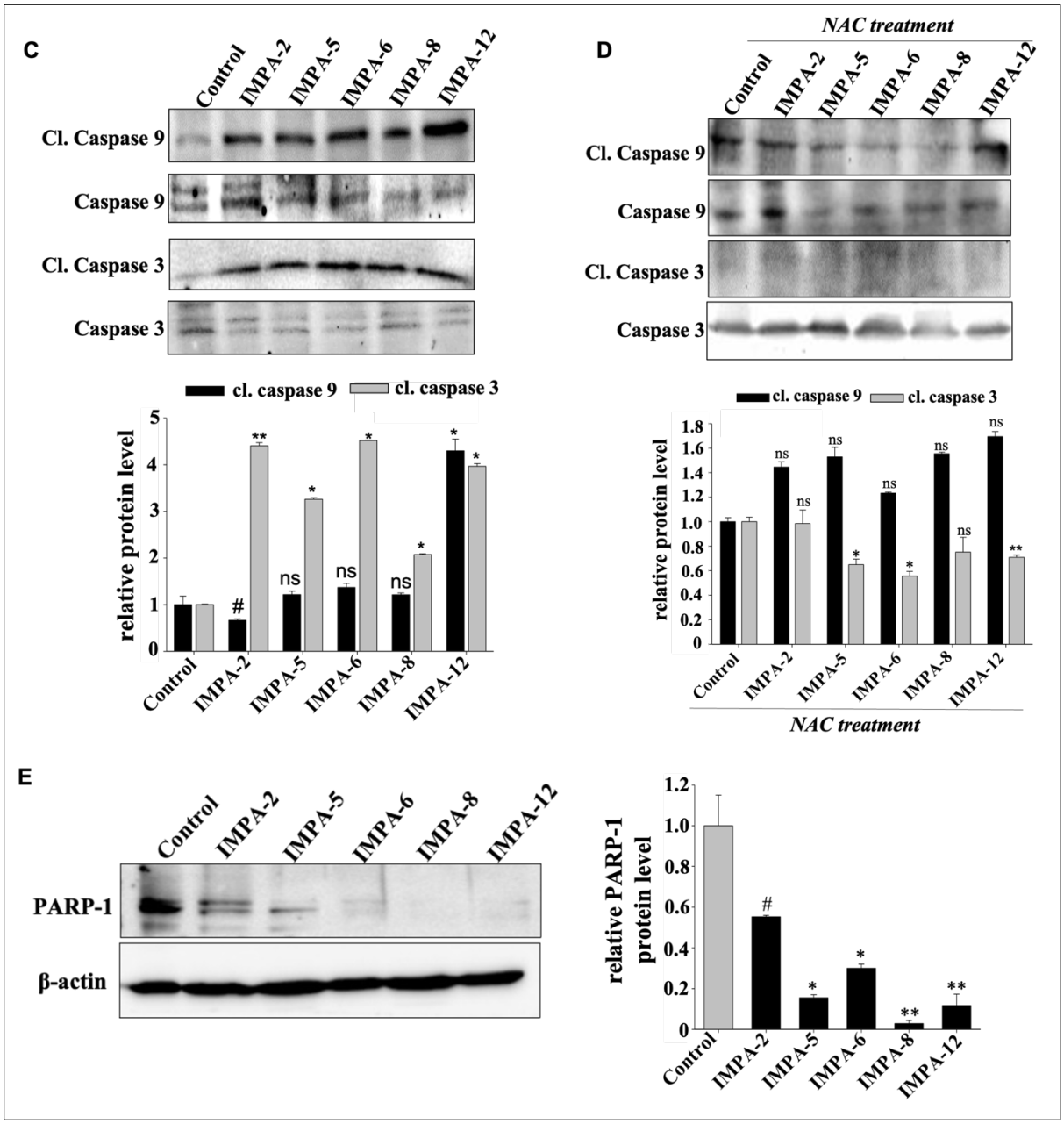

Figure 3.4: IMPAs induced A549 cell death by activating caspase9/3 dependent apoptosis. (A,B) *Flow cytometric analysis of Annexin V-FITC/PI staining (A) and its quantifications (B) indicating A549 cells apoptosis in response to IMPA -2,-5,-6,-8, and -12 incubation for 24h.* ***(C, D)*** *Immunoblot image (upper) and its quantification (lower) showing abundance of cleaved caspase 3, and 9 levels in A549 cells treated without or with IMPA-2, -5, -6, -8 and -12 in absence* ***(C)*** *or presence* ***(D)*** *of NAC (5mM) for 24 h. β-actin was used as loading control.* ***(E)*** *Immunoblot image (upper panel) and its quantification (lower panel) showing abundance of PARP-1 protein level in control and IMPA-2, -5, -6, -8 and -12 treated A549 cells at 24 h. β-actin was used as loading control. Data are expressed as mean ± SD from three independent experiments, *p<0.05, **p<0.01, and ***p<0.001 vs Con; #p<0.05, ##p<0.01 vs IMPAs.*

3.2.5 p38 MAPK inactivation and cell cycle arrest in A549 cells by IMPAs

Dysregulation of cell cycle progression is commonly associated with many human cancers [19] Therefore, we investigated the effect of these IMPAs on cell cycle distribution in A549 cells using flow cytometry. We observed a marked increase in the cell populations in the G0/G1 phase, accompanied by a proportional decrease in the S phase populations in A549 cells treated with IMPA-2, -5, -6 and -12. Interestingly, IMPA-8 did not increase the G0/G1 cell populations; instead, it enhanced the G2/M phase cell populations **(Fig. 3.5A, B)**. These results suggest that while IMPA-2, -5, -6, and -12 inhibit NSCLC growth by blocking the G1/S transition, IMPA-8 induces cell cycle arrest at the G2/M phase.

Given that p38 MAPK signaling regulates both G1/S and G2/M cell cycle checkpoints in response to cellular stress such as ROS and DNA damage, [20-22] we assessed p38 MAPK activation by western blot analysis. A significant reduction in activated p38 MAPK was observed in A549 cells treated with IMPA-2, -5, -6, -8, and -12 **(Fig. 3.5C, D)**. Activated p38 is known to induce phosphorylation-mediated degradation of p53, a tumor suppressor that regulates cell cycle checkpoints [22,23]. Treatment of A549 cells with IMPA-2, -5, -6, -8, and -12 markedly increased p53 gene expression **(Fig. 3.5E)**, whereas cotreatment with NAC notably restored p53 expression **(Fig. 3.5E)**. Furthermore, analysis of p53 downstream targets, including p16INK4A, p21Cip1, and p27Kip1, revealed significant induction of these genes in A549 cells in response to IMPAs **(Fig. 3.5F)**. These findings provide mechanistic insights into the cell cycle arrest induced by these IMPA derivatives.

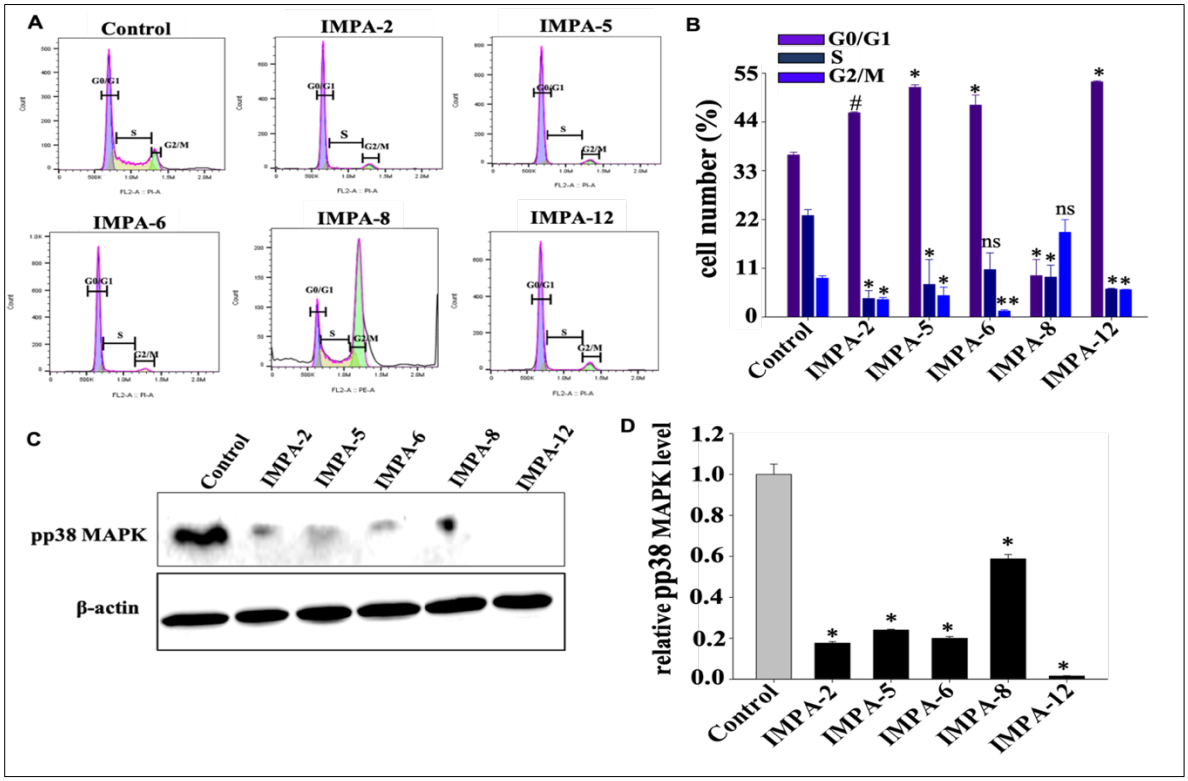

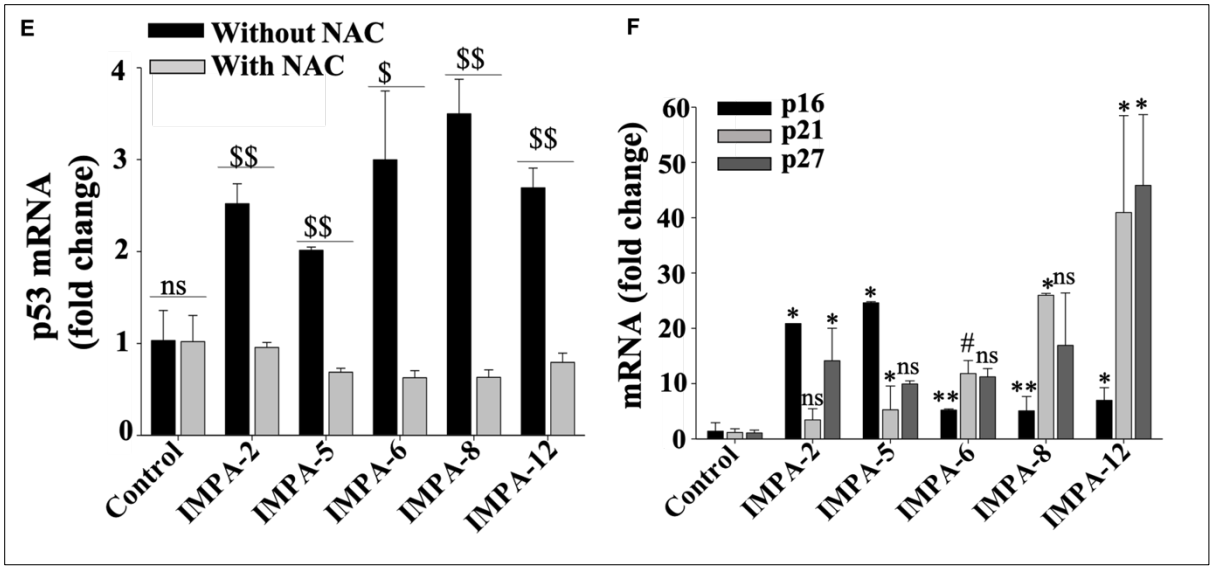

Figure 3.5: IMPAs promote cell cycle arrest by the induction of p53 tumor suppressor protein in A549 cells via p38 MAPK activation. ***(A,B)*** *Flow cytometric analysis of cell cycle distribution* ***(A)*** *and its quantification* ***(B)*** *showing % of G0/G1, S, and G2/M cell populations in response to IMPA-2,-5,-6,-8 and -12 treated A549 cells at 24 h.* ***(C)*** *Immunoblot image and its* ***(D)*** *quantification showing phospho-p38 MAPK abundance in A549 cells treated without or with IMPAs for 24 h. β-actin was used as loading control.* ***(E)*** *RT-qPCR analysis of p53 gene expression in A549 cells treated without or with IMPA-2, -5, -6, -8, and -12 in absence or presence of NAC (5mM) for 24 h. 18sRNA served as an internal control for normalization.* ***(F)*** *RT-qPCR analysis of p16, p21, and p27 gene expression in untreated and IMPA-2, -5, -6, -8 and -12 treated A549 cells at 24 h. 18sRNA served as an internal control for normalization. Data are expressed as mean ± SD from three independent experiments, *p<0.05, **p<0.01, and ***p<0.001 vs Con; #p<0.05, ##p<0.01 vs IMPAs.*

3.2.6 IMPAs restricts the growth and progression of 3D lung tumor spheroids

Since 3D multicellular tumor spheroids can better reflect the *in-vivo* features of a tumor microenvironment compared to 2D monolayers, [24-26] we analyzed the effects of various IMPA derivatives on a 3D multicellular tumor spheroid model. Phase-contrast imaging demonstrated a significant impact of the IMPA derivatives on the size and characteristics of lung tumor spheroids. We observed that these spheroids were sensitive to IMPAs, showing a reduction in size and diameter after 24 hours of treatment and a marked increase in spheroid disintegration after 48 hours **(Fig. 3.6 A)**. A live/dead assay indicated a striking reduction in viable cells and a notable increase in dead cells in tumor spheroids treated with IMPA-2, -5, -6, -8, and -12 at both 24 and 48 hours compared to controls **(Fig. 3.6 A)**.

To confirm that the observed tumor cell death was due to apoptosis, we performed FITC-Annexin V/Propidium Iodide (PI) staining followed by flow cytometry. As shown in (**Fig. 3.6 B-D)**, treatment with these IMPAs significantly decreased the percentage of live cells and concomitantly increased the

proportion of early and late apoptotic cells in the tumor spheroids compared to untreated controls, both at 24 and 48 hours. Additionally, we checked the cytotoxicity of IMPA derivatives on non-malignant 3D spheroid by phase contrast microscopy and calcein AM/ PI live dead assay, and we found that there was no size reduction, and enhanced green signal (Indicating viable non-malignant spheroids) in non-malignant tumor spheroids treated with IMPA-2, -5, -6, -8, and -12 at 48 hours **(Fig 3.6 E)** with respect to controls. These results indicate that the IMPA derivatives IMPA-2, -5, -6, -8, and -12 effectively reduce the growth and viability of lung cancer cells in 3D multicellular lung tumor spheroids, on the other hand there was no detrimental effect observed in non-malignant tumor spheroids.

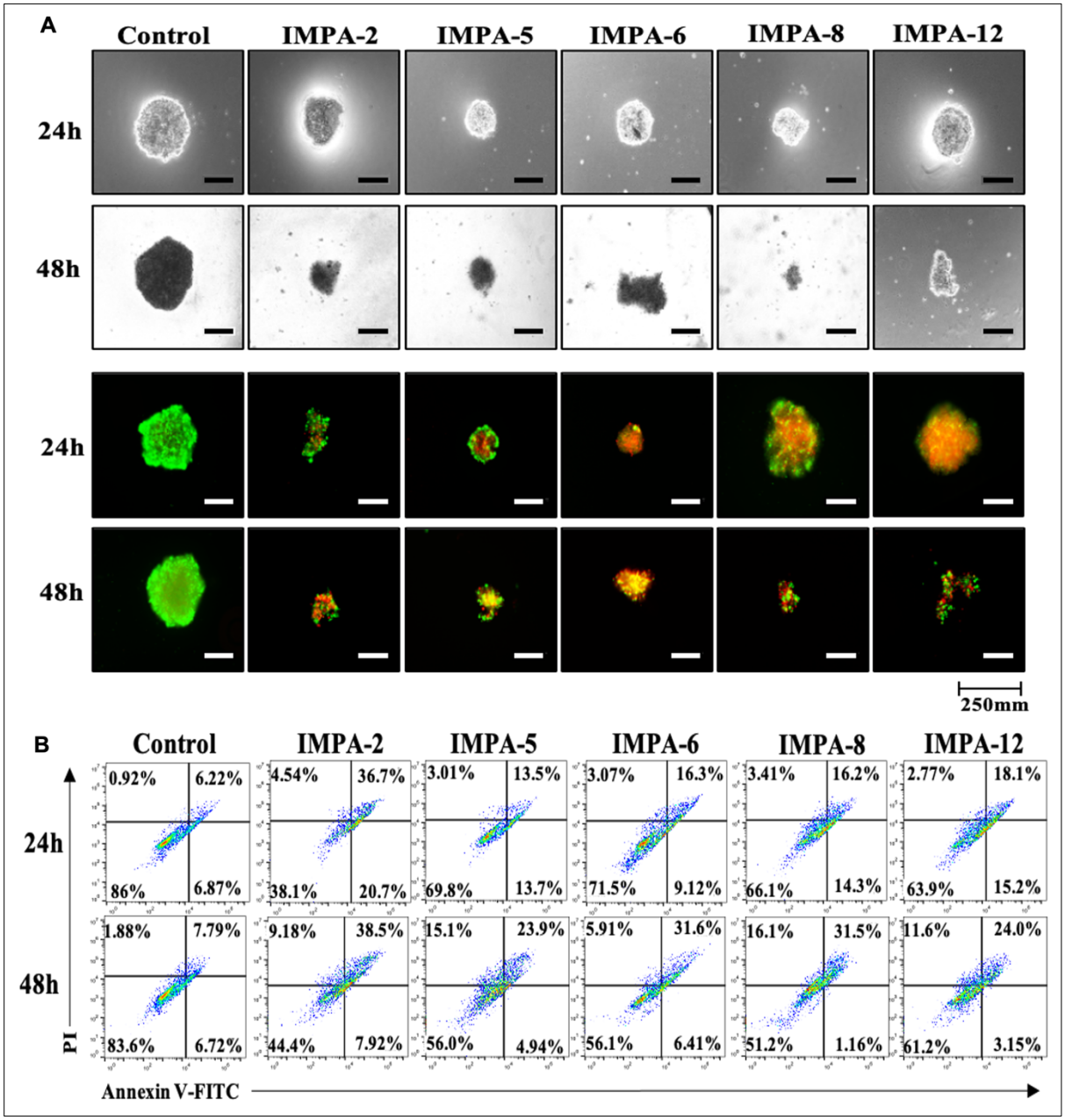

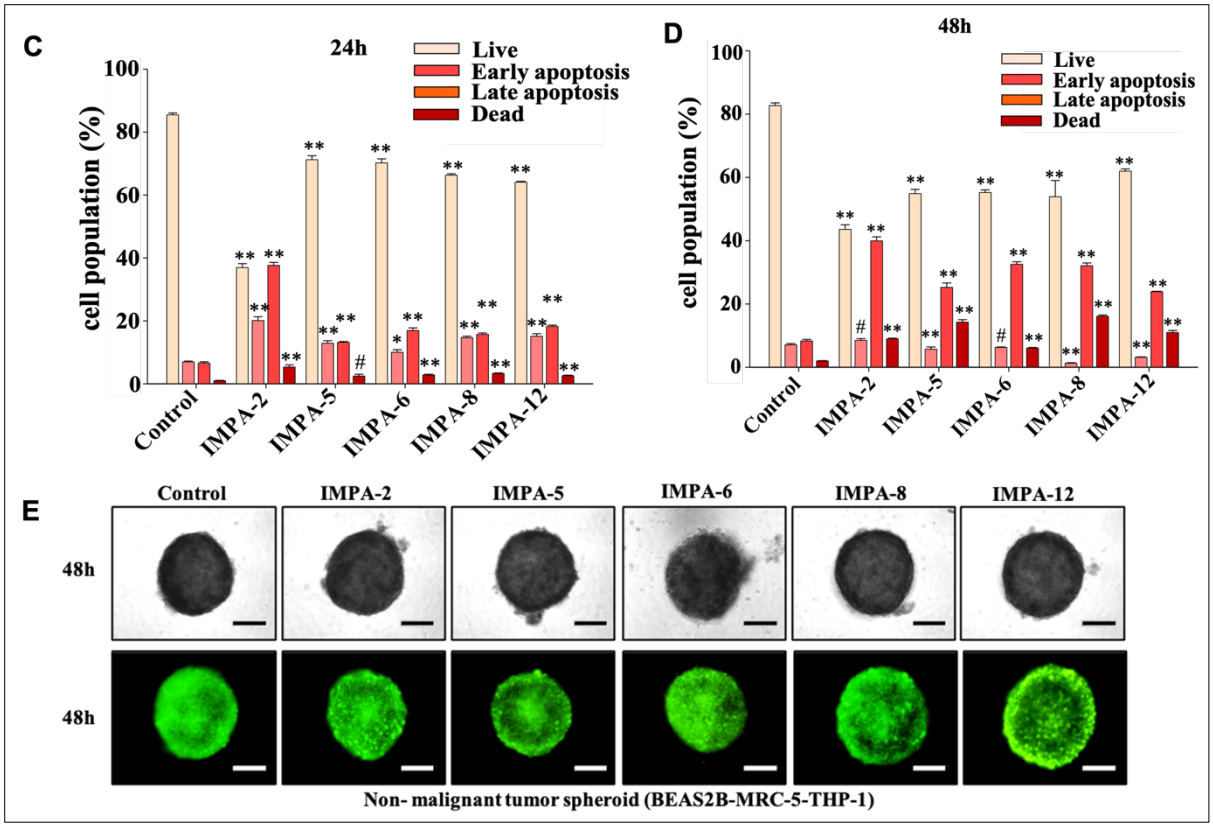

Figure 3.6: IMPAs stimulate cell death and promote apoptosis in 3D lung tumor spheroids. (A) *Microscopic phase-contrast images of multicellular tumor spheroids (A549, MRC-5 and THP-1) treated without or with IMPA-2, -5, -6, -8, and -12 for 24 h and 48 h (upper panel) and representative fluorescence microscopic images of Calcein AM (green) and propidium iodide (red) staining of multicellular tumor spheroids (Lower panel) treated without or with IMPA-2, -5, -6, -8, and -12 for 24 h and 48 h.* ***(B,C,D)*** *Flow cytometric apoptosis assay (Annexin-v and PI) indicating percentage of early apoptotic, late apoptotic and dead cells in multicellular tumor spheroids at 24 h and 48 h* ***(B)*** *in response to IMPA-2, -5, -6, -8, and -12 treatment and quantification of flow cytometric analysis of Annexin V-FITC/PI staining representing percentage of early apoptotic, late apoptotic and dead cells in multicellular tumor spheroids at 24 h* ***(C)*** *and 48 h* ***(D)*** *in response to IMPA-2, -5, -6, -8, and -12 treatment.* ***(E)*** *Fluorescence microscopic images of Calcein AM (green) and propidium iodide (red) staining of multicellular non-malignant (BEAS-2B, MRC-5 and THP-1) spheroids (Lower panel) treated without or with IMPA-2, -5, -6, -8, and -12 for 24 h and 48 h. Data are expressed as mean ± SD from three independent experiments, *p<0.05, **p<0.01, and ***p<0.001.*

3.3 Discussion

Heterocycles are crucial in the metabolism of living cells and are found in natural products, veterinary and agrochemical components, luminophores, and as building blocks in many pharmaceutical drugs. Several drugs on the market or in clinical stages have imidazo[1,2-a]pyridine as

a core unit, including Zolimidine, SCH 28080, and Alpidem [13,14], due to their potent pharmacological activities and biological applications. However, they have limitations, including toxic side effects and poor bioavailability. Therefore, there is a need to develop novel molecules with anti-cancer potential. Oxygen-accommodated heterocycles, particularly the pyran family, have shown excellent pharmacological efficacy [27]. Among these, 2-amino-4H-pyrans are of particular interest in medicinal chemistry [13-16]. In this study, novel IMPA derivatives were designed and synthesized by coupling imidazo[1,2-a]pyridine with 2-amino-4H-pyran to enhance bioactivity. The study demonstrated potent anti-cancer activity of five IMPA derivatives (IMPA-2, -5, -6, -8, -12) against lung adenocarcinoma.

Lung adenocarcinoma is highly metastatic and a major cause of cancer-related mortality, necessitating therapeutic agents that target both cancer cell proliferation and tumor metastasis [28]. The IMPA derivatives, particularly IMPA-2, -5, -6, -8, and -12, showed potent anti-proliferative activity in lung adenocarcinoma cells, inducing apoptotic cell death and cell cycle arrest. These derivatives also significantly reduced cancer cell migration and invasion, key features of tumor metastasis.

Apoptosis can be initiated via two principal pathways: one involves the activation of death receptors and caspase-8, and the other involves mitochondrial membrane alterations leading to caspase-9 activation [29-31]. To investigate the effect of these IMPAs on the induction of apoptosis, we first performed flow cytometry with PI/annexin V staining, and western blot of caspase proteins. We found that these IMPA derivatives significantly increased intrinsic apoptosis in A549 cells by markedly induced cleaved caspase-9 formations. We then look into the probable factors for upregulating intrinsic apoptotic pathway by IMPAs.

Due to uncontrolled metabolic processes, cancer cells produce more reactive oxygen species (ROS) than normal cells, resulting in a higher level of antioxidative capacity [32]. Anti-cancer therapies that increase ROS levels beyond the cytotoxic threshold are effective in selectively killing cancer cells. This imbalance in cellular redox homeostasis generates excessive ROS, which reacts with DNA, causing damage. Consequently, this heightened ROS makes cancer cells more vulnerable than normal cells, leading to cell death through apoptosis activation. We observed a significant induction of ROS production in lung cancer cells by IMPA-2,-5,-6,-8, and -12 due to the enhancement of NADPH oxidase (NOX) activity, a major cellular source of ROS generation [33].

Various studies have found that increased ROS production causes the change of mitochondrial membrane potential [32,34,35]. The anti-apoptotic Bcl2 to pro-apoptotic Bax ratio regulates mitochondrial membrane permeability, which governs cell survival or apoptosis [36]. In this study, we discovered that IMPA derivative treatment significantly increased pro-apoptotic Bax and Bak1 expression while decreasing anti-apoptotic Bcl-2 expression, resulting in loss of mitochondrial

membrane potential and permeability, caspase activation, and DNA damage [37]. The application of NAC (a known free radical scavenger) significantly reduces IMPAs-induced NOX activity and pro-apoptotic gene expression, implying that ROS-mediated apoptosis is involved in IMPAs-treated A549 cells. When DNA is damaged, Poly(ADP-ribose) Polymerase-1 (PARP-1) is recruited at the damage site to either facilitate DNA repair and cell viability or to cause DNA fragmentation, which favours cell death [38]. Because PARP-1 is a key target of active caspase-3, we studied PARP-1 cleavage in response to IMPA incubations. We observed a substantial increase in PARP-1 degradation in A549 cells, which indicates IMPA-induced apoptosis. Many chemotherapy medications work by inducing cancer cell apoptosis, and apoptosis resistance is a major contributor to chemotherapeutic drug resistance. As a result, using targeted therapies to restore apoptotic signalling in cancer cells holds huge potential for improving cancer treatment outcomes.

Dysregulation of cell cycle progression is a hallmark of many human cancers [19] and thus, targeting cell cycle arrest has long been considered a viable option for cancer treatment [39]. To determine if the growth inhibitory impact of IMPA derivatives was also caused by suppression of cell cycle progression, we used flow cytometry to examine cell cycle distribution in IMPA-treated A549 cells. Cancer cells treated with IMPA-2,-5,-6, and -12 arrest at G0/G1 phase and are unable to enter S phase, but IMPA-8 inhibits cell cycle progression at G2/M. The tumour suppressor p53, one of the most frequently altered genes in cancer, regulates cell cycle progression and apoptosis [40, 41] The p53 regulates the production of target genes such as p16INK4A, p21Cip1, and p27Kip1, which act as inhibitors of the cyclin/CDK complex, a master regulator of cell cycle checkpoints [42, 43]. In A549 cells, IMPA-2,-5,-6,-8, and -12 treatment significantly increased the expression of p53 and its downstream target genes. It is now well documented that abnormal p38 MAPK signalling is a common occurrence in several human malignancies [22]. Activated p38 MAPK targets p53 degradation, allowing cancer cells to proliferate [21,44]. Our findings revealed that incubation with IMPA-2,-5,-6,-8, and -12 significantly inactivates p38 MAPK, potentially facilitating activation of p53 expression and concomitant cell cycle arrest in A549 lung cancer cells.

In-vivo solid tumours have many similarities with multi-cellular tumour spheroids, which are a relevant 3D model for in-vitro preclinical investigation because they mimic the tumour microenvironment, which is made up of various cell types such as fibroblasts, macrophages, endothelial cells, and immune cells [45,46]. IMPA derivatives IMPA-2,-5,-6,-8, and -12 demonstrated substantial anti-proliferative effects in multi-cellular lung tumour spheroids, and the increased rate of apoptotic cell counts in 3D tumour spheroids in response to these IMPA derivatives suggests their potential usefulness *in vivo*.

In conclusion, IMPA-2,-5,-6,-8, and -12 act by inducing p53-dependent cell cycle arrest and activating the intrinsic apoptotic pathway, respectively, to exacerbate ROS-mediated cell cycle arrest and apoptosis in human A549 lung adenocarcinoma cells. As a result, recent research demonstrates the

pleiotropic effects of these IMPA derivatives on A549 cells, raising the prospect of using them to treat lung cancer. Therefore, IMPA derivatives may be used even more as lead chemicals in the treatment of non-small cell lung cancer in humans.

3.4 Materials and Methods

3.4.1 Reagents and antibodies: The list of all antibodies and reagents provided in **Tables A** and **C (Appendix)**.

3.4.2 Design and synthesis of IMPAs

For synthesis of different IMPA derivatives, all the required chemicals were purchased from Sigma-Aldrich, SpectrochemPvt. Ltd. and Combi Blocks, USA. Reactions were monitored by silica gel coated aluminium plates and visualized by UV light. Spectra of 1H NMR and 13C NMR were recorded on Avance (400 & 300 MHz), Bruker instruments. Spectral values were assigned in δ and TMS as the internal standard. Mass was analyzed in ESI+APCI instrument and IR data was recorded on FT-IR instrument recorded in cm-1for major peaks. The purity of compounds was determined by HPLC (Agilent Technologies 1200).

(a) ***Synthesis of 2-amino-1-(2-ethoxy-2-oxoethyl)pyridin-1-ium (2)***

In a 100 mL multi neck RBF pyridine-2-amine (1, 1 gm) was charged at room temperature. Then the ethyl 2-bromoacetate (5 vol.) was added slowly over 5 min and allowed to stir for 16 h at rt. MTBE was added and filtered the precipitated solid and washed twice with MTBE and dried to obtain 2-amino-1-(2-ethoxy-2-oxoethyl) pyridine-1-ium (2) as brown color solid with a quantitative yield which was used for next step without any further purification.

(b) ***Synthesis of imidazo[1,2-a]pyridin-2-ol(3)***

To a stirred solution of 2-amino-1-(2-ethoxy-2-oxoethyl)pyridine-1-ium (2, 1 mmol) in ethanol was added sodium ethoxide solution in ethanol (2 mmol) drop wise over 15 min at room temperature. The resulting reaction mixture was stirred for 3h at RT, the progress of the reaction monitored by TLC. After completion of starting material neutralized the reaction by 1N HCl solution and extracted with dichloromethane. Combined organic layers were dried over Na2SO4 and filtered, concentrated under reduced pressure to obtain imidazo[1,2-a]pyridin-2-ol (3) as light brown solid with 80% yield.

(c) ***General procedure for the synthesis of designed compounds (IMPAs)***

To a stirred solution of Malononitrile (4, 1 mmol) in an equity ratio of ethanol and water, was added corresponding aldehyde [(5 a-o, 1 mmol] at rt and allowed to stir for 10 min followed by addition of imidazo[1,2-a] pyridin-2-ol (3, 1 mmol). The reaction mixture was heated to 100° C and maintained for 16 h. After the completion of the reaction cooled the reaction mixture to room temperature and filtered the solid and washed with ethanol to yield title compounds (IMPA-1 to 15).

3.4.3 Treatment conditions

The cells were cultured at 37°C in a 90% humidified incubator with 5% CO2 environment. Cells when attained 80% confluency were sub-cultured in fresh media. IMPA derivatives IMPA-2,-5,-6,-8,-12 and curcumin were dissolved in DMSO (HiMedia, India) to prepare a stock solution at a concentration of 1 mg/ml and stored in -20°C. The working solutions of these compounds were freshly prepared in the culture medium before use. The cells were seeded in a 6-well plate with 3.0 $x10^5$ cells/well and allowed to adhere for 24h. Then, the cells were incubated with varied concentration of IMPA derivatives or curcumin for different time periods. Control and treated cells images were captured using a light microscope (Evos XL core, USA). Upon termination of incubations, cells were washed twice with ice-cold Dulbecco's phosphate-buffered saline (DPBS) and harvested with trypsin–EDTA (Gibco, UK) solution. Harvested cells were centrifuged for 5 min for 2000 rpm to collect the cell pellets which were used to perform various assays.

3.4.4 Cytotoxicity assay

Cell cytotoxicity was measured by MTT assay following the method described previously [47]. Briefly, cells ($1X10^4$ cells/ml) were seeded into a 96-well plate after overnight adherence, the cells were incubated with a two-fold serial dilution of IMPAs starting from 0.1 µg/ml with the maximum concentration of 100 µg/ml for 24 h. Curcumin with similar dose concentrations were also tested for 24 h serving as a positive control. Then 10µl (5mg/ml) MTT solution was added to each well and incubated for 4 h and on termination of incubation the supernatants were removed and 100µl MTT solubilizing agent was added to each well for 30 min at 37°C to dissolve the formazan crystals. The cell viability was estimated spectrophotometrically by measuring absorbance at 570 nm with Multiskan GO (Thermo scientific, USA). The cell viability percentage was calculated after absorbance values were blanked against acidic isopropanol and the absorbance of cells exposed to medium only (without any treatment) were taken as 100% cell viability (control).

3.4.5 Wound healing assay

A549 cells ($1X10^5$ cells/well) were seeded in 12-well cell culture plates and cultured until they reach 90% confluency. Cells were then serum starved for 12 h and treated with mitomycin C (1 µg/ml) for 1 h to stop cell proliferation. A straight scratch area was created to simulate wound formation in each well using a sterile micropipette tip and washed once to remove non-adherent cells. Cells were then treated without or with IMPA derivatives individually. Cells migrations on the wound surface were observed under a microscope and images were captured at various time points (0h, 4h, 8h, 12h and 24h). The percentage of wound closure was measured from 3 random fields for each well by calculating the width of the wound remaining compared to the initial wound width area.

3.4.6 Trans-well migration and invasion assay

Trans-well cell migration and invasion assays were performed using trans-well inserts containing 8.0 μm pores (HiMedia, India). The serum-starved A549 cells (5 x10^4 cells/well) were incubated without or with different IMPA derivatives in a serum-free medium for 24 h. On termination of incubations, cells were trypsinised and resuspended in serum free media. For migration assay, cells were directly placed in the upper chamber of transwell inserts; whereas, for invasion assay, cells were placed in the upper chamber of Matrigel coated transwell inserts. The lower chamber was filled with 10% FBS containing media in both the cases and then incubated for 24 h. The upper surface of the membrane were gently scrubbed with a cotton swab, and the cells that migrated or invaded to the lower membrane surface were fixed with 2.5% glutaraldehyde for 10 min and stained with 0.5% crystal violet solution for 2 h. The bright field images of migrated and invaded cells were captured by a microscope (Nikon, Japan) at a magnification of 200x. The migrated and invaded cell numbers also counted for at least 5 random fields for each membrane.

3.4.7 Double staining cell apoptosis assay:

Apoptosis assessment was conducted using flow cytometry to determine the phosphatidylserine exposed apoptotic cells by Annexin V–FITC and propidium iodide (PI) double staining (FITC-Annexin V apoptosis detection kit, BD Biosciences) in accordance with manufacturers protocol. Briefly, A549 monolayer samples (1X10^5 cells/well) or 3D-multicellular tumor spheroid were treated without or with different IMPA derivatives. On termination of incubations, single-cell suspensions were collected in tubes and thoroughly washed with PBS. Cells were then resuspended in Binding Buffer, and subjected to incubation with FITC-Annexin V/Propidium Iodide (PI) solution in the dark for 15 min. Each cell samples were subjected to flow cytometric analysis within 1 h using FACS Calibur (Becton Dickinson, CA). Data analysis was performed with FlowJo software (BD Bioscience). Dot-plot graphs were used to illustrate the viable cells (the lower left quadrant), early-phase apoptotic cells (the lower right quadrant), late-phase apoptotic or dead cells (the upper right quadrant), and the necrotic cells (the upper left quadrant).

3.4.8 Real-time quantitative PCR (RT-qPCR) analysis

Gene expression was analyzed by two-step qRT–PCR. Total RNA was extracted from the cells of different incubations using RNeasy Mini Kit (Qiagen, Germany) according to the manufacturer's instruction. RNA was treated with DNase I and reverse transcribed using the iScript Reverse Transcription Supermix. We used PowerUp SYBR® Green Master Mix qPCR (2X) Universal to perform RT-qPCR analysis inQuantStudio 5 Real-Time PCR System (Applied Biosystem, USA) to quantify the relative mRNA expression levels using gene specific primers. Primer sequences used for RT-qPCR were listed in **Supplementary Table 4**. Thermal cycling was initiated at 95°C for 2 minutes,

followed by 40 cycles consisting of denaturation at 95°C for 10 seconds and combined annealing/extension steps at 60°C for 1 minute. A melt curve analysis was performed by gradually heating the samples from 70°C to 95°C with a 0.5°C increment per second while the fluorescence was measured continuously after the final extension to ensure the specificity of the products. All data were normalized to the expression of the reference gene 18s RNA.

3.4.9 Western blot analysis

Control and treated cells were lysed in NuPAGE lysis buffer (Invitrogen, USA) supplemented with the Halt protease and phosphatase inhibitor cocktail and protein concentrations were determined by BCA method [48]. Western blot analysis was performed following our previously described method [49]. Briefly, cell lysates (50 µg of protein) were subjected to either 10% or 12.5% SDS–PAGE and transferred on to ImmbilonP PVDF membranes (Millipore, Bedford, MA) with the help of Wet/Tank Blotting System (Bio-Rad Laboratories, Hercules, CA). Membranes were first blocked with 5% BSA in TBS (Tris-buffered saline) buffer for 1 h followed by the overnight incubation with primary antibodies (1:500 or 1:1000 dilutions) in a rotating shaker at 4°C. The membranes were then washed three times with TBST (TBS containing 0.1% Tween 20) buffer for 10 min interval and incubated with peroxidise conjugated goat anti-rabbit or goat anti-mouse secondary antibodies (1:20000 dilution) for 2 h at room temperature. Membranes were then washed three times with TBST for 10 min interval and subjected to Clarity^{TM} Western ECL Substrate incubation for 5 min at room temperature. Protein bands were visualized and quantified in Chemidoc XRS+ System (Bio-Rad Laboratories, USA) using Image Lab Software.

3.4.10 Colony formation assay

A549 cells (100 cells/plate) were seeded into 6-well platesand allowed to adhere for 24 h. Cells were then treated without or with different IMPA derivatives and continued to grow for two weeks. After that, cell culture media was discarded; cells were washed with PBS twice and fixed with 4% paraformaldehyde for 15 min. After fixation, cells were stained with 0.5% crystal violet solution at room temperature for 10 min and then plates were rinsed with distilled water and air-dried. Cell plates were photographed and cellular clones in each well was counted under an inverted microscope (Leica DMi8, Germany).

3.4.11 Scanning electron microscopy

For the scanning electron microscopy studies, A549 cells ($1X10^4$cells) were grown on a glass cover slip for 24 h and treated without or with different IMPAs. Cells were fixed with 2.5% glutaraldehyde for 30 min at room temperature and then dehydrated through graded ethanol concentrations (25%, 50%, 75%, 95%, and 100%) for 15min at each step followed by drying with hexamethyldisilane (HMDS). The cell samples were mounted to remove charging and sputtering using a sputter coater. The samples were then

examined using variable pressure scanning electron microscope (SEM LaB6, JEOL, Model: 6610LV) at 3500x and 5000x magnification.

3.4.12 Measurement of mitochondrial membrane potential

Mitochondrial membrane potential ($\Delta\psi_m$) assay was performed using JC-1 fluorescent probe following previously described method [50]. Briefly, A549 cells ($3X10^5$ cells/well) were seeded into 6-well plates and allowed to adhere for 24 h. The cells were then treated without or with IMPA derivatives for 24 h. Cells were then incubated with 5 μM of JC-1 stain (Invitrogen, USA) for 30 min at 37°C in the dark. On termination of incubations, cells were washed twice with PBS and fluorescent images were captured using fluorescence microscope (Leica DMi8, Germany). The JC-1 probe was excited by 488 nm laser light and emission was captured at 568 nm. The green/red fluorescence intensity ratio was calculated from 5 random fields for each sample.

3.4.13 DCFDA ROS assay

Intracellular reactive oxygen species (ROS) were detected using the DCFDA fluorescent probe (#D6883, Sigma) following a previously described method [51]. In summary, A549 cells (2.5 × 10^4 cells/well) were seeded into 96-well plates and allowed to reach approximately 70–80% confluency. The media was then aspirated, and the cells were rinsed with DPBS. Subsequently, the cells were treated with 100 μl/well of a 10 μM DCFDA solution, diluted in serum-free media, and incubated for 45 minutes at 37 °C in the dark. After incubation, the media was removed, and 150 μl/well of RPMI-1640 media, with or without IMPA derivatives, was added and incubated for 24 hours. As a positive control, 0.03% hydrogen peroxide was used, while a negative control consisted of cells not treated with IMPAs but stained with DCFDA. An unstained control was also included, where cells were not exposed to DCFDA staining. ROS levels were measured using a microplate reader at an excitation/emission wavelength of 495/529 nm.

3.4.14 NOX activity assay

To assess NOX (NADPH oxidase) activity, a major source of free radicals in nonphagocytic cells, a lucigenin-based assay was performed following the method of Zhang et al. [52]. Lucigenin, a reagent that generates luminescence upon interacting with free radicals, allows for quantitative analysis using a luminometer. Briefly, after the cells (1 × 10^6) were treated, they were thoroughly washed with PBS and sonicated in ice-cold Krebs buffer (pH 7.4) containing 130 mM NaCl, 5 mM KCl, 2 mM MgCl2, 1.5 mM CaCl2, 5 mM glucose, 35 mM phosphoric acid, and 20 mM HEPES. The cell homogenate was then centrifuged at 1000 g, and the resulting pellet was resuspended in a luminescence buffer (Krebs buffer containing 0.5 mM lucigenin). NADPH (0.1 mM) was added as a substrate, and the luminescence emitted was measured using a luminometer (FluoStar Optima; BMG Labtech, Durham, NC). The NOX

activity was expressed in relative luminescence units (RLU). A549 cells were assessed for NOX activity both with and without NAC (5 mM) following treatment with IMPA derivatives.

3.4.15 Cell cycle analysis by flow cytometry

The cell cycle analysis was performed using BD Cycletest^{TM}Plus DNA kit following manufacturer instructions. Briefly, A549 cells ($1X10^4$ cells/well) seeded in 6-well plates and treated without or with IMPA derivatives for 24 h. On termination of incubations, cells were trypsinized and centrifuged for 5 min at 1500 rpm at room temperature. After discarding the supernatant, cell pellets were resuspended in buffer solution and incubate with PI stain solution on ice for 10 min in the dark. Cells were then filtered and used for analysis on the FACS Calibur (Becton Dickinson, CA) flow cytometer. The data acquisition and analysis were performed using FlowJo (10.6.0) software.

3.4.16 3D multicellular tumor spheroid culture

3D multi-cellular tumor spheroids were generated by following hanging drop plate method [53,54]. Briefly, cell suspension (30µl) of A549 ($3.5x10^4$ cells), MRC-5 ($5x10^4$ cells) and THP-1 ($5x10^4$ cells) mixtures were spotted onto the lid of 90 mm cell culture dish through pipette drop. The lid was then placed on the plate and 4 to 5 ml of autoclaved Milli-Q water was added in the bottom of the dish to keep the cells hydrated. The plate was labelled and was maintained at 37°C in humidified incubator with 5% CO2 environment for five days to allow the spheroids to form. Cells were routinely observed under microscope and imaged to examine cell aggregation and proliferation. The growth media was exchanged every alternate day by taking 10 µl media from a drop and adding 14µl fresh media into a drop to provide enough nutrients for cells. The 3D multi-cellular tumor spheroids were then incubated without or with different IMPA derivatives for 24h and 48h and on termination of incubations, phase contrast images were captured by a microscope (Nikon, Japan).

3.4.17 Live/Dead assay of 3D tumor spheroids

To examine the viability of cells in multi-cellular (A549, MRC-5 and THP-1) tumor spheroids treated without or with different IMPA derivatives for 24h and 48h followed by the determination of viability and cytotoxicity with the live/dead assay. The culture media were aspirated and the cells were treated with 5 µM of Calcein AM (Invitrogen, USA) and Propidium Iodide (BD Biosciences, USA) for 2 h at 37°C. Images of cell spheroids were subsequently captured using an inverted fluorescent microscope (Leica DMi8, Germany).

3.4.18 Statistical analysis

Data were obtained from at least three separate experiments and values were presented as the mean ± SD. T-test was employed for comparison among multiple groups using SigmaPlot 10.0 software. A level of $P < 0.05$ was considered statistically significant.

References

1. Youlden, D. R., Cramb, S. M., & Baade, P. D. (2008). The International Epidemiology of Lung Cancer: geographical distribution and secular trends. *Journal of thoracic oncology*, *3*(8), 819-831.
2. Torre, L. A., Siegel, R. L., & Jemal, A. (2016). Lung cancer statistics. *Lung cancer and personalized medicine: current knowledge and therapies*, 1-19.
3. Molina, J. R., Yang, P., Cassivi, S. D., Schild, S. E., & Adjei, A. A. (2008). Non-small cell lung cancer: epidemiology, risk factors, treatment, and survivorship. In *Mayo clinic proceedings* (Vol. 83, No. 5, pp. 584-594). Elsevier.
4. Huang, C. Y., Ju, D. T., Chang, C. F., Reddy, P. M., & Velmurugan, B. K. (2017). A review on the effects of current chemotherapy drugs and natural agents in treating non–small cell lung cancer. *Biomedicine*, *7*(4).
5. Ali, I., Lone, M. N., & Aboul-Enein, H. Y. (2017). Imidazoles as potential anticancer agents. *MedChemComm*, *8*(9), 1742-1773.
6. Baraldi, P. G., Bovero, A., Fruttarolo, F., Preti, D., Tabrizi, M. A., Pavani, M. G., & Romagnoli, R. (2004). DNA minor groove binders as potential antitumor and antimicrobial agents. *Medicinal research reviews*, *24*(4), 475-528.
7. Lang, D. K., Kaur, R., Arora, R., Saini, B., & Arora, S. (2020). Nitrogen-containing heterocycles as anticancer agents: An overview. *Anti-Cancer Agents in Medicinal Chemistry (Formerly Current Medicinal Chemistry-Anti-Cancer Agents)*, *20*(18), 2150-2168.
8. Bagdi, A. K., Santra, S., Monir, K., & Hajra, A. (2015). Synthesis of imidazo [1, 2-a] pyridines: a decade update. *Chemical Communications*, *51*(9), 1555-1575.
9. Vitaku, E., Smith, D. T., & Njardarson, J. T. (2014). Analysis of the structural diversity, substitution patterns, and frequency of nitrogen heterocycles among US FDA approved pharmaceuticals: miniperspective. *Journal of medicinal chemistry*, *57*(24), 10257-10274.
10. Reddy Gangireddy, M., Mantipally, M., Gundla, R., Nayak Badavath, V., Paidikondala, K., & Yamala, A. (2019). Design and synthesis of piperazine-linked imidazo [1, 2-a] pyridine derivatives as potent anticancer agents. *ChemistrySelect*, *4*(46), 13622-13629.
11. Mohana Roopan, S., Patil, S. M., & Palaniraja, J. (2016). Recent synthetic scenario on imidazo [1, 2-a] pyridines chemical intermediate. *Research on Chemical Intermediates*, *42*, 2749-2790.
12. Karrouchi, K., Radi, S., Ramli, Y., Taoufik, J., Mabkhot, Y. N., Al-Aizari, F. A., & Ansar, M. H. (2018). Synthesis and pharmacological activities of pyrazole derivatives: A review. *Molecules*, *23*(1), 134.
13. Enguehard-Gueiffier, C., & Gueiffier, A. (2007). Recent Progress in the Pharmacology of Imidazo [1, 2-a] pyridines. *Mini Reviews in Medicinal Chemistry*, *7*(9), 888-899.

14. Deep, A., Kaur Bhatia, R., Kaur, R., Kumar, S., Kumar Jain, U., Singh, H., ... & Kishore Deb, P. (2017). Imidazo [1, 2-a] pyridine scaffold as prospective therapeutic agents. *Current topics in medicinal chemistry*, *17*(2), 238-250.
15. Mohana Roopan, S., Patil, S. M., & Palaniraja, J. (2016). Recent synthetic scenario on imidazo [1, 2-a] pyridines chemical intermediate. *Research on Chemical Intermediates*, *42*, 2749-2790.
16. Fesatidou, M., Petrou, A., & Athina, G. (2020). Heterocycle compounds with antimicrobial activity. *Current pharmaceutical design*, *26*(8), 867-904.
17. Mandha, S. R., Alla, M., Bommena, V. R., Nanubolu, J. B., Lingala, S. K., & Yarasi, S. (2012). Oxidative Difunctionalization of 2-Amino-4 H-pyrans in Iodobenzene Diacetate and N-Chlorosuccinimide: Reactivity, Mechanistic Insights, and DFT Calculations. *The Journal of Organic Chemistry*, *77*(23), 10648-10654.
18. Deng, X., Xiong, F., Li, X., Xiang, B., Li, Z., Wu, X., ... & Zeng, Z. (2018). Application of atomic force microscopy in cancer research. *Journal of nanobiotechnology*, *16*, 1-15.
19. Park, M. T., & Lee, S. J. (2003). Cell cycle and cancer. *BMB Reports*, *36*(1), 60-65.
20. Kennedy, N. J., Cellurale, C., & Davis, R. J. (2007). A radical role for p38 MAPK in tumor initiation. *Cancer cell*, *11*(2), 101-103.
21. Bradham, C., & McClay, D. R. (2006). p38 MAPK in development and cancer. *Cell cycle*, *5*(8), 824-828.
22. Thornton, T. M., & Rincon, M. (2009). Non-classical p38 map kinase functions: cell cycle checkpoints and survival. *International journal of biological sciences*, *5*(1), 44.
23. Lafarga, V., Cuadrado, A., Lopez de Silanes, I., Bengoechea, R., Fernandez-Capetillo, O., & Nebreda, A. R. (2009). p38 Mitogen-activated protein kinase-and HuR-dependent stabilization of p21Cip1 mRNA mediates the G1/S checkpoint. *Molecular and cellular biology*, *29*(16), 4341-4351.
24. Gong, X., Lin, C., Cheng, J., Su, J., Zhao, H., Liu, T., ... & Zhao, P. (2015). Generation of multicellular tumor spheroids with microwell-based agarose scaffolds for drug testing. *PloS one*, *10*(6), e0130348.
25. Kumar, H. R., Zhong, X., Hoelz, D. J., Rescorla, F. J., Hickey, R. J., Malkas, L. H., & Sandoval, J. A. (2008). Three-dimensional neuroblastoma cell culture: proteomic analysis between monolayer and multicellular tumor spheroids. *Pediatric surgery international*, *24*, 1229-1234.
26. Lazzari, G., Couvreur, P., & Mura, S. (2017). Multicellular tumor spheroids: a relevant 3D model for the in vitro preclinical investigation of polymer nanomedicines. *Polymer Chemistry*, *8*(34), 4947-4969.
27. Peng, X. M., LV Damu, G., & Zhou, H. (2013). Current developments of coumarin compounds in medicinal chemistry. *Current pharmaceutical design*, *19*(21), 3884-3930.

28. Altorki, N. K., Markowitz, G. J., Gao, D., Port, J. L., Saxena, A., Stiles, B., ... & Mittal, V. (2019). The lung microenvironment: an important regulator of tumour growth and metastasis. *Nature Reviews Cancer*, *19*(1), 9-31.
29. Fulda, S., & Debatin, K. M. (2006). Extrinsic versus intrinsic apoptosis pathways in anticancer chemotherapy. *Oncogene*, *25*(34), 4798-4811.
30. Haupt, S., Berger, M., Goldberg, Z., & Haupt, Y. (2003). Apoptosis-the p53 network. *Journal of cell science*, *116*(20), 4077-4085.
31. Kim, H. E., Du, F., Fang, M., & Wang, X. (2005). Formation of apoptosome is initiated by cytochrome c-induced dATP hydrolysis and subsequent nucleotide exchange on Apaf-1. *Proceedings of the National Academy of Sciences*, *102*(49), 17545-17550.
32. Redza-Dutordoir, M., & Averill-Bates, D. A. (2016). Activation of apoptosis signalling pathways by reactive oxygen species. *Biochimica et Biophysica Acta (BBA)-Molecular Cell Research*, *1863*(12), 2977-2992.
33. Nogueira, V., & Hay, N. (2013). Molecular pathways: reactive oxygen species homeostasis in cancer cells and implications for cancer therapy. *Clinical Cancer Research*, *19*(16), 4309-4314.
34. Chen, P., Luo, X., Nie, P., Wu, B., Xu, W., Shi, X., ... & Zou, Z. (2017). CQ synergistically sensitizes human colorectal cancer cells to SN-38/CPT-11 through lysosomal and mitochondrial apoptotic pathway via p53-ROS cross-talk. *Free Radical Biology and Medicine*, *104*, 280-297.
35. Lee, I., Bender, E., Arnold, S., & Kadenbach, B. (2001). New control of mitochondrial membrane potential and ROS formation A hypothesis.
36. Tomek, M., Akiyama, T., & Dass, C. R. (2012). Role of Bcl-2 in tumour cell survival and implications for pharmacotherapy. *Journal of Pharmacy and Pharmacology*, *64*(12), 1695-1702.
37. Ouyang, L., Shi, Z., Zhao, S., Wang, F. T., Zhou, T. T., Liu, B., & Bao, J. K. (2012). Programmed cell death pathways in cancer: a review of apoptosis, autophagy and programmed necrosis. *Cell proliferation*, *45*(6), 487-498.
38. Soldani, C., & Scovassi, A. I. (2002). Poly (ADP-ribose) polymerase-1 cleavage during apoptosis: an update. *Apoptosis*, *7*, 321-328.
39. Otto, T., & Sicinski, P. (2017). Cell cycle proteins as promising targets in cancer therapy. *Nature Reviews Cancer*, *17*(2), 93-115.
40. Haupt, S., Berger, M., Goldberg, Z., & Haupt, Y. (2003). Apoptosis-the p53 network. *Journal of cell science*, *116*(20), 4077-4085.
41. Soussi, T. (1999). The p53 tumor suppressor gene: from molecular biology to clinical investigation. *Lung biology in health and disease*, *124*, 453-471.

42. Jackson, M. W., Agarwal, M. K., Yang, J., Bruss, P., Uchiumi, T., Agarwal, M. L., ... & Taylor, W. R. (2005). p130/p107/p105Rb-dependent transcriptional repression during DNA-damage-induced cell-cycle exit at G2. *Journal of cell science*, *118*(9), 1821-1832.
43. Taylor, W. R., & Stark, G. R. (2001). Regulation of the G2/M transition by p53. *Oncogene*, *20*(15), 1803-1815.
44. Innocente, S. A., Abrahamson, J. L., Cogswell, J. P., & Lee, J. M. (1999). p53 regulates a G2 checkpoint through cyclin B1. *Proceedings of the National Academy of Sciences*, *96*(5), 2147-2152.
45. Jeong, S. Y., Lee, J. H., Shin, Y., Chung, S., & Kuh, H. J. (2016). Co-culture of tumor spheroids and fibroblasts in a collagen matrix-incorporated microfluidic chip mimics reciprocal activation in solid tumor microenvironment. *PloS one*, *11*(7), e0159013.
46. Kimlin, L. C., Casagrande, G., & Virador, V. M. (2013). In vitro three-dimensional (3D) models in cancer research: an update. *Molecular carcinogenesis*, *52*(3), 167-182.
47. Choudhary, S. A., Bora, N., Banerjee, D., Arora, L., Das, A. S., Yadav, R., ... & Dasgupta, S. (2019). A novel small molecule A2A adenosine receptor agonist, indirubin-3′-monoxime, alleviates lipid-induced inflammation and insulin resistance in 3T3-L1 adipocytes. *Biochemical Journal*, *476*(16), 2371-2391.
48. Smith, P. E., Krohn, R. I., Hermanson, G. T., Mallia, A. K., Gartner, F. H., Provenzano, M., ... & Klenk, D. C. (1985). Measurement of protein using bicinchoninic acid. *Analytical biochemistry*, *150*(1), 76-85.
49. Pal, D., Dasgupta, S., Kundu, R., Maitra, S., Das, G., Mukhopadhyay, S., ... & Bhattacharya, S. (2012). Fetuin-A acts as an endogenous ligand of TLR4 to promote lipid-induced insulin resistance. *Nature medicine*, *18*(8), 1279-1285.
50. Sivandzade, F., Bhalerao, A., & Cucullo, L. (2019). Analysis of the mitochondrial membrane potential using the cationic JC-1 dye as a sensitive fluorescent probe. *Bio-protocol*, *9*(1), e3128-e3128.
51. Eruslanov, E., & Kusmartsev, S. (2010). Identification of ROS using oxidized DCFDA and flow-cytometry. *Advanced protocols in oxidative stress II*, 57-72.
52. Zhang, W., Wang, Y., Chen, C. W., Xing, K., Vivekanandan, S., & Lou, M. F. (2006). The positive feedback role of arachidonic acid in the platelet-derived growth factor-induced signaling in lens epithelial cells. *Mol Vis*, *12*(7), 821-831.
53. Foty, R. (2011). A simple hanging drop cell culture protocol for generation of 3D spheroids. *JoVE (Journal of Visualized Experiments)*, (51), e2720.
54. Ware, M. J., Colbert, K., Keshishian, V., Ho, J., Corr, S. J., Curley, S. A., & Godin, B. (2016). Generation of homogenous three-dimensional pancreatic cancer cell spheroids using an improved hanging drop technique. *Tissue Engineering Part C: Methods*, *22*(4), 312-321.

Chapter 4

Oxygen Nanobubbles restricts hypoxia-induced epithelial-to-mesenchymal transition and metastasis in lung and breast tumor

4.1 Background and Challenges

The initiation and progression of cancer are closely associated with the abnormal and extensive proliferation of tumor cells and the formation of abnormal tumor blood vessels, [1] resulting in increased nutrient consumption and reduced oxygen delivery [1-3]. This leads to the creation of hypoxic microenvironments, which are hallmarks of solid tumor development [1-4]. It drives tumor aggressiveness through heightening epithelial-to-mesenchymal transition (EMT), dysregulated angiogenesis, and enhanced cancer cell migration, invasion, and metastasis [4-8]. Furthermore, cancer cells under chronic hypoxia exhibit increased resistance to various cancer therapies, including chemotherapy, radiotherapy, and photodynamic therapy [6-10]. Numerous studies have shown that hypoxia within tumors induces EMT in epithelial cancer cells, promoting invasion and migration through the enhanced production of matrix metalloproteinases (MMPs) [5-9]. Hypoxia stabilizes HIF-1α, which would otherwise be degraded under normal oxygen conditions. Stabilized HIF-1α triggers a range of responses, including EMT initiation, apoptosis suppression, autophagy promotion, and the induction of metastatic processes [10-13]. HIF-1α modulates the expression of various genes and signaling pathways, such as those involving Transforming Growth Factor-β (TGF-β), Notch, Sonic Hedgehog, and Wnt [2,3,6,7,9], and it plays a crucial role in regulating EMT and metastasis by influencing key transcription factors like Twist, Snail, Slug, Smad interacting protein 1 (Sip1), and ZEB1 [5,11,12,14–16]. Thus, targeting HIF-1α could reduce hypoxia severity and alleviate hypoxia-induced cancer aggressiveness and improved the drug efficacy [16–18].

In response to the challenges posed by tumor hypoxia, oxygenation therapy is emerging as a novel anti-cancer strategy. Oxygen nanobubbles (ONBs), a recent advancement in gas-liquid systems, are submicron-sized oxygen-filled cavities stabilized by surfactants. They are highly efficient in delivering oxygen to tissues [19–21], and have gained significant attention in various scientific and industrial fields [22,23]. ONBs possess unique properties, such as a high surface charge, [23–25] neutral buoyancy enabling them to reach surfaces through Brownian motion, and longevity in suspension for extended periods [26–28]. These characteristics make them attractive for medical applications. ONBs can penetrate biological membranes and tissues, releasing oxygen into hypoxic cells and tissues, thereby attenuating hypoxic effects [21,26,28–32] and improving the efficacy of cancer treatments, including

radiation therapy and chemotherapy [33–39]. Existing ONBs face several limitations in cancer therapy. Despite their small size and robust polymer shells, they can exhibit instability in complex physiological environments, leading to inconsistent delivery of oxygen and therapeutic agents. Premature oxygen release is also a concern, as maintaining adequate oxygen levels during circulation is critical for effective hypoxia-targeted therapy. Additionally, the high interstitial fluid pressure and deregulated extracellular matrix in tumors can hinder the deep and uniform penetration of ONBs, reducing their overall therapeutic efficacy. L-ONBs address these limitations by incorporating a lipid-polymer bilaminar shell for enhanced stability and controlled oxygen release, allowing for better tumor penetration and retention. Their precise response to external stimuli enables targeted activation and localized drug release, significantly improving therapeutic outcomes.

In this study, we prepared highly stable liposome-encapsulated oxygen nanobubbles (L-ONBs) using dipalmitoyl phosphatidylcholine (DPPC) lipid via an acoustic cavitation approach. We investigated their efficacy in mitigating hypoxia-induced aggressiveness in lung adenocarcinoma (LUAD) and mammary adenocarcinoma (MAC). Our findings demonstrated that L-ONBs effectively reduced LUAD and MAC tumor progression and aggressiveness by targeting the HIF-1α-mediated EMT pathway.

4.2 Results

4.2.1 Fabrication, physiochemical-characterization and stability of liposome-encapsulated oxygen nanobubbles (L-ONB)

In this study, we developed liposome-encapsulated oxygen nanobubbles (L-ONB) that provide a larger surface area and greater colloidal stability compared to existing oxygen bubble systems [20,21]. Our formulation involves encapsulating oxygen nanobubbles within liposomes made from dipalmitoyl phosphatidylcholine (DPPC) and cholesterol. DPPC has a high phase transition temperature, while cholesterol enhances structural integrity and fortifies the lipid bilayer when combined with DPPC. Cholesterol also helps reduce liposome fusion and aggregation. The fabrication process of L-ONB is schematically illustrated in **(Fig. 4.1A)**. The liposomes, ONB, and L-ONB were characterized by using Nanoparticle Tracking Analysis (NTA), Dynamic Light Scattering (DLS), Cryo-Transmission Electron Microscopy (Cryo-TEM), and Transmission Electron Microscopy (TEM). The NTA study revealed that the average sizes were 107-509 nm for liposomes, 150-180 nm for ONB, and 100-468 nm for L-ONB **(Fig. 4.1B)**. Zeta potential measurements showed negative charges for all samples: -11.3 ± 0.5 for liposomes, -33.8 ± 1.5 for ONB, and -25.6 ± 0.8 for L-ONB **(Fig. 4.1C)**, which is likely due to the OH- ion adsorption at the gas-liquid interface. This electric double layer acts as a repulsive force preventing bubble aggregation [23,36,37]. The mean diameters were 217 ± 117.6 nm for liposomes, 158.7 ± 74.2 nm for ONB, and 274.8 ± 115.6 nm for L-ONB **(Fig. 4.1 D)**. NTA-based particle number density measurements were approximately 1.41 ± 0.0903 x 10^8 particles/mL for liposomes, 3.71 ± 0.376 x 10^8 bubbles/mL for ONB, and 3.16 ± 0.676 x 10^8 bubbles/mL for L-ONB **(Fig. 4.1 E)**. Further,

dynamic light scattering analyses showed the size of L-ONBs as 267 ± 37 nm, **(Fig. 4.1 F)** which aligns with tumor vasculature openings (400 to 800 nm), suggesting potential passive targeting to tumor tissues due to its enhanced permeability and retention (EPR) effect [5]. L-ONB exhibited a polydispersity index (PDI) of 0.157 ± 0.161, indicating sample homogeneity. Comprehensive data on mean size, PDI, and zeta potential are presented in **Table S3**. Cryo-TEM and TEM techniques were used to visualize the morphological structure of L-ONB **(Fig. 4.1 G and 4.1 H)**. An increase in the mean diameter of L-ONB serves as an acoustic trigger for drug release. We performed the oxygen release kinetics study [32] and calculated the dissolved oxygen by monitoring the oxygen release from L-ONB in hypoxic solutions at two different pH levels. Before L-ONB injection, the oxygen concentration in deoxygenated water was 0.35 ± 0.21 mg/L at pH 7.4 and 0.4 ± 0.07 mg/L at pH 4.4. After L-ONB injection, a time-dependent increase in oxygen concentration was observed, reaching a plateau after 12 hours at pH 4.4 and 55 hours at pH 7.4 **(Fig. 4.1 I)**. Oxygen release was higher at low pH due to a higher gas mass transfer rate as the zeta potential decreases with pH. Intracellular oxygen levels in cancer cells showed greater oxygen uptake in L-ONB-treated cells compared to ONB-treated ones **(Fig. 4.1J)**. FITC-labelled L-ONBs were used to confirm delivery to MDA-MB-231 cells, showing internalization through cytoplasmic green fluorescence signals **(Fig. 4.1 K-L)**. To explore tumor-targeting specificity, 3D lung and breast tumor spheroid models were treated with FITC-tagged L-ONBs, showing significant accumulation in immunofluorescence analysis **(Fig. 4.1 M-N)**. The indirect method of oxygen release from L-ONB was examined by quantifying HIF-1α gene expression in hypoxic MDA-MB-231 cells treated with L-ONB, showing a significant reduction, indicating effective oxygen release and its utilization. Moreover, L-ONB stability was assessed in water, PBS, and FBS over 15 days using DLS, zeta potential measurements, and Cryo-TEM imaging. Interestingly, the particle size and zeta potential values of L-ONBs exhibited minimal changes over time from day 0 to day 15 in water, PBS, and FBS **(Fig. 4.1 O-P)**. This stable size and zeta potential profile may be attributed to the use of DPPC lipid, known for its high phase transition temperature. Cryo-TEM imaging at days 0 and 10 **(Fig. 4.1 Q)** further confirmed no significant morphological changes in L-ONBs over time.

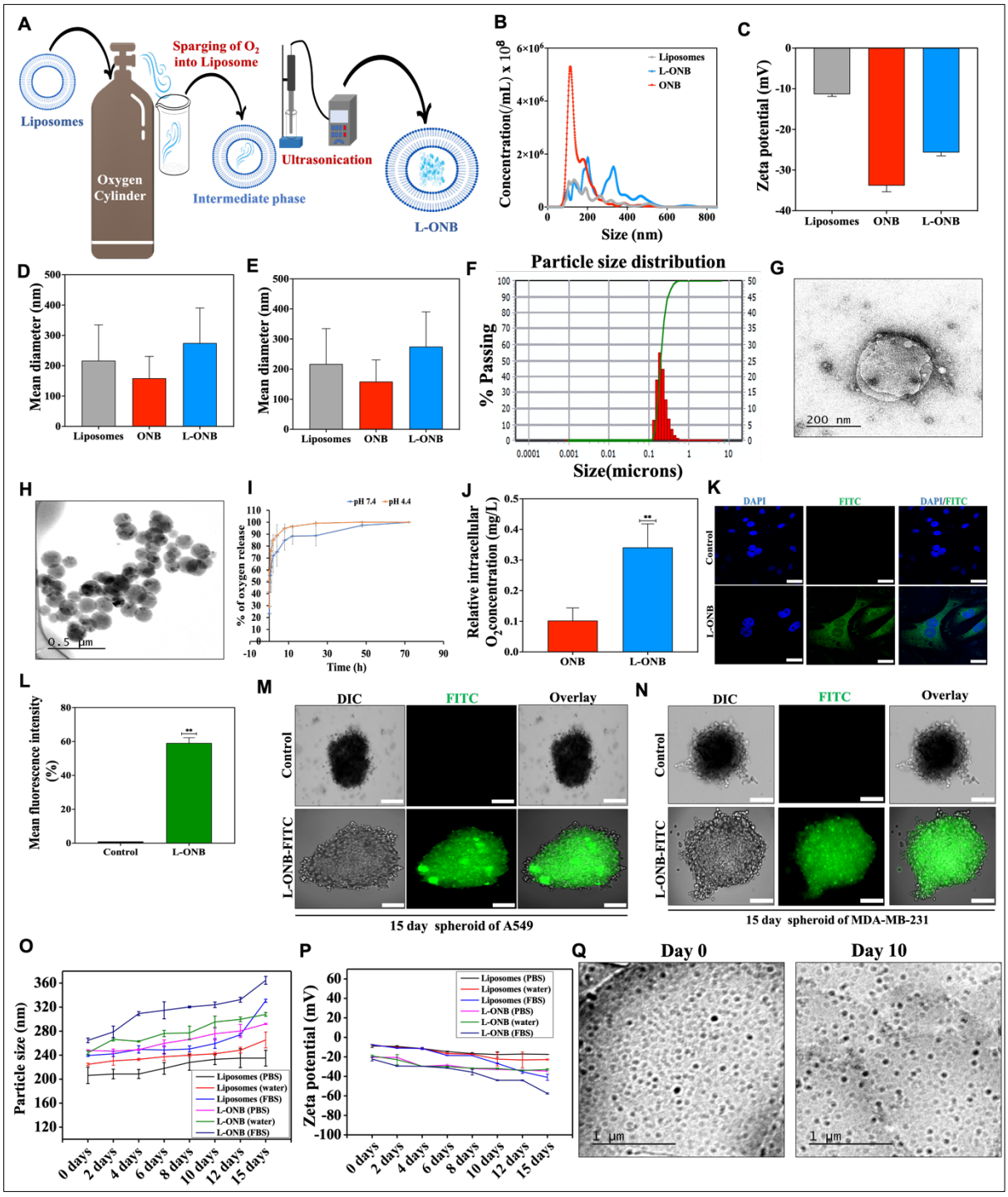

Figure 4.1: Synthesis and fabrication of liposomes, ONB, and L-ONB and their characterizations*; (A) Schematic diagram of L-ONB generation system. (B) Measurement of bubble size distributions of liposomes, ONBs, and L-ONBs by NTA analysis. (C) Zeta potential estimation by Zetasizer. (D, E) The mean bubble diameter and bubble number density of liposomes, ONB, and L-ONBs by NTA analysis. (F) Dynamic light scattering characterization of L-ONB using Microtrac/Nanotrac Flex. (G) Cryo-TEM image of L-ONBs. (H) TEM image of L-ONB. (I) In vitro oxygen release kinetics assay of the L-ONBs under hypoxic condition incubated at pH 7.4 and 4.4 at different time interval (0 min., 5 min., 10 min., 30 min., 1 h, 2 h, 4 h, 8 h, 12 h, 24 h, 48 h, and 72h) (J) Intracellular oxygen level of ONB and L-ONB treated MDA-MB-231 cells at 24*

*h. (K, L) Confocal laser microscopy images and the quantification of mean fluorescence intensity showing subcellular localization of L-ONB-FITC in the MDA-MB-231 cells treated with FITC-labelled L-ONBs for 8 h (Magnification, 40x). DAPI was used for nuclear counterstaining. (M, N) Fluorescence microscopy images of cellular uptake of untreated and L-ONB-FITC treated 3D spheroids of A549 (M), and MDA-MB-231 cells (N) Scale bar, 250 µm; Magnification 20x. (O, P) A line graph of DLS (Dynamic Light Scattering) for size analysis (O) and Zeta potential (P) for particle charge of Liposome and L-ONB in PBS, water and FBS at different time interval. (Q) Cryo-TEM image of L-ONB at day 0 and day 10; Scale bar, 1µm. Scale bar, 20 µm. Data are expressed as mean ± SD of three independent experiments (n = 3), and #p<0.05; *p<0.01; and **p<0.001 were considered significant difference.*

4.2.2 L-ONB destabilizes hypoxia-induced HIF-1α in cancer cells, enhancing ROS generation and cytotoxicity

In solid tumors, cells deprived of oxygen exhibit hypoxia, a key factor driving tumor progression and metastasis [1-3,40]. Under hypoxic conditions, the transcription factor HIF-1α is stabilized and translocated to the nucleus, where it forms a heterodimer with ARNT (Aryl Hydrocarbon Receptor Nuclear Translocator). This complex binds to the hypoxia response element (HRE) of target genes, influencing their expression [5-7,41]. Recently, *in vitro* 3D tumor spheroid models have gained popularity for their ability to mimic many *in vivo* solid tumor features, including a hypoxic core zone [1,3,5]. Using MDA-MB-231 cells, 3D breast tumor spheroids were developed to simulate the hypoxic core and assess the efficacy of L-ONB in reducing hypoxia. A live/dead assay confirmed the viability and plasma membrane integrity of the tumor spheroids, (**Fig. 4.2 A**) while image-iT green hypoxia staining demonstrated hypoxia induction in MDA-MB-231 monolayer cells and spheroids under 1% oxygen conditions. After an 8 h incubation with 20% L-ONB under 1% oxygen conditions, a significant reduction in hypoxia was observed, as shown by image-iT green hypoxia staining in **Fig. 4.2 B-D.**

Comparative analysis of L-ONB's effect on HIF-1α gene and protein levels was conducted in both A549 and MDA-MB-231 cells. Significant down-regulation of HIF-1α gene and protein expression was observed in these hypoxic lung and breast cell lines treated with L-ONB (**Fig. 4.2 E, F**). Additionally, cells preincubated with the proteasomal inhibitor MG132 [11] followed by L-ONB treatment showed restored HIF-1α protein levels in both cell lines, suggesting that L-ONB induces HIF-1α destabilization (**Fig. 4.2 G**). Persistent hypoxia leads to inefficient electron transfer in the electron transport chain due to the lack of oxygen molecules at the mitochondria, resulting in the accumulation of reactive oxygen species (ROS), which can cause irreversible cellular damage [42]. Therefore, the effect of L-ONB on cellular ROS production was analyzed [44,52]. The DCFDA staining results showed a significant increase in ROS generation (27.5 ± 2.3%) in hypoxic A549 cells treated with L-ONB, (**Fig. 4.2 H**) potentially contributing to cancer cell death.

A study by Chen SY et al. (2021) indicated that non-small cell lung adenocarcinoma A549 cells become more aggressive under oxygen-deficient conditions and can metastasize. Hyperbaric oxygen treatment

not only improves tumor hypoxia but also suppresses tumor growth in murine xenograft models [43,44]. Thus, this study aimed to evaluate the cytotoxic potential of L-ONB against cancer cells. MTT cell viability assays performed on A549 and MDA-MB-231 cells with varying concentrations of L-ONB revealed a significant reduction in cell viability: 58.06 ± 6.12% and 54.57 ± 3.87% in A549 cells, and 66.28 ± 2.06% and 63.72 ± 4.29% in MDA-MB-231 cells, after 24 and 48 hours of treatment, respectively (**Fig. 4.2 I-J**). In contrast, normal mouse fibroblast L929 cells showed no significant viability reduction (**Fig. 4.2 K**). Collectively, these results demonstrate that L-ONB delivery destabilizes HIF-1α in A549 and MDA-MB-231 cells, leading to increased ROS production and cancer cell death.

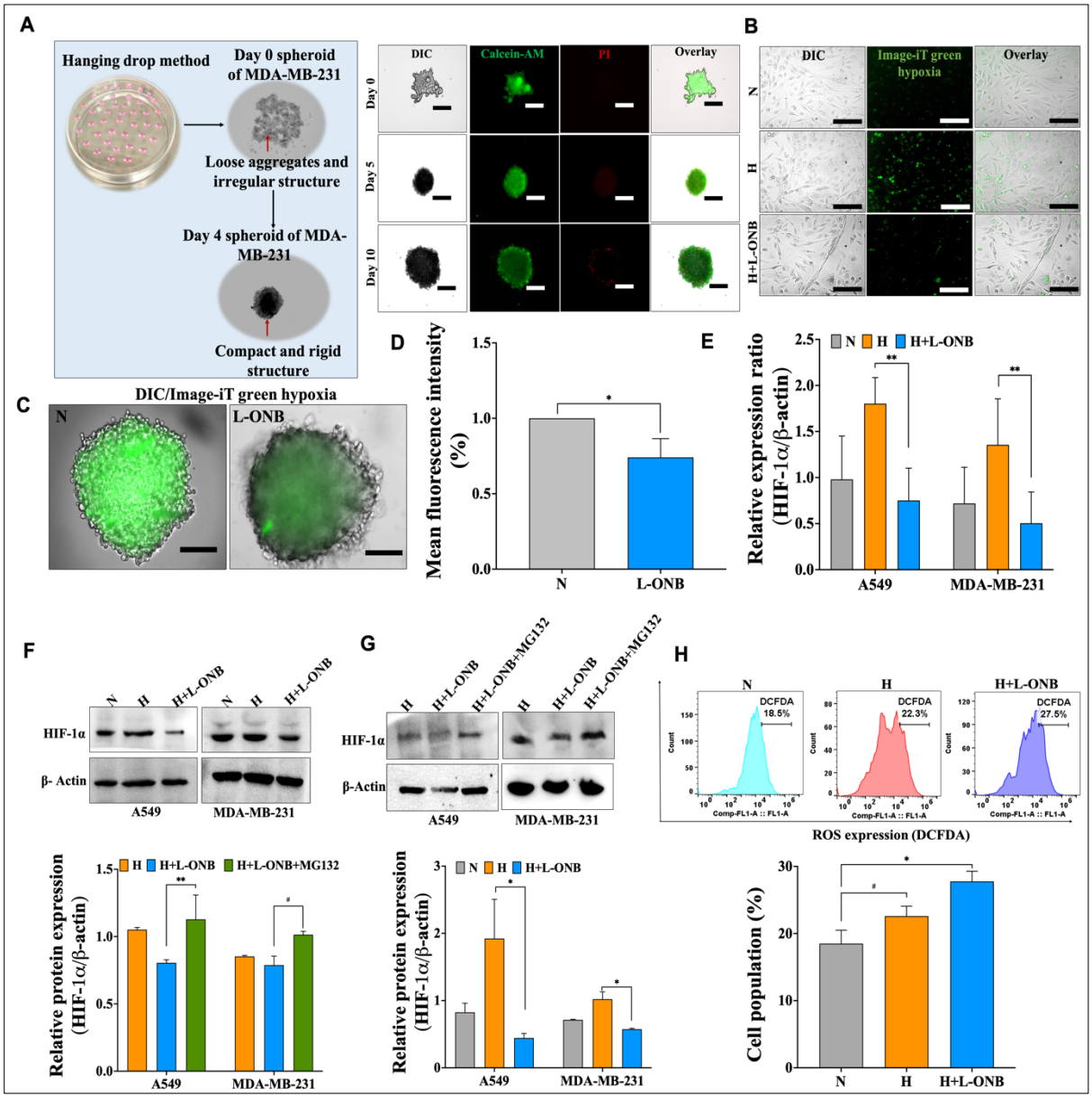

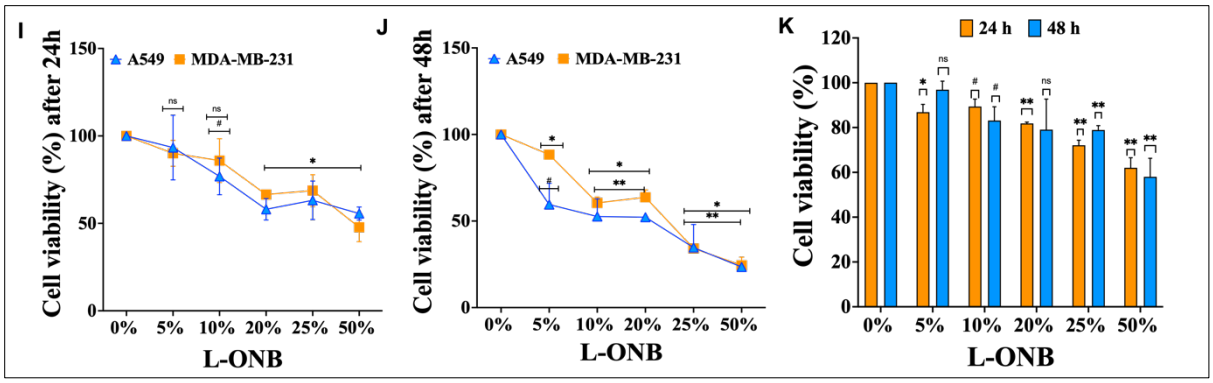

Figure 4.2: The uptake of L-ONB destabilizes HIF-1α, and induces ROS production in hypoxic A549 and MDA-MB-231 cancer cells; *(A) Schematic representation of 3D spheroid preparation of MDA-MB-321 by hanging drop method at day 0 and day 4 (left panel). Fluorescence microscopic images (20x) demonstrating viability of 3D unicellular spheroid of MDA-MB-231 cells at day 0, day 5 and day 10 by live/dead assay (right panel). Scale bar, 200 µm (B-D) Fluorescence microscopy images (20x) of Image iT green hypoxia staining of MDA-MB-231 cells exposed to normoxia (N) or hypoxia (H) or hypoxia with 20% L-ONB (H+L-ONB) for 24 h (B) (Scale bar: 100 µm); and N and L-ONB treated of 3D unicellular spheroid of MDA-MB-231 of day 10 (C) and their quantifications (D) Scale bar, 280 µm. (E) RT-qPCR analysis of HIF-1α gene expression in A549 and MDA-MB-231 cells treated with N, H, and H+L-ONB. (F, G) Western blot analysis of HIF-1α protein and its quantification in presence or absence of MG132 treated A549 and MDA-MB-231 cells. β-actin served as loading control. (H) Flow cytometric analysis of ROS production in A549 cells treated with N, H, and H+L-ONB at 24 h by measuring the DCFDA levels. (I-J) MTT assay exhibiting concentration-dependent alteration of A549 and MDA-MB-231 cells viability when exposed to L-ONB for 24 h (I) or 48 h (J). (K) Cell cytotoxicity assay of concentration-dependent alteration of L929 cells viability at 24 h and 48 h.Data are expressed as mean ± SD of three independent experiments (n = 3), and #p<0.05; *p<0.01; and **p<0.001 were considered as significant difference.*

4.2.3 L-ONB reduces hypoxia-induced tumor aggressiveness in lung and breast cancer cells by modulating the EMT pathway

Hypoxia-driven epithelial-to-mesenchymal transition (EMT) plays a crucial role in cancer progression, where epithelial cells gain mesenchymal characteristics and increased invasiveness. This process enhances tumor aggressiveness by increasing the invasiveness and metastatic potential of solid tumors [44-48]. Given that L-ONB significantly reduced HIF-1α expression, we investigated its effect on hypoxia-mediated tumor aggressiveness and the gene expression profile of epithelial (E-cadherin) and mesenchymal markers (N-cadherin, Fibronectin, Vimentin, and Snail) using the RT-qPCR assay. L-ONB treatment resulted in a significant increase in E-cadherin gene expression in hypoxic A549 and MDA-MB-231 cells **(Fig. 4.3 A)**, while the expressions of N-cadherin, Fibronectin, Vimentin, and Snail were significantly suppressed (**Fig. 4.3 B - E**). Immunoblot analyses confirmed these findings, showing increased E-cadherin protein levels and reduced vimentin protein levels in hypoxia-exposed, L-ONB-treated cells (**Fig. 4.3 F - G**), indicating that L-ONB delivery mitigates the hypoxia-induced EMT

pathway. Additionally, transwell and wound scratch assays demonstrated that L-ONB treatment significantly inhibited the invasion and migration of A549 and MDA-MB-231 cells under hypoxic conditions (**Fig. 4.3 H - K**), suggesting L-ONB's potential to reduce cancer cell migration and invasion in a hypoxic microenvironment.

To further explore the effect of L-ONB on HIF-1α-activated TGF-β and VEGFA expressions, which promote tumor progression and metastasis through the activation of the Smad pathway [39,58-60], we conducted a series of *in vitro* and *in vivo* experiments. L-ONB treatment significantly suppressed HIF-1α-induced TGF-β and VEGFA gene expressions in hypoxic A549 and MDA-MB-231 cells compared to the control (**Fig. 4.3 L - M**). Notably, L-ONB treatment caused significant changes in pSmad2/3 protein deactivation in hypoxic A549 cells, with a slight downregulation observed in MDA-MB-231 cells (**Fig. 4.3 N - O**), suggesting the involvement of the pSmad2/3 pathways in mediating L-ONB's effects.

Collectively, these findings indicate that L-ONB holds significant potential for mitigating the epithelial-to-mesenchymal transition (EMT) and inhibiting the migratory behaviour of cancer cells. Furthermore, to evaluate the combined effect of L-ONBs on tumor treatment, we selected doxorubicin, an anthracycline class chemotherapeutic agent known for effectively inhibiting the transcriptional activity of HIF-1α [49,50] and enhancing the sensitivity of hypoxic tumor cells to chemotherapy. We observed a significant increase in doxorubicin's cytotoxic effect in the presence of L-ONBs in A549 and MDA-MB-231 cells (**Fig. 4.3 P**). Additionally, we investigated the combined effect of doxorubicin and L-ONBs on the gene expression of HIF-1α, E-cadherin, vimentin, TGF-β, and VEGFA in A549 and MDA-MB-231 cells, finding that doxorubicin's effects were significantly enhanced (**Fig. 4.3 Q - U**) in the presence of L-ONBs.

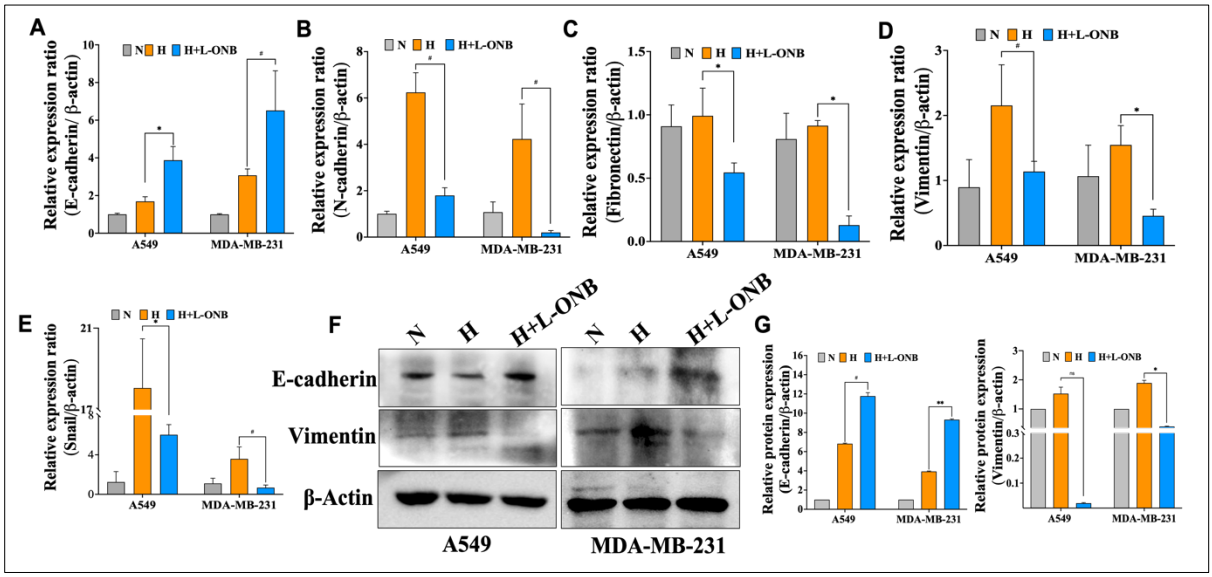

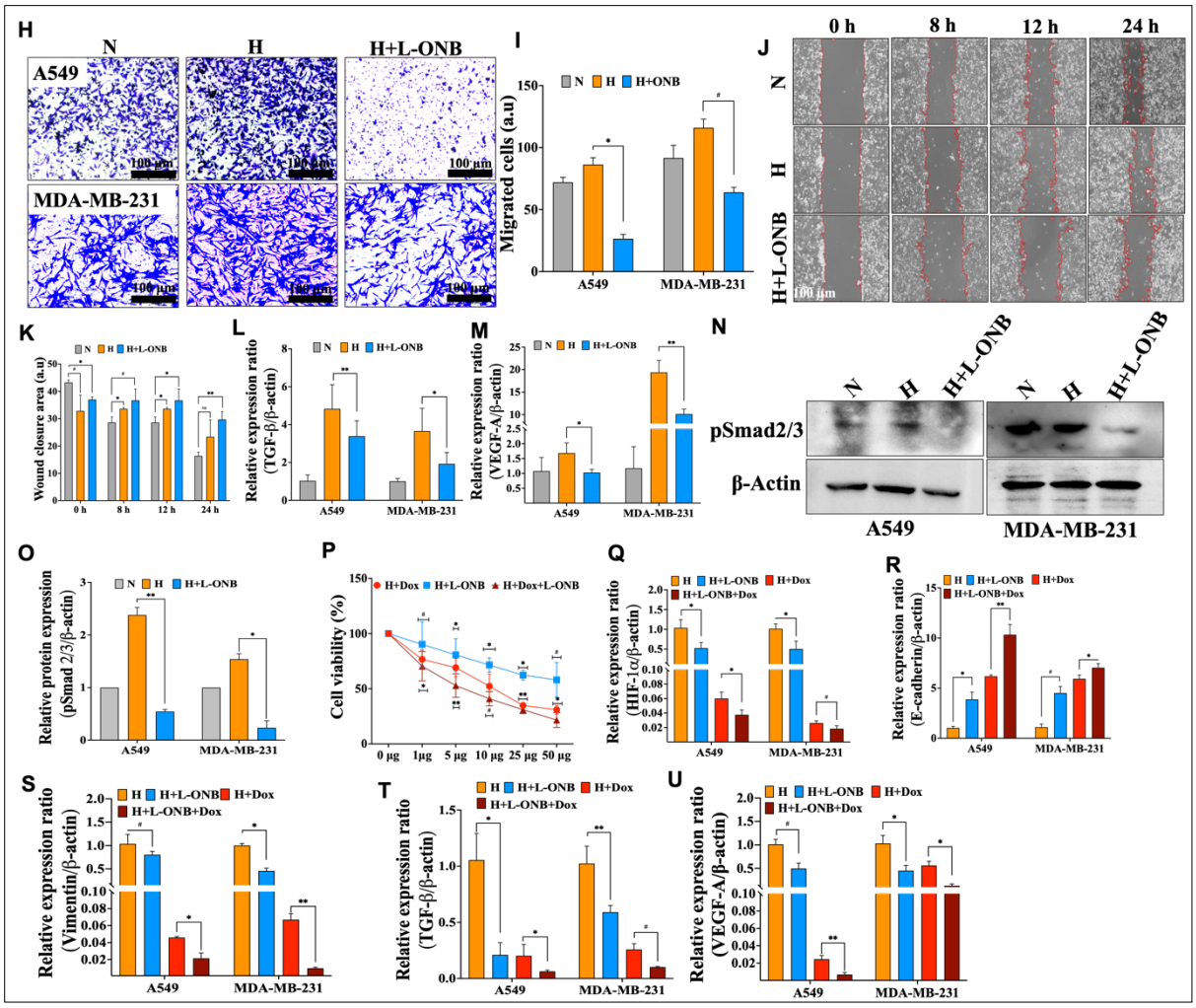

Figure 4.3: L-ONB treatment reverts hypoxia-induced tumor aggressiveness in A549 and MDA-MB-231 cell lines. *RT-qPCR analysis of epithelial marker E-cadherin (A) and mesenchymal markers N-cadherin (B), Fibronectin (C), Vimentin (D), and Snail (E) gene expressions in A549 and MDA-MB-231 cells exposed to N, H, and H+L-ONB at 24 h. Western blots analyses (F) and their quantifications (G) showing protein expression of E-cadherin and Vimentin proteins in N, H, H+L-ONB treated A549 and MDA-MB-231 cells at 24 h. β-actin served as loading control. (H, I) Trans-well migration and their quantifications in A549 and MDA-MB-231 cells treated with N, H, and H+L-ONB (Scale bar: 200 µm). (J, K) Wound scratch assay and their quantification showing migration potential of MDA-MB-231 cells exposed to N, H, and H+L-ONB for 0 h, 8 h, 12 h, and 24 h at 20x (Scale bar: 100 µm). RT-qPCR analysis of TGF-β (L) VEGF-A (M) of N, H, and H+L-ONB treated A549 and MDA-MB-231 cells at 24 h. (N-O) Western blot analysis (N) and their quantifications (O) showing pSmad2/3 levels in A549 and MDA-MB-231 cells treated with N, or H, or H+L-ONB for 24 h. β-actin served as loading control. (P) Cell cytotoxicity assay of H+Dox, H+L-ONB, and H+L-ONB+Dox treated A549 cells for 24 hours at different Dox concentrations shown on the X axis, and 20%-L-ONBs concentration were utilised. (Q-U) RT-qPCR analysis of HIF-1α (Q), E-cadherin (R), VIM (Vimentin) (S), VEGF-A (T) and TGF-β (U) genes in A549 and MDA-MB-231 treated cells with H, H+L-ONB, H+Dox and H+L-ONB+Dox respectively. (H = Hypoxia, L-ONB= Liposomal oxygen nanobubble,*

*Dox = Doxorubicin). Data are expressed as mean ± SD of three independent experiments (n = 3), and #p<0.05; *p<0.01; and **p<0.001 were considered significant difference.*

4.2.4. L-ONB reduces growth of lung and breast tumors in zebrafish and mouse models

To assess the therapeutic potential of L-ONB in lung adenocarcinoma (LUAD) tumorigenesis, an adult zebrafish tumour xenograft model with A549 cells was developed. The adult zebrafish tumor xenograft model offers an *in-vivo* approach for high-throughput screening of potential anti-cancer compounds [51-54]. In this model, significant reductions in tumor size and weight were observed in L-ONB treated zebrafish compared to those treated with liposomes (**Fig. 4.4 A - C**). The L-ONB treated group also showed a substantial decrease in HIF-1α gene expression, accompanied by a significant increase in E-cadherin gene expression and suppression of N-cadherin and vimentin compared to the liposome and control groups (**Fig. 4.4 D**). These results highlight the efficacy of L-ONB in reducing LUAD in the zebrafish xenograft model. Subsequently, we examined the effects of L-ONB in an in-vivo 4T1 BALB/c breast tumor xenograft model. The experimental protocol, study duration, and treatment regimen for L-ONB compared to the vehicle (control) and bare liposomes are depicted in the **Fig. 4.4 E**. Significant reductions in tumor size, weight, and volume were observed in L-ONB treated mice over a 14-day period, (**Fig. 4.4 F - H)** without any notable changes in body weight between treated and control animals. RT-qPCR analysis revealed a marked down-regulation of HIF-1α, TGF-β, VEGFA, and Vimentin gene expressions, alongside an up-regulation of E-cadherin gene expression in tumor samples from the L-ONB treated group compared to the liposome and control groups (**Fig. 4.4 J**). Immunoblot analysis corroborated these findings, showing increased levels of E-cadherin protein and decreased levels of HIF-1α, Vimentin, and pSmad2/3 proteins in tumor samples (**Fig. 4.4 K - N)** from the L-ONB treated group.

To further investigate L-ONB's efficacy in metastasis attenuation, we collected spleen, lung, liver, and kidney tissues from untreated and L-ONB-treated 4T1 tumor-bearing mice for hematoxylin and eosin (H&E) and immunohistochemistry (IHC) staining. Histological examination of tumor tissues from untreated mice revealed poor differentiation, considerable pleomorphism, and inflammatory cell infiltration, characteristic of aggressive cancer tissues [47]. In contrast, tumor sections from L-ONB-treated mice displayed inflammatory edema and nuclear fragments (**Fig. 4.4 O**), indicating cytotoxic effects leading to cancer cell death. In order to determine the protein level of treated and untreated section of tumor tissue, therefore immunostaining for HIF-1α, E-cadherin, and Vimentin were performed and showed decreased intensity for HIF-1α and Vimentin proteins, and increased intensity for E-cadherin (**Fig. S 4.4 Q, R**) in L-ONB-treated tumor tissues compared to controls.

Histopathological analysis of spleen, lung, liver, and kidney sections from control 4T1 tumor-bearing mice revealed unusual pleomorphism, whereas sections from L-ONB-treated mice exhibited inflammatory edema, severe necrosis, fibrosis, and nuclear fragments (**Fig. 4.4 P** and **Fig. 4.4 S)**.

Collectively, these findings suggest that L-ONB treatment not only reduced tumors by targeting HIF-1α-mediated EMT but also inhibited organ metastasis in the *in-vivo* mice xenograft model, underscoring L-ONB's therapeutic potential for managing lung and breast cancers.

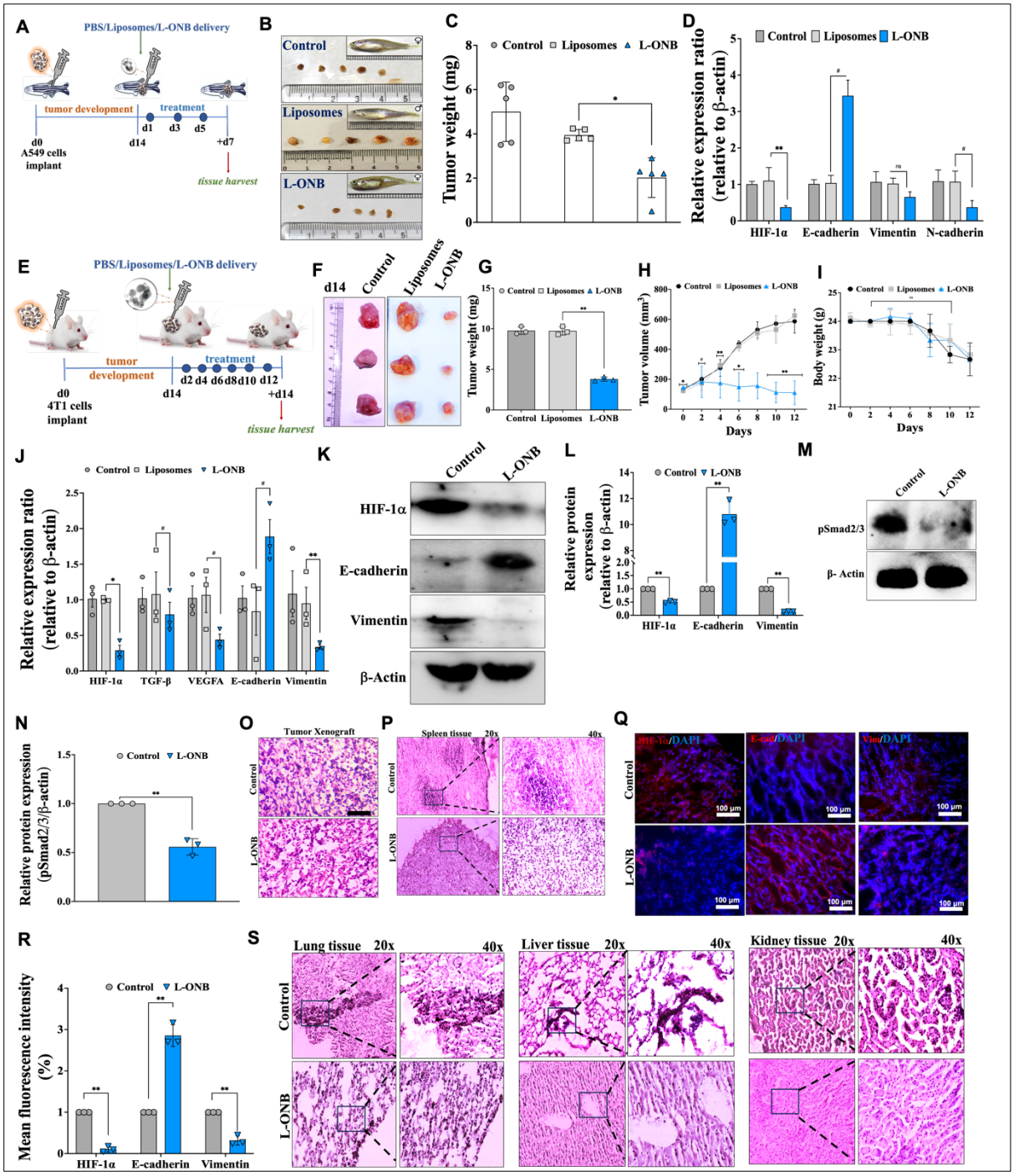

Figure: 4.4: The administration of L-ONB results in regression of lung and breast tumor growth in zebrafish and BALB/c tumor xenograft models; *(A) The schematic diagram explains experimental design with zebrafish lung tumor xenograft model treated with control (PBS), or liposomes (bare liposomes), or L-ONB. (B-C) Photographic tumor images and of lung tumor xenograft zebrafishes (B), and bar diagram representing tumor weight of control and L-ONB treated groups. (D) RT-qPCR analyses of HIF-1α, E-*

*cadherin, Vimentin, and N-cadherin gene expressions in control and L-ONB treated tumor. (E) Schematic diagram of the experimental design of 4T1 breast tumor xenograft model in BALB/c mice treated with either control (PBS) or liposomes (bare liposomes), or L-ONB for 14 days, (F) photographic images of respective tumors, (G) tumor weight, (H) tumor volume and (I) body weight of control (PBS), liposomes (bare liposomes), and L-ONB treated BALB/c tumor xenograft mice. (J) RT-qPCR analyses of HIF-1α, TGF-β, VEGF-A, E-cadherin and Vimentin gene expressions of tumor samples. (K, L) Western blot analysis of HIF-1α, E-cadherin, and Vimentin proteins in the tumor tissue samples (K) and its quantification (L). (M,N) Western blot analysis and (M) its quantification (N) of pSmad2/3 in the control and L-ONB treated tumor tissue samples of 4T1 tumor xenograft BALB/c mice. β-actin used as loading control. (O) Haematoxylin and eosin (H&E) staining of 4T1 tumor tissue sections of control and L-ONB treated sample. (P) H&E-stained images of spleen tissue sections (20x and 40x); Scale bars: 50 µm, 200 µm. (Q, R) Immunofluorescence staining of HIF-1α, E-cadherin, and Vimentin proteins in tumor tissue sections, mice treated with control or L-ONB for 14 days (Q) and their quantification (R). (S) H&E stained images of lung, liver, and kidney tissue sections (20x and 40x). Data are expressed as mean ± SD (n = 3) of each group, and #p<0.05; *p<0.01; and **p<0.001 were considered as significant difference.*

4.3 Discussion

Recent rise in the importance of oxygen nanobubbles (ONBs) is attributed to their potential in various medical and therapeutic applications. Various research groups have developed ONBs alone or combined with other compounds or drugs to enhance tissue oxygenation and deliver therapies for managing different cancers in *in vivo* models [18,28,30,55]. Bhandari et al., (2017) reported that hypoxic tumor regions contain hypomethylated sites at 5-methylcytosine (5mC), which can be effectively reversed with ONBs, thus enhancing cancer treatment by modulating epigenetic regulation [42]. Compared to oxygen microbubbles (OMBs) and haemoglobin-based oxygen carriers (HBOCs), ONBs offer significant advantages: (i) their smaller size facilitates efficient passage through tumor vasculature with increased permeability and retention (EPR) effects, and (ii) they have extended intravascular dwell times for precise tumor targeting [33,57]. Despite these benefits, ONBs face instability in solutions over time, limiting their clinical applicability. Addressing the challenge of fabricating stable ONBs is essential due to the significant pressure gradient and surface tension that currently limit their stability, potentially compromising effective oxygen delivery at tumor sites. Wu et al., (2021) highlighted the potential of oxygen microcapsules as an effective strategy for targeting tumors. Oxygen microcapsules combined with gemcitabine have been used to target hypoxia in pancreatic cancer [58]. Additionally, modified oxygen microcapsules have shown promise in enhancing immune checkpoint blockade by alleviating hypoxia in pancreatic ductal adenocarcinoma [59]. In our study, we developed liposome-encapsulated oxygen nanobubbles (L-ONB), utilizing only oxygen nanobubbles to target hypoxia in various tumors. L-ONBs provide a larger surface area and greater

colloidal stability compared to other oxygen bubble systems. Our formulation involves entrapping oxygen nanobubbles within liposomes composed of dipalmitoyl phosphatidylcholine (DPPC) and cholesterol. DPPC has a high phase transition temperature, while cholesterol maintains structural integrity and strengthens the lipid bilayer, reducing fusion and aggregation of liposomes. Due to their nano-dimensions, L-ONBs are expected to target tumors more efficiently via the EPR effect. Encapsulating oxygen nanobubbles within liposomes provides protection and stability, allowing for sustained release over time.

Our investigation also highlighted the potent therapeutic potential of L-ONB as an anti-cancer agent. *In-vitro* analysis of O2 release kinetics and efficient delivery of FITC-labelled L-ONB to MDA-MB-231 cancer cells underscored its promise as an anti-cancer agent. L-ONB delivery effectively inhibited hypoxia-induced tumor aggressiveness by mitigating EMT and cancer cell migration through the destabilization of HIF-1α. Furthermore, histopathological examinations using hematoxylin and eosin (H&E) staining of spleen, lung, liver, and kidney tissues demonstrated the efficiency of L-ONB in attenuating breast cancer metastasis in the 4T1 BALB/C mice model. These collective findings emphasize the therapeutic efficacy of L-ONB in combating hypoxia-associated adverse effects.

To date, no studies have explored the effect of L-ONB in the HIF-1α-mediated epithelial-to-mesenchymal transition (EMT), either *in vitro* or *in vivo*. We are the first to elucidate the mechanistic action of L-ONB in significantly inhibiting hypoxia-induced tumor aggressiveness, and metastasis of cancer cells through disturbing HIF-1α – TGFb/VEGF pathway. Therefore, our fabricated L-ONB emerges as a highly promising adjuvant therapeutic candidate for solid tumor therapy, offering considerable potential for clinical application.

4.4 Materials and Methods

4.4.1 Reagents and Antibodies: The list of all antibodies and reagents provided in Tables A and C (Appendix).

4.4.2 Fabrication of oxygen nanobubbles (ONB), liposome, and liposomes encapsulated ONB (L-ONB)

Ultrapure water from a Milli-Q purification system (conductivity: 1.055 $\mu S.cm^{-1}$, pH: 6.85, surface tension: 71.89 mN/m at 20 °C) was used to synthesize oxygen nanobubbles (ONB), liposomes, and liposome-encapsulated ONBs (L-ONB). An in-house setup with a gas regulator and flow meter was used to generate nanoscale bubbles. O_2 gas (>99.5% purity) and ultrapure water were used as the gas and liquid phases. Compressed O_2 at 2 bar pressure was diffused through nanopores into the liquid to create bulk ONBs. Liposomes were fabricated using the thin film hydration method. DPPC (25 mg/mL) and cholesterol were mixed in a 2:1 molar ratio, dissolved in chloroform, and dried to a thin film using a rotary evaporator. The film was rehydrated with PBS above the lipid transition temperature using a

bath sonicator. The solution was extruded through a 0.1 μm polycarbonate membrane. For L-ONB fabrication, the liposome solution was sparged with O_2 gas and ultrasonicated (20 kHz, 750W, 60% amplitude) for 5 min. The L-ONBs were characterized by DLS, NTA, and TEM.

4.4.3 Characterization of L-ONBs using nanoparticle tracking analysis and zetasizer

The bubble size distribution and concentration of fabricated liposomes, ONBs, and L-ONBs were analyzed using NTA (NanoSight NS 300) with a 405 nm laser, 20x microscope objective, and sCMOS camera. The hydrodynamic diameter was calculated using the Stokes-Einstein equation given below:

$$D_t = \frac{k_B T}{3\pi\eta d} \quad \text{----------(1)}$$

where, k_B, T, and η are Boltzmann constant, temperature, and liquid viscosity, respectively. Samples were diluted 1:10 for measurements. Mean size, polydispersity index (PDI), and surface charge (ζ-potential) were measured using a Zetasizer (Nano ZSP) with a 633 nm laser. Zeta potential is influenced by pH, ionic strength, and temperature based on the interaction of particles with counter-ions and co-ions.

4.4.4 Transmission electron microscopy (TEM)

Nested-nanobubbles (Nested-NBs) in drug-loaded liposomes were characterized using TEM [20,33]. TEM samples for L-ONBs were prepared with negative staining using a 1% uranyl acetate solution, followed by placing 2 μL of the sample onto holey carbon-coated grids. Images were taken at high magnification using a Tecnai-G2 12 TWIN TEM (120 KV) and analyzed with ImageJ software to determine particle diameter.

4.4.5 Cryo-Transmission electron microscopy (Cryo-TEM) imaging

Briefly, 5 μL of ONB was applied on Quantifoil holy carbon EM grids (R2/2, 400 mesh; EMS) before and after ultrasound disruption. The samples were vitrified within an hour of sonication. TEM grids were glow-discharged for 30 seconds at 15 mA, blotted, and plunged into liquid ethane. Cryo-TEM grids were scanned using a JEOL 2200FS transmission electron microscope with a Tietz TVIPS 4k CMOS camera at 200 kV. Micrographs were taken with a total electron dosage of 60 e/A² and a defocus range of 4 to 4.5 μm. A total electron dose of 900 e/A² was dispersed over 45 frames, with each frame exposed for 800 ms over 40 s. ImageJ software was used for image analysis.

4.4.6 *In vitro* oxygen release

Oxygen release from liposomal ONBs was determined using a dissolved oxygen meter. A 20 ml saline solution was deoxygenated with N_2 gas, and 3 ml of liposomal solution was oxygenated for 10 min and sonicated to prepare liposomal ONBs. The ONBs were mixed with deoxygenated water in a 1:9 ratio. Oxygen release was measured at various intervals up to 48 hours using a dissolved oxygen meter (Hanna #H198198) at pH 7.4 and pH 4.

4.4.7 Cell culture

Human lung adenocarcinoma A549, human triple-negative breast adenocarcinoma MDA-MB-231, and mouse fibroblast L929 cell lines were obtained from the NCCS, Pune, India. A549 and L929 cells were cultured in a complete RPMI 1640 growth medium supplemented with 10% FBS, and penicillin (10,000 units/ml)-streptomycin (10 mg/ml) solution in a humidified incubator supplied with 5% CO_2 at 37 °C. MDA-MB-231cells were cultured in a complete growth medium of Leibovitz's L15 with 2 mM glutamine supplemented with 10% FBS, and penicillin (10,000 units/ml)-streptomycin (10 mg/ml) solution in a humidified incubator supplied with 5% CO_2 at 37 °C.

4.4.8 *In vitro* measurement of the relative intracellular oxygen concentration

MDAMB231 cells were seeded into a 35-mm dish and treated with ONB and L-ONB for 24 h. The cells were trypsinized, collected in microcentrifuge tubes, washed with 1x PBS, and resuspended in 3 ml of cell culture media. Cells were lysed by ultrasonication to measure relative intracellular oxygen concentration using a dissolved oxygen meter.

4.4.9 3D unicellular spheroid preparation

The hanging drop method was used to prepare unicellular 3D tumorigenic spheroids of MDA-MB-231 cells in a 90 mm culture dish [61]. MDA-MB-231 cells were cultured in complete growth medium in T25 flasks. At 80-85% confluency, cells were washed with PBS, treated with Trypsin-EDTA (0.25%) for 3-4 min at 37 °C, neutralized with 4 ml growth medium, and collected in a 15 ml falcon tube. After centrifugation at 800 rpm for 5 min, cells were resuspended in DMEM complete medium. Approximately 10,000 cells/ml were dispensed as 25 µl drops onto the lid of a 90 mm dish, which was then placed on a plate with 6 ml autoclaved water at the bottom. The setup was incubated at 37 °C with 5% CO_2 for 3 days. Spheroids were monitored under a microscope for cell aggregation and proliferation. For cell viability, a live/dead assay was performed on days 5 and 10. Five spheroids were collected, washed with PBS, and incubated with calcein-AM (100 µM) and propidium iodide (750 µM) for 10 min. Spheroids were washed with PBS, placed on a 35 mm dish, and imaged using an inverted fluorescence microscope (Leica DMi8, Germany).

4.4.10 Hypoxia induction

A549 and MDA-MB-231 cells were exposed to hypoxia (1% O_2, 5% CO_2) or normoxia conditions for 24 h at 37 °C using a HERACELL VIOSTM 160i incubator (Thermo Scientific).

4.4.11 Cellular uptake assay

MDA-MB-231 cells were cultured on 22 × 22 mm coverslips in 35 mm dishes. Cells were transfected with L-ONB (Control) or L-ONB-FITC at a 20% concentration in basal medium. Control cells remained untreated and were maintained in their respective basal media. After 8 h of transfection, cells were washed with PBS and stained with DAPI for nuclear staining for 5 min. Subsequently, cells were washed again with PBS and fixed using a 4% paraformaldehyde solution. After additional washing with 1X DPBS, cells on coverslips were mounted on slides using DPX medium. Images were acquired using

confocal laser microscopy (CLSM, Zeiss LSM 900 with Airyscan 2) at 40x and 63x magnification, capturing DAPI and rhodamine channels.

4.4.12 Measurement of hypoxia using Image-iT green hypoxia reagents

MDA-MB-231 cells were seeded in 35 mm dishes and exposed to three conditions: Normoxia (N, 5% O_2), Hypoxia (H, 1% O_2), and Hypoxia with Liposomal-oxygen nanobubbles (H+L-ONBs, 20%). After washing with 1X PBS, the cells and 3D spheroids (day 10, five each) were incubated in serum-free L15 medium containing 10 µM Image-iT green hypoxia reagent for 30 min and 1 h, respectively, in a humidified CO_2 incubator. Cells were then washed with 1X PBS and fresh culture media was added. Imaging was performed using a fluorescence microscope (Leica, DMi8, Germany) at 20x magnification in DIC and FITC channels (Ex/Em 498/517).

4.4.13 Quantitative Real time polymerase chain reaction (qPCR) assay: As described earlier in section 3.4.7

4.4.14 Immunoblot analysis

Control (N), hypoxia (H), and H+ONB treated cells were lysed using NuPAGE lysis buffer with protease and phosphatase inhibitors. Tissue samples from 4T1 BALB/c mice were lysed with RIPA buffer using the TissueLyser II instrument. Protein concentrations were measured by the BCA method. Western blot analysis was performed as previously described [42]. Briefly, cell/tissue lysates (50 µg protein) were subjected to 10% or 12.5% SDS-PAGE and transferred to PVDF membranes. Membranes were blocked with 5% BSA in TBS for 1 h, incubated overnight with primary antibodies at 4 °C, washed with TBST, and then incubated with peroxidase-conjugated secondary antibodies for 2 h at room temperature. After further washing, membranes were treated with Clarity Western ECL Substrate and protein bands were visualized and quantified using the Chemidoc XRS+ System and Image Lab Software.

4.4.15 Transwell migration assay

Transwell cell migration assays were conducted using 8.0 µm pore transwell inserts according to our established protocol [62]. Serum-starved A549 and MDA-MB-231 cells (5×10^4 cells/well) were incubated under hypoxia (H) with or without L-ONBs for 24 h. After incubation, cells were trypsinized and suspended in serum-free media. Cells were then placed in the upper chamber of transwell inserts, with the lower chamber containing media supplemented with 10% FBS, and incubated for 24 h. Following incubation, non-migratory cells on the upper surface of the membrane were removed by gentle scrubbing with a cotton swab. Cells that had migrated to the lower membrane surface were fixed with 2.5% glutaraldehyde for 10 min and stained with 0.5% crystal violet solution for 2 h. Bright-field images of migrated cells were captured using a microscope (Leica DMi8, Germany) at 200x magnification. The number of migrated cells was counted in at least 5 random fields for each membrane.

4.4.16 Wound scratch assay

The wound scratch assay [63] assessed cell migration in MDA-MB-231 cells (1×10^5 cells/well) seeded in 12-well plates and cultured until reaching 90% confluency. A straight scratch was made in each well using a sterile micropipette tip to simulate wound formation, followed by a wash to remove non-adherent cells. Cells were then treated with H alone, or H+L-ONB. Cell migration was monitored under a microscope, capturing images at 0 h, 8 h, 12 h, and 24 h intervals. Wound width was quantified using ImageJ 1.53k software, and wound healing percentage was calculated using the appropriate formula.

$$Wound\ healing\ (\%) = 1 - \frac{Wound\ width}{Wound\ width\ at\ 0\ h}\ X\ 100 \quad \text{.....(2)}$$

4.4.17 Cell cytotoxicity assay

Cancerous cells (A549 and MDA-MB-231) along with normal mouse fibroblast cells L929 were seeded in a 96-well plate at a concentration of 1×10^4 cells/ml and allowed to adhere overnight. The cells were then treated with various concentrations of L-ONB (0%, 5%, 10%, 20%, 25%, and 50%) in incomplete media for 24 h and 48 h. Additionally, different concentrations of doxorubicin (1 mg, 5 mg, 10 mg, 25 mg, and 50 mg) were used in this study. After incubation, 10 µl (5 mg/ml) of MTT solution was added to each well and incubated for 4 h. The supernatants were removed, and 100 µl of MTT solubilizing agent was added to dissolve the formazan precipitate. Cell viability was assessed spectrophotometrically by measuring absorbance at 570 nm using a Multiskan GO (Thermo Scientific, USA). Percentage cell viability was calculated by blanking absorbance values against acidic isopropanol, with absorbance of untreated cells considered as 100% cell viability (control).

$$Cell\ viability\ (\%) = \frac{OD\ test\ at\ 570nm - OD\ blank\ at\ 570\ nm}{OD\ control\ at\ 570nm - OD\ blank\ at\ 570nm} \times 100 \quad \text{.....(3)}$$

4.4.18 ROS measurement by flow cytometry

The oxidation-sensitive fluorescent probe, 2',7'-dichlorofluorescein diacetate (DCFH-DA), was used to detect the mitochondrial reactive oxygen species (ROS). DCFH-DA enters cells and is enzymatically converted to fluorescent 2',7'-dichlorofluorescin (DCF), which reacts with intracellular peroxides. Control and treated cells were exposed to 50 µM DCFH-DA and incubated in a dark, humidified incubator at 37 ºC for 60 min. Fluorescence intensity was measured using a flow cytometer (FACS Calibur, BD Bioscience) with FL-1 band pass filter and Cyflogic v.1.2.1 software, analyzing at an average of 10,000 events per determination.

4.4.19 Zebrafish tumor xenograft model and treatments

The fish (male and female, wild type strain) were kept in an automatic stand-alone housing system with autoclaved sterilized water containing penicillin and streptomycin solution at a constant temperature of 28 °C under a 14 h light/10 h dark cycle. All procedures regarding fish maintenance and experimentation were performed following the principles of Good Animal Practice guidelines. The study protocol and procedures were approved by the Institutional Animal Ethics Committee, University of Delhi (Protocol no: DU/KR/IAEC/ZF2021/1) and Institute Biosafety Committee (IBSC/1/2020/A/2). The fish were fed

three times daily with a commercially available dry fish feed (MicroMac, Aqua World, India). The zebrafish lung cancer xenograft model was developed following a modified protocol described previously [41,45,46]. Prior to A549 cell transplantation, immune suppression was induced by intraperitoneally administering caerulomycin at a dose of 100 mg/Kg body weight for three consecutive days and fish were maintained in water containing 1% penicillin and streptomycin. On the third day, 10^5 cells/fish were suspended in PBS and injected into the peritoneal cavity of the zebrafish using a 5µl Hamilton syringe (Hamilton, Nevada USA). Subsequently, fish were maintained in distilled water with 1% penicillin and streptomycin for the next 14 days to allow tumor xenograft development. On the 14th day post-injection, PBS or bare liposomes or liposomal ONBs (L-ONBs) at a dose of 0.5 mg/kg (100 µl) were administered intratumorally, and fish were sacrificed on day 7 post-treatment. Tumor tissue was obtained, tumor weight and size were measured, and photographs were taken (n = 5).

4.4.20 4T1 BALB/c mice tumor xenograft model

The study protocol and procedures for the experimentation on BALB/c mice were approved by the Institutional Animal Ethics Committee, Kirori Mal College, University of Delhi (Protocol no. DU/KR/IAEC/2019/10). The 4T1 cell line was purchased from the American Type Culture Collection (Manassas, VA, USA) [47 ,64]. The cells were cultured in RPMI-1640 media with L-glutamine supplemented with 10% fetal bovine serum (FBS) along with 0.11 mg/ml sodium pyruvate, 100 U/ml penicillin, and 100 µg/ml streptomycin (Biological Industries, Israel) at 37 °C in a humidified CO_2 incubator. Female BALB/c mice (aged 6-8 weeks and weighing 20-24 g) were injected subcutaneously with 1 x 10^6 4T1 breast cancer cells into the mammary fat pad. After 14 days, the tumor size was measured, with each 4T1 BALB/c mouse having a tumor size ranging from 90-120 mm^3. PBS or Bare liposomes or Liposomal ONBs (L-ONBs) were administered intratumorally to mice at a dosage of 0.5 mg/kg (100 µl) at 24 h intervals for a duration of 14 days. Following the completion of the treatment regimen, the mice were euthanized, and tumor tissues were collected for immunohistochemical staining. The tumor volume was calculated by the following formula

$$Tumor\ volume\ (mm)^3 = \frac{length \times width^2}{2} \quad \text{..... (4)}$$

Additionally, vital organs were harvested and subjected to hematoxylin-eosin (HE) staining for morphological examination. Thereafter, the mice were sacrificed, and the xenograft tumors were excised, weighed, and photographed.

4.4.21 Histological sections

4T1 tumor tissues from mice were fixed in 10% neutral buffered formalin, processed by dehydration in increasing ethanol concentrations (50%, 70%, 80%, 90%, and 100%) followed by the xylene treatment, and embedded in paraffin. The embedded samples were cooled and solidified, and paraffin blocks were prepared for further histological analysis.

4.4.22 Hematoxylin & eosin (H&E) staining

The paraffin blocks were sectioned in microtome (Leica, Germany) at approximately 5 micrometers thickness. Sections were placed onto glass slides. The slides underwent a series of steps- they were immersed three times in xylene solution for 5 min each, followed by a descending ethanol sequence (100% twice, 95% twice, 80%, and 70%). Next, the slides were washed with tap water and subjected to hematoxylin staining for 10 min. After rinsing with tap water for a while, the slides were briefly dipped in 0.3% acetic acid, washed with water, and replaced with 0.3% ammonia water. Subsequently, they were washed with water and then dipped into 80% alcohol. Following this, the slides were immersed in eosin for 5 to 10 sec and dehydrated with 95% and 100% ethanol for 20 sec each. They were then transferred to xylene for one min before a final wash in 100% ethanol. Finally, the slides were mounted using DPX

4.4.23 Immunohistochemistry (IHC) staining

Tissue sections were fixed with 100% methanol for 5 min at -20 °C, washed with PBS, and then permeabilized with 0.1% Triton X-100 in PBS (v/v) for 10 min at room temperature. To block non-specific binding, tissue sections were incubated with 1% BSA in PBS (w/v) containing 0.05% Tween (v/v) for 2 h at room temperature. The cells were then placed in a humidified chamber and incubated with primary antibodies (HIF-1α, 1:100 dilution; E-cadherin, 1:100 dilution; and Vimentin, 1:200 dilution) in 1% BSA in PBS containing 0.05% Tween overnight at 4 °C on a rotating platform. Afterwards, the slides were washed thrice with ice-cold PBST for 5 min each, followed by the incubation with Alexa Fluor 594-tagged anti-rabbit antibody (1:1 000) for 1 h at room temperature in the dark. Tissue sections were then washed thrice for 5 min each with ice-cold PBS and coverslips were mounted onto glass slides using VECTASHIELD HardSet™ Antifade Mounting Medium with DAPI. Cellular images were captured by an inverted fluorescence microscope (Leica DMi8, Germany) and image analysis was performed using LAS X software. Fluorescence intensity measurements were quantified using ImageJ software (1.48v, NIH, USA).

4.4.24 Statistical analysis

Data were obtained from three separate experiments and presented as the mean ± standard deviation of the mean. T-test was employed for comparison among multiple groups using GraphPad Prism 6 software. A value of $p<0.05$ was considered statistically significant.

References

1. Hanahan, D., & Weinberg, R. A. (2011). Hallmarks of cancer: the next generation. *cell*, *144*(5), 646-674.
2. Hockel, M., & Vaupel, P. (2001). Tumor hypoxia: definitions and current clinical, biologic, and molecular aspects. *Journal of the National Cancer Institute*, *93*(4), 266-276.
3. Benizri, E., Ginouves, A., & Berra, E. (2008). The magic of the hypoxia-signaling cascade. *Cellular and molecular life sciences*, *65*, 1133-1149.
4. Vaupel, P. (2004). The role of hypoxia-induced factors in tumor progression. *The oncologist*, *9*(S5), 10-17.
5. Rankin, E. Á., & Giaccia, A. J. (2008). The role of hypoxia-inducible factors in tumorigenesis. *Cell Death & Differentiation*, *15*(4), 678-685.
6. Harris, A. L. (2002). Hypoxia—a key regulatory factor in tumour growth. *Nature reviews cancer*, *2*(1), 38-47.
7. Tam, S. Y., Wu, V. W., & Law, H. K. (2020). Hypoxia-induced epithelial-mesenchymal transition in cancers: HIF-1α and beyond. *Frontiers in oncology*, *10*, 486.
8. Xing, F., Okuda, H., Watabe, M., Kobayashi, A., Pai, S. K., Liu, W., ... & Watabe, K. (2011). Hypoxia-induced Jagged2 promotes breast cancer metastasis and self-renewal of cancer stem-like cells. *Oncogene*, *30*(39), 4075-4086.
9. Iwatsuki, M., Mimori, K., Yokobori, T., Ishi, H., Beppu, T., Nakamori, S., ... & Mori, M. (2010). Epithelial–mesenchymal transition in cancer development and its clinical significance. *Cancer science*, *101*(2), 293-299.
10. Cho, E. S., Kang, H. E., Kim, N. H., & Yook, J. I. (2019). Therapeutic implications of cancer epithelial-mesenchymal transition (EMT). *Archives of pharmacal research*, *42*, 14-24.
11. Birle, D. C., & Hedley, D. W. (2007). Suppression of the hypoxia-inducible factor-1 response in cervical carcinoma xenografts by proteasome inhibitors. *Cancer research*, *67*(4), 1735-1743.
12. Liu, Q., Liu, L., Zhao, Y., Zhang, J., Wang, D., Chen, J., ... & Liu, Z. (2011). Hypoxia induces genomic DNA demethylation through the activation of HIF-1α and transcriptional upregulation of MAT2A in hepatoma cells. *Molecular cancer therapeutics*, *10*(6), 1113-1123.
13. Kim, S. J., Khadka, D., & Seo, J. H. (2022). Interplay between solid tumors and tumor microenvironment. *Frontiers in Immunology*, *13*, 882718.
14. Kim, Y., Nam, H. J., Lee, J., Park, D. Y., Kim, C., Yu, Y. S., ... & Baek, S. H. (2016). Methylation-dependent regulation of HIF-1α stability restricts retinal and tumour angiogenesis. *Nature communications*, *7*(1), 10347.
15. Masoud, G. N., & Li, W. (2015). HIF-1α pathway: role, regulation and intervention for cancer therapy. *Acta Pharmaceutica Sinica B*, *5*(5), 378-389.

16. Jaakkola, P., Mole, D. R., Tian, Y. M., Wilson, M. I., Gielbert, J., Gaskell, S. J., ... & Ratcliffe, P. J. (2001). Targeting of HIF-α to the von Hippel-Lindau ubiquitylation complex by O2-regulated prolyl hydroxylation. *Science*, *292*(5516), 468-472.
17. Jing, X., Yang, F., Shao, C., Wei, K., Xie, M., Shen, H., & Shu, Y. (2019). Role of hypoxia in cancer therapy by regulating the tumor microenvironment. *Molecular cancer*, *18*, 1-15.
18. Khan, M. S., Hwang, J., Seo, Y., Shin, K., Lee, K., Park, C., ... & Choi, J. (2018). Engineering oxygen nanobubbles for the effective reversal of hypoxia. *Artificial cells, nanomedicine, and biotechnology*, *46*(sup3), 318-327.
19. Song, R., Peng, S., Lin, Q., Luo, M., Chung, H. Y., Zhang, Y., & Yao, S. (2019). pH-responsive oxygen nanobubbles for spontaneous oxygen delivery in hypoxic tumors. *Langmuir*, *35*(31), 10166-10172.
20. Cavalli, R., Bisazza, A., Giustetto, P., Civra, A., Lembo, D., Trotta, G., ... & Trotta, M. (2009). Preparation and characterization of dextran nanobubbles for oxygen delivery. *International Journal of Pharmaceutics*, *381*(2), 160-165.
21. Orel, V. B., Zabolotny, M. A., & Orel, V. E. (2017). Heterogeneity of hypoxia in solid tumours and mechanochemical reactions with oxygen nanobubbles. *Medical Hypotheses*, *102*, 82-86.
22. Xiong, R., Xu, R. X., Huang, C., De Smedt, S., & Braeckmans, K. (2021). Stimuli-responsive nanobubbles for biomedical applications. *Chemical Society Reviews*, *50*(9), 5746-5776.
23. Li, M., Ma, X., Eisener, J., Pfeiffer, P., Ohl, C. D., & Sun, C. (2021). How bulk nanobubbles are stable over a wide range of temperatures. *Journal of Colloid and Interface Science*, *596*, 184-198.
24. Nirmalkar, N., Pacek, A. W., & Barigou, M. (2018). Interpreting the interfacial and colloidal stability of bulk nanobubbles. *Soft matter*, *14*(47), 9643-9656.
25. Atkinson, A. J., Apul, O. G., Schneider, O., Garcia-Segura, S., & Westerhoff, P. (2019). Nanobubble technologies offer opportunities to improve water treatment. *Accounts of chemical research*, *52*(5), 1196-1205.
26. Song, R., Hu, D., Chung, H. Y., Sheng, Z., & Yao, S. (2018). Lipid-polymer bilaminar oxygen nanobubbles for enhanced photodynamic therapy of cancer. *ACS applied materials & interfaces*, *10*(43), 36805-36813.
27. Nirmalkar, N., Pacek, A. W., & Barigou, M. (2018). On the existence and stability of bulk nanobubbles. *Langmuir*, *34*(37), 10964-10973.
28. Favvas, E. P., Kyzas, G. Z., Efthimiadou, E. K., & Mitropoulos, A. C. (2021). Bulk nanobubbles, generation methods and potential applications. *Current Opinion in Colloid & Interface Science*, *54*, 101455.
29. Sun, Y., Zhao, D., Wang, G., Wang, Y., Cao, L., Sun, J., ... & He, Z. (2020). Recent progress of hypoxia-modulated multifunctional nanomedicines to enhance photodynamic therapy:

opportunities, challenges, and future development. *Acta Pharmaceutica Sinica B*, *10*(8), 1382-1396.

30. Batchelor, D. V., Abou-Saleh, R. H., Coletta, P. L., McLaughlan, J. R., Peyman, S. A., & Evans, S. D. (2020). Nested nanobubbles for ultrasound-triggered drug release. *ACS applied materials & interfaces*, *12*(26), 29085-29093.
31. Prabhakar, A., & Banerjee, R. (2019). Nanobubble liposome complexes for diagnostic imaging and ultrasound-triggered drug delivery in cancers: a theranostic approach. *ACS omega*, *4*(13), 15567-15580.
32. Messerschmidt, V., Ren, W., Tsipursky, M., & Irudayaraj, J. (2023). Characterization of Oxygen Nanobubbles and In Vitro Evaluation of Retinal Cells in Hypoxia. *Translational Vision Science & Technology*, *12*(2), 16-16.
33. Jannesari, M., Akhavan, O., Madaah Hosseini, H. R., & Bakhshi, B. (2020). Graphene/CuO2 nanoshuttles with controllable release of oxygen nanobubbles promoting interruption of bacterial respiration. *ACS applied materials & interfaces*, *12*(32), 35813-35825.
34. Lee, W., Sarkar, S., Ahn, H., Kim, J. Y., Lee, Y. J., Chang, Y., & Yoo, J. (2020). PEGylated liposome encapsulating nido-carborane showed significant tumor suppression in boron neutron capture therapy (BNCT). *Biochemical and Biophysical Research Communications*, *522*(3), 669-675.
35. Dhand, C., Prabhakaran, M. P., Beuerman, R. W., Lakshminarayanan, R., Dwivedi, N., & Ramakrishna, S. (2014). Role of size of drug delivery carriers for pulmonary and intravenous administration with emphasis on cancer therapeutics and lung-targeted drug delivery. *RSC advances*, *4*(62), 32673-32689.
36. Agarwal, K., Trivedi, M., & Nirmalkar, N. (2022). Does salting-out effect nucleate nanobubbles in water: Spontaneous nucleation?. *Ultrasonics sonochemistry*, *82*, 105860.
37. Jadhav, A. J., & Barigou, M. (2021). On the clustering of bulk nanobubbles and their colloidal stability. *Journal of Colloid and Interface Science*, *601*, 816-824.
38. Maruyama, K., Ishida, O., Kasaoka, S., Takizawa, T., Utoguchi, N., Shinohara, A., ... & Yanagie, H. (2004). Intracellular targeting of sodium mercaptoundecahydrododecaborate (BSH) to solid tumors by transferrin-PEG liposomes, for boron neutron-capture therapy (BNCT). *Journal of controlled release*, *98*(2), 195-207.
39. Muz, B., De La Puente, P., Azab, F., & Kareem Azab, A. (2015). The role of hypoxia in cancer progression, angiogenesis, metastasis, and resistance to therapy. *Hypoxia*, 83-92.
40. Nozato, M., Kaneko, S., Nakagawara, A., & Komuro, H. (2013). Epithelial-mesenchymal transition-related gene expression as a new prognostic marker for neuroblastoma. *International journal of oncology*, *42*(1), 134-140.

41. Gamerith, G., Rainer, J., Huber, J. M., Hackl, H., Trajanoski, Z., Koeck, S., ... & Amann, A. (2017). 3D-cultivation of NSCLC cell lines induce gene expression alterations of key cancer-associated pathways and mimic in-vivo conditions. *Oncotarget*, *8*(68), 112647.
42. Bhandari, P. N., Cui, Y., Elzey, B. D., Goergen, C. J., Long, C. M., & Irudayaraj, J. (2017). Oxygen nanobubbles revert hypoxia by methylation programming. *Scientific reports*, *7*(1), 9268.
43. Chen, S. Y., Tsuneyama, K., Yen, M. H., Lee, J. T., Chen, J. L., & Huang, S. M. (2021). Hyperbaric oxygen suppressed tumor progression through the improvement of tumor hypoxia and induction of tumor apoptosis in A549-cell-transferred lung cancer. *Scientific reports*, *11*(1), 12033.
44. Davis, F. M., Stewart, T. A., Thompson, E. W., & Monteith, G. R. (2014). Targeting EMT in cancer: opportunities for pharmacological intervention. *Trends in pharmacological sciences*, *35*(9), 479-488.
45. Hugo, H. J., Gunasinghe, N. P. A. D., Hollier, B. G., Tanaka, T., Blick, T., Toh, A., ... & Thompson, E. W. (2017). Epithelial requirement for in vitro proliferation and xenograft growth and metastasis of MDA-MB-468 human breast cancer cells: oncogenic rather than tumor-suppressive role of E-cadherin. *Breast Cancer Research*, *19*, 1-25.
46. Däster, S., Amatruda, N., Calabrese, D., Ivanek, R., Turrini, E., Droeser, R. A., ... & Muraro, M. G. (2017). Induction of hypoxia and necrosis in multicellular tumor spheroids is associated with resistance to chemotherapy treatment. *Oncotarget*, *8*(1), 1725.
47. Shen, W., Pu, J., Sun, J., Tan, B., Wang, W., Wang, L., ... & Zuo, Y. (2020). Zebrafish xenograft model of human lung cancer for studying the function of LINC00152 in cell proliferation and invasion. *Cancer Cell International*, *20*, 1-11.
48. Krock, B. L., Skuli, N., & Simon, M. C. (2011). Hypoxia-induced angiogenesis: good and evil. *Genes & cancer*, *2*(12), 1117-1133.
49. Pilco-Ferreto, N., & Calaf, G. M. (2016). Influence of doxorubicin on apoptosis and oxidative stress in breast cancer cell lines. *International journal of oncology*, *49*(2), 753-762.
50. Lovitt, C. J., Shelper, T. B., & Avery, V. M. (2018). Doxorubicin resistance in breast cancer cells is mediated by extracellular matrix proteins. *BMC cancer*, *18*, 1-11.
51. AJ, V. R. (2017). The potential of zebrafish as a model organism for improving the translation of genetic anticancer nanomedicines. *Genes*, *8*(12), 349.
52. Syed, V. (2016). TGF-β signaling in cancer. *Journal of cellular biochemistry*, *117*(6), 1279-1287.
53. Song, L., Wang, G., Hou, X., Kala, S., Qiu, Z., Wong, K. F., ... & Sun, L. (2020). Biogenic nanobubbles for effective oxygen delivery and enhanced photodynamic therapy of cancer. *Acta biomaterialia*, *108*, 313-325.
54. Peñaloza, J. P., Márquez-Miranda, V., Cabaña-Brunod, M., Reyes-Ramírez, R., Llancalahuen, F. M., Vilos, C., ... & Otero, C. (2017). Intracellular trafficking and cellular uptake mechanism of

PHBV nanoparticles for targeted delivery in epithelial cell lines. *Journal of nanobiotechnology*, *15*, 1-15.

55. Khan, M. S., Kim, J. S., Hwang, J., Choi, Y., Lee, K., Kwon, Y., ... & Choi, J. (2020). Effective delivery of mycophenolic acid by oxygen nanobubbles for modulating immunosuppression. *Theranostics*, *10*(9), 3892.
56. Kung-Chun Chiu, D., Pui-Wah Tse, A., Law, C. T., Ming-Jing Xu, I., Lee, D., Chen, M., ... & Chak-Lui Wong, C. (2019). Hypoxia regulates the mitochondrial activity of hepatocellular carcinoma cells through HIF/HEY1/PINK1 pathway. *Cell death & disease*, *10*(12), 934.
57. Song, X., Liu, X., Chi, W., Liu, Y., Wei, L., Wang, X., & Yu, J. (2006). Hypoxia-induced resistance to cisplatin and doxorubicin in non-small cell lung cancer is inhibited by silencing of HIF-1α gene. *Cancer chemotherapy and pharmacology*, *58*, 776-784.
58. Wu, B., Sun, Z., Wu, J., Ruan, J., Zhao, P., Liu, K., ... & Chen, D. (2021). Nanoparticle-Stabilized Oxygen Microcapsules Prepared by Interfacial Polymerization for Enhanced Oxygen Delivery. *Angewandte Chemie International Edition*, *60*(17), 9284-9289.
59. Wu, J., Wang, X., Chen, L., Wang, J., Zhang, J., Tang, J., ... & Liang, T. (2023). Oxygen microcapsules improve immune checkpoint blockade by ameliorating hypoxia condition in pancreatic ductal adenocarcinoma. *Bioactive materials*, *20*, 259-270.
60. Iijima, M., Gombodorj, N., Tachibana, Y., Tachibana, K., Yokobori, T., Honma, K., ... & Yamanouchi, D. (2018). Development of single nanometer-sized ultrafine oxygen bubbles to overcome the hypoxia-induced resistance to radiation therapy via the suppression of hypoxia-inducible factor-1α. *International journal of oncology*, *52*(3), 679-686.
61. Arora, L., Kalia, M., Dasgupta, S., Singh, N., Verma, A. K., & Pal, D. (2022). Development of a multicellular 3D tumor model to study cellular heterogeneity and plasticity in NSCLC tumor microenvironment. *Frontiers in Oncology*, *12*, 881207.
62. Bhavya, K., Mantipally, M., Roy, S., Arora, L., Badavath, V. N., Gangireddy, M., ... & Pal, D. (2022). Novel imidazo [1, 2-a] pyridine derivatives induce apoptosis and cell cycle arrest in non-small cell lung cancer by activating NADPH oxidase mediated oxidative stress. *Life Sciences*, *294*, 120334.
63. Wang, X., Lu, H., Luo, F., Wang, D., Wang, A., Wang, X., ... & Xia, G. (2024). Lipid-like gemcitabine diester-loaded liposomes for improved chemotherapy of pancreatic cancer. *Journal of Controlled Release*, *365*, 112-131.
64. Mahjour, A., Khazaei, M., Nourmohammadi, E., Khoshdel-Sarkarizi, H., Ebrahimzadeh-Bideskan, A., Rahimi, H. R., & Safipour Afshar, A. (2019). Evaluation of antitumor effect of oxygen nanobubble water on breast cancer-bearing BALB/c mice. *Journal of Cellular Biochemistry*, *120*(9), 15546-15552.

Chapter 5

Delineating the role of Zeb1siRNA as targeted therapy against tumor angiogenesis

5.1 Background and Challenges

Tumor angiogenesis is critical for the growth and spread of solid tumors, as it facilitates the formation of new blood vessels to supply the tumor with oxygen and nutrients [1-2]. Folkman et al., (2007) postulate that angiogenesis is a fundamental biological process in maintaining normal body functions and causing various diseases, including cancer [2]. The tumor hypoxia characterized by acidic conditions within tumor, and high interstitial fluid pressure, drives this angiogenic process [3]. Zinc-finger E-box binding homeobox 1 (Zeb1), a transcription factor regulated by HIF-1α, plays a key role in promoting tumor invasion and metastasis by inducing epithelial-mesenchymal transition (EMT) and enhancing the expression of pro-angiogenic factors in carcinoma cells [4].

Zeb1 is predominantly found in tumor endothelial cells. Many researchers, including Sanchez-Tilló et al., (2011) and Liu et al., (2016), findings reported that tumors with high Zeb1 expression upregulate VEGF in the tumor endothelium, stimulating angiogenesis and increasing the likelihood of metastasis [4,5]. Deleting Zeb1 in tumor endothelial cells reduces angiogenesis, normalizes the remaining tumor vessels, improves oxygenation, decreases haemorrhagic necrosis, and enhances the efficacy of anticancer drugs [6-8]. However, Zeb1 is also implicated in promoting inflammation within the tumor microenvironment (TME) by regulating pro-inflammatory cytokine secretion in breast cancer [9]. Under hypoxic conditions, Zeb1 drives macrophage polarization towards a pro-tumor M2 phenotype, contributing to tumor progression and angiogenesis [10]. This process involves Zeb1-induced metabolic reprogramming of macrophages, leading to increased glycolysis, glucose uptake, pyruvate production, lactate secretion, and ATP generation, which ultimately affects tumor endothelial cell function [11 - 13]. Current evidence suggests that targeting endothelial Zeb1 can inhibit tumor angiogenesis and progression[6]. In response to tumor hypoxia, Zeb1 induces gaining of endothelial characteristics by the tumor-associated macrophages, thereby enhancing tumor invasiveness and metastasis. We employed an RNA interference (RNAi)-based therapy using Zeb1-specific siRNA delivered via cationic liposome nanoparticles (LNPs) [11-14]. Although siRNA therapies face challenges such as poor cellular uptake, low biological stability, and unfavourable pharmacokinetics, this approach aims to overcome these hurdles [15,16].

Our study is the first to investigate Zeb1's role in macrophage-to-tumor endothelial cell transformation differentiation using a 3D spheroid tumor models. By utilizing cationic LNPs to deliver Zeb1 siRNA, we aim to enhance cellular uptake and biological stability, effectively inhibiting tumor angiogenesis

and reducing invasiveness and metastasis in lung adenocarcinoma cells, 3D lung tumor spheroids, and xenograft 4T1 C57BL/6 mouse tumor models. Consequently, silencing Zeb1 through siRNA therapy is a promising strategy to impede angiogenesis and metastasis in lung and beast tumor.

5.2 Results

5.2.1 High Zeb1 expression correlates with poor prognosis in lung adenocarcinoma

To explore the potential role of Zeb1 in LUAD, we first analysed the expression levels of Zeb1 in LUAD using the available datasets from the GEPIA database (http://gepia.cancer-pku.cn/detail.php). Relatively high level of Zeb1 was detected in LUAD patients (left bar) compared with normal patients (right bar) (**Fig. 5.1 A**). Moreover**,** Kaplan-Meier analysis demonstrated that LUAD patients with overexpression of Zeb1 exhibited poor overall survival (**Fig. 5.1 B**). These bioinformatics results indicate a possible link between Zeb1 and LUAD progression. To substantiate the bioinformatics data, we conducted in vitro experiments to assess Zeb1 expression at both gene and protein levels. Using RT-qPCR, western blotting, and immunofluorescence staining, we compared Zeb1 expression between BEAS-2B (normal lung epithelial) and A549 (LUAD) cell lines. Our results showed that A549 cells exhibited significantly higher Zeb1 gene and protein expression compared to BEAS-2B cells (**Fig. 5.1 C-G**). In parallel, we analyzed Zeb1 protein levels in LUAD patients' tissue samples. Immunohistochemical analysis revealed a marked increase in Zeb1 protein abundance in cancerous tissues compared to non-cancerous tissues from the same patients (**Fig. 5.1 H-I**). Collectively, these findings reinforce the idea that Zeb1's presence is critical in LUAD progression. The significant upregulation of Zeb1 in both LUAD cell lines and patient tissue samples suggests that Zeb1 could be a key driver of poor prognosis in LUAD. Additionally, these data imply that targeting Zeb1 might represent a promising therapeutic strategy in the management of LUAD.

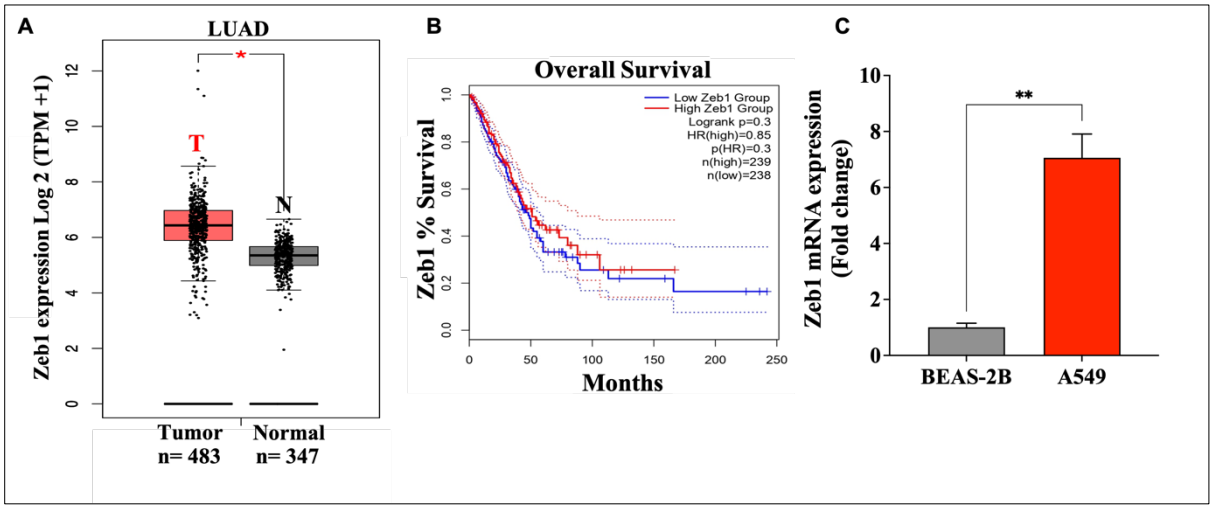

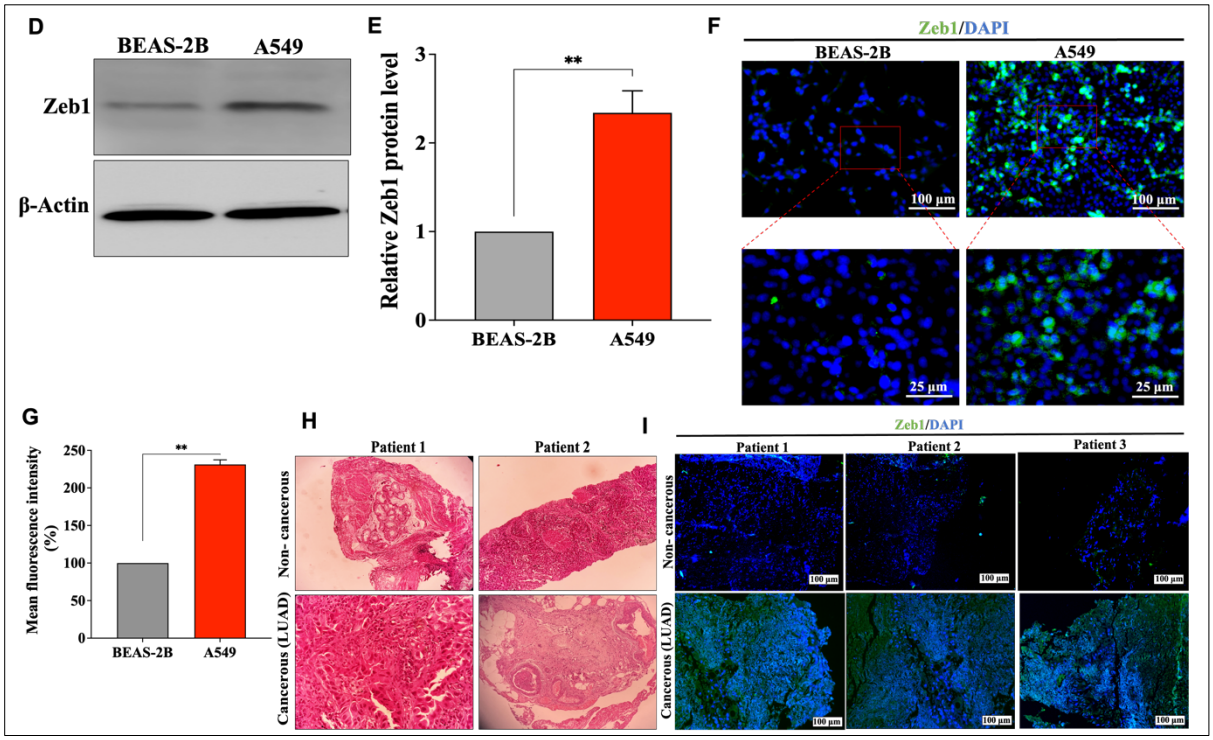

Figure 5.1: Zeb1 is aberrantly overexpressed in lung adenocarcinoma and associated with poor prognosis;

*Box plots for Zeb1 gene expression in LUAD and normal tissues from GEPIA. (B) Kaplan-Meier survival plot of overall survival of LUAD patients in GEPIA, categorized according to Zeb1 gene expression (high vs. low, based on mean expression). (C) Relative mRNA expression of Zeb1 in lung epithelial cell (BEAS-2B) vs. lung adenocarcinoma cell (A549). (D-E) Western blot analysis of Zeb1 protein and its qualification ; β-actin was used as loading control. (F-G). Immunofluorescent staining of Zeb1 (F) and mean fluorescence intensity quantification (G) in BEAS-2B and A549 (40x and 20x magnification). DAPI was used to stain nucleus (H) H&E-stained images of non-cancerous and lung adenocarcinoma patient tissue sections showing morphological structures (I) Immunofluorescent staining of Zeb-1 in non-cancerous and lung adenocarcinoma tissue sections. Nuclei were stained with DAPI (blue). Data are presented as the mean ± SD of three independent experiments. #P < 0.05; *P < 0.01; **P < 0.001; ns, non-significant, compared with the normal group.*

5.2.2 Synthesis, characterization and cellular uptake of cationic liposomal nanoparticles

To ensure the efficient delivery of Zeb1siRNA in solid tumors, we therefore, synthesized cationic DC-Chol/DOTAP liposomal nanoparticles (LNP) using a modified ethanol injection method [17-18] **(Fig. 5.2 A)**. The formulation was synthesized with the permanently charged cationic lipid DOTAP combined with the cationic lipid 3β-[N-(N',N'-dimethyl amino ethane) carbamoyl] cholesterol (DC-Chol) which contains a three-atom spacer, a hydrolyzable carbamoyl linkage, and a tertiary amino group. Then it combined with the lipid dioleoyl phosphatidylethanolamine (DOPE) at a 1:2 molar ratio

to form unilamellar liposomes. The synthesized liposomes were characterized using DLS, zeta potential measurements, and field emission scanning electron microscopy (FESEM). The average mean size of the liposomes was approximately 177 ± 6.2 nm, with an average polydispersity index (PDI) of 0.11 ± 0.09, indicating uniformity in particle size **(Fig. 5.2 B - C)**. The surface charge was approximately +47.5 ± 2.5 mV, **(Fig. 5.2 D - E)**. indicating a positive charge on the LNP particles, which ensures particle stability. FESEM and Cryo-TEM techniques were employed to visualize the morphological characteristics of the LNPs **(Fig. 5.2 F)**.

To further assess their biological activity, LNP particles were conjugated with Zeb1siRNA (length 21mer) based on their N/P ratio, utilizing electrostatic interactions. A 3:1 N/P ratio (The cationic lipid (N) exhibits positive charges, while the phosphate groups of siRNA carry negative charges) was determined to be optimal, as confirmed by the gel retardation assay, which verified the successful conjugation of Zeb1 siRNA to the LNP particles **(Fig. 5.2 G)**. In order to confirm the cellular internalization of Zeb1 siRNA within endothelial and tumor cells, Cy3-tagged LNP-Zeb1 siRNA was utilized. The successful delivery of Zeb1 siRNA into the cells was indicated by the presence of a red fluorescence signal **(Fig. 5.2 H - I)** at 8 h . This method allows for the visualization and verification of the intracellular uptake of the siRNA, ensuring that the LNPZeb1siRNA effectively reaches its target within the cells. Additionally we found that the DOTAP/DC Chol LNP formulation exhibits the greatest transfection efficiency in LUAD and ECs cells *in vitro*.

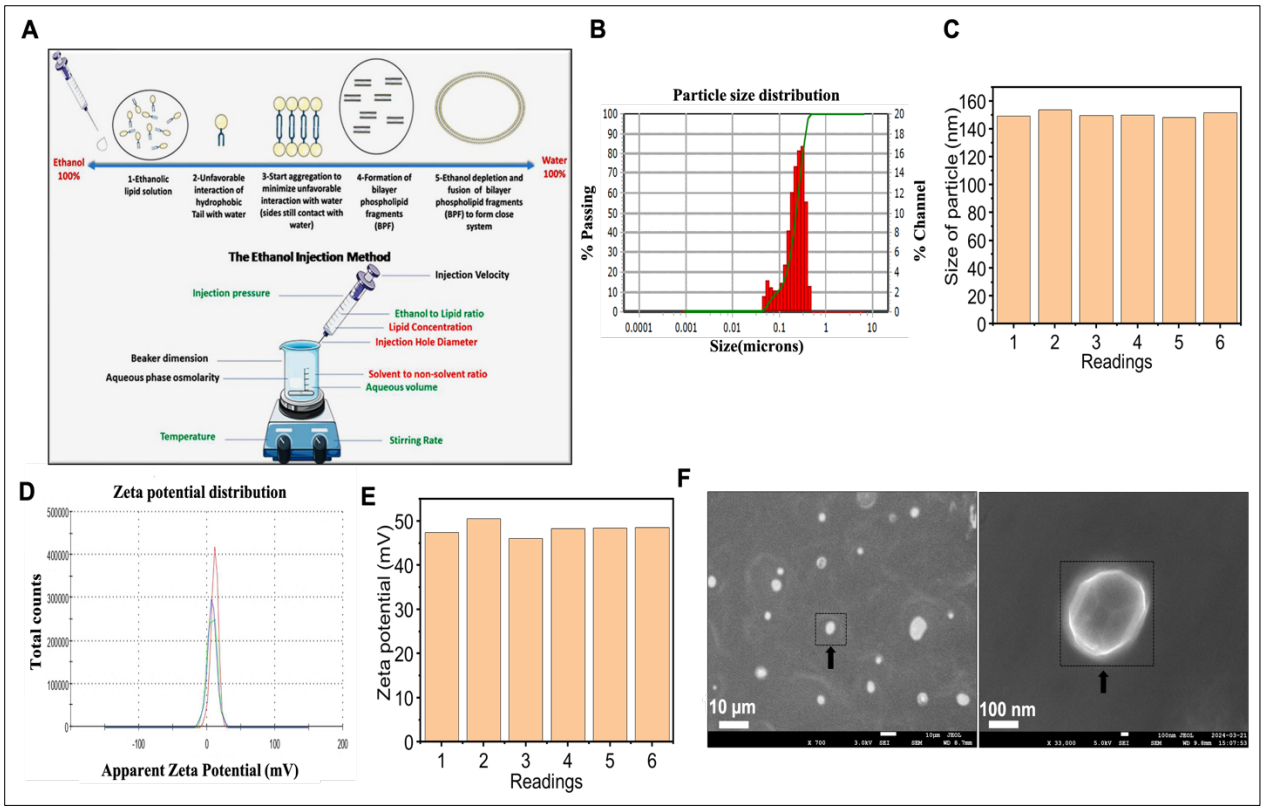

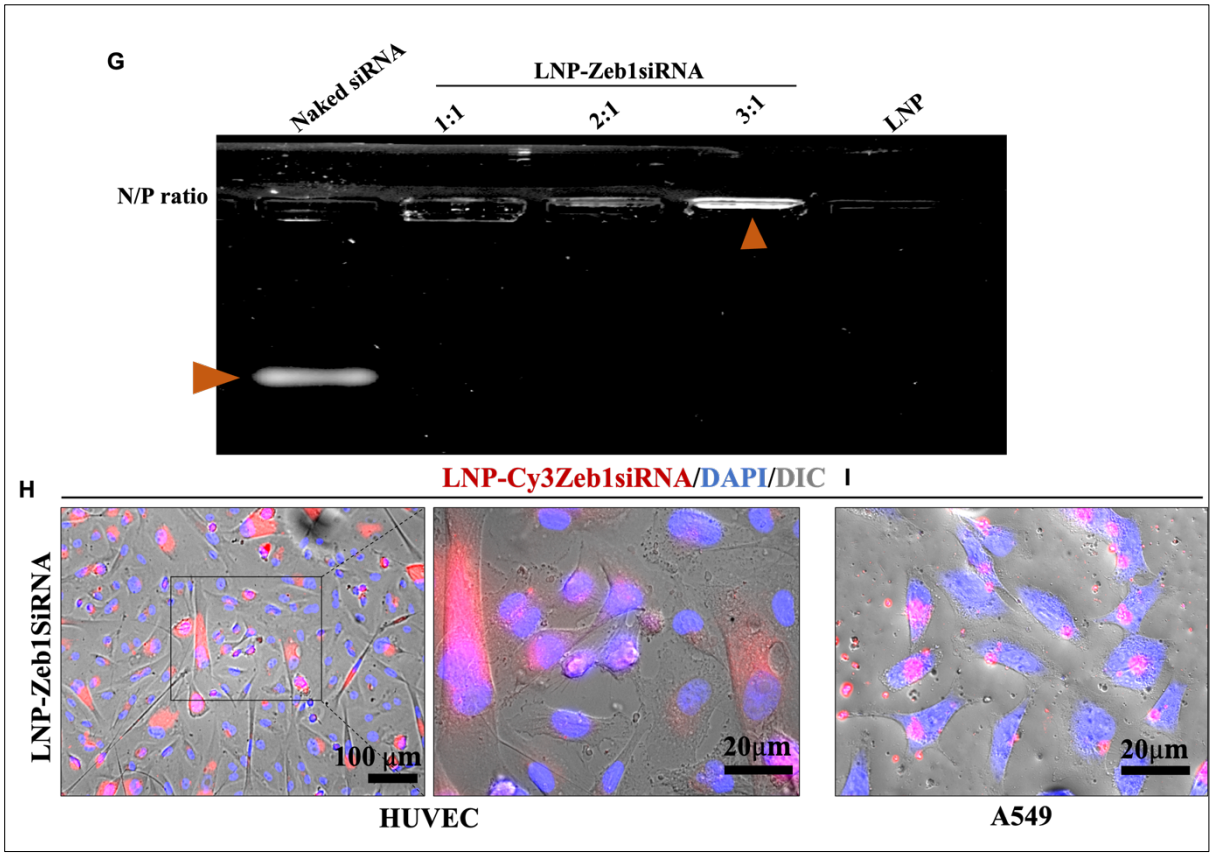

Figure 5.2: Synthesis and characterization of cationic liposome nanoparticle (LNP), and cellular uptake LNP- Zeb1siRNA

Schematic representation of the LNP synthesis from modified ethanol injection method (B - C) Dynamic light scattering (DLS) assay and (D - E) Zeta potential and their bar graph (F) Field emission scanning electron microscopy (FESEM) of LNP. (G) Agarose gel retardation assay of LNP-conjugated Zeb1siRNA demonstrated electrostatic interactions. This interaction ensures encapsulation at a 3:1 N/P ratio, where Zeb1siRNA remains immobilized in the lane. (H - I) A cellular uptake assay was performed using LNP-Cy3 tagged Zeb1siRNA in endothelial and tumor cells at 8 hours, (20x and 63x magnification). Data presented in this figure are representative of 3 independent experiment n = 3.

5.2.3 LNP-Zeb1siRNA inhibits angiogenesis in tumor endothelial cells

Zeb1, a transcription factor, plays a key role in the epithelial-to-mesenchymal transition (EMT), enhancing tumor invasiveness and metastasis [19,20]. Given the elevated expression of Zeb1 in LUAD, We aimed to explore the effect of Zeb1 silencing on tumor angiogenesis. To achieve this, we designed a co-culture experiment, placing HUVEC cells in the bottom chamber and A549 cells in the upper chamber under hypoxic conditions for 2 days. Interestingly, we observed a significant increase in the expression of traditional endothelial markers on the HUVEC cells, indicating the influence of the tumor hypoxic environment and the crosstalk between cancer cells and endothelial cells, which led to enhanced endothelial activation (**Fig. 5.2 A, B**). These HUVEC cells were subsequently used in further experiments.

After 24 h of transfection with consiRNA and Zeb1siRNA, there was a significant downregulation of *Zeb1* as well as angiogenic markers, including *CD31*, *eNOS*, *VEGFA*, *VE-cadherin*, and *vWF* in endothelial cells, compared to the control group (**Fig. 5.3 C**). An *in vitro* AcLDL uptake assay revealed that endothelial cells treated with LNP-Zeb1siRNA exhibited significantly lower acetylated LDL uptake compared to those treated with LNP-consiRNA (**Fig. 5.3 D, E**). Furthermore, Zeb1, CD31, and VE-cadherin protein expression were significantly reduced in endothelial cells when transfected with Zeb1siRNA (**Fig. 5.3 F, G**). To assess the anti-angiogenic effects of LNP-Zeb1siRNA, we performed an *in vitro* tubule formation assay using Matrigel. The results demonstrated a significant decrease in the number of tube formations in LNP-Zeb1siRNA-treated endothelial cells compared to the control (**Fig. 5.3 H**). This reduction in tube formation further supports the efficacy of LNP-Zeb1siRNA in inhibiting angiogenic processes, highlighting the therapeutic potential of LNP-Zeb1siRNA in targeting tumor angiogenesis.

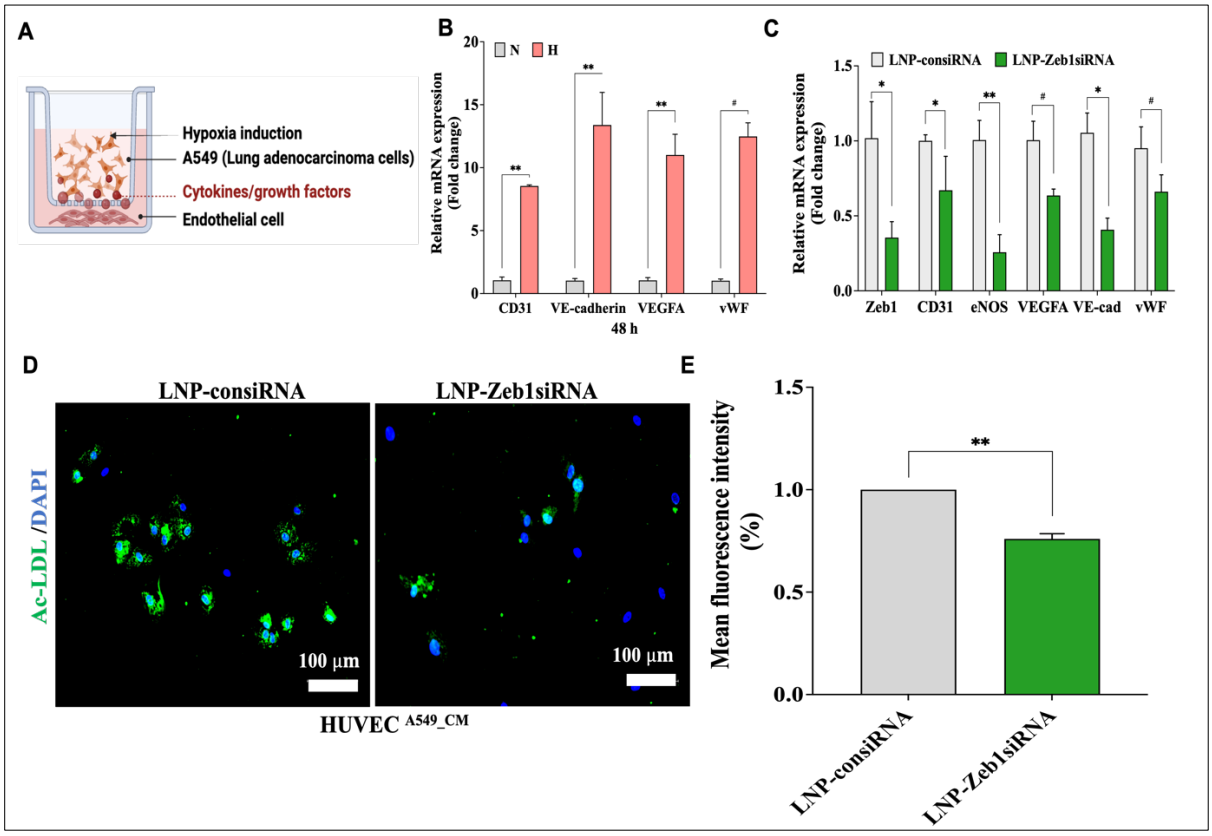

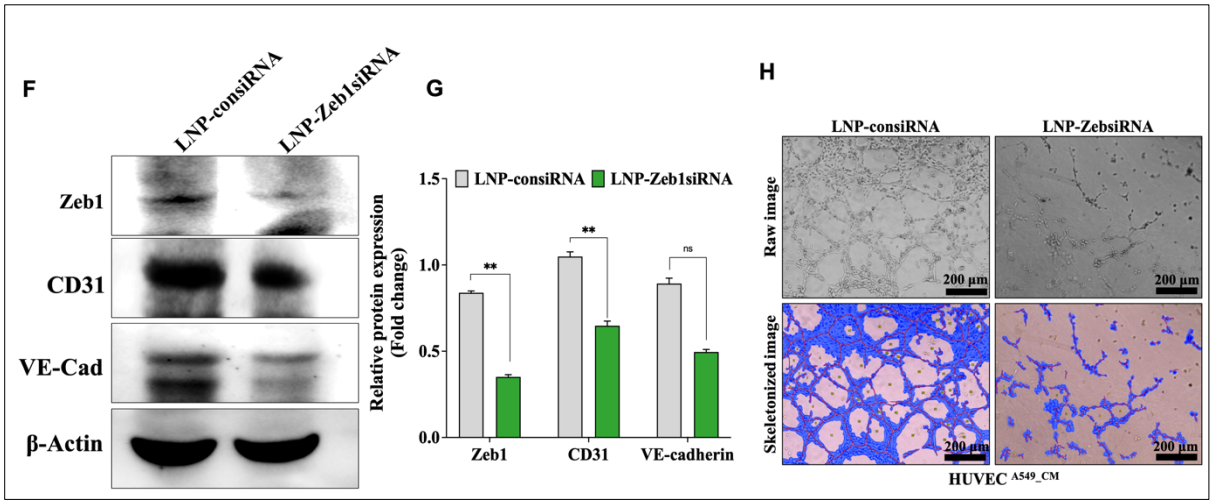

Figure 5.3 : LNP-Zeb1siRNA suppresses in vitro angiogenic markers in tumor endothelial cells

(A) Schematic presentation of experimental coculture assay setup of HUVEC endothelial cells in the presence of A549 and hypoxia mimetic Cocl2. (B) Relative mRNA expression analysis of CD31, VE-cadherin, VEGFA and vWF in cocultured HUVEC cell at 48h. (C) Relative mRNA expression analysis of Zeb1, CD31, eNOS, VEGFA, VE-cad, and vWF in HUVEC cell transfected with LNP-consiRNA and LNP-Zeb1siRNA. (D-E) Fluorescence microscopy images of acetylated LDL uptake assay in the LNP-consiRNA and LNP-Zeb1siRNA treated endothelial cells at 24 h (D), and mean fluorescence intensity (E) at 20x.. (F-G) Western blot analysis of Zeb1, CD31, and VE-cadherin (F) of LNP-consiRNA and LNP-Zeb1siRNA treated endothelial cells at 24 h and relative protein quantification (G), β-Actin served as a loading control. (H)Phase contrast microscopy images of in vitro Matrigel tube formation assay in LNP-consiRNA and LNP-Zeb1siRNA treated endothelial cells, images captured at 10x magnification, (upper) and processed skeletonized images (lower) were analysed by wimasis analysis software, Scale bar, 200 µm. Data are presented as the mean ± SD of three independent experiments. $^{\#}P < 0.05$; $*P < 0.01$; $**P < 0.001$; ns, non-significant.

5.2.4 LNP-Zeb1siRNA administration inhibits angiogenesis in 4T1 C57BL/6 breast tumor xenograft models

We evaluated the efficacy of LNP-Zeb1siRNA *in vivo* using a 4T1 breast tumor xenograft model in C57BL/6 mice. A detailed schematic of tumor xenograft development and LNP-Zeb1siRNA delivery is shown in **Fig. 5.4 A**. The treatment groups included PBS, LNP-consiRNA (as the control), and LNP-Zeb1siRNA. On day 14, the mice were sacrificed, and tumor photographs were taken. The results showed significant reductions in tumor size, volume, and weight in the LNP-Zeb1siRNA-treated group compared to the controls (**Fig. 5.4 B - D**), with no notable differences in body weight between the treated and control animals (**Fig. 5.4 E**). RT-qPCR analysis revealed significant downregulation of *Zeb1, CD31, VEGFA*, and *VE-cadherin* expression in the LNP-Zeb1siRNA-treated tumors compared to the LNP-consiRNA group (**Fig. 5.4 F**). Additionally, western blot analysis demonstrated reduced levels of Zeb1 and CD31 proteins in tumor tissues treated with LNP-Zeb1siRNA (**Fig. 5.4 G, H**).

Histological examination of tumor sections stained with Haematoxylin and Eosin (H&E) revealed that the LNP-consiRNA-treated tumors exhibited dense cellularity, poorly organized structures, and high rates of cellular proliferation and tumor growth. In contrast, tumors from the LNP-Zeb1siRNA treated group showed a marked reduction in cellular density (**Fig. 5.4 I**). Immunostaining further confirmed a decrease in Zeb1 expression in LNP-Zeb1siRNA-treated tissues compared to the control group (**Fig. 5.4 J, K**).

To assess the *in vivo* anti-angiogenic activity of LNP-Zeb1siRNA, we conducted a Matrigel plug assay. As shown in **Fig. 5.4 L M**, LNP-Zeb1siRNA treatment significantly reduced vascularization, while the control group exhibited strong vascularity, with the plugs appearing dark red due to blood. The blood vessels in the treated group were more uniformly distributed and less chaotic, indicating reduced abnormal angiogenesis. Further at gene level we found there was decreased expression of *CD31* and *VE-cadherin* in the LNP-Zeb1siRNA treated plug tumor tissue section. Moreover, Haematoxylin and Eosin (H&E) staining demonstrated the less of number cell proliferation and formation of blood vessels, with respect to untreated and also we observed there was decreased expression of CD31 protein in the Immunostaining assay. These findings underscore the therapeutic potential of LNP-Zeb1siRNA in targeting Zeb1, effectively reducing endothelial cell populations and angiogenesis within breast tumor xenografts model.

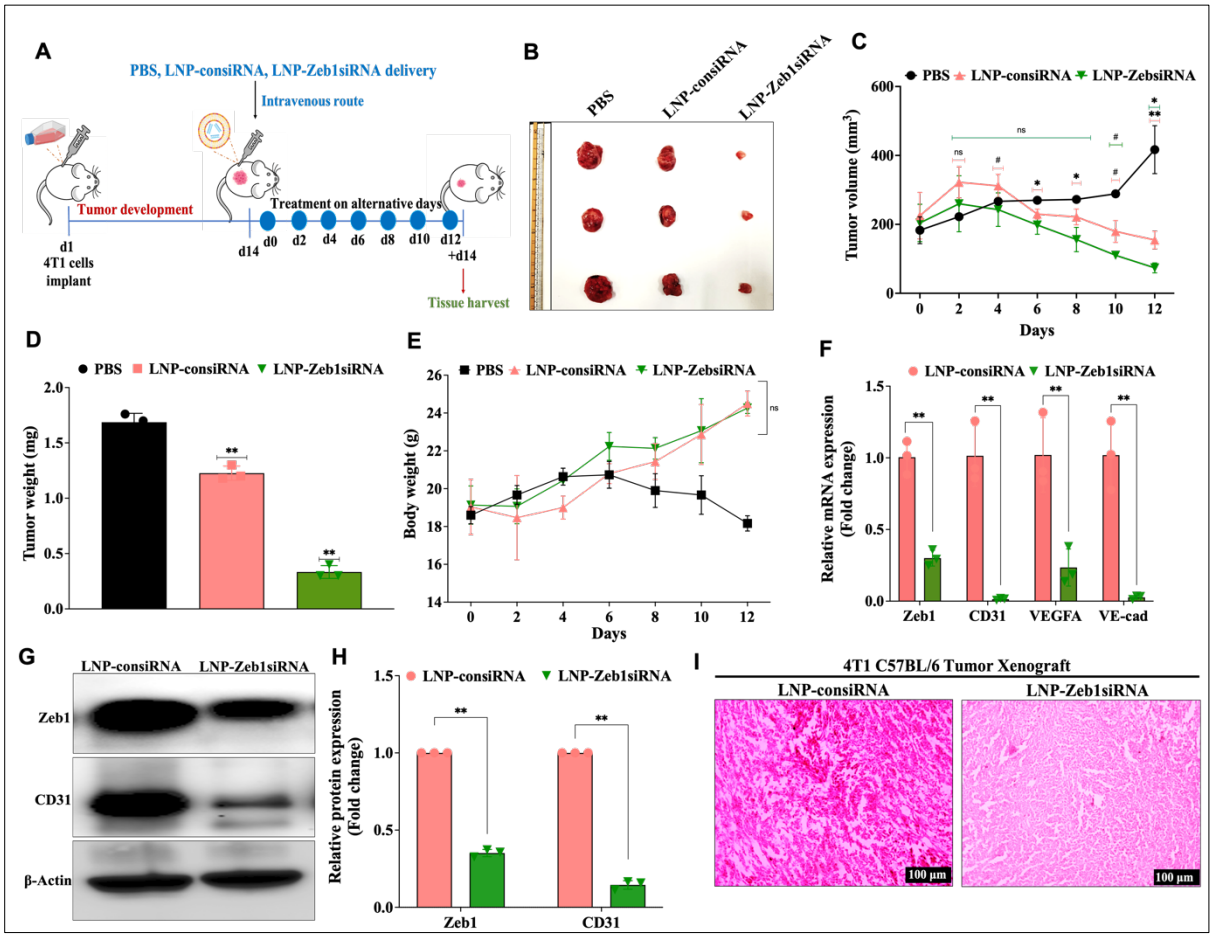

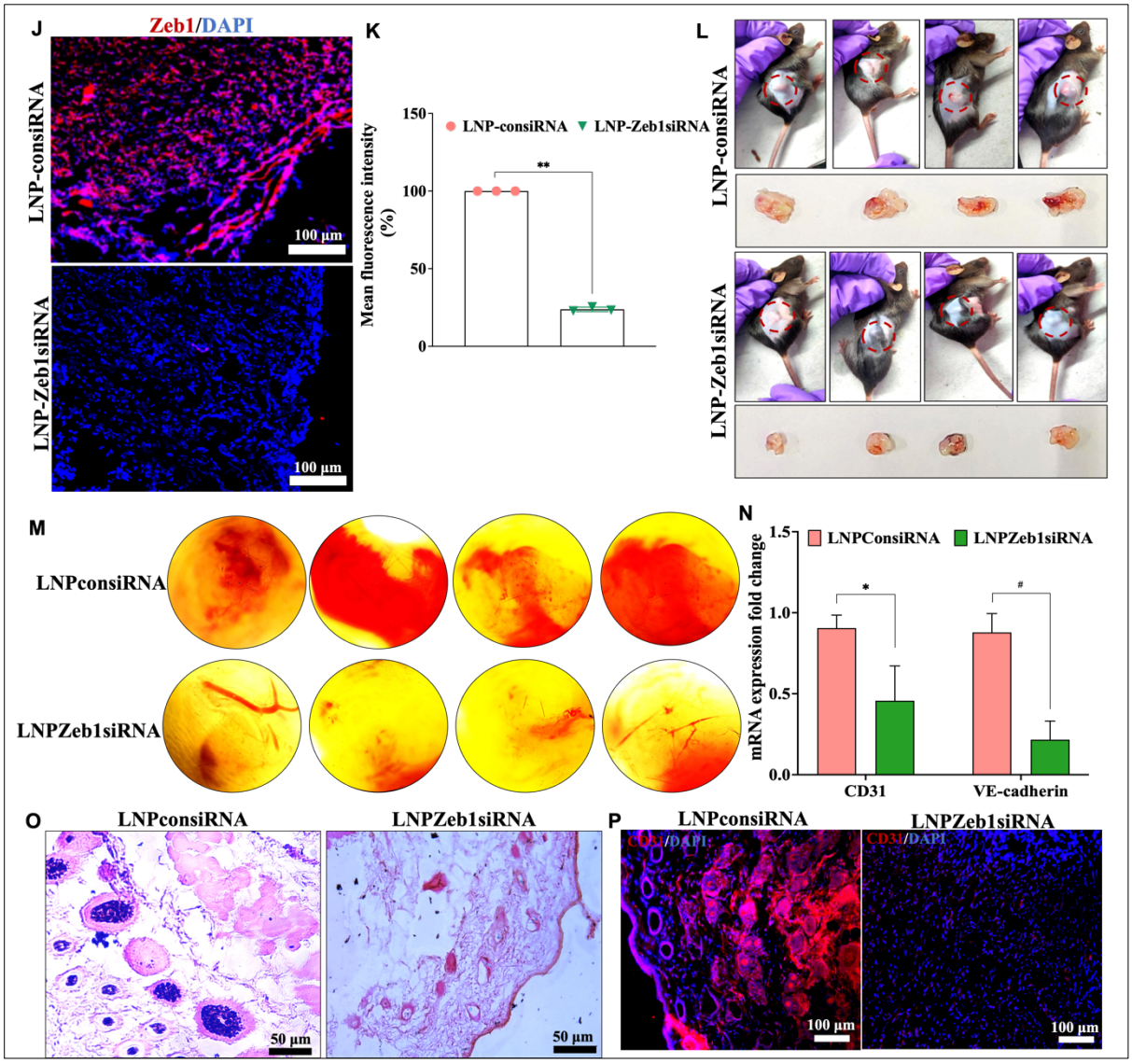

Figure 5.4: LNP-Zeb1siRNA suppress endothelial cell gene expressions in 4T1 C57BL/6 breast tumor xenograft models.

(A) Schematic diagram representing experimental design. The tumor xenograft mice were divided into three groups i.e, PBS, LNP-consiRNA, and LNP-Zeb1siRNA for 14 days (n = 3) . (B) Representative photographs of tumor size. (C-E) Tumor regression analysis by measuring tumor volume, (D) tumor weight (D) and (E) body weight of LNP-consiRNA and LNP-Zeb1siRNA treated 4T1 C57BL/6 mice.(F)Relative mRNA expression analysis of Zeb1, CD31 and VEGFA gene expression in the tumor tissue samples of LNP-Zeb1siRNA treated C57BL/6 mice compared with LNP-consiRNA group; β-actin was used for normalization (G - H) Western blot analysis of Zeb1, CD31 proteins (H) and their relative protein quantification in the tumor tissue samples. β-actin used as loading control. (I) Haematoxylin and eosin (H&E) staining of 4T1 tumor tissue sections of LNP-consiRNA and LNP-Zeb1siRNA treated mice. (J,K) Immunohistochemistry assay of Zeb1 in tumor tissue sections of LNP-consiRNA and LNP-Zeb1siRNA treated mice (J) and their mean fluorescence quantification (K). In vivo Matrigel plug assay (L-M) Representative photographs (L)

*and microscopy images of Matrigel plugs (M) containing LNP-consiRNA and LNP-Zeb1siRNA. Plugs were removed from C57BL/6 mice at 10 days post implantation. (N)Relative mRNA expression analysis CD31 and VE-cadherin in Matrigel plug tissue sample of LNP-Zeb1siRNA treated C57BL/6 mice compared with LNP-consiRNA group. (O) Haematoxylin and eosin (H&E) staining of Matrigel plug tissue section of LNP-consiRNA and LNP-Zeb1siRNA treated mice. (P) Immunohistochemistry assay of Matrigel plug tissue section of CD31 LNP-consiRNA and LNP-Zeb1siRNA treated mice. Data are presented as the mean ± SD of three independent experiments. $^{\#}P < 0.05$; *$P < 0.01$; **$P < 0.001$; ns, non-significant.*

The findings from our study demonstrate that LNP-Zeb1siRNA treatment significantly inhibits tumor growth and disrupts abnormal angiogenesis both *in vitro* and *in vivo*, highlighting LNP-Zeb1siRNA as a promising therapeutic candidate for targeting tumor angiogenesis in breast and lung cancers.

Building on these results, we further explored the potential role of Zeb1 in enhancing endothelial cell expression and hypothesized that Zeb1 plays a critical role in promoting tumor angiogenesis by influencing macrophage plasticity into tumor endothelial-like cells within the hypoxic tumor microenvironment. This hypothesis is supported by previous work from our lab Arora et al., (2022), who reported that within tumorigenic multicellular 3D spheroids, a significant population of macrophages (CD144+ cells) exhibited endothelial characteristics, marked by the expression of endothelial-specific markers such as VE-cadherin**,** VEGF, and CD31 [27,28]. These M2-polarized macrophages were identified as key contributors to endothelial cell formation in the tumor microenvironment. Therefore, further investigation into the molecular mechanisms by which Zeb1 influences the formation of macrophage-derived endothelial cells, particularly in 3D multicellular lung tumor spheroid models, is essential to gaining a better understanding of its role in tumor angiogenesis [29].

5.2.5 Macrophages exhibiting endothelial properties with elevated Zeb1 expression

To study the interactions between cancer cells and macrophages within the tumor microenvironment [30, 31]. We cocultured the cancer cells A549 with the macrophages together in the hypoxic condition and observe the change in the macrophage phenotype at different time points. We have used THP1 human monocytes in this study and were differentiated into macrophages using 25 nM phorbol 12-myristate 13-acetate (PMA) for 24 h (**Fig. 5.4 A**). The differentiated macrophages were then cocultured with A549 cells under hypoxic condition. RT-qPCR analysis revealed a significant upregulation of Zeb1 mRNA expression in macrophages cocultured with hypoxic A549 cells at days 3 and 5 compared to day 0. Similarly we found that the significant high expression of Zeb1, CD31 and VE-cadherin at days 3 and 5, indicating a time-dependent enhancement of the endothelial-like phenotype in these macrophages **(Fig. 5.4 B - D)**. Additionally, western blot and immunofluorescence staining revealed a time-dependent increase of Zeb1 and CD31 protein expressions in macrophages **(Fig. 5.4 E - H)**. In addition, we extracted the Zeb1 gene expression in the endothelial cell type from the existing data set of a public "Lung tumor ECTax" (https://endotheliomics.shinyapps.io/lung_ectax/)

which revealed abundant expression of Zeb1 in the tumor patients compared to normal group **(Fig. 5.4 I)**. Next, LNP-consiRNA or LNP-Zeb1siRNA transfected macrophages are cocultured with A549 and we observed that there was a significant reduction of *Zeb1*, *CD31* and *VE-cadherin* gene expression in the Zeb1siRNA transfected macrophages compared to control ones **(Fig. 5.4 J)**. These results suggest that Zeb1 level in macrophage playing a key role in gaining angiogenic properties, potentially influencing endothelial formation and their functional contributions to tumor angiogenesis. Overall, the data highlights the importance of Zeb1 in hypoxic tumor microenvironment and underscores the relevance of this molecule in tumor angiogenesis.

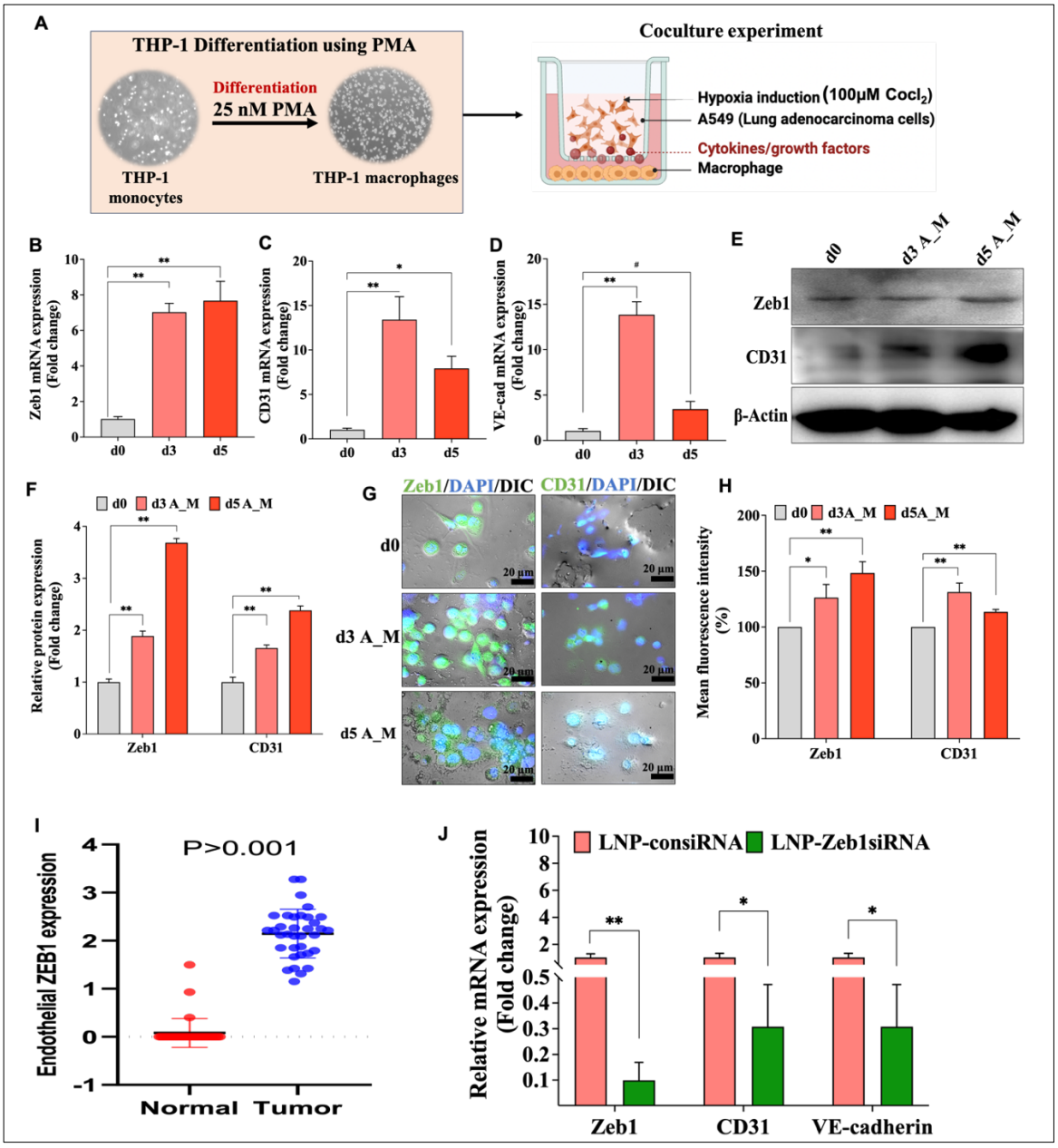

Figure 5.5: Macrophages exhibiting tumor endothelial characteristics with elevated Zeb1 expression *(A) Schematic representation of THP-1 differentiated macrophage using PMA and their coculture experiment in the presence of A549; A549 cells grown on upper chamber and THP-1 macrophages cells were grown on the bottom chamber well, further treated with $cocl_2$ and incubated for day 3 and day 5. (B - D) Relative mRNA expression of Zeb1 (B) CD31 (C) and VE-cadherin (D) of macrophages at day 0, day 3 and day 5. (E - F) Western blot analysis of Zeb1 and CD31 protein levels (E) and relative protein quantification (F) of macrophages in day 3 (d3 A_M) and day 5 (day 5 A_M); β-Actin served as a loading control. (G, H) DIC images of differentiated macrophages after immunofluorescent staining with Zeb1 and CD31 (G) and their mean fluorescence intensity (H). (I) Bioinformatic analysis of Zeb1 mRNA levels in the endothelial cell of normal and lung adenocarcinoma patient samples. The data were collected from a public data set of endothelial gene expression in human lung cancer https://endotheliomics.shinyapps.io/lung_ectax/, two side student t-test. (J) Relative mRNA expression of Zeb1, CD31 and VE-cadherin of LNP-consiRNA or LNP-Zeb1siRNA transfected macrophages, cocultured with A549. Data are presented as the mean ± SD of three independent experiments. $^{\#}P < 0.05$; *P < 0.01; **P < 0.001; ns, non-significant, compared with the normal group.*

5.2.6 CD11b+ macrophages from 3D lung tumor spheroids gained endothelial phenotypes

Fig. 5.6 A image illustrates the process of isolating CD11b+ macrophages using magnetic-activated cell sorting (MACS) from 3D spheroids of AT (A549 + THP-1) and BT (BEAS-2B + THP-1) for downstream analysis. Flow cytometric analysis revealed a significant increase in expressing VE-cadherin (5.09%) and CD31 (17%) in CD11b+ macrophages isolated from the day10 late AT spheroids **(Fig. 5.6 B – C)**, with respect to the day 4 early AT spheroid indicates attaining of endothelial markers. Also in this study we examined CD163 as M2 macrophage control marker to monitor the shift from TAM to tumor endothelial cell (TEC) phenotypes by assessing CD163 expression. Additionally there was a notable increase in VE-cadherin (4.26%), and CD31 (19%) cell population observed in the day 10 AT spheroid compared to the day10 BT spheroid **(Fig. 5.6 D - E)**.These results indicate gaining of endothelial properties by the macrophage in the day 10 A549 + THP-1 spheroids, which indicating the transformation of macrophage into tumor endothelial cell phenotype like. Furthermore, mRNA expression analysis of MACS sorted macrophages showed significant upregulation of *Zeb1*, *CD31*, *VE-cadherin*, and iPSC markers *Oct-4* and *Sox-2* (**Fig. 5.6 F - G**) in CD11b+ macrophages from day10 lung adenocarcinoma AT spheroids compared to normal lung epithelial BT spheroids. Overall, these findings highlight the TAMs plasticity towards endothelial is augmented in advanced tumors which could be the reason for tumor angiogenesis.

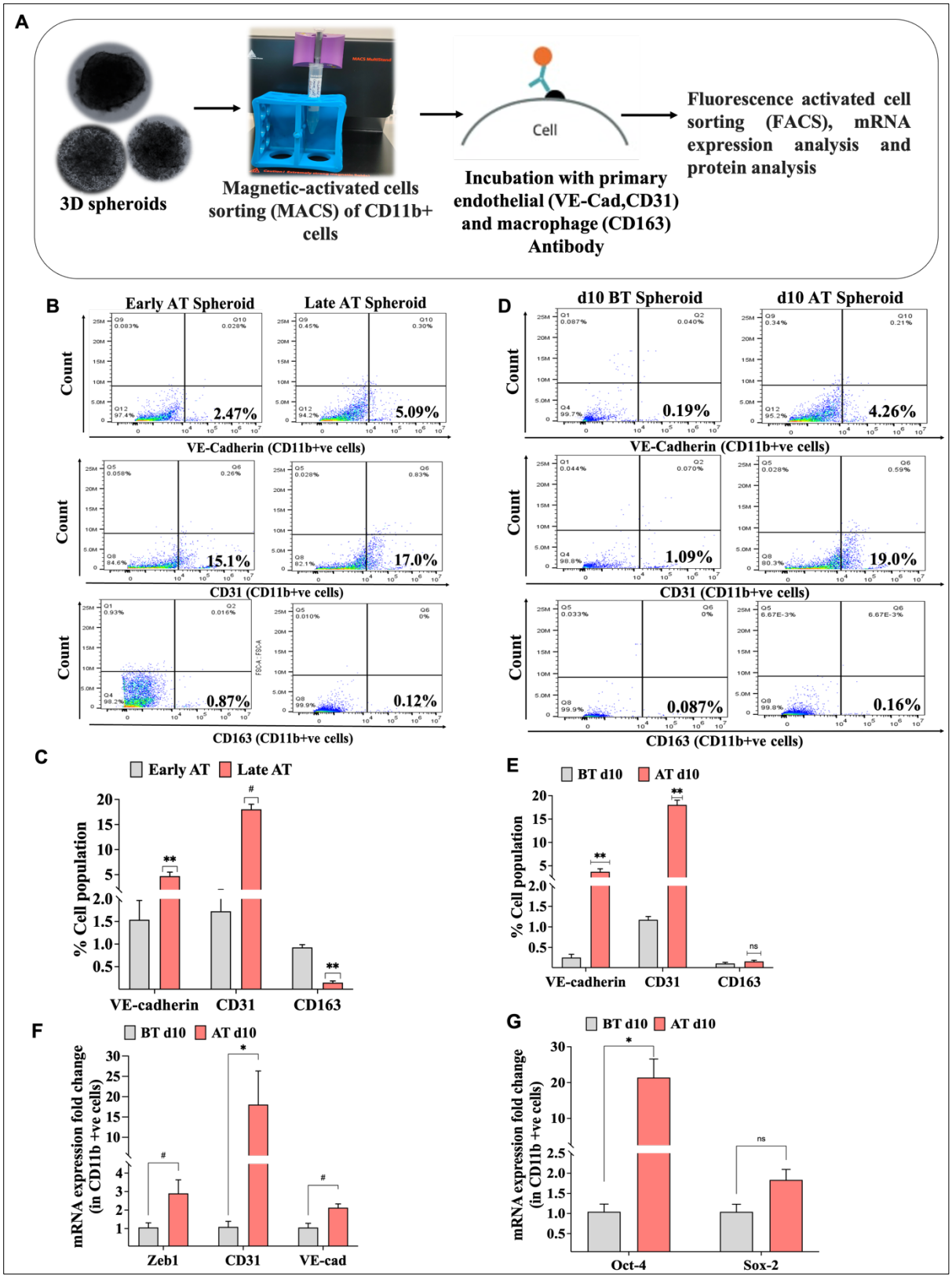

Figure 5.6: Endothelial marker expression in CD11b + macrophages from tumor spheroids

(A) Schematic representation of the isolation process for CD11b+ macrophages from 3D spheroids (A549 + THP-1 and BEAS-2B + THP-1) using magnetic-activated cell sorting with anti-human CD11b+

*microbeads. (B-E) Flow cytometric analysis and quantification of VE-cadherin+, CD31+, and CD163+ cells in early (day 4) and late (day 10) A549 + THP-1 (AT) spheroids (B-C), and comparison of day 10 BEAS-2B + THP-1 (BT) spheroids versus day 10 AT spheroids (D-E). (F-G) mRNA expression analysis of Zeb1, CD31, VE-cadherin (F), and Oct-4, Sox-2 (G) in CD11b+ macrophages isolated from day 0 BT versus AT spheroids. Data are presented as the mean ± SD of three independent experiments. Statistical significance is indicated as #P < 0.05; *P < 0.01; **P < 0.001; ns, not significant.*

5.3 Discussion

Tumor angiogenesis is a crucial process for the growth and metastasis of solid tumors, as it provides the sufficient oxygen and nutrients to sustain tumor progression and their development [1-3, 17-25]. The tumor microenvironment (TME), characterized by hypoxia, acidic conditions, and high interstitial fluid pressure, drives the angiogenic process [25-33]. Zinc-finger E-box binding homeobox 1 (Zeb1) has emerged as a significant regulator in this context [4-6,34]. Zeb1 is not only involved in promoting epithelial-mesenchymal transition (EMT) but also plays a pivotal role in enhancing the expression of pro-angiogenic factors within tumor endothelial cells [35]. Our study provides novel insights into the role of Zeb1 in tumor angiogenesis, particularly within the TME. Previous research has shown that Zeb1 is predominantly expressed in tumor endothelial cells rather than tumor epithelial cells, and its overexpression is associated with poor prognosis in lung adenocarcinoma (LUAD) [4-6, 36]. Zeb1 drives the angiogenic process by upregulating VEGF and other pro-angiogenic factors, leading to the formation of abnormal blood vessels that facilitate tumor growth and metastasis [37-39].

We hypothesized that targeting Zeb1 could be an effective strategy to disrupt angiogenesis and impede tumor progression. To test this hypothesis, in the present study, we developed a Zeb1 specific siRNA therapy delivered via cationic liposome nanoparticles (LNPs). Our LNP-Zeb1siRNA formulation demonstrated efficient cellular uptake, stability, and silencing of Zeb1 expression both *in vitro* and *in vivo*. The downregulation of Zeb1 led to a significant reduction in the expression of angiogenic markers, such as CD31, VEGFA, and VE-cadherin, which are critical for endothelial cell function and tumor vascularization.

In vitro and *in vivo* plug Matrigel assay of LNP-Zeb1siRNA treatment resulted in a marked inhibition of endothelial cell tubule formation, indicating impaired tumor angiogenesis. Moreover, in a 4T1 C57BL/6 mouse tumor xenograft model, LNP-Zeb1siRNA treatment significantly reduced tumor size, volume, and weight, with a corresponding decrease in Zeb1 and angiogenic marker expression. These findings demonstrate the therapeutic potential of LNP-Zeb1siRNA in targeting tumor angiogenesis.

Beyond its role in forming blood vessels, Zeb1 also influence macrophage plasticity within the hypoxic TME [40]. Our results suggest that Zeb1 may drive the differentiation of macrophages into tumor endothelial-like cells, thereby contributing to abnormal angiogenesis. In hypoxic coculture conditions with A549 cells, macrophages exhibited increased expression of Zeb1, CD31, and VE-cadherin, markers associated with an endothelial-like phenotype. This observation aligns with the hypothesis that

Zeb1 facilitates the plasticity of tumor-associated macrophages (TAMs) into tumor endothelial cells (TECs)

The use of a 3D spheroid model of lung adenocarcinoma, further revealed the potential of TAMs to adopt endothelial characteristics under the influence of Zeb1. CD11b+ macrophages isolated from 3D lung adenocarcinoma spheroids showed enhanced expression of endothelial markers such as VE-cadherin and CD31. While successful silencing of Zeb1 inhibit tumor growth and metastasis by targeting angiogenesis. Furthermore, the observed plasticity of TAMs also disrupt, thus, offering a promising therapeutic strategy to cancer therapy. Future research is required especially on LUAD tumor mice model and for elucidating the molecular mechanisms underlying Zeb1-mediated macrophage transformation and its impact on tumor angiogenesis, the Zeb-1 knockout model is vital one.

In conclusion, the successful silencing of Zeb1 using LNP-Zeb1siRNA presents a promising therapeutic strategy to inhibit tumor growth and metastasis by targeting tumor angiogenesis. Targeting Zeb1 may also disrupt macrophages to endothelial conversion within the hypoxic TME. Overall this study suggest that Zeb1 could be a potential therapeutic candidate for the treatment of solid tumors, particularly, in context of lung and breast tumors.

5.4 Materials and methods

5.4.1 Reagents and antibodies: The list of all antibodies, siRNA and reagents provided in Tables A - C (Appendix)

5.4.2 Synthesis of cationic liposomes nanoparticle (LNP)

For preparation of cationic liposomes previously optimised modified [16,17] ethanol injection (MEI) method was used, in which all the lipids i.e. DC-Chol and DOPE were dissolved in about 5ml of ethanol in 1:2 (DC-Chol: DOPE), and the ethanol was removed with a rotary evaporator leaving behind about 2ml of the ethanol solution. Next, a constant volume of sterile water was added to the ethanol solution. Liposomes formed after further evaporation of the residual ethanol. The liposome suspension was immediately filtered through 0.45-µm Millex-HA filters for sterilization. The particle size distribution of liposomes was determined using a dynamic light-scattering instrument, and the zeta-potential of them were determined by the electrophoresis light-scattering method at 25^{o}C after by diluting of dispersion to an appropriate volume with water.

5.4.3 Characterization of liposome nanoparticle

The particle mean size, polydispersity index (PDI) and surface charge (ζ-potential) of these prepared liposomes nanoparticle's were determined using Dynamic Light Scattering (DLS) and zetasizer (Nano ZSP) with a 633 nm laser method respectively. Samples were diluted 1:10 for measurements. Zeta potential is influenced by pH, ionic strength, and temperature based on the interaction of particles with counter-ions and co-ions. Moreover, field emission scanning electron microscopy (FESEM) was applied to verify the shape and nanoliposomes size dimensions.

5.4.4 Conjugation of cationic liposome with Zeb1siRNA

Zeb1siRNA (Stock concentration 10μM; SC-38643) was complexed with cationic liposomes at different varied molar ratios (N/P ratios), including 1:1 (1μM liposomes: 10nM siRNA), 2:1 (2μM liposomes: 10nM siRNA), and 3:1 (3μM liposomes:10nM siRNA) in 1.5ml Eppendorf tube. Subsequently both mixtures were combined at the appropriate concentrations in tris buffer (pH 80), followed by a quick centrifugation and 1–2 hours of RT incubation. Meanwhile, a short centrifugation procedure was carried out in a tabletop microcentrifuge.

Loading Efficiency determination

5.4.5 Gel retardation assay

A gel retardation experiment was used to confirm the formation of the complexes formed when Zeb1siRNA (SC-38643) was complexed with the cationic liposomes at varied molar ratios. 1.5% agarose gel was prepared in 1xTBE buffer for the gel retardation experiment. Conjugated liposome Zeb1siRNA 10 μl were loaded on the gel at different ratios of N/P 1:1 (1μM liposomes: 10nM siRNA), 2:1 (2μM liposomes: 10nM siRNA), and 3:1 (3μM liposomes:10nM siRNA), run at 100 volt for 30min. N/P ratio refers to the proportion of nitrogen groups (which are responsible for +ve Charge in cationic liposomes) to phosphate groups in Zeb1siRNA (an anionic give –ve charge**).** We were able to produce siRNA lipoplexes that could be loaded very effectively, did not aggregate, could be stored at 4 °C for at least 6 months with just a minimal release of siRNA (1–5%), and were improved.

5.4.6 Cell culture

The human lung adenocarcinoma cell line A549 was obtained from the National Centre for Cell Science (NCCS), Pune, India, while the human umbilical vein endothelial cell line (HUVEC) was sourced from the American Type Culture Collection (ATCC), USA. The normal human bronchial epithelial cell line BEAS-2B and the acute human monocytic leukemia cell line THP-1 were generously provided by Prof. Anita K. Verma and Dr. R. Mukhopadhyay from Tezpur University, Assam, respectively. BEAS-2B cells were cultured in LHC-9 medium (Gibco™/Life Technologies, catalog no. 12680013), and THP-1 and A549 cells were cultured in RPMI 1640 medium, both supplemented with 10% fetal bovine serum (FBS) and a penicillin-streptomycin solution (10,000 units/ml penicillin, 10 mg/ml streptomycin). All cells were maintained in a humidified incubator with 5% CO2 at 37 °C. HUVEC cells were cultured in EBM2 basal medium (Lonza, USA, catalog no. CC-3156) supplemented with the endothelial cell growth medium Bulletkit (EGM2) (Lonza, USA, catalog no. CC-3162), 10% FBS, and a penicillin-streptomycin solution under the same incubation conditions.

5.4.7 3D Spheroid preparation

The hanging drop method was used to prepare the multicellular 3D tumorigenic and non-tumorigenic spheroids of A549 + THP-1 (AT) and BEAS-2B + THP-1 (BT) cells respectively, in a 90 mm culture dish [27]. A549, BEAS-2B and THP-1 cells were cultured in complete growth medium in T25 flasks. At 80-85% confluency, cells were washed with PBS, treated with Trypsin-EDTA (0.25%) for 3-4 min at 37 °C, neutralized with 4 ml growth medium, and collected in a 15 ml falcon tube. After

centrifugation at 800 rpm for 5 min, cells were resuspended in DMEM complete medium. Approximately 8,000 cells/ml of A549 and 2,000 cells/ml of THP-1 (AT spheroid) and similarly, 8,000 cells/ml of BEAS-2B and 2,000 cells/ml of THP-1 (BT spheroid) were dispensed as 25 µl drops onto the lid of a 90 mm dish, which was then placed on a plate with 6 ml autoclaved water at the bottom. The setup was incubated at 37 °C with 5% CO_2 for 3 days. Spheroids were monitored under a microscope for cell aggregation and proliferation. For cell viability, a live/dead assay was performed on days 5 and 10. Five spheroids were collected, washed with PBS, and incubated with calcein-AM (100 µM) and propidium iodide (750 µM) for 10 min. Spheroids were washed with PBS, placed on a 35 mm dish, and imaged using an inverted fluorescence microscope (Leica DMi8, Germany).

5.4.8 Hypoxia induction: As described earlier in section 4.4.10.

5.4.9 Cellular uptake assay

A549 and HUVEC cells were grown on 22 X 22 mm coverslips. The cells were transfected with LNPcy3ZebsiRNA with 3µM liposomes nanoparticle (LNP) :10nM cy3Zeb1siRNA of concentration ratios and prepared in basal medium. Control cells were untreated and maintained in the respective basal media. After the transfection for 8 h the cells were rinsed with PBS and stained DAPI for nuclear staining for 5 minutes then after cells were washed with PBS and fixed with 4% paraformaldehyde solution. Then further cells washed with 1X DPBS. Cells with coverslip inverted mount on the slide with DPX medium and images acquired by fluorescence microscopy at (Leica, DMi8, Germany) DAPI and Rhodamine channel at 20x and 63x magnification.

5.4.10 RTqPCR assay: As described earlier in section 3.4.7.

5.4.11 Western blot assay: As described earlier in section 3.4.8.

5.4.12 Acetylated low density lipoprotein uptake (AcLDL) uptake assay

HUVEC Cells were seeded into 35mm dish, after 24h cells transfected with liposome alone and LPzeb1siRNA for 24h, before to proceed with transfection cells incubated in an optiMEM media (Gibco) for 10 to 15 min, meanwhile LP and LPZeb1siRNA incubated in an optiMEM media for 10 min. Further cells were treated with LP and LPZeb1siRNA optiMEM media for 8hr. After 8hr cells replaced with the complete media for further 24h. Cells were incubated with Alexa Flour (488 nm) acetylated LDL (Cat no L23380; Invitrogen) (5µg/ml) in EBM2 media at 37 º c for 4hr, on termination of incubations cells were washed in 1x PBS and fixed with 4% paraformaldehyde for 30 min. The uptake of Ac-LDL was analysed by fluorescence microscopy.

5.4.13 *In vitro* Matrigel assay

HUVEC cells were seeded on Matrigel-coated 96-well plates. After treatment with LNP-consiRNA and LNP-Zeb1siRNA, the cells were incubated for 8 hours. Following incubation, tube formation was observed under a phase contrast microscope to assess the effects of the treatments.

5.4.14 Human samples

Human lung tissue samples, pleural fluid, and blood serum were collected from patients with or without non-small cell lung cancer (demographic details provided in Table E, appendix) from the Indira Gandhi Medical College and Hospital (IGMCH), Shimla, India. The Institute Ethics Committee (IEC), PGIMER, Chandigarh, (Protocol # IEC-12/2017-794) and institute biosafety committee (IBSC/1/2020/A/2) approved all human studies. The Declaration of Helsinki protocols were followed, and informed written consent was obtained from all the patients.

5.4.15 4T1 C57BL/6 mice tumor xenograft model

C57BL/6 mice were purchased from NIPER, Mohali, India, and acclimatized for 7 days under controlled temperature and light conditions (25 ºC with a 12:12 hr light/dark cycle). The mice were provided with a standard ad libitum chow diet and distilled water. All experimental procedures adhered to ethical care guidelines, with approval from the Institutional Animal Ethics Committee of Kirori Mal College, University of Delhi (Protocol # KMC/IAEC/2024/01) and the Institute Biosafety Committee (IBSC/1/2020/A/2). The 4T1 cell line was obtained from the American Type Culture Collection (Manassas, VA, USA) and cultured in RPMI-1640 medium with L-glutamine, supplemented with 10% fetal bovine serum (FBS), 0.11 mg/ml sodium pyruvate, 100 U/ml penicillin, and 100 µg/ml streptomycin (Biological Industries, Israel). The cells were maintained at 37 °C in a humidified CO2 incubator. Female C57BL/6 mice (aged 6-8 weeks, weighing 20-24 g) were subcutaneously injected with 1 x 10^6 4T1 breast cancer cells in 100 µL per site on the dorsal flank region [25,26]. Following injection, the mice were housed for 7 days to allow tumor development. After 14 days, the tumor sizes were measured, ranging from 90-120 mm^3 in volume per mouse. Tumor-bearing mice were then divided into four groups (n = 3 per group): PBS (control), LNP (vehicle control), Zeb1siRNA (free siRNA), and LNPZeb1siRNA (treatment). Mice were administered intravenous injections of LNPZeb1siRNA (1.24 mg/kg; 100 µL) and respective controls on alternate days for up to 14 days. Tumor size was measured using vernier calipers in two perpendicular diameters, and the tumor volume was calculated using the formula.

$$Tumor\ volume\ (mm)^3 = \frac{length \times width^2}{2} \quad \text{..... (4)}$$

Following the completion of the treatment regimen, the mice were euthanized, and serum and tumors were harvested for various biochemical, molecular and histopathological studies.

5.4.16 Histological sections: As described earlier in section 4.4.20.

5.4.17 Hematoxylin & eosin (H&E) staining: As described earlier in section 4.4.21.

5.4.18 Immunohistochemistry (IHC) staining: As described earlier in section 4.4.22

5.4.19 *In vivo* plug Matrigel assay

LNP-Zeb1siRNA and 4T1 cells **(2** × 10^6 cells resuspended in 50 µL complete media) were mixed with Matrigel growth factor-reduced media (150 µL, #354263) to form the treatment group. The control group consisted of LNP-consiRNA**,** 4T1 cells**,** and Matrigel growth factor-reduced media**,** with both groups at a concentration of 1.0 µg/mL.The mice were anesthetized using the isoflurane-oxygen inhalation method. The fur on the right flank was shaved, and 500 µL of the freshly prepared cocktail was injected into the right side using a pre-chilled syringe equipped with a 28G needle. A total of 0.5 mL of the prepared mixture was injected subcutaneously into the right flank of 8-week-old C57BL/6 mice.After the mixture solidified into a gel plug within the animals, the mice were returned to their cages with access to food and water. On day 10, the mice were euthanized via chlorofom inhalation, and the Matrigel plugs were carefully extracted. Photographs of the plugs were taken using a digital camera to document the results.

5.4.20 Statistical analysis

Data were obtained from three separate experiments and presented as the mean ± standard deviation of the mean. T-test was employed for comparison among multiple groups using GraphPad Prism 6 software. A value of $p<0.05$ was considered statistically significant.

References

1. Folkman, J. (1971). Tumor angiogenesis: therapeutic implications. *N Engl j Med*, *285*(21), 1182-1186.
2. Folkman, J. (2007). Angiogenesis: an organizing principle for drug discovery?. *Nature reviews Drug discovery*, *6*(4), 273-286.
3. Hapke, R. Y., & Haake, S. M. (2020). Hypoxia-induced epithelial to mesenchymal transition in cancer. *Cancer letters*, *487*, 10-20.
4. Sánchez-Tilló, E., Siles, L., De Barrios, O., Cuatrecasas, M., Vaquero, E. C., Castells, A., & Postigo, A. (2011). Expanding roles of ZEB factors in tumorigenesis and tumor progression. *American journal of cancer research*, *1*(7), 897.
5. Liu, Lingjia, et al. "ZEB1 upregulates VEGF expression and stimulates angiogenesis in breast cancer." *PLoS One* 11.2 (2016): e0148774.
6. Fu, R., Li, Y., Jiang, N., Ren, B. X., Zang, C. Z., Liu, L. J., ... & Wu, Z. Q. (2020). Inactivation of endothelial ZEB1 impedes tumor progression and sensitizes tumors to conventional therapies. *The Journal of Clinical Investigation*, *130*(3), 1252-1270.
7. Seaman, S., Stevens, J., Yang, M. Y., Logsdon, D., Graff-Cherry, C., & Croix, B. S. (2007). Genes that distinguish physiological and pathological angiogenesis. *Cancer cell*, *11*(6), 539-554.
8. Croix, B. S., Rago, C., Velculescu, V., Traverso, G., Romans, K. E., Montgomery, E., ... & Kinzler, K. W. (2000). Genes expressed in human tumor endothelium. *Science*, *289*(5482), 1197-1202.
9. Sistigu, A., Di Modugno, F., Manic, G., & Nisticò, P. (2017). Deciphering the loop of epithelial-mesenchymal transition, inflammatory cytokines and cancer immunoediting. *Cytokine & growth factor reviews*, *36*, 67-77.
10. Arora, L., & Pal, D. (2021). Remodeling of stromal cells and immune landscape in microenvironment during tumor progression. *Frontiers in Oncology*, *11*, 596798.
11. Lorenzo-Sanz, L., & Muñoz, P. (2019). Tumor-infiltrating immunosuppressive cells in cancer-cell plasticity, tumor progression and therapy response. *Cancer microenvironment*, *12*(2), 119-132.
12. Jiang, H., Wei, H., Wang, H., Wang, Z., Li, J., Ou, Y., ... & Yang, S. (2022). Zeb1-induced metabolic reprogramming of glycolysis is essential for macrophage polarization in breast cancer. *Cell Death & Disease*, *13*(3), 206.
13. Darwiche, N. (2020). Epigenetic mechanisms and the hallmarks of cancer: An intimate affair. *American journal of cancer research*, *10*(7), 1954.

14. Yoshimoto, S., Tanaka, F., Morita, H., Hiraki, A., & Hashimoto, S. (2019). Hypoxia-induced HIF-1α and ZEB1 are critical for the malignant transformation of ameloblastoma via TGF-β-dependent EMT. *Cancer Medicine*, *8*(18), 7822-7832.
15. Bardoliwala, D., Patel, V., Javia, A., Ghosh, S., Patel, A., & Misra, A. (2019). Nanocarriers in effective pulmonary delivery of siRNA: current approaches and challenges. *Therapeutic delivery*, *10*(5), 311-332.
16. Gomes-da-Silva, L. C., Fonseca, N. A., Moura, V., Pedroso de Lima, M. C., Simões, S., & Moreira, J. N. (2012). Lipid-based nanoparticles for siRNA delivery in cancer therapy: paradigms and challenges. *Accounts of chemical research*, *45*(7), 1163-1171.
17. Maitani, Y., Igarashi, S., Sato, M., & Hattori, Y. (2007). Cationic liposome (DC-Chol/DOPE= 1: 2) and a modified ethanol injection method to prepare liposomes, increased gene expression. *International journal of pharmaceutics*, *342*(1-2), 33-39.
18. Gentine, P., Bourel-Bonnet, L., & Frisch, B. (2013). Modified and derived ethanol injection toward liposomes: development of the process. *Journal of liposome research*, *23*(1), 11-19.
19. Perez-Oquendo, M., & Gibbons, D. L. (2022). Regulation of ZEB1 function and molecular associations in tumor progression and metastasis. *Cancers*, *14*(8), 1864.
20. Zhang, P., Sun, Y., & Ma, L. (2015). ZEB1: at the crossroads of epithelial-mesenchymal transition, metastasis and therapy resistance. *Cell cycle*, *14*(4), 481-487.
21. Abdul Zani, I., Stephen, S. L., Mughal, N. A., Russell, D., Homer-Vanniasinkam, S., Wheatcroft, S. B., & Ponnambalam, S. (2015). Scavenger receptor structure and function in health and disease. *Cells*, *4*(2), 178-201.
22. Abumrad, N. A., Cabodevilla, A. G., Samovski, D., Pietka, T., Basu, D., & Goldberg, I. J. (2021). Endothelial cell receptors in tissue lipid uptake and metabolism. *Circulation research*, *128*(3), 433-450.
23. Kim, S. W., Kim, H., Cho, H. J., Lee, J. U., Levit, R., & Yoon, Y. S. (2010). Human peripheral blood-derived CD31+ cells have robust angiogenic and vasculogenic properties and are effective for treating ischemic vascular disease. *Journal of the American College of Cardiology*, *56*(7), 593-607.
24. Lugano, R., Ramachandran, M., & Dimberg, A. (2020). Tumor angiogenesis: causes, consequences, challenges and opportunities. *Cellular and Molecular Life Sciences*, *77*, 1745-1770.
25. Xiao, W., Zhang, W., Huang, H., Xie, Y., Zhang, Y., Guo, X., ... & Song, X. (2019). Cancer targeted gene therapy for inhibition of melanoma lung metastasis with eiF3i shRNA loaded liposomes. *Molecular Pharmaceutics*, *17*(1), 229-238.

26. Katsuta, E., DeMasi, S. C., Terracina, K. P., Spiegel, S., Phan, G. Q., Bear, H. D., & Takabe, K. (2016). Modified breast cancer model for preclinical immunotherapy studies. *journal of surgical research*, *204*(2), 467-474.
27. Arora, L., Kalia, M., Dasgupta, S., Singh, N., Verma, A. K., & Pal, D. (2022). Development of a multicellular 3D tumor model to study cellular heterogeneity and plasticity in NSCLC tumor microenvironment. *Frontiers in Oncology*, *12*, 881207.
28. Delgado-Bellido, D., Serrano-Saenz, S., Fernández-Cortés, M., & Oliver, F. J. (2017). Vasculogenic mimicry signaling revisited: focus on non-vascular VE-cadherin. *Molecular cancer*, *16*, 1-14.
29. Boutilier, A. J., & Elsawa, S. F. (2021). Macrophage polarization states in the tumor microenvironment. *International journal of molecular sciences*, *22*(13), 6995.
30. Zhang, X., Zhu, M., Hong, Z., & Chen, C. (2021). Co-culturing polarized M2 Thp-1-derived macrophages enhance stemness of lung adenocarcinoma A549 cells. *Annals of Translational Medicine*, *9*(8).
31. Silva, V. L. (2017). Exploiting the cancer niche: tumor-associated macrophages and hypoxia as promising synergistic targets for nano-based therapy. *Journal of Controlled Release*, *253*, 82-96.
32. Bai, R., Li, Y., Jian, L., Yang, Y., Zhao, L., & Wei, M. (2022). The hypoxia-driven crosstalk between tumor and tumor-associated macrophages: mechanisms and clinical treatment strategies. *Molecular Cancer*, *21*(1), 177.
33. Baghban, R., Roshangar, L., Jahanban-Esfahlan, R., Seidi, K., Ebrahimi-Kalan, A., Jaymand, M., ... & Zare, P. (2020). Tumor microenvironment complexity and therapeutic implications at a glance. *Cell Communication and Signaling*, *18*, 1-19.
34. Kim, H. R., Seo, C. W., & Kim, J. (2022). Zinc Finger E-Box Binding Homeobox 1 as Prognostic Biomarker and Its Correlation with Infiltrating Immune Cells and Telomerase in Lung Cancer. *Biomedical Science Letters*, *28*(1), 9-24.
35. Jin, L., Zhang, Y., Liang, W., Lu, X., Piri, N., Wang, W., ... & Liu, Y. (2020). Zeb1 promotes corneal neovascularization by regulation of vascular endothelial cell proliferation. *Communications Biology*, *3*(1), 349.
36. Wu, H. T., Zhong, H. T., Li, G. W., Shen, J. X., Ye, Q. Q., Zhang, M. L., & Liu, J. (2020). Oncogenic functions of the EMT-related transcription factor ZEB1 in breast cancer. *Journal of translational medicine*, *18*, 1-10.
37. Ribatti, D., Tamma, R., & Annese, T. (2020). Epithelial-mesenchymal transition in cancer: a historical overview. *Translational oncology*, *13*(6), 100773.
38. Yehya, A. H. S., Asif, M., Petersen, S. H., Subramaniam, A. V., Kono, K., Majid, A. M. S. A., & Oon, C. E. (2018). Angiogenesis: managing the culprits behind tumorigenesis and metastasis. *Medicina*, *54*(1), 8.

39. Muz, B., De La Puente, P., Azab, F., & Kareem Azab, A. (2015). The role of hypoxia in cancer progression, angiogenesis, metastasis, and resistance to therapy. *Hypoxia*, 83-92.
40. Cortés, M., Sanchez-Moral, L., de Barrios, O., Fernández-Aceñero, M. J., Martínez-Campanario, M. C., Esteve-Codina, A., ... & Postigo, A. (2017). Tumor-associated macrophages (TAMs) depend on ZEB1 for their cancer-promoting roles. *The EMBO journal*, *36*(22), 3336-3355.

Chapter 6

Summary

6.1 Highlights

This thesis explores three different therapeutic approaches to manage solid tumors especially NSCLC and TNBC tumors, showcasing the versatility in cancer therapeutics. Also discovers the detailed mechanistic insights - how IMPA derivatives, L-ONB, and LNP-Zeb1siRNA exert their therapeutic effects against non-small cell lung cancer and/or breast cancer, thereby deepening our knowledge on the potential cancer treatment strategies against hypoxia mediated chemoresistance and metastasis. The following key findings have emerged from this study were highlighted below:

1. Five novel IMPA derivatives (IMPA-2, -5, -6, -8, -12) were designed and synthesized, combining imidazo[1,2-a]pyridine with 2-amino-4H-pyran, showing potent anti-cancer activity against lung adenocarcinoma by inducing apoptosis and cell cycle arrest.
2. These IMPA derivatives enhance ROS production, leading to mitochondrial membrane disruption and activation of the intrinsic apoptotic pathway. IMPA-2, -5, -6, and -12 derivatives induced cell cycle arrest at the G0/G1 phase, while IMPA-8 arrested cells at the G2/M phase with associated upregulation of p53 and its target genes while inactivating p38 MAPK, which is linked to tumor progression. In addition to their anti-proliferative properties, the IMPA derivatives significantly reduce cancer cell migration and invasion, key features associated with tumor metastasis.
3. IMPA derivatives demonstrated significant anti-proliferative and pro-apoptotic effects also in *in vitro* lung cancer cells and 3D multicellular lung tumor spheroids, suggesting their potential utility *in vivo* and making them promising candidates for further development as treatments for non-small cell lung cancer.
4. Among the five IMPA derivatives, IMPA-2 showed the most promising anti-cancer efficacy against A549 and NCI-H23 lung cancer cells based on IC50 values. The hydrophobic -CH3 group in IMPA-2 enhances its biological activity by fitting into the active site of NADPH oxidase. Future SAR (structure activity relationship) analysis could explore more hydrophobic substitutions to further improve its efficacy.
5. L-ONBs were developed to target hypoxia within tumors, showing improved colloidal stability and sustained oxygen release compared to other oxygen bubble systems. The encapsulation within liposomes composed of DPPC and cholesterol provided protection and stability, maintaining size and charge consistency for nearly two weeks.

6. L-ONB treatment destabilizes HIF-1α in both lung adenocarcinoma cells and 4T1 BALB/c tumor xenograft models and mitigate hypoxia's effect on tumor aggressiveness including suppression of EMT, cancer cell invasion and migration.
7. Histopathological examinations of spleen, lung, liver, and kidney tissues in the 4T1 BALB/c mice model confirmed the effectiveness of L-ONB in attenuating breast cancer migratory behaviour, highlighting its therapeutic potential in in vivo applications.
8. A significant increase in doxorubicin's cytotoxic effect in the presence of L-ONBs elucidate the role of L-ONB in enhancing the sensitivity of hypoxic tumor cells to chemotherapy, thus L-ONB also work as a highly promising adjuvant candidate for solid tumor therapy, with potential clinical application.
9. Zeb1 plays a crucial role in promoting angiogenesis within the hypoxic tumor microenvironment (TME) by upregulating pro-angiogenic factors such as VEGF, leading to the formation of abnormal blood vessels that support tumor growth and metastasis.
10. Zeb1 influences the transformation of tumor-associated macrophages (TAMs), into tumor endothelial-like cells (TECs) that contribute to abnormal angiogenesis. Targeting Zeb1 could potentially disrupt both the pro-angiogenic and immunosuppressive roles of macrophages within the TME.
11. The study demonstrated that silencing Zeb1 using a specific siRNA delivered via cationic liposome nanoparticles (LNP-Zeb1siRNA) effectively reduced angiogenic markers and tumor vascularization, leading to a significant decrease in tumor size and progression in both *in vitro* and *in vivo* models.

6.2 Conclusions

This pivotal study has not only elucidated the mechanisms of IMPA derivatives, L-ONB, and LNP-Zeb1siRNA against non-small cell lung cancer (NSCLC) and/or triple-negative breast cancer (TNBC) but also shed light on the crucial role of Zeb1 in gaining endothelial characteristics by tumor-associated macrophage within the tumor microenvironment. This findings offer significant insights into overcoming hypoxia-induced chemoresistance and metastasis, as well as targeting Zeb1-mediated tumor angiogenesis and open up new avenues for therapeutic interventions combating the challenges of tumor progression and treatment resistance.

It has been found that IMPA-2, -5, -6, -8, and -12 effectively induce ROS-mediated cell cycle arrest and apoptosis in human lung adenocarcinoma cells through the activation of p53-dependent pathways and the intrinsic apoptotic mechanism. Among these, IMPA-2 and IMPA-6 stand out as the most potent anti-cancer agents against A549 and NCI-H460 non-small cell lung cancer cells. These findings underscore the multifaceted potential of IMPA derivatives, particularly IMPA-2 and IMPA-6, as

promising candidates for the treatment of lung adenocarcinoma. Consequently, these compounds merit further exploration and development as lead agents in lung cancer therapy.

Coming to the second objectives of this study, emphasize the significant potential of liposome-encapsulated oxygen nanobubbles (L-ONB) as an innovative therapeutic approach for targeting hypoxia-associated cancers. L-ONBs demonstrated exceptional stability, efficient oxygen delivery, and potent anti-cancer effects by inhibiting hypoxia-induced tumor aggressiveness. Notably, L-ONBs effectively suppressed the HIF-1α-mediated epithelial-to-mesenchymal transition (EMT), migration, and metastasis of cancer cells, showcasing their potential as a promising adjuvant therapy for solid tumors. While these findings highlight the therapeutic efficacy of L-ONB, future studies should explore their impact on immune responses to fully understand their clinical applicability. Thus, L-ONBs offer a novel and effective strategy for enhancing cancer treatment by targeting tumor hypoxia.

However, the successful silencing of Zeb1 using LNP-Zeb1siRNA highlights a promising therapeutic approach for inhibiting tumor growth and metastasis by specifically targeting tumor angiogenesis. Zeb1, as a key regulator within the tumor microenvironment (TME), plays a pivotal role in promoting angiogenesis by upregulating pro-angiogenic factors in tumor endothelial cells and influencing in the gaining of endothelial characteristics by tumor-associated macrophages (TAMs). Our study also demonstrates that targeting Zeb1 not only disrupts angiogenesis but also impairs the transdifferentiation of TAMs into tumor endothelial-like cells, contributing to abnormal blood vessel formation within tumors. The therapeutic potential of LNPZeb1siRNA was evident through its ability to reduce angiogenic markers, impair LUAD cell migration, and significantly decrease tumor size *in vivo*. Moreover, by inhibiting Zeb1, this strategy may also mitigate the pro-angiogenic and immunosuppressive roles of TAMs within the TME, providing a multifaceted approach to cancer therapy. Overall, the findings suggest that Zeb1 is a critical target for developing anti-angiogenic therapies, with the potential to enhance treatment efficacy and improve outcomes for patients with solid tumors. Further research is warranted to explore the molecular mechanisms underlying Zeb1-mediated macrophage polarization and to validate the clinical applicability of LNP-Zeb1siRNA in different cancer models.

6.3 Future Perspectives

The promising results obtained from the study of IMPA derivatives, particularly IMPA-2, -5, -6, -8, and -12, in inducing apoptosis and cell cycle arrest in lung adenocarcinoma cells, along with the therapeutic potential of liposome-encapsulated oxygen nanobubbles (L-ONBs) and LNP-Zeb1 siRNA, underline the need for further research. It is crucial to further elucidate the role of Zeb1 in tumor angiogenesis

and macrophage plasticity, particularly in non-small cell lung cancer (NSCLC) and triple-negative breast cancer (TNBC).

In this thesis, we emphasize the significance of the current findings and outlined the key future perspectives:

1. While the current study demonstrated the anti-cancer potential of IMPA derivatives *in vitro* 2D and 3D model cancer cell lines, it is essential to evaluate their efficacy and safety *in vivo* animal models of lung adenocarcinoma. Such studies will provide critical insights into the pharmacokinetics, biodistribution, toxicity, and therapeutic index of these compounds, paving the way for their translation into clinical settings.
2. Given the complex nature of cancer, future studies should explore the potential of IMPA derivatives in combination with other therapeutic agents, such as chemotherapy, targeted therapy, or immunotherapy. Combining IMPA derivatives with existing treatments could enhance therapeutic outcomes, overcome drug resistance, and reduce the likelihood of cancer recurrence.
3. One of the significant challenges in cancer therapy is the development of resistance to chemotherapeutic agents. Future studies should investigate whether long-term treatment with IMPA derivatives could lead to the emergence of drug-resistant cancer cell populations and, if so, explore strategies to overcome or prevent resistance.
4. To enhance the therapeutic efficacy and reduce off-target effects, future studies should explore the development of advanced drug delivery systems, such as nanoparticles, liposomes, or hydrogels, for the targeted delivery of IMPA derivatives to lung tumors. These delivery systems could improve the bioavailability, stability, and tumor-specific accumulation of IMPA derivatives, maximizing their therapeutic potential.
5. The ultimate goal of preclinical research is to translate promising compounds into clinical practice. Future efforts should focus on the early-phase clinical trials of the most potent IMPA derivatives to assess their safety, tolerability, and preliminary efficacy in patients with lung adenocarcinoma. Success in clinical trials could lead to the development of a new class of anti-cancer agents for the treatment of lung cancer.
6. Given the multifaceted role of hypoxia in tumor progression, combining L-ONBs with existing therapies, such as chemotherapy, radiotherapy, or targeted therapies, could enhance therapeutic outcomes. Future studies should explore the synergistic effects of such combination approaches, with the goal of maximizing anti-tumor efficacy while minimizing side effects.
7. While this study primarily focused on lung and breast cancer models, the potential of L-ONBs to target hypoxia could be extended to other solid tumors, such as pancreatic, liver, and ovarian cancers. Future research should explore the applicability of L-ONBs across a broader spectrum of cancer types.

8. A deeper understanding of the molecular pathways through which Zeb1 regulates macrophage transdifferentiation to endothelial cells and angiogenesis is essential that will provide valuable insights for refining therapeutic strategies.
9. Given the multifaceted role of Zeb1 in tumor progression, combining LNP-Zeb1siRNA with other therapeutic approaches, such as immune checkpoint inhibitors, chemotherapy, or radiotherapy, could enhance anti-tumor efficacy. Exploring such combination strategies may offer synergistic effects, leading to more robust and durable responses in cancer patients.
10. To bridge the gap between preclinical success and clinical application, future studies should explore the safety, pharmacokinetics, and pharmacodynamics of LNP-Zeb1siRNA in various other cancer models. Conducting comprehensive toxicology studies and phase I clinical trials will be important steps in validating its potential as a viable cancer therapy.

In summary, the future perspectives emphasize the need for rigorous *in vivo* studies to evaluate the safety and efficacy of IMPA derivatives aiming for their translation into clinical practice. Combining these compounds with existing therapies could enhance therapeutic outcomes, overcome drug resistance, and target hypoxic tumor microenvironments. Advanced drug delivery systems are proposed to improve the specificity and bioavailability of these agents. Furthermore, understanding the molecular mechanisms and identifying biomarkers associated with treatment responses will be critical for patient stratification and personalized therapy. Early-phase clinical trials are essential to validate these promising therapeutic approaches for lung adenocarcinoma and other solid tumors.

Table A: List of antibodies and their details

Antibody	Dilution	Company	Catalog No.
p44/42 MAPK (Erk1/2) (Thr-202/Tyr D13.14.4E	1:2000 for WB	Cell Signaling Technology	#4370
Phospho-p38 MAPK (Thr-180/Tyr-182; D3F9	1:1000 for WB	Cell Signaling Technology	#4511
Cleaved Caspase 3 (Asp-175)	1:1000 for WB	Cell Signaling Technology	#9661S
PARP-1	1:1000 for WB	Bio Bharati Life Science	#BB-AB0280
Anti-caspase 9 Rabbit	1:2000 for WB	Bio Bharati Life Science	#BB-AB0245
Caspase 8	1:2000 for WB	Bio Bharati Life Science	#BB-AB0244
HIF1α	1:2000 for WB 1:200 for IHC	Affinity Bioscience	#AF1009
Anti - Zeb1 mouse	1:5000 for WB 1:200 for ICC	Abcam	#ab181451
Anti- Zeb1Rabbit	1:1000 for WB 1:100 for IHC	Abclonal	#A1500
Ant-CD31mouse	1:1000 for WB 1:800 for ICC	Cell Signaling Technology	#3528S
Anti-CD31/PECAM1 Rabbit	1:2000 for WB 1:500 for ICC/IHC	Abclonal	#A19014
Anti-VE-cadherin Rabbit	1:1000 for WB 1:100 for IF	Cell Signaling Technology	#2158S
β-actin	1:1000 for WB	Invitrogen	#AM4302
E-cadherin	1:2000 for WB 1:100 for IHC	Affinity Biosciences	#AF0131
Vimentin	1:2000 for WB 1:100 for IHC	Affinity Biosciences	#AF7013
pSmad2/3	1:5000 for WB 1:100 for IHC	Affinity Bioscience	#AF3367
Anti-Rabbit IgG (Alexa Fluor 568 conjugated)	2µg/ml for ICC 2µg/ml for IHC	Invitrogen	#A-1101
HRP conjugated Anti-Mouse IgG antibody	1:20000 for WB	Sigma-Aldrich	#A9044
HRP conjugated Anti-Rabbit IgG antibody	1:20000 for WB	Sigma-Aldrich	#A9169
Anti-human CD144 (VE-cadherin) PE	5µl/million cells for FC	BioLegend	#348505
Anti-human CD163 APC	5µl/million cells for FC	Invitrogen	#17-1639-41
Anti-human CD31 FITC	5µl/million cells for FC	BioLegend	#303104
TruStainFcX™ (anti-mouse CD16/32)	0.1µg/million cells for FC	BioLegend	#101319
CD11b microbead human, mouse	20 µl/million cells for LS column	Miltenyi	#130-049-601

Table B: List of siRNAs and their details

siRNA	Concentration	Company	Catalog No.
Zeb1siRNA (h)	10 μM	Santa cruz Biotechnology	#SC-38643
Cy3Zeb1siRNA sequence		Sigmaaldrich	
Zeb 1_1975-S [Cyanine3] CAGUCUGGGUGUAAUCGUA [dT][dT] UACGAUUACACCCAGACUG [dT][dT]			VC30002N
Zeb 1_1976-S [Cyanine3] GGCGAUAGAUGGUAAUGUA [dT][dT] UACAUUACCAUCUAUCGCC [dT][dT]			VC30002N

Table C: List of chemicals

Chemicals		
RPMI-1640	Gibco	Cat#11875093
DMEM	Gibco	Cat#11995073
EMEM	Lonza	Cat#12-125Q
LHC-9	Gibco	Cat# 12680013
EGM™ Endothelial growth medium -2 Bulletkit	Lonza	Cat#CC-3162
Leibovitz's L15 medium with 2mM glutamine	HIMEDIA	Cat#AL01AA
FBS US origin	HIMEDIA	CatRM10409
Penicillin/Streptomycin	Gibco	Cat#15140122
DPBS	Gibco	Cat# 14190-144
Trypsin 0.25% EDTA	Gibco	Cat# 25200072
Calcein-AM	Thermo fisher scientific	Cat# C3099
Curcumin	Sigma	C1386
Propidium iodide	Thermo fisher scientific	Cat# P1304MP
DAPI	Thermo fisher scientific	Cat# D1306
Trizol reagent	Invitrogen	Cat# 15596018
Image-iT green hypoxia reagent	Invitrogen	Cat# I14834
iScript cDNA synthesis kit	BIO-RAD	Cat# 1708891
Universal SYBR Green Supermix	BIO-RAD	Cat# 172-5124
Single Cell Lysis Kit	Thermo Fisher Scientific	Cat# 4458235
16% Formaldehyde Solution	Thermo fisher scientific	Cat# 28906
Tissue freezing medium	Leica	Cat#14020108926
Triton X-100	Sigma	Cat#T8787
Isopropanol	HIMEDIA	Cat# MB063
Acetone	Merk	Cat# SD7F670190

cDNA kit	Biobharti	Cat#E0043
Chloroform	SRL	Cat# 84155
Methanol	Merck	Cat# SGOP700408
Ethanol molecular grade	Merck	Cat#100983
Geltrex™ LDEV-Free Matrigel	Invitrogen	Cat#A1413301
MTT powder	HIMEDIA	Cat#TC191
DCFDA	sigma	Cat# D6883
JC-1 dye	Thermo Fisher Scientific	Cat# T3168
Sodium dodecyl sulphate (SDS) powder	BIO-RAD	Cat#1610301
Ammonium persulphate	Sigma	Cat#A3678
Tris Base	BIO-RAD	Cat#1610719
Sodium chloride	HIMEDIA	Cat#GRM031
Glycine	BIO-RAD	Cat#1610718
TEMED	Thermo Fisher Scientific	Cat#17919
PVDF membrane	Merck	Cat#IPVH00010
Clarity Western ECL substrate	BIO-RAD	Cat#1705061
Doxorubicin	TCI	Cat#D4193
Cobalt Chloride	Sigma	Cat#232696
FITC	Sigma	Cat#46950
MG132	Thermo Fisher Scientific	Cat#ALF-J63250-MA
DPPC (Dipalmitoyl phosphatidylcholine)	Avanti Polar Lipids	Cat#850355
Cholesterol	HIMEDIA	Cat#GRM335
Diethyl ether	Merck	Cat#107024
BCA protein assay kit	Thermo Fisher Scientific	Cat#23227
Protease inhibitor cocktail (200x)	Cell Signalling Technology	Cat#7012
NP40 cell lysis buffer	Thermo Fisher Scientific	Cat#FNN0021
DPX Mountant	SRL	Cat#88147
DOTAP	Avanti Polar Lipids	Cat#890890
DC-chol	Avanti Polar Lipids	Cat700001
Acetylated LDL uptake assay kit (Alexa Fluor™ 488 AcLD)	Thermo Fisher Scientific	Cat#L23380

Table D: Primer sequence

Human primers		
Gene	Forward (5'-3')	Reverse (5'-3')
Bax	*TCTGACGGCAACTTCAA CTG*	*AGTCCAATGTCCAGCCC ATG*
Bak1	*CCTGCCCTCTGCTTCTGA*	*CTGCTGATGGCGGTAAAAA*
BCL2L11	*CTGCTGGACACACACAT ACA*	*GGGCTGAGGAAACAGAGTAAA*
18s	*AGC TTA TGA CCC GCA CTT C*	*GTC TGT GAT GCC CTT AGA TG*
GAPDH	*AGC CAC ATC GCT CAG ACA*	*GCC CAA TAC GAC CAA ATC C*
P16	*CTGCCCAACGCACCGAATAG*	*CCACCAGCGTGTCCAGGAAG*
P21	*TGCCGAAGTCAGTTCCTTGT*	*GTTCTGACATGGCGCCTCC*
P27	*GGCTTTCAGATTCCCAACTT*	*AGCCTCCCCACTCTCGTCT*
P53	*TGA CAC GCT TCC CTG GAT TG*	*GCT CGA CGC TAG GAT CTG AC*
HIF-1α	*GTG GTG GTT ACT CAG CACT*	*CGT CCC TCA ACC TCT CAG TT*
E-cadherin	*CGGGAATGCAGTTGAGGATC*	*AGGATGGTGTAAGCGATGGC*

Fibronectin	*TGAAAGACCAGCAGAGGCATAAG*	*CTCATCTCCAACGGCATAATGG*
N-cadherin	*ACCAGGTTTGGAATGGGACAG*	*ATGTTGGGTGAAGGGGTGCTTG*
Snail	*ATCGGAGCCTAACTACAGCGAGC*	*CAGAGTCCCAGATGAGCATTGG*
Vimentin	*TACAGGAAGCTGCTGGAAGG*	*ACCAGAGGGAGTGAATCCAG*
TGF-β	*ACTGCGGATCTCTGTGTCAT*	*AGTAGTGTTCCCCACTGGTC*
VEGFA	*CAG CAC AAC AAA TGT GAA TGC A*	*ACA CGT CTG CGG ATC TTG TAC A*
β-Actin	*GAGCACAGAGCCTCGCCTTT*	*ACATGCCGGAGCCGTTGTC*
Zeb1	*TACCAGAGGATGACCTGCCA*	*TGCCCTTCCTTTCCTGTGTC*
CD31	*AAGTGGAGTCCAGCCGCATATC*	*ATGGAGCAGGACAGGTTCAGTC*
VE-cadherin	*GAAGCCTCTGATTGGCACAGTG*	*TTTTGTGACTCGGAAGAACTGGC*
eNOS	*CAACAGCATCTCCTGCTCAGA*	*CGAACACACAGAACCTGAGGG*
vWF	*GTGTGTCCGAGTGAAGGAGG*	*CAGCACGCTGAGGTCTTACA*
Oct-4	*CCTGAAGCAGAAGAGGATCAC*	*AAAGCGGCAGATGGTCGTTTGG*
Sox-2	*GCTACAGCATGATGCAGGACCA*	*TCTGCGAGCTGGTCATGGAGTT*
Mouse primers		
Gene	Forward (5'-3')	Reverse (5'-3')
HIF-1α	*AGG ATG AGT TCT GAA CGT CGA AA*	*ACA TTG TGG GGA AGT GGC AA*
E-cadherin	*CGCCACAGATGATGGTTCAC*	*GCAGTAAAGGGGGACGTGTT*
TGF-β	GCT GAA CCA AGG AGA CGG AAT	GTT CAT GTC ATG GAT GGT GCC
Vimentin	AGACCAGAGATGGACAGGTGA	TTGCGCTCCTGAAAAACTGC
VEGFA	CGGGCCTCGGTTCCA	GCAGCCTGGGACCACTTG
β-Actin	GTACTCTGTGTGGATCGGTGG	AGGGTGTAAAACGCAGCTCAG
Zeb1	GCTGGCAAGACAACGTGAAAG	GCCTCAGGATAAATGACGGC
CD31	GAGCCTCACCAAGAGAACGG	AGCGCCTCTGAGTCTCTGTA
VE-cadherin	TGCTCACGGACAAGATCAGC	GTGCGAAAACACAGGCCAAT
Zebrafish primers		
Gene	Forward (5'-3')	Reverse (5'-3')
HIF-1α	*CCACACATTACTGGATGGCT*	*GCAATGTTTCCGCGACAGG*
E-cadherin	*TCGGGAGGGTGAATCTCAGG*	*GAAGAAGAGCAAGCAATAGCAG*
N-cadherin	*TTCACCCGAGAGACTTTCCA*	*TGTCGGTCACGGTGAGATTG*
Vimentin	*ATCATTAAGCCTGCGAGAGTCC*	*GTCTCTGGTCTCGATGGTCTT*
β-Actin	*GGCAATGAGCGTTTCCGTTG*	*ATACCGCAAGATTCCATACCCAG*

A-1: Spectral characterization of synthesized compounds:

2-Amino-4-phenyl-4*H*-pyrano[2',3':4,5]imidazo[1,2-*a*]pyridine-3-carbonitrile (IMAP-1):

Yield: 74%; off-white solid; mp: 241-245 °C; IR (KBr, cm^{-1}) 3150, 2196, 1660, 1412, 1036, 738; ^{1}H-NMR (400 MHz, DMSO-*d*6): δ 7.68 (d, J = 6.8 Hz, 1H), 7.54 (d, J = 9.2 Hz, 1H), 7.36–7.33 (m, 2H), 7.29–7.23 (m, 4H), 7.12 (s, 2H), 6.89–6.85 (m, 1H), 5.18 (s, 1H); ^{13}C-NMR (100 MHz, DMSO-*d*6): δ160.54, 149.43,

140.89, 140.04, 128.85, 127.62, 127.54, 124.82, 123.94, 120.13, 116.11, 112.65, 100.71, 57.85, 36.89; LC-MS (APCI + ESI) *m/z*: 289 $[M + H]^+$; Anal. Calcd for $C_{17}H_{12}N_4O$: C, 70.82; H, 4.20; N, 19.43. Found: C, 70.98; H, 4.21; N, 19.49.

2-Amino-4-(*p*-tolyl)-4*H*-pyrano[2',3':4,5]imidazo[1,2-*a*]pyridine-3-carbonitrile (IMAP-2): Yield: 69%; off-white solid; mp: 246-250 °C; IR (KBr, cm^{-1}) 3149, 2193, 1657, 1404, 1035, 736; ^{1}H-NMR (400 MHz, DMSO-*d*6):*δ* 7.68 (d, *J* = 6.8 Hz, 1H), 7.54 (d, *J* = 8.8 Hz, 1H), 7.26 (t, *J* = 7.6 Hz, 1H), 7.15–7.10 (m, 6H), 6.87 (t, *J* = 6.8 Hz, 1H), 5.13 (s, 1H), 2.26 (s, 3H); ^{13}C-NMR (100 MHz, DMSO-*d*6): *δ*160.46, 149.37, 139.99, 137.87, 136.70, 129.41, 127.52, 124.75, 123.96, 120.14, 116.08, 112.62, 100.81, 58.00, 36.54, 20.60; LC-MS (APCI + ESI) *m/z*: 303 $[M + H]^+$; Anal. Calcd for $C_{18}H_{14}N_4O$: C, 71.51; H, 4.67; N, 18.53. Found: C, 71.69; H, 4.69; N, 18.61.

2-Amino-4-(4-methoxyphenyl)-4*H*-pyrano[2',3':4,5]imidazo[1,2-*a*]pyridine-3-carbonitrile (IMAP-3):

Yield: 72%; off-white solid; mp: 223-226 °C; IR (KBr, cm^{-1}) 3171, 2196, 1659, 1403, 1036, 734; ^{1}H-NMR (400 MHz, DMSO-*d*6):*δ* 7.67 (d, *J* = 6.8 Hz, 1H), 7.54 (d, *J* = 9.2 Hz, 1H), 7.26 (t, *J* = 8.0 Hz, 1H), 7.16 (d, *J* = 8.8 Hz, 2H), 7.08 (s, 2H), 6.90–6.86 (m, 3H), 5.12 (s, 1H) 3.72 (s,3H); ^{13}C-NMR (100 MHz, DMSO-*d*6): *δ*160.38, 158.52, 149.33, 139.98, 132.74, 128.73, 124.73, 123.95, 120.18, 116.07, 114.17, 112.60, 100.92, 58.20, 54.99, 36.14; LC-MS (APCI + ESI) *m/z*: 319 $[M + H]^+$; Anal. Calcd for $C_{18}H_{14}N_4O_2$: C, 67.91; H, 4.43; N, 17.60. Found: C, 68.02; H, 4.44; N, 17.65.

2-Amino-4-(4-(dimethylamino)phenyl)-4*H*-pyrano[2',3':4,5]imidazo[1,2-*a*]pyridine-3-carbonitrile (IMAP-4): Yield: 71%; off-white solid; mp: 230-233 °C; IR (KBr, cm^{-1}) 3169, 2194, 1657, 1406, 1036, 741; ^{1}H-NMR (400 MHz, DMSO-*d*6):*δ* 7.67 (d, *J* = 6.8 Hz, 1H), 7.53 (d, *J* = 9.2 Hz, 1H), 7.25 (t, *J* = 7.2 Hz, 1H), 7.05–7.01 (m, 4H), 6.87 (t, *J* = 6.8 Hz, 1H), 6.66 (d, *J* = 8.4 Hz, 2H), 5.03 (s, 1H), 2.86 (s, 6H); ^{13}C-NMR (100 MHz, DMSO-*d*6): *δ*160.24, 149.66, 149.24, 139.87, 128.17, 127.96, 124.58, 124.00, 120.30, 116.02, 112.47, 101.25, 58.57, 36.09; LC-MS (APCI + ESI) *m/z*: 332 $[M + H]^+$; Anal. Calcd for $C_{19}H_{17}N_5O$: C, 68.87; H, 5.17; N, 21.13. Found: C, 68.99; H, 5.18; N, 21.18.

2-Amino-4-(4-chlorophenyl)-4H-pyrano[2',3':4,5]imidazo[1,2-*a*]pyridine-3-carbonitrile (IMAP-5): Yield: 76%; off-white solid; mp: 248-251 °C; IR (KBr, cm^{-1}) 3140, 2195, 1659, 1428, 1037, 738; ^{1}H-NMR (400 MHz, DMSO-*d*6):*δ* 7.70 (d, *J* = 6.8 Hz, 1H), 7.55 (d, *J* = 9.2 Hz, 1H), 7.42–7.40 (m, 2H), 7.31–7.26 (m, 3H), 7.12 (s, 2H), 6.88 (td, *J* = 6.8, 0.8 Hz, 1H), 5.22 (s, 1H); ^{13}C-NMR (100 MHz, DMSO-*d*6): *δ*160.59, 149.49, 140.14, 139.90, 132.08, 129.53, 128.86, 124.98, 123.96, 120.00, 116.15, 112.79, 100.25, 57.43, 36.25; LC-MS (APCI + ESI) *m/z*: 323 $[M + H]^+$; Anal. Calcd for $C_{17}H_{11}ClN_4O$: C, 63.26; H, 3.44; N, 17.36. Found: C, 63.40; H, 3.45; N, 17.41.

2-Amino-4-(4-fluorophenyl)-4*H*-pyrano[2',3':4,5]imidazo[1,2-*a*]pyridine-3-carbonitrile (IMAP-6): Yield: 78%; off-white solid; mp: 236-239 °C; IR (KBr, cm^{-1}) 3141, 2198, 1659, 1410, 1040, 737; ^{1}H-NMR (400 MHz, DMSO-*d*6):*δ* 7.69 (d, *J* = 6.8 Hz, 1H), 7.55 (d, *J* = 9.2 Hz, 1H), 7.30–7.26 (m, 3H), 7.19–7.16 (m, 4H), 6.89 (t, *J* = 6.8 Hz, 1H), 5.22 (s, 1H); ^{13}C-NMR (100 MHz, DMSO-*d*6): *δ*160.52, 149.43, 140.10, 137.09, 137.06, 129.65, 129.56, 124.92, 123.94, 120.05, 116.14, 115.75, 115.53, 112.73, 100.52, 57.75, 36.13; LC-MS (APCI + ESI) *m/z*: 307 $[M + H]^{+}$; Anal. Calcd for $C_{17}H_{11}FN_4O$: C, 66.66; H, 3.62; N, 18.29. Found: C, 66.76; H, 3.63; N, 18.35.

2-Amino-4-(2,4-difluorophenyl)-4*H*-pyrano[2',3':4,5]imidazo[1,2-*a*]pyridine-3-carbonitrile (IMAP-7): Yield: 80%; off-white solid; mp: 219-222 °C; IR (KBr, cm^{-1}) 3138, 2192, 1660, 1412, 1039, 740; ^{1}H-NMR (400 MHz, DMSO-*d*6):*δ* 7.67 (d, *J* = 6.8 Hz, 1H), 7.56 (d, *J* = 9.2 Hz, 1H), 7.31–7.21 (m, 5H), 7.05 (t, *J* = 8.4 Hz, 1H), 6.92 (t, *J* = 6.8 Hz, 1H), 5.45 (s, 1H); ^{13}C-NMR (100 MHz, DMSO-*d*6): *δ*161.04, 149.72, 140.09, 131.17, 131.12, 124.92, 123.70, 123.61, 123.46, 119.89, 116.20, 112.96, 112.26, 112.04, 99.18, 55.97, 30.92; LC-MS (APCI + ESI) *m/z*: 325 $[M + H]^{+}$; Anal. Calcd for $C_{17}H_{10}F_2N_4O$: C, 62.96; H, 3.11; N, 17.28. Found: C, 63.10; H, 3.12; N, 17.34.

2-Amino-4-(3-bromophenyl)-4*H*-pyrano[2',3':4,5]imidazo[1,2-*a*]pyridine-3-carbonitrile (IMAP-8): Yield: 79%; off-white solid; mp: 242-245 °C; IR (KBr, cm^{-1}) 3152, 2193, 1658, 1404, 1037, 739; ^{1}H-NMR (400 MHz, DMSO-*d*6):*δ* 7.74 (d, *J* = 6.8 Hz, 1H), 7.57 (d, *J* = 9.2 Hz, 1H), 7.49–7.47 (m, 2H), 7.33–7.28 (m, 2H), 7.23–7.21 (m, 3H), 6.92 (td, *J* = 6.8, 1.2 Hz, 1H), 5.22 (s, 1H); ^{13}C-NMR (100 MHz, DMSO-*d*6): *δ*160.68, 149.54, 143.76, 140.18, 131.13, 130.56, 130.32, 126.73, 125.07, 123.96, 122.08, 119.96, 116.19, 112.87, 100.08, 57.31, 36.46; LC-MS (APCI + ESI) *m/z*: 367 $[M + H]^{+}$; Anal. Calcd for $C_{17}H_{11}BrN_4O$: C, 55.61; H, 3.02; N, 15.26. Found: C, 55.73; H, 3.02; N, 15.30.

2-Amino-4-(4-cyanophenyl)-4*H*-pyrano[2',3':4,5]imidazo[1,2-*a*]pyridine-3-carbonitrile (IMAP-9): Yield: 82%; off-white solid; mp: 247-250 °C; IR (KBr, cm^{-1}) 3123, 2197, 1661, 1405, 1040, 750; ^{1}H-NMR (400 MHz, DMSO-*d*6):*δ* 7.82 (d, *J* = 8.4 Hz, 2H), 7.71 (d, *J* = 6.4 Hz, 1H), 7.56 (d, *J* = 9.2 Hz, 1H), 7.46 (d, *J* = 8.4 Hz, 2H), 7.32–7.26 (m, 3H), 6.89 (t, *J* = 6.8 Hz, 1H), 5.33 (s, 1H); ^{13}C-NMR (100 MHz, DMSO-*d*6): *δ*160.80, 149.66, 146.46, 140.27, 132.91, 128.74, 125.16, 123.96, 119.86, 118.53, 116.22, 112.91, 110.44, 99.73, 56.80, 36.79; LC-MS (APCI + ESI) *m/z*: 314 $[M + H]^{+}$; Anal. Calcd for $C_{18}H_{11}N_5O$: C, 69.00; H, 3.54; N, 22.35. Found: C, 69.15; H, 3.55; N, 22.42.

2-Amino-4-(4-nitrophenyl)-4*H*-pyrano[2',3':4,5]imidazo[1,2-*a*]pyridine-3-carbonitrile (IMAP-10): Yield: 85%; light yellow solid; mp: 243-246 °C; IR (KBr, cm^{-1}) 3126, 2198, 1662, 1405, 1041, 721; ^{1}H-NMR (400 MHz, DMSO-*d*6):*δ* 8.21 (d, *J* = 8.4 Hz, 2H), 7.73 (d, *J* = 6.8 Hz, 1H), 7.58–7.53 (m, 3H), 7.32–7.28 (m, 3H), 6.89 (t, *J* = 6.8 Hz, 1H), 5.41 (s, 1H); ^{13}C-NMR (100 MHz, DMSO-*d*6): *δ*160.84, 149.65, 148.45, 146.92, 140.33, 129.07, 125.24, 124.17, 124.03, 119.85, 116.25, 112.96, 99.71, 56.66, 36.58; LC-MS (APCI + ESI) *m/z*: 334 $[M + H]^{+}$; Anal. Calcd for $C_{17}H_{11}N_5O_3$: C, 61.26; H, 3.33; N, 21.01. Found: C, 61.40; H, 3.34; N, 21.08.

Methyl 4-(2-amino-3-cyano-4*H*-pyrano[2',3':4,5]imidazo[1,2-*a*]pyridin-4-yl)benzoate (IMAP-11): Yield: 83%; off-white solid; mp: 245-248 °C; IR (KBr, cm^{-1}) 3136, 2193, 1658, 1403, 1038, 728; ^{1}H-NMR (400 MHz, DMSO-*d*6):*δ* 7.94 (d, *J* = 8.4 Hz, 2H), 7.68 (d, *J* = 6.8 Hz, 1H), 7.56 (d, *J* = 9.2 Hz, 1H), 7.41 (d, *J* = 8.0 Hz, 2H), 7.30–7.26 (m, 1H), 7.23 (s, 2H), 6.87 (td, *J* = 6.8, 0.8 Hz, 1H), 5.30 (s, 1H), 3.83 (s, 3H); ^{13}C-NMR (100 MHz, DMSO-*d*6): *δ*165.86, 160.71, 149.54, 146.22, 140.19, 129.83, 128.93, 128.12, 125.04, 123.94, 119.92, 116.18, 112.81, 100.10, 57.12, 52.09, 36.78; LC-MS (APCI + ESI) *m/z*: 347 $[M + H]^{+}$; Anal. Calcd for $C_{19}H_{14}N_4O_3$: C, 65.89; H, 4.07; N, 16.18. Found: C, 65.98; H, 4.09; N, 16.22.

2-Amino-4-(4-(trifluoromethyl)phenyl)-4*H*-pyrano[2',3':4,5]imidazo[1,2-*a*]pyridine-3-carbonitrile (IMAP-12): Yield: 81%; off-white solid; mp: 258-260 °C; IR (KBr, cm^{-1}) 3136, 2198, 1661, 1405, 1068, 731; ^{1}H-NMR (400 MHz, DMSO-*d*6):*δ* 7.73–7.71 (m, 3H), 7.57 (d, *J* = 9.2 Hz, 1H), 7.48 (d, *J* = 7.6 Hz, 2H), 7.31–7.24 (m, 3H), 6.90 (t, *J* = 7.2 Hz, 1H), 5.34 (s, 1H); ^{13}C-NMR (100 MHz, DMSO-*d*6): *δ*160.73, 149.62, 145.62, 140.24, 128.54, 125.86, 125.82, 125.10, 123.96, 122.76, 119.93, 116.20, 112.90, 99.97, 57.09, 36.60; LC-MS (APCI + ESI) *m/z*: 357 $[M + H]^{+}$; Anal. Calcd for $C_{18}H_{11}F_3N_4O$: C, 60.68; H, 3.11; N, 15.72. Found: C, 60.81; H, 3.12; N, 15.76.

2-Amino-4-(pyridin-3-yl)-4*H*-pyrano[2',3':4,5]imidazo[1,2-*a*]pyridine-3-carbonitrile(IMAP-13): Yield: 79%; off-white solid; mp: 234-237 °C; IR (KBr, cm^{-1}) 3156, 2190, 1656, 1402, 1034, 741; ^{1}H-NMR (400 MHz, DMSO-*d*6):*δ* 8.57 (d, *J* = 1.6 Hz, 1H), 8.49 (dd, *J* = 1.2, 4.8 Hz, 1H), 7.75 (d, *J* = 6.8 Hz, 1H), 7.58–7.56 (m, 2H), 7.37–7.28 (m, 2H), 7.25 (s, 2H), 6.90 (t, *J* = 6.8 Hz, 1H), 5.28 (s, 1H); ^{13}C-NMR (100 MHz, DMSO-*d*6): *δ*160.75, 149.66, 148.99, 148.95, 140.22, 136.29, 135.27, 125.08, 124.15, 123.93, 119.97, 116.21, 112.87, 99.73, 57.05, 34.45; LC- MS (APCI + ESI) *m/z*: 290 $[M + H]^{+}$; Anal. Calcd for $C_{16}H_{11}N_5O$: C, 66.43; H, 3.83; N, 24.21. Found: C, 66.55; H, 3.84; N, 24.26.

2-Amino-4-(2-chloropyridin-4-yl)-4*H*-pyrano[2',3':4,5]imidazo[1,2-*a*]pyridine-3-carbonitrile (IMAP-14): Yield: 80%; off-white solid; mp: 235-238 °C; IR (KBr, cm^{-1}) 3099 2191, 1656, 1408, 1040, 737; ^{1}H-NMR (400 MHz, DMSO-*d*6):*δ* 8.37 (d, *J* = 5.2 Hz, 1H), 7.80 (d, *J* = 6.8 Hz, 1H), 7.58 (d, *J* = 9.2 Hz, 1H), 7.49 (s, 1H), 7.35–7.30 (m, 3H), 7.24 (d, *J* = 4.4 Hz, 1H), 6.94 (t, *J* = 6.8 Hz, 1H), 5.29 (s, 1H); ^{13}C-NMR (100 MHz, DMSO-*d*6): *δ*161.04, 153.63, 150.85, 150.69, 149.80, 140.41, 125.36, 124.07, 123.23, 122.20, 119.71, 116.27, 113.09, 98.77, 55.84, 35.92; LC-MS (APCI + ESI) *m/z*: 324 $[M + H]^{+}$; Anal. Calcd for $C_{16}H_{10}ClN_5O$: C, 59.36; H, 3.11; N, 21.63. Found: C, 59.51; H, 3.13; N, 21.71.

2-Amino-4-(5-bromopyridin-3-yl)-4*H*-pyrano[2',3':4,5]imidazo[1,2-*a*]pyridine-3-carbonitrile (IMAP-15): Yield: 83%; off-white solid; mp: 253-256 °C; IR (KBr, cm^{-1}) 3137, 2192, 1654, 1406, 1034, 742; ^{1}H-NMR (400 MHz, DMSO-*d*6):*δ* 8.65 (d, *J* = 2.0 Hz, 1H), 8.53 (d, *J* = 2.0 Hz, 1H), 7.91 (t, *J* = 2.0 Hz, 1H), 7.81 (d, *J* = 6.8 Hz, 1H), 7.58 (d, *J* = 9.2 Hz, 1H), 7.34– 7.30 (m, 3H), 6.93 (td, *J* = 6.8, 0.8 Hz, 1H), 5.31 (s, 1H); ^{13}C-NMR (100 MHz, DMSO-*d*6): *δ*160.89, 149.79, 149.73, 147.64, 140.33, 138.61, 137.76, 125.25, 123.98, 120.65, 119.87, 116.26, 113.02, 99.09, 56.49, 34.15; LC-MS (APCI + ESI) *m/z*: 368 $[M + H]^{+}$; Anal. Calcd for $C_{16}H_{10}BrN_5O$: C, 52.19; H, 2.74; N, 19.02. Found: C, 52.29; H, 2.75; N, 19.08.

A-2: NMR (Nuclear Magnetic Resonance) (^{1}H &^{13}C), MS (Mass Spectrometry) and IR (Infrared spectroscopy) , and HPLC (High Performance Liquid Chromatography) spectral of IMPA- 2, 5, 6, 8 and 12

IMPA-2

NMR ^{1}H

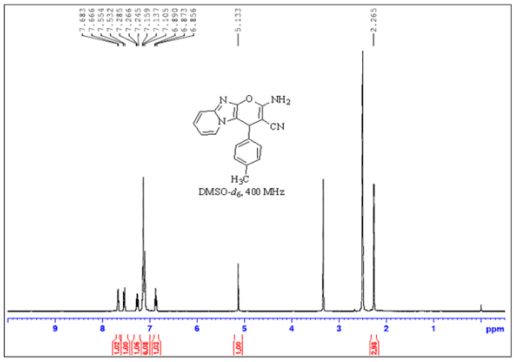

NMR ^{13}C

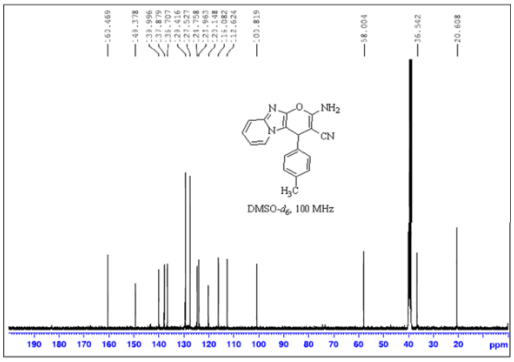

MS

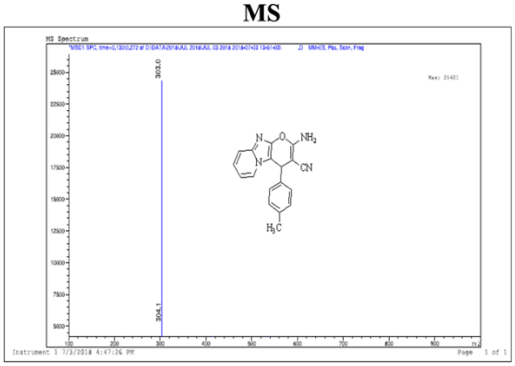

IR

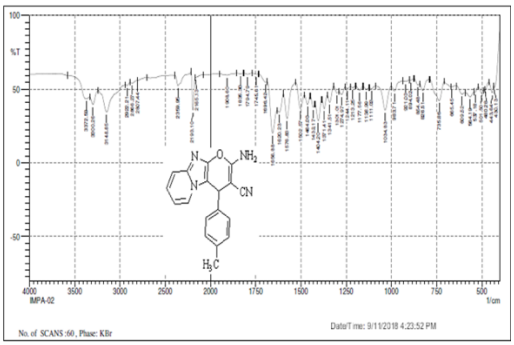

IMPA-5

NMR ^{1}H

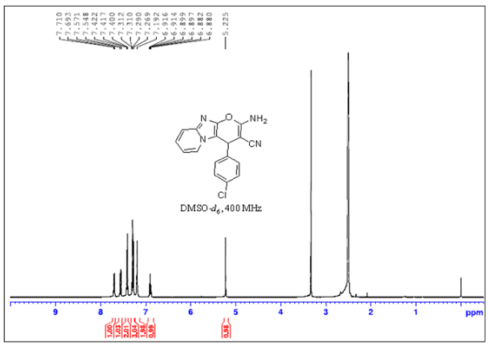

NMR ^{13}C

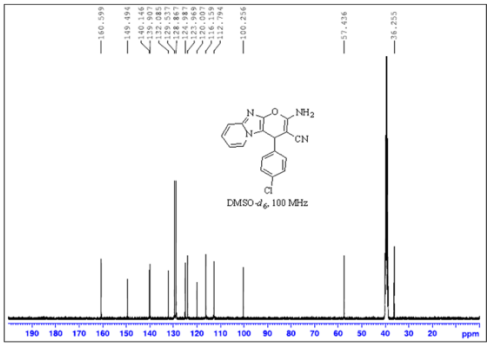

MS

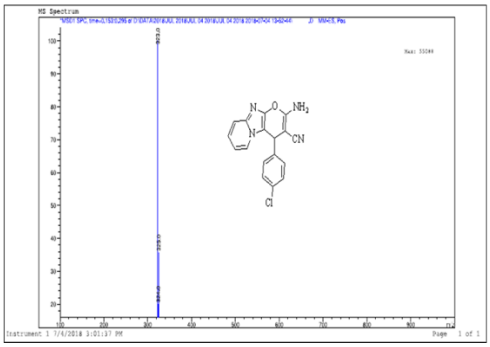

IR

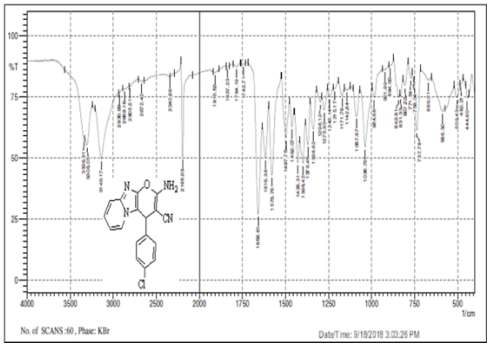

IMPA-6

NMR ^{1}H

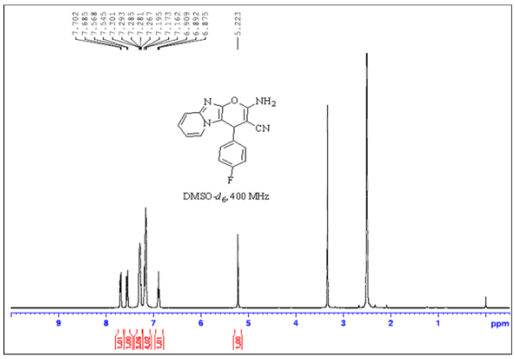

NMR ^{13}C

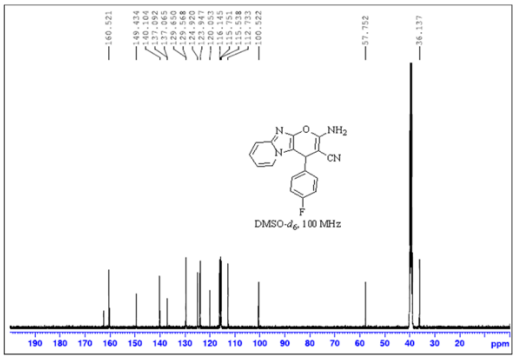

MS

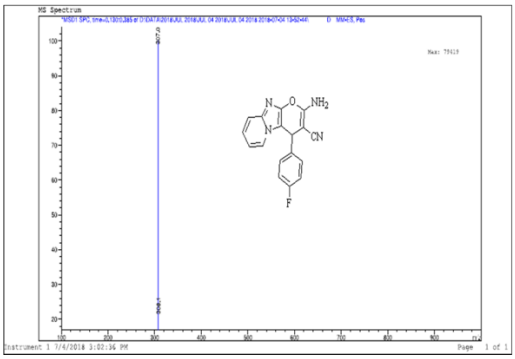

IR

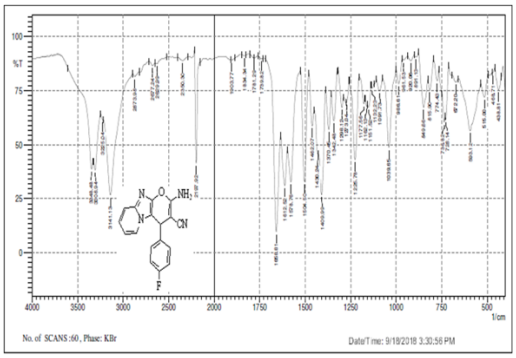

IMPA-8

NMR ^{1}H

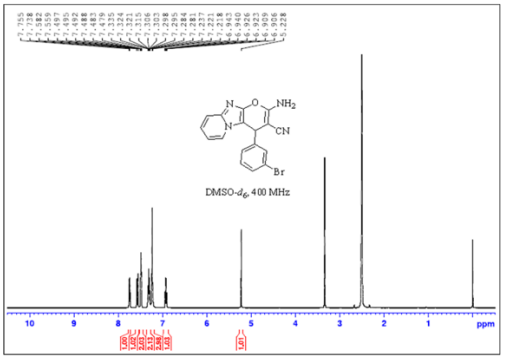

NMR ^{13}C

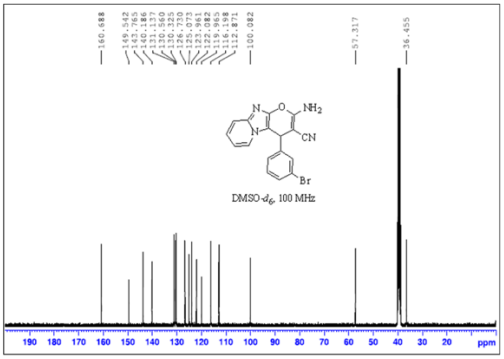

MS

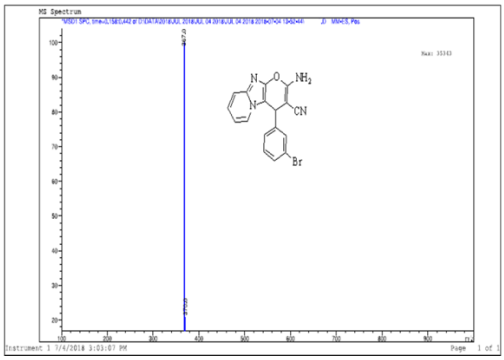

IR

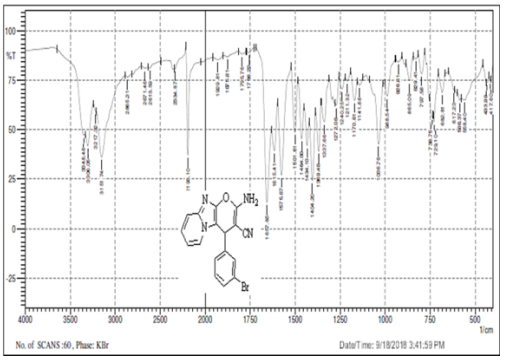

IMPA-12

NMR ^{1}H

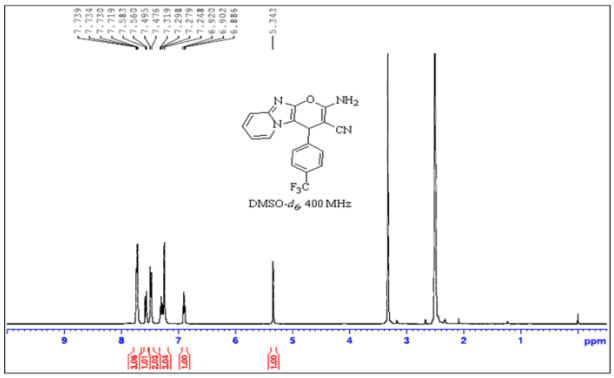

NMR ^{13}C

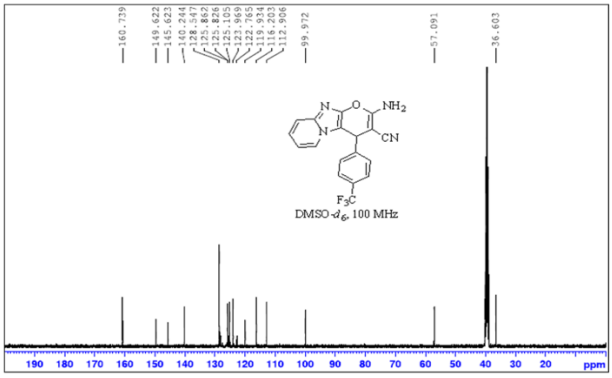

MS

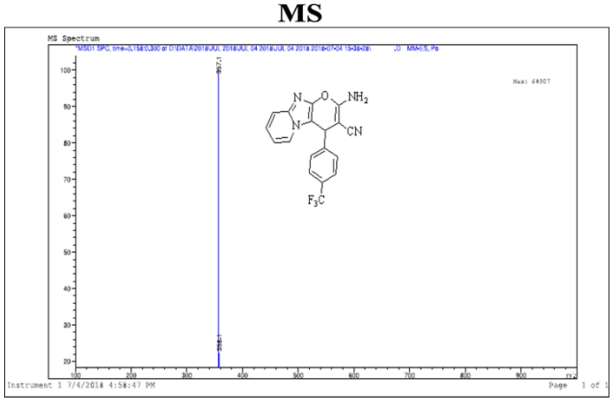

IR

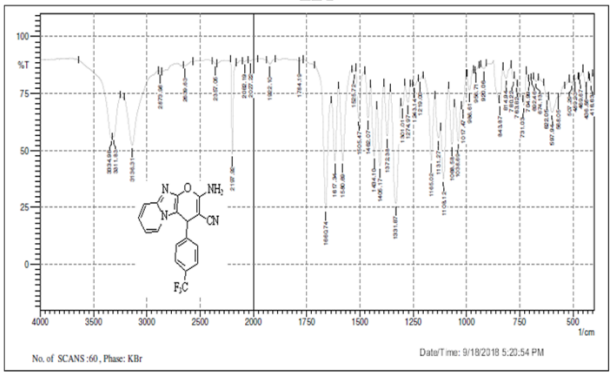

HPLC spectral

IMPA-2

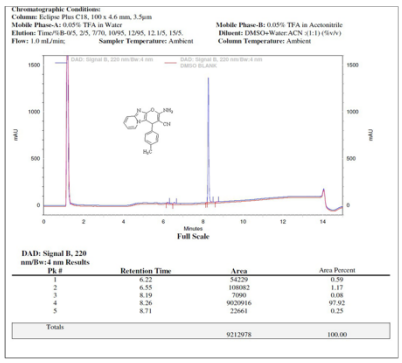

IMPA-5

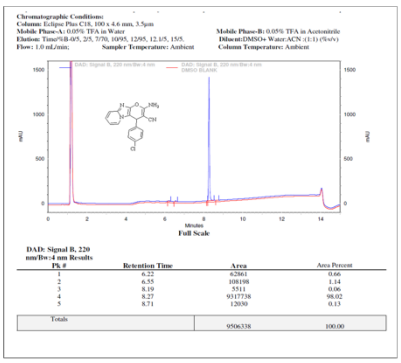

IMPA-6

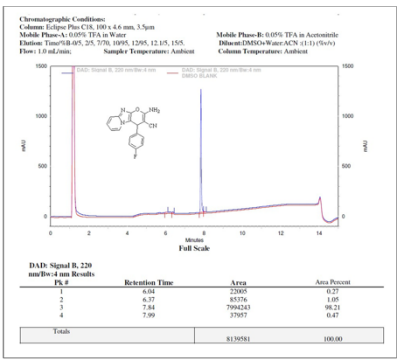

IMPA-8

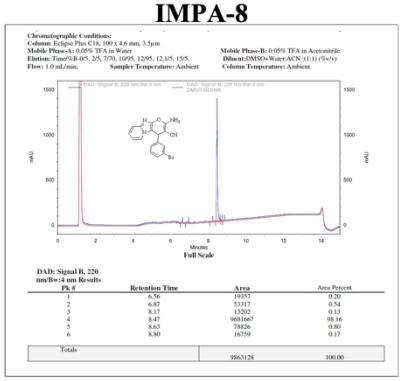

IMPA-12